UNIVERSITY of CALIFORNIA

Santa Barbara

Magnetostructural and magnetodielectric coupling in spinel oxides

A Dissertation submitted in partial satisfaction of the

requirements for the degree

Doctor of Philosophy

in

Materials

by

Moureen Chemurgor Kemei

Committee in charge:

Professor Ram Seshadri, Chair

Professor S. Jim Allen

Professor Chris Palmstrøm

Professor Ed Kramer

September 2014

The dissertation of Moureen Chemurgor Kemei is approved.

Professor S. Jim Allen

Professor Chris Palmstrøm

Professor Ed Kramer

Professor Ram Seshadri, Committee Chair

July 2014

Magnetostructural and magnetodielectric coupling in spinel oxides

by

Moureen Chemurgor Kemei

for my family

Acknowledgements

As I approach the end of one journey in life and the start of another, it is a pleasure to reflect on the wonderful people that have made this trip so memorable. It has been a wonderful experience to spend the last few years in scenic Santa Barbara, learning and researching in the one-of-a-kind materials program here. I will start by thanking my adviser, Professor Ram Seshadri, for his incredible mentorship and support during my PhD career. Ram's enthusiasm, generosity, creativity, and positive attitude has made my graduate school experience exceptional and truly inspiring. I will reflect on Ram's refreshing approach to science that reminds me of the treasure in every scientific puzzle. Professor Jim Allen has fueled my enthusiasm for science by sharing his curiosity for knowledge. I am thankful for Jim's unwavering support during my career. I thank my committee members, Professor Chris Palmstrøm and Professor Ed Kramer for generously sharing their time, advice, and support.

My appreciation goes to the Schlumberger Faculty for the Future foundation for the incredible opportunity to pursue a graduate education. I also thank my fellow Schlumberger fellows, who by example, inspire me to succeed.

Home is where the journey began. I thank my wonderful family for the continuous love and support. I thank my mother for dreaming with me and for

the gift of education. Thank you to my siblings for the wonderful times growing up and for the conversations over the phone during my stay in the US. Your love for life gives me joy.

Friends have helped me find a home away from home. I thank my best friend Bryan Myers for his immeasurable kindness, love, and support. Your companionship has made the last few years of my PhD exceptionally memorable. I am excited and thankful for the wonderful experiences we have shared and I can't wait for what the future holds. I thank Bryan's family for welcoming me and sharing many special moments with me including graduation.

Great contributions from collaborators have been at the heart of every project I have pursued. I thank Dr. Matthew Suchomel of Argonne National Laboratory for great collaboration over the years as we studied structural distortions in spinel oxides. I am also indebted to Dr. Daniel Shoemaker, Dr. Taylor Sparks, Professor Young-Il Kim, Dr. Vivien Zapf, Dr. Kate Page, and Dr. Josh Kurzman for many successful collaborations over the years.

Seshadri group members are a remarkable crew. Thank you all for your friendship. Doing science with you has been one of the best experiences in my life. I thank Dr. Phillip Barton for the wonderful discussions about magnetic oxides, the trips to National Laboratories, and travel to the American Physical

Society meetings. I acknowledge Dr. Brent Melot and Dr. Jamie Nielsen for guiding me during my first days in the lab. I am deeply grateful to my interns Stephanie, Lucy, Madeline, Laura, Josef, and David for generously contributing to my scientific efforts. My time with you was very enjoyable and your contributions are important to my work. I thank Kristin Denault my colleague for sharing with me many crucial milestones in graduate school. I thank Dr. Lauren Misch and Jason Douglas for being outstanding office mates. You put a smile on every minute of our times together. I thank Kim See for the many runs we shared. Kim, your energy is infectious and I am thankful for your friendship and encouragement. I thank Megan Butala for the many engaging discussions about manganese oxides, phase transformations, and life. I thank Mike Gaultois for always adding zest to life. Mike, thank you for always bringing insight to my thought process when I was puzzling over data. Your unceasing willingness to lend a helping hand inspires me to help others. Many thanks to Jaye Harada for being a wonderful source of help. Jaye, I am especially thankful for your willingness to help me set up many capacitance measurements. I thank Dr. Jakoah Brgoch for assisting me with density functional theory calculations and for helping me think though my data on many occasions. I always enjoyed encounters with Bethany Lettier. I thank Leo Lamontagne and Dr. Anna Lehner for shared conversations and laughs in lab.

I thank the MRL staff, Amanda, Maureen, Joe, Janet, Fuzzy and Sylvia for helping me navigate the essential activities that are integral to the graduate school experience such as getting access to labs, processing reimbursements, and training on lab equipment. Your assistance made things run smoothly during my PhD. I thank Amanda Strom for being incredibly helpful in the lab while I attempted new synthesis techniques.

I thank my host family for welcoming me into your home. You helped me navigate my very first days in the US and you continue to be my friends and family. I am very grateful for your support over the years. I thank my friends Paul(and family), Abby, Caroline, Patricia, Jackie, Judith, Constantina, Chandra, Sheena, and Hati, just to name a few. I cherish all the times we have shared together and I am thankful that you were always present to celebrate the good times and to help me though the challenging times. I also thank my undergraduate adviser, Professor Kathy Aidala, for helping me throughout my undergraduate career and for being a constant source of support. I also acknowledge the support of many of my undergraduate professors including Professor Shubha Tewari.

Finally, words cannot express my gratitude to God for his wonderful guidance throughout my life. Ephesians 3:20: *Now unto him that is able to do exceeding abundantly above all that we ask or think, according to the power that worketh*

in us.

Curriculum Vitæ

Moureen Chemurgor Kemei

Education

2010–2014	Ph.D. in Materials, Materials Department, University of California, Santa Barbara, CA.
2006–2010	B.A. in Physics (Magma cum laude), Department of Physics, Mount Holyoke College, South Hadley, MA.

Publications

12. M. C. Kemei, J. K. Harada, M. R. Suchomel, and R. Seshadri, Structural phase coexistence in the magnetodielectric spinel Mn_3O_4. (*submitted*) (2014) arXiv:1407.2299

11. P. T. Barton, M. C. Kemei, M. W. Gaultois, S. L. Moffitt, L. E. Darago, R. Seshadri, M. R. Suchomel, B. C. Melot, Structural distortion below the Néel temperature in spinel $GeCo_2O_4$. (*submitted*) (2014) arXiv:1405.7099

10. Y. Zheng, M. Miao, M. C. Kemei, R. Seshadri, and F. Wudl, The pyrenotriazinyl radical - magnetic and sensor properties, *Israel J. Chem.* **54** (2014) 774)

9. M. C. Kemei, S. L. Moffitt, L. E. Dagaro, R. Seshadri, M. R. Suchomel, D. P. Shoemaker, K. Page, and J. Siewenie, Structural ground states of $(A, A')Cr_2O_4$(A=Mg, Zn; A' = Co, Cu) spinel solid solutions: Spin-Jahn-Teller and Jahn-Teller effects, *Phys. Rev. B* **89** (2014) 174410

8. T. D. Sparks, M. C. Kemei, P. T. Barton, R. Seshadri, E. D. Mun, and V. Zapf, Magnetocapacitance as a sensitive probe of magnetostructural changes in $NiCr_2O_4$, *Phys. Rev. B* **89** (2014) 0244051

7. M. C. Kemei, P. T. Barton, S. L. Moffitt, M. W. Gaultois, J. A. Kurzman, R. Seshadri, M. R. Suchomel, and Y-Il. Kim, Crystal structures of spin-Jahn-Teller-ordered $MgCr_2O_4$ and $ZnCr_2O_4$, *J. Phys.: Condens. Matter* **25** (2013) 326001

6. F. Wrobel, M. C. Kemei, and S. Derakhshan, Antiferromagnetic spin correlations between corner-shared $[FeO_5]^{7-}$ and $[FeO_6]^{9-}$ units in the novel iron-based compound: $BaYFeO_4$, *Inorg. Chem.* **52** (2013) 2671

5. M. R. Suchomel, D. P. Shoemaker, L. Ribaud, M. C. Kemei, and R. Seshadri, Spin-induced symmetry breaking in orbitally ordered $NiCr_2O_4$ and $CuCr_2O_4$, *Phys. Rev. B* **86** (2012) 0544061

4. B. C. Melot, G. Rousse, J-N. Chotard, M. Ati, M. C. Kemei, and J-M. Tarascon, Magnetic structure and properties of $NaFeSO_4F$ and $NaCoSO_4F$, *Phys.*

Rev. B **85** (2012) 094415

3. M. C. Kemei, S. L. Moffitt, D. P. Shoemaker, and R. Seshadri, Evolution of magnetic properties in the normal spinel solid solution $Mg_{1-x}Cu_xCr_2O_4$, *J. Phys.: Condens. Matter* **24** (2012) 046003

2. B. C. Melot, G. Rousse, J-N. Chotard, M. Ati, J-R. Carvajal, M. C. Kemei, and J-M. Tarascon, Magnetic structure and properties of the Li-ion battery materials $FeSO_4F$ and $LiFeSO_4F$, *Chem. Mater.* **23** (2011) 2922

1. T. Yang, N. R. Pradhan, A. Goldman, A. S. Licht, Y. Li, M. C. Kemei, M. T. Tuominen, K. E. Aidala., Manipulation of magnetization states of ferromagnetic nanorings by an applied azimuthal Oersted field, *Appl. Phys. Lett.* **98** (2011) 242505

Abstract

Magnetostructural and magnetodielectric coupling in spinel oxides

by

Moureen Chemurgor Kemei

Spinels oxides are of great interest functionally as multiferroic, battery, and magnetic materials as well as fundamentally because they exhibit novel spin, structural, and orbital ground states. Competing interactions are at the heart of novel functional behavior in spinels. Here, we explore the intricate landscape of spin, lattice, and orbital interactions in magnetic spinels by employing variable-temperature high-resolution synchrotron x-ray powder diffraction, total neutron scattering, magnetic susceptibility, dielectric, and heat capacity measurements. We show that the onset of long-range magnetic interactions often gives rise to lattice distortions. We present the complete crystallographic descriptions of the ground state structures of several spinels, thereby paving the way for accurate modeling and design of structure-property relationships in these materials. We also report the emergence of magnetodielectric coupling in the magnetostructural phases of some of the studied spinels.

We begin by examining spin-lattice coupling in the Jahn-Teller active systems $NiCr_2O_4$ and $CuCr_2O_4$. Orbital ordering yields a cubic to tetragonal lattice distortion in these materials above their magnetic ordering temperatures, however, we find that magnetic ordering also drives structural distortions in these spinels through exchange striction. We provide the first orthorhombic structural descriptions of $NiCr_2O_4$ and $CuCr_2O_4$. Our observation of strong spin-lattice coupling in $NiCr_2O_4$ and $CuCr_2O_4$ inspired the study of magnetodielectric coupling in these spinels. Magnetocapacitance measurements of $NiCr_2O_4$ reveal multiferroic behavior and new magnetostructural distortions below the Néel temperature. This observation illustrates the sensitivity of dielectric measurements to magnetostructural transitions in spinel materials. Finally, in the examination of $NiCr_2O_4$ we show that magnetodielectric coupling is well described by Ginzburg-Landau theory.

In addition to exchange striction, geometric frustration couples spin interactions to the lattice of the spinels $MgCr_2O_4$ and $ZnCr_2O_4$. Novel spin ground states that are important for memory and quantum computing applications are predicted to exist in these spinels. However, their structural and spin ground states are not well understood. We find that tetragonal and orthorhombic phases coexist in antiferromagnetic $MgCr_2O_4$ and $ZnCr_2O_4$. The structural deformations in these materials lift spin degeneracy by primarily distorting the pyrochlore Cr

sublattice. In subsequent studies, we probe the effect of adding dilute spins on the non-magnetic cation sites of $MgCr_2O_4$ and $ZnCr_2O_4$. Substitution of Co^{2+} cations in $Zn_{1-x}Co_xCr_2O_4$ completely suppress the spin-Jahn-Teller distortion of $ZnCr_2O_4$ while, Cu^{2+} substitutions in $Mg_{1-x}Cu_xCr_2O_4$ and $Zn_{1-x}Cu_xCr_2O_4$ induce Jahn-Teller distortions at temperatures above their magnetic ordering temperatures. The Jahn-Teller distortions of $Mg_{1-x}Cu_xCr_2O_4$ and $Zn_{1-x}Cu_xCr_2O_4$ do not lift spin degeneracy, therefore magnetic ordering is still suppressed down to low temperatures. We show that only more than 20% magnetic A substituents can lift spin degeneracy in $MgCr_2O_4$ and $ZnCr_2O_4$.

We have also examined the magnetostructural phase transition of the spinel Mn_3O_4. We show that Mn_3O_4 undergoes a magnetostructural phase transition from tetragonal $I4_1/amd$ symmetry to a phase coexistence regime consisting of tetragonal $I4_1/amd$ and orthorhombic $Fddd$ symmetries. Phase coexistence in Mn_3O_4 is mediated by strain due to a significant lattice mismatch between the low temperature orthorhombic phase and the high temperature tetragonal phase. We propose that strain could be used to control the structure and properties of Mn_3O_4.

Our investigations of spin-driven lattice distortions in spinel oxides illustrate that structural phase coexistence is prevalent for spinels with Néel temperatures below 50 K.

Contents

List of Figures

List of Tables

Chapter 1

Introduction: Magnetic spinel oxides

Spinels are an intriguing class of materials that exhibit rich complex behavior and novel ground states such as spin liquid states,[1] large magnetoresistance effects,[2] non-collinear spin configurations,[3] and magnetodielectric coupling.[4] Stong interactions between spin, orbital, and structural degrees of freedom give rise to complex states. An example of emergent behavior that has motivated much interest in these materials occurs when the lattice geometry inhibits magnetic ordering, an effect commonly known as geometric frustration.[5–7] Frustrated magnets are solid analogues of liquid-

and ice- like states. Investigations of frustrated spin systems have shown that novel states such as zero-energy excitations[8] and complex spin and structural configurations[1, 8] occur in these materials. Here, we examine the interaction between spin and structural degrees of freedom in spinel oxides which undergo concomitant structural and magnetic phase transitions. We present the first descriptions of the low temperature structures of several spinel oxides and develop an understanding of the mechanisms behind lattice distortions in spinels. The determination of structure in spinel oxides is pivotal to developing structure-property relationships and predicting new properties, and it gives insight about the unknown ground states of frustrated materials. We begin by examining first the spinel structure and second the electronic and magnetic interactions that are important in magnetic spinel oxides.

Named after the mineral $MgAl_2O_4$, spinels are characterized by two cation sites: a tetrahedral site and an octahedral site. They adopt face-centered cubic symmetry at high temperatures and are described by the space group $Fd\bar{3}m$. Tetrahedral cations occupy the special Wyckoff positions $8d$ while their octahedral counterparts occupy special Wyckoff positions $16d$. The anions are located at general Wyckoff $32e$ positions that are assigned the parameter u, which takes on various values around the ideal position u =0.25 for different spinels. When u =0.25, the spinel structure has perfect tetrahedral and octahedral units. The

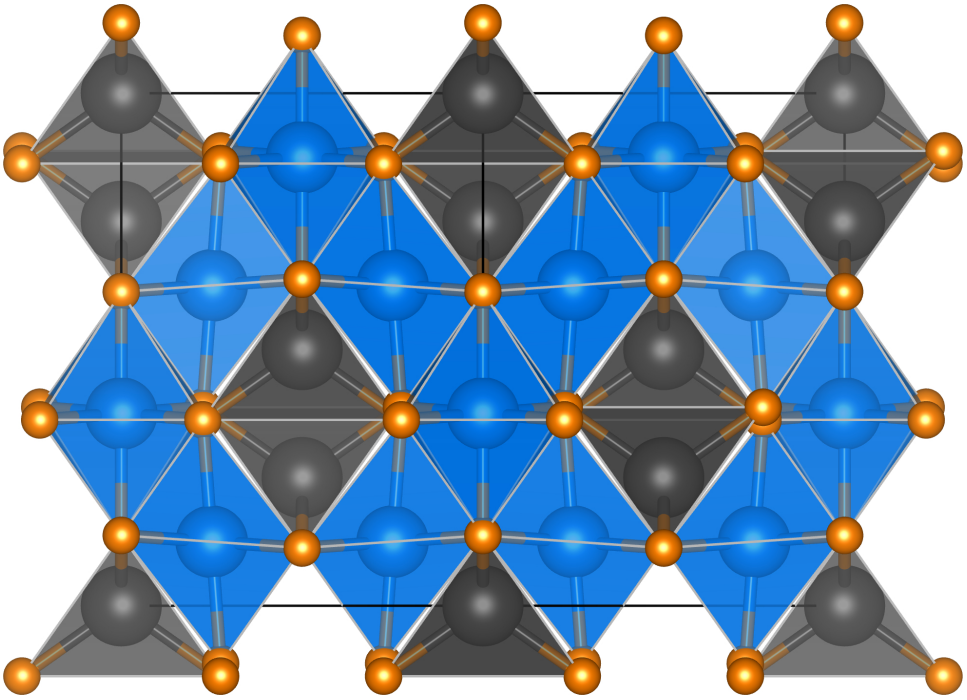

Figure 1.1: The cubic spinel structure of $MgAl_2O_4$. Mg^{2+} cations(grey) are tetrahedrally coordinated while Al^{3+} cations(blue) are octahedrally coordinated. Oxygen ligands are in orange. The cubic lattice constant of $MgAl_2O_4$ is 8.08060 Å and the oxygen parameter u is 0.3873. This spinel is described by the cubic space group $Fd\bar{3}m$.

cubic spinel structure of $MgAl_2O_4$ is illustrated in fig. 1.1.

Many spinels have the general formula $A^{2+}[B^{3+}]_2[X^{2-}]_4$, tetrahedral A cations are divalent, octahedral B cations are trivalent, and X anions are divalent. The site preference is partially determined by the cation size, larger cations preferring the tetrahedral site. $A^{2+}[B^{3+}]_2[X^{2-}]_4$ spinels are further classified as normal or inverse. In a normal spinel for example $MgCr_2O_4$, the tetrahedral sites are solely populated by divalent Mg^{2+} cations while the octahedral voids are

fully occupied by trivalent Cr^{3+} cations taking the general form $A^{2+}[B^{3+}]_2O_4$. On the other hand, in inverse spinels such as $FeFe_2O_4(Fe_3O_4)$,[9] trivalent Fe^{3+} cations populate the tetrahedral sites leaving the octahedral sites to be shared equally between trivalent Fe^{3+} cations and divalent Fe^{2+} cations as illustrated in the general form $B^{3+}[A^{2+}B^{3+}]_2O_4$. In practice, many spinels show some level of inversion without adopting the fully inverse configuration and are described as $(A_{1-x}B_x)[A_{\frac{x}{2}}B_{1-\frac{x}{2}}]_2O_4$. Although not as common, there are also $A^{4+}[B^{2+}]_2O_4$ spinels. In these "2-4" spinels, the larger cations prefer the octahedral site. In addition to size considerations, crystal-field stabilization plays an important role in determining whether a spinel has a normal or inverse configuration. Cr^{3+} B site spinels are typically normal spinels with the crystal-field stabilization of the t_{2g}^3 orbitals primarily giving a strong preference for the normal configuration.

1.1 Crystal fields in spinel oxides

In a free $3d$ cation, all the d states are degenerate, however, this degeneracy is broken when the cation is in a crystal. This effect arises from the asymmetry of $3d$ orbitals. In spinel oxides, $3d$ transition metal cations are in tetrahedral and octahedral coordination environments. When in an octahedral environment, Coulombic repulsion between the transition metal $3d$ orbitals and the electron

shells of coordination anions breaks the degeneracy of the $3d$ states. Direct overlap between the d_{x^2-y2} and d_{z^2} states that lie along the x, y, and z axes and the oxygen p states increases the energy of these orbitals. On the other hand, the xy, yz, and xz states that lie in between the x, y, and z axes are stabilized. Octahedral coordination therefore yields lower energy triply degenerate t_{2g} states and higher energy doubly degenerate e_g states as illustrated in fig. 1.2.

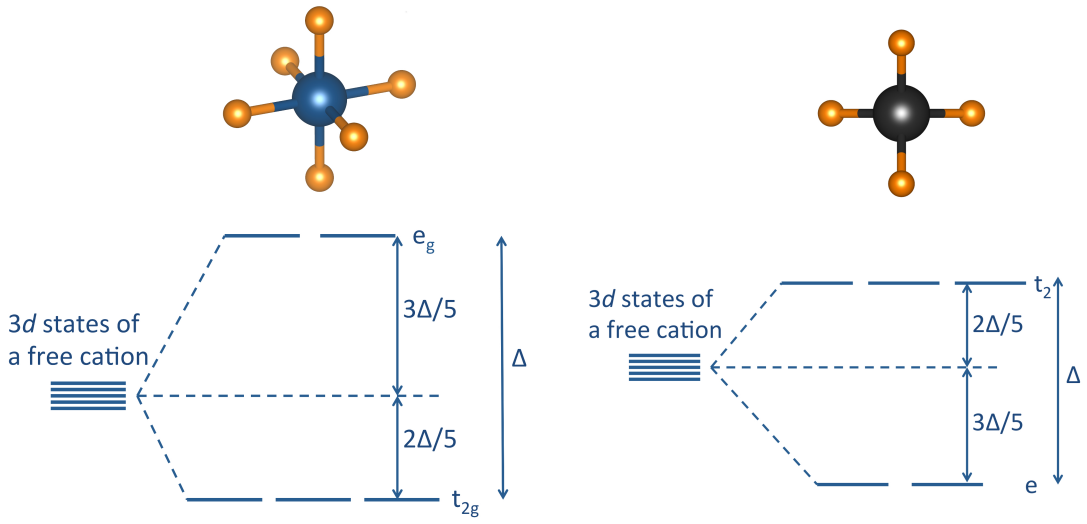

Figure 1.2: Crystal field splitting of the $3d$ states of transition metal cations in octahedral and tetrahedral coordination environments. Octahedral coordination yields a larger crystal field separation(Δ) compared to tetrahedral coordination. Triply degenerate t_{2g} states are stabilized in octahedral coordination environments while the doubly degenerate e_g states are destabilized. Due to smaller overlap of the d_{z^2} and $d_{x^2-y^2}$ orbitals of transition metal cations with the oxygen p states when in tetrahedral coordination, the e states are stabilized while the t_2 states are destabilized.

The symmetry of the coordination environment determines the crystal field. In tetrahedral coordination, Coulombic repulsion is enhanced in the xy, yz, and

Table 1.1: Stabilization of cations in tetrahedral and octahedral coordination environments in spinel oxides. The octahedral crystal field splitting parameter (Δ_{oct}) was determined from octahedral hydrates while the tetrahedral crystal field (Δ_{tet}) is approximated to be about $\frac{4}{9}$ths of the octahedral crystal field. Columns labelled 'oct' and 'tet' denote the ionic stabilization in octahedral and tetrahedral environments in units of (kcal/mole). The octahedral site preference, denoted 'oct-tet', is the energy gain per mole when the ion is in octahedral coordination compared to when it is in a tetrahedral environment. Data are obtained from reference [10]

d electrons	ion	$\Delta_{oct}(cm^{-1})$	$\Delta_{tet}(cm^{-1})$	Oct	Tet	Oct-Tet
1	Ti^{3+}	2030	900	23.1	15.4	7.7
2	Vi^{3+}	1800	840	30.7	28.7	2.0
3	Vi^{2+}	1180	520	40.2	8.7	31.5
3	Cr^{3+}	1760	780	60.0	13.3	46.7
4	Cr^{2+}	1400	620	24.0	7.0	17.0
4	Mn^{3+}	2100	930	35.9	10.6	25.3
5	Mn^{2+}	750	330	0	0	0
5	Fe^{3+}	1400	620	0	0	0
6	Fe^{2+}	1000	440	11.4	7.5	3.9
7	Co^{2+}	1000	440	17.1	15.0	2.1
8	Ni^{2+}	860	380	29.3	6.5	22.8
9	Cu^{2+}	1300	580	22.2	6.6	15.6
10	Zn^{2+}	0	0	0	0	0

xz states that are in close proximity to tetrahedral anion orbitals. As a result, the t_2 states of tetrahedrally coordinated cations are destabilized while the e states are stabilized (fig. 1.2). The magnitude of the tetrahedral crystal field (Δ) is less than that of the octahedral crystal field due to fewer coordinating ligands.

The importance of electronic energies in determining cation distribution in transition metal spinel oxides is demonstrated by the work of McClure.[10] Spectroscopic data of transition metal ions in tetrahedral and octahedral environments was examined to determine the stabilization achieved in the various coordination environments (Table 1.1). Cr^{3+} shows a strong electronic stabilization in an octahedral crystal field where it has a non-degenerate electronic ground state configuration $3d^3$:t_{2g}^3 (Table 1.1). As a result, Cr^{3+} primarily forms normal spinels.

Understanding the electronic stabilization of various cations in the tetrahedral and octahedral voids of $A^{2+}[B^{3+}]_2O_4$ oxide spinels enables remarkable prediction of cation distribution in these materials. Table 1.2 compares predictions of cation distribution based on crystal field stabilization to actual experimental findings. The cation distribution predictions show exceptional agreement with experimental observations. Cr^{3+} cations show a strong preference for the octahedral site where the d^3 electrons half fill the t_{2g} states (Table 1.1). As a result, chromium oxide spinels typically adopt a normal spinel configuration (Table

Table 1.2: Cation distributions in $A^{2+}[B^{3+}]_2O_4$ oxide spinels. Cation distributions predicted from crystal field stabilization (Th.) are compared with cation distributions determined experimentally (Exp.). " *N* " denotes a normal spinel, " *I* " is an inverse spinel, 0 indicates no prediction. All unreferenced data are taken from reference [10]

B / A	Fe^{3+} Exp.	Fe^{3+} Th.	Cr^{3+} Exp.	Cr^{3+} Th.	Mn^{3+} Exp.	Mn^{3+} Th.
Mg^{2+}	*I*[11]	0	*N*[11]	*N*		*N*
Zn^{2+}	*N*[11]	0	*N*[12]	*N*	*N*	*N*
Cd^{2+}	*N*[11]	0	*N*[11]	*N*		*N*
Mn^{2+}	*I*/*N*[13]	0	*N*	*N*	*N*[Ch. 6]	*N*
Fe^{2+}	*I*[11]	*I*	*N*	*N*		*N*
Co^{2+}	*I*	*I*	*N*[4]	*N*		*N*
Ni^{2+}	*I*	*I*	*N*[11]	*N*		*I*+*N*
Cu^{2+}	*I*[11]	*I*	*N*[14]	*N*		*N*

1.2). On the contrary, Fe^{3+} $3d^5$ has half filled d states and therefore shows no crystal-field stabilization on either the tetrahedral or octahedral sites (Table 1.1). Consequently, spinels with Fe^{3+} cations are typically inverse (Table 1.2). In the present work, we will explore the coupling of spin and lattice degrees of freedom in the normal spinels $A^{2+}[Cr^{3+}]_2O_4$, where A = (Mg, Zn, Cu, Ni, and Co), and $Mn^{2+}[Mn^{3+}]_2O_4$.

1.2 Jahn-Teller effects

Octahedral and tetrahedral crystal fields partially lift the degeneracy of $3d$ orbitals in transition metal oxides as discussed in the previous section. Any remanent orbital degeneracy in octahedral and tetrahedral transition metal complexes yields a lattice instability.[15] Orbitally degenerate spinel oxides show a propensity to undergo lattice distortions, typically from cubic to tetragonal symmetry. The degree of distortion depends on the bonding and antibonding power of the degenerate electrons. Degeneracy in the relatively non-bonding t_{2g} orbitals of octahedral complexes leads to small distortions. Small distortions are expected in cations with 1, 2, 6, and $7-d$ electrons with the respective electron configurations (t_{2g}^1), (t_{2g}^2), $(t_{2g}^4e_g^2)$, and $(t_{2g}^5e_g^2)$. On the other hand, cations with electronic configurations $(t_{2g}^3e_g^1)$ and $(t_{2g}^6e_g^3)$ - these are cations with 4 and 9 -d

electrons - show large Jahn-Teller distortions due to the presence of degeneracy in the strongly antibonding e_g orbitals. In tetrahedral coordination, the e orbitals are non-bonding while the t_2 orbitals are antibonding. Degeneracy in the t_2 antibonding states of tetrahedrally coordinated transition metal cations gives rise to large Jahn-Teller distortions.

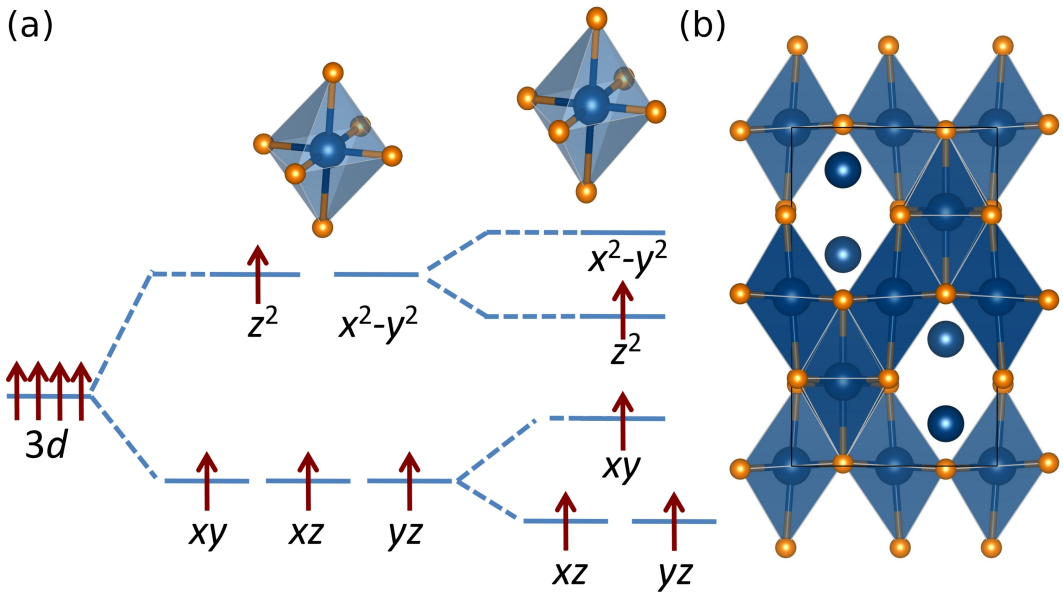

Figure 1.3: (a) Mn^{3+} cations, which occupy octahedral sites in Mn_3O_4 are orbitally degenerate in the cubic structure with the electronic configuration $3d^4$: $t_{2g}^3\, e_g^1$. A Jahn-Teller distortion elongates the MnO_6 octahedra stabilizing the d_{z^2} orbital, thus giving rise to a unique electronic configuration for Mn^{3+} cations. (b) Cooperative Jahn-Teller ordering drives a cubic-tetragonal lattice distortion. The tetragonal room temperature structure of Mn_3O_4 is illustrated here.

Let us examine Jahn-Teller ordering in Mn_3O_4 due to the orbitally degenerate e_g^1 states of octahedral Mn^{3+}. A lattice instability that shifts the apical oxygen

Table 1.3: Several spinels which exhibit Jahn-Teller ordering are tabulated below.

Spinel	Degeneration	High symmetry structure	Distorted structure	Transition temperature (°C)	Distortion
$CuFe_2O_4$ (*I*)[17]	Oct. Cu^{2+} $t_{2g}^6 e_g^3$	cubic $Fd\bar{3}m$	Tetragonal $I4_1/amd$	760	c/a = 1.06
$CuCr_2O_4$ (*N*)[18]	Tet. Cu^{2+} $e^4 t_2^5$	cubic $Fd\bar{3}m$	Tetragonal $I4_1/amd$	857	c/a = 0.91
$NiCr_2O_4$ (*N*)[14]	Tet. Ni^{2+} $e^4 t_2^4$	cubic $Fd\bar{3}m$	Tetragonal $I4_1/amd$	310	c/a = 1.03
Mn_3O_4 (*N*)[16]	Oct. Mn^{3+} $t_{2g}^3 e_g^1$	cubic $Fd\bar{3}m$	Tetragonal $I4_1/amd$	1170	c/a = 1.16

anions further from the Mn^{3+} metal center, resulting in closer Mn-O bonds along the equatorial plane, lifts the orbital degeneracy of Mn^{3+} cations as illustrated in Fig. [1.3]. A cooperative elongation of MnO_6 octahedra in Mn_3O_4 results in an average cubic $-$ tetragonal structural distortion at 1170 °C.[16]

The effects of Jahn-Teller ordering cannot be neglected when understanding the structure and properties of spinel oxides. The present study will exam-

ine spin−lattice coupling in the Jahn-Teller active spinels Mn_3O_4, $NiCr_2O_4$, and $CuCr_2O_4$. Properties of some Jahn-Teller active spinels are illustrated in Table 1.3.

1.3 Geometric frustration

Transition metal oxides have enabled many advances in the understanding of magnetic materials since the discovery of the first magnet - lodestone (magnetite). Magnetite is a spinel with the chemical formula Fe_3O_4. It was also in transition metal oxides that neutron diffraction revealed a form of magnetism which has no macroscopic signature − antiferromagnetism.[19] In this section, I describe how transition metal oxide spinels exhibit another unique magnetic property, geometric spin frustration.

Often, spin interactions can be fully satisfied as illustrated in figure 1.4 (a) where spins on a lattice plane adopt a simple collinear antiferromagnetic arrangement. However, when spin interactions cannot be fully satisfied due to the geometry of the lattice, we encounter a phenomenon known as geometric spin frustration. A simple illustration of this effect is observed when one considers the presence of three antiferromagnetically coupled spins located at the vertices of a triangular lattice [Fig 1.4 (b)]. All antiferromagnetic inter-

actions cannot be fully satisfied in triangular geometries and such spin systems are called frustrated. Frustrated magnets are an exciting challenge in condensed matter physics because they exhibit novel spin and structural ground states that are poorly understood.[20]

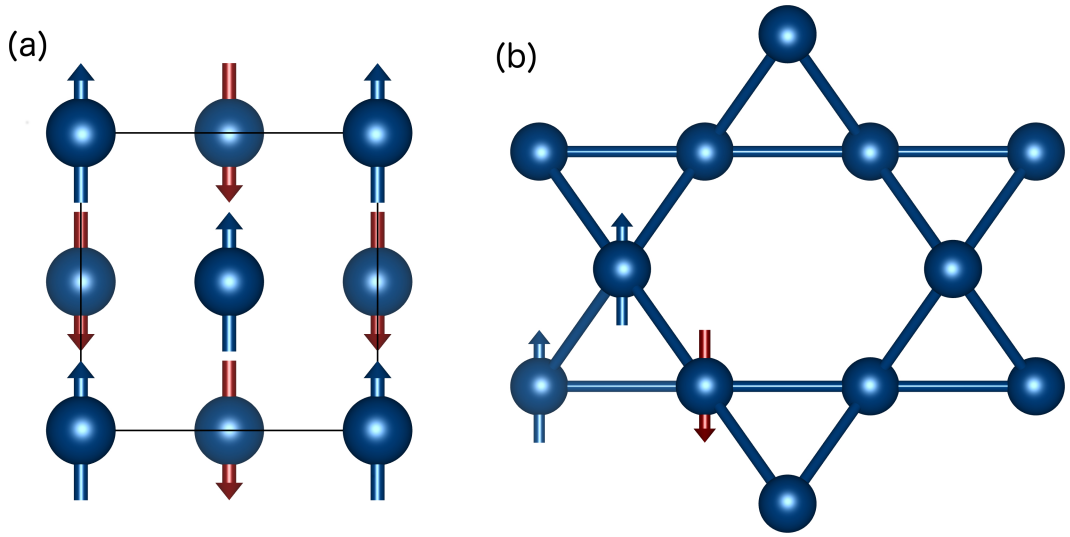

Figure 1.4: (a) Collinear G-type antiferromagnetic ordering of a 2 dimensional plane of spins (b) Antiferromagnetic interactions in a Kagome lattice plane. The triangular motif of the Kagome plane frustrates antiferromagnetic ordering

The hallmark of a frustrated system is a large ground state degeneracy. The six-fold ground state degeneracy of three antiferromagnetically coupled spins on a simple triangular lattice is illustrated in fig. 1.5. Weak perturbations of the highly degenerate ground states of frustrated systems often give rise to novel states of matter such as zero energy excitations and collective degrees of freedom.[8] As such, frustrated spin systems act as a window to new forms of

matter. The large ground state degeneracy of frustrated materials results in significant entropy close to 0 K. The presence of finite entropy close to 0 K appears in contrast to the third law of thermodynamics, which predicts that the entropy of crystalline materials is exactly zero at 0 K. However, frustrated systems normally freeze at low temperatures,[1] selecting one of the possible ground states, thus conforming to the third law of thermodynamics.

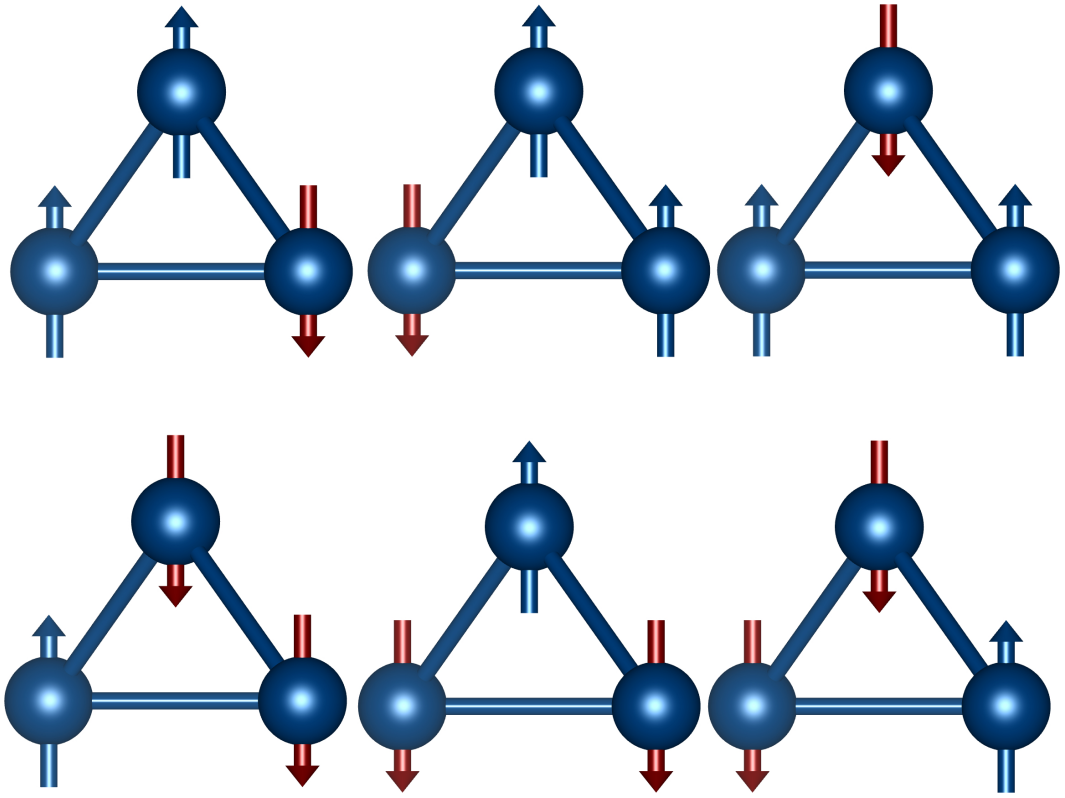

Figure 1.5: The six-fold degenerate ground states of antiferromagnetically coupled spins located at the vertices of a triangle.

Geometric frustration is not unique to magnetic systems. Frustration was ob-

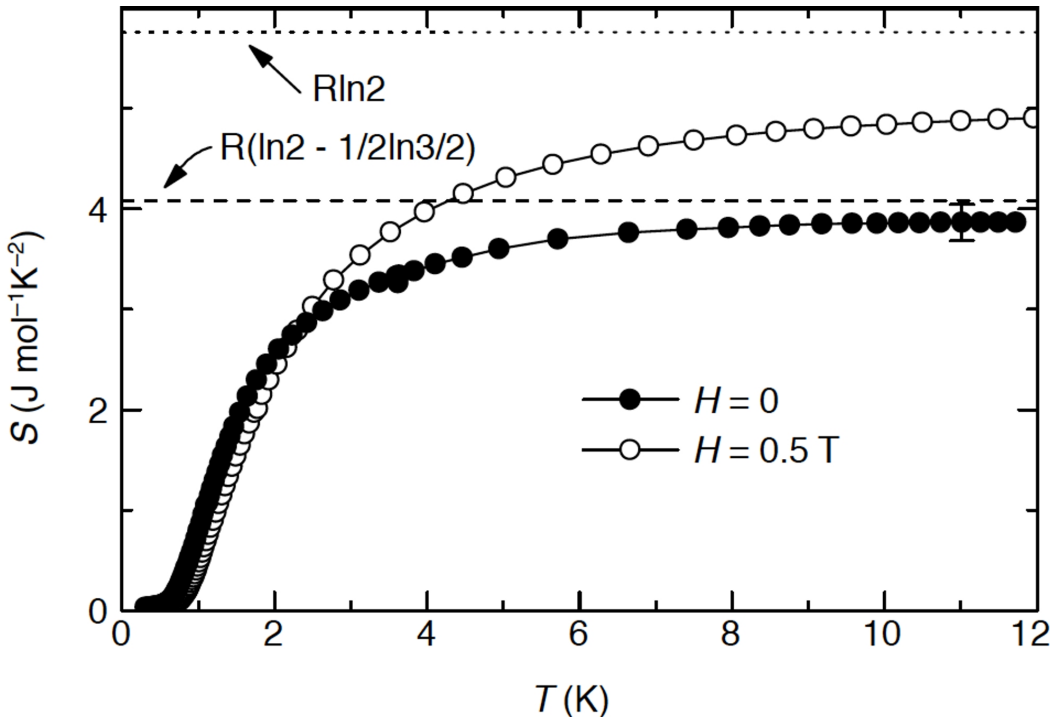

Figure 1.6: Entropy measurements of the spin ice $Dy_2Ti_2O_7$. The residual entropy $R(\ln 2 - 1/2\ln 3/2)$ is attributed to degenerate spin ground states near 0 K. An applied field enhances spin ordering resulting in a decrease in spin entropy at low temperatures. Reprinted by permission from Macmillan Publishers Ltd: Nature [21], © 1999 Nature publishing group.

served first in water ice due to the presence of two different O−H bond lengths in the OH_4 tetrahedra. The OH_4 tetrahedra are characterized by two short O−H bonds and two long O−H bonds. However, there are six different ways for each of the corner sharing OH_4 tetrahedra to have two short O−H bonds and two long O−H bonds. Linus Pauling computed residual entropy in ice due to the frustration of O−H bonding interactions.[22] Comparable residual entropy has been measured in the spin ice $Dy_2Ti_2O_7$. Ising Dy^{3+} spins populate a pyrochlore

network of corner sharing tetrahedra in the spin frustrated rare earth pyrochlore $Dy_2Ti_2O_7$. The spin interactions are ferromagnetic, yet, the Ising spins are constrained to lie along the easy axis of the tetrahedra. This results in two spins pointing toward the center of the Dy_4 tetrahedron and two spins pointing out but due to the corner sharing network of Dy_4 tetrahedral units, spin frustration results because a single spin is shared by two tetrahedral units.[23] There is a large ground state degeneracy of the ferromagnetically interacting spins in the network of corner sharing tetrahedra in spin ice materials. Ramirez $et\,al.$ have measured the residual spin entropy of $Dy_2Ti_2O_7$ (Fig. 1.6).[21] While frustration in water ice is challenging to study because of the liquid state of water under ambient conditions, magnetic spin ice materials are enabling the investigation of frustrated systems. The presence of remanent spin entropy in $Dy_2Ti_2O_7$ is the first direct measurement of frustration induced disorder at low temperatures in a frustrated system.[21]

In addition to spin frustration in ferromagnetically coupled Ising spins of rare earth pyrochlore materials such as $Dy_2Ti_2O_7$, spin frustration is also observed in transition metal oxide spinels such as $ZnCr_2O_4$ and $MgCr_2O_4$.[8, 24, 25] In these spinels, antiferromagnetic Cr^{3+} cations populate a pyrochlore sub-lattice where the triangular motif inhibits complete antiferromagnetic order (figure 1.7). Monte Carlo simulations of antiferromagnetic spins in a pyrochlore lattice

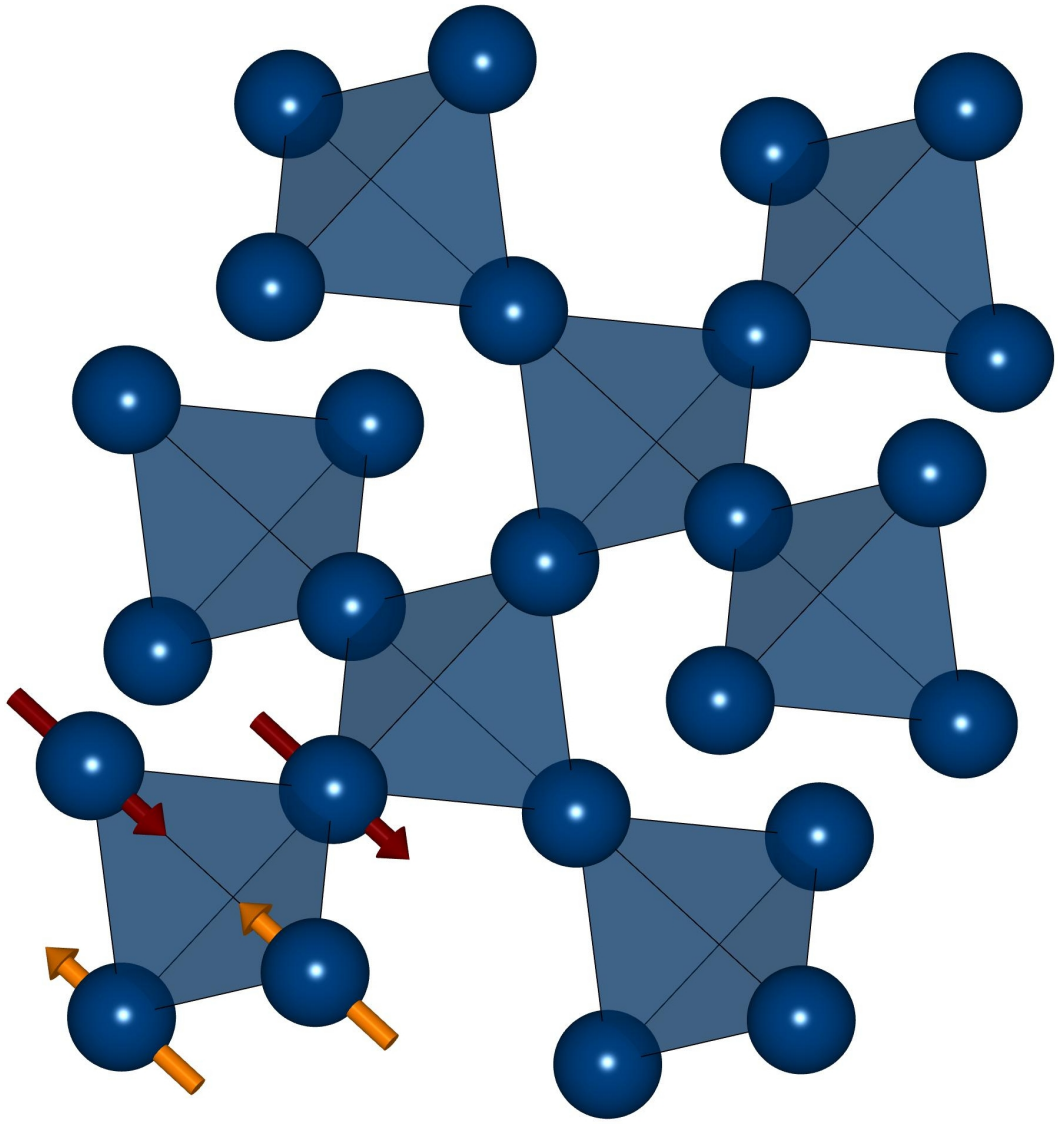

Figure 1.7: Frustration of the antiferromagnetic interactions of the $S = 3/2$ spins of Cr^{3+} cations that populate a corner sharing tetrahedral network.

predict a disordered ground state at all temperatures.[26] However, instead of retaining spin disorder to 0 K, further-neighbor interactions and spin-lattice coupling effects drive the systems to select a ground state out of the large manifold

of possible ground states. For example, $MgCr_2O_4$ and $ZnCr_2O_4$ each undergo a structural distortion at the onset of long range antiferromagnetic order. A detailed investigation of the low temperature structures of $MgCr_2O_4$ and $ZnCr_2O_4$ will be presented in chapter 4. The spin-driven lattice distortion partially lifts spin degeneracy by creating Cr-Cr bonds of different lengths.

Strong exchange coupling interactions in a frustrated magnet give rise to a high Curie-Weiss temperature ($|\Theta_{CW}|$), however, the onset of long-range magnetic order occurs at very low temperatures. As a result, spin-frustrated systems are identified based on the criterion $|\Theta_{CW}|/T_N \gg 10$, where T_N is the Néel temperature. The ratio $|\Theta_{CW}|/T_N$ is known as the frustration index (f). Θ_{CW} is determined by fitting the temperature-dependent susceptibility in the paramagnetic regime to the Curie-Weiss equation (eq. 1.1). We consider the example of the frustrated spinel $MgCr_2O_4$. The susceptibility of $MgCr_2O_4$ in the temperature range 300 K< T <390 K, is fit to the Curie-Weiss equation (eq. 1.1). This fit yields a $|\Theta_{CW}|$ of 350 K, which is 27 times larger that the actual antiferromagnetic ordering temperature T_N = 12.9 K. A Curie constant (C), which is related to the effective moment (μ_{eff}) through equation 1.2, is also obtained from the fit. The constants k_B, N_A, and μ_B of equation 1.2 are Boltzman's constant, Avagadro's number, and the Bohr magneton respectively. The temperature range $T_N \leq T \leq |\Theta_{CW}|$ is the spin liquid regime because, although there is no long-

Table 1.4: Magnetic properties of spin frustrated $A\mathrm{Cr_2O_4}$ spinels. T_S is the structural distortion temperature. Θ_{CW}, T_N, and f have been defined in the text. $\mathrm{Cr^{3+}}$ spinels have a spin quantum number $S = \frac{3}{2}$.

Spinel	Θ_{CW} (K)	T_N (K)	$f = \frac{\lvert\Theta_{CW}\rvert}{T_N}$	T_S (K)
$\mathrm{MgCr_2O_4}$ [1, 27–29]	−400	12.5	32	12.5
$\mathrm{ZnCr_2O_4}$ [1, 29–31]	−390	12.5	31.2	12.5
$\mathrm{CdCr_2O_4}$ [27, 32, 33]	−70	7.8	9	7.8
$\mathrm{HgCr_2O_4}$ [34, 35]	−32	5.8	5.5	5.8

range spin order, neighboring spins are highly correlated. In an ideal frustrated magnet the spin liquid regime would persist to 0 K. In reality, ideal spin liquids are elusive. Perturbations such as spin-lattice coupling and further-neighbor interactions preclude the realization of ideal spin liquid states in spinels. $\mathrm{MgCr_2O_4}$, for example, exhibits a spin-driven lattice distortion at 12.9 K that occurs concomitantly with the onset of long-range antiferromagnetic order. The magnetic properties of $A\mathrm{Cr_2O_4}$ spinels are summarized in Table 1.4.

$$\chi = \frac{C}{T - \theta_{CW}} \tag{1.1}$$

$$\mu_{eff} = \frac{1}{\mu_B}\sqrt{\frac{3k_B C}{N_A}} \tag{1.2}$$

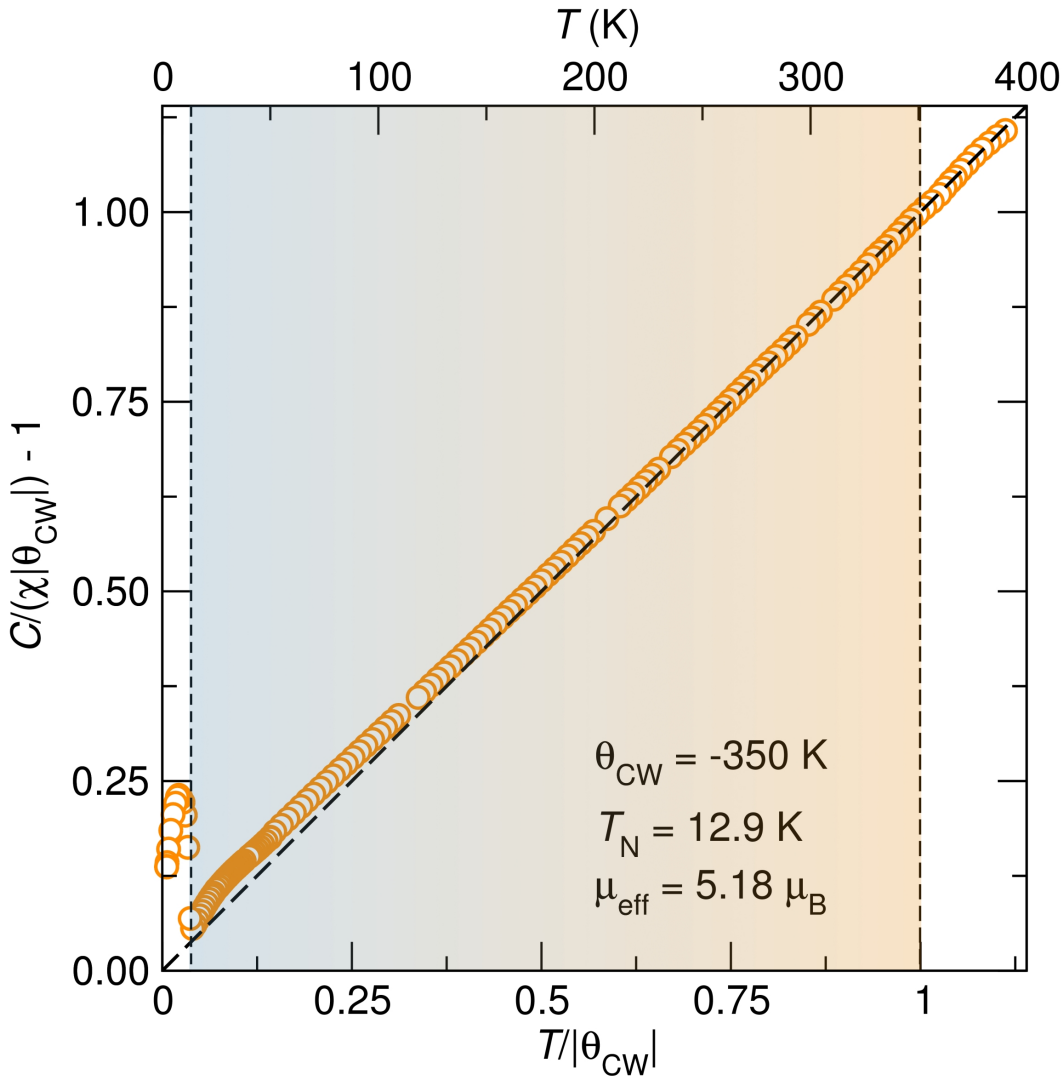

Figure 1.8: The inverse scaled susceptibility of $MgCr_2O_4$ plotted as a function of temperature. On the bottom axis is the normalized temperature scale $T/|\Theta_{CW}|$, which indicates strong frustration in $MgCr_2O_4$. A system that is not frustrated would order at $T_N/|\Theta_{CW}| = 1$. The highlighted temperature regime 12.9 K$< T <$350 K is the spin liquid phase of $MgCr_2O_4$. Long-range antiferromagnetic order in $MgCr_2O_4$ occurs below $T_N =$12.9 K.

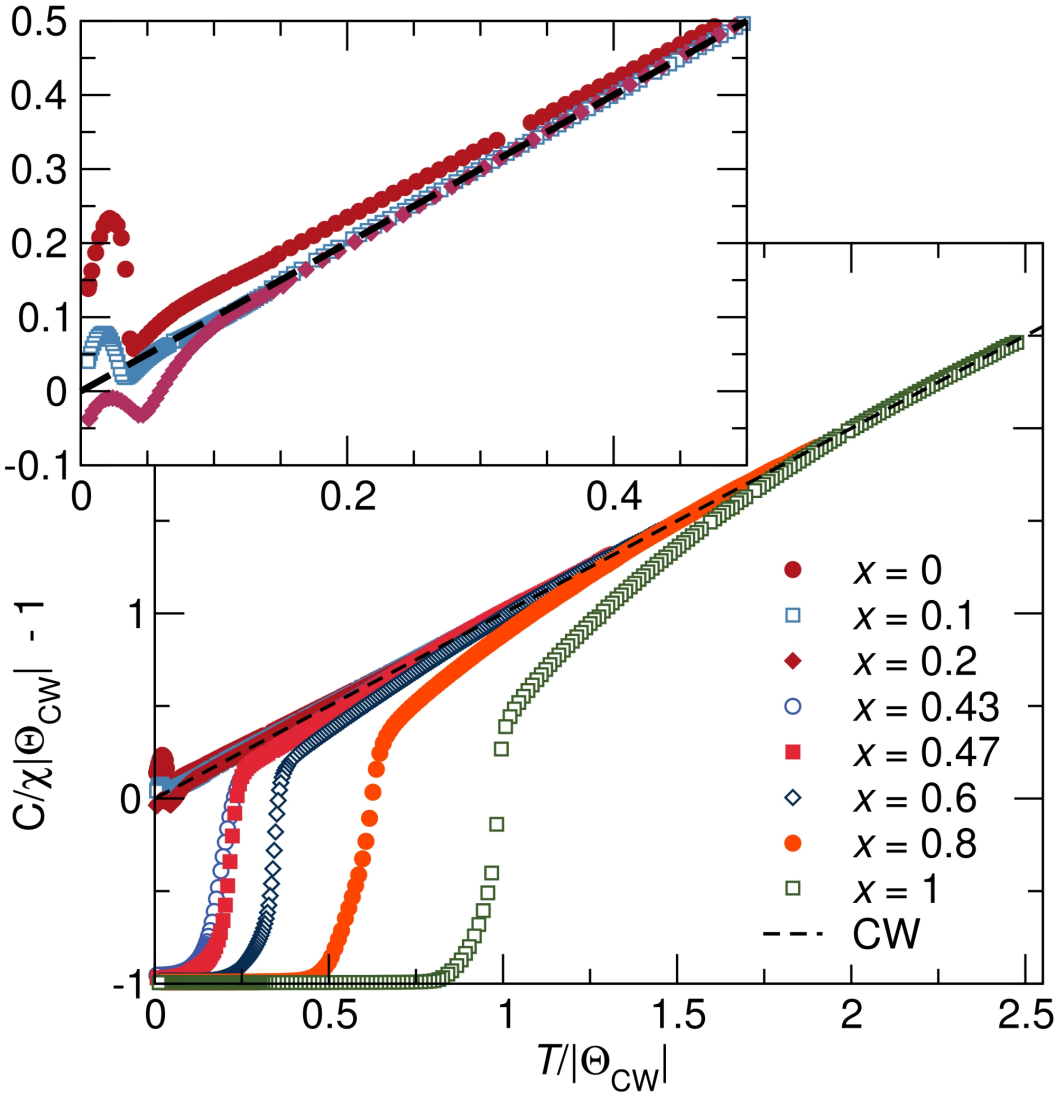

Figure 1.9: The inverse scaled susceptibility measurements of the systems $Mg_{1-x}Cu_xCr_2O_4$ show the evolution of magnetism from compensated frustrated antiferromagnetism in $MgCr_2O_4$ to ferrimagnetism in $CuCr_2O_4$. The black dashed line is the Curie-Weiss paramagnetic model. Positive deviations from the Curie-Weiss model indicate compensated antiferromagnetic interactions while negative deviations from the model illustrate ferrimagnetic uncompensated interactions. Reproduced with permission from reference [36] © 2012 IOP Publishing Ltd.

To understand the nature of magnetic interactions in spinel oxides and particularly to probe the evolution of magnetism with composition, it is helpful to plot the scaled inverse susceptibility $(\frac{C}{\chi|\Theta_{CW}|}-1)$ as a function of the normalized temperature (T/Θ_{CW}). This approach was developed in our group[37] and is used extensively in this dissertation. This representation derives from the Curie-Weiss model in the steps shown below:

$$\chi = \frac{C}{T-\Theta_{CW}} \tag{1.3}$$

$$\frac{C}{\chi\Theta_{CW}} = \frac{T}{\Theta_{CW}} - 1 \tag{1.4}$$

In the case of $\Theta_{CW} < 0$:

$$-\frac{C}{\chi|\Theta_{CW}|} = -\frac{T}{|\Theta_{CW}|} - 1 \tag{1.5}$$

The plot of $\frac{C}{\chi|\Theta_{CW}|} - 1$ versus $\frac{T}{|\Theta_{CW}|}$ yields a Curie-Weiss fit with a slope of 1 that intersects the origin. This representation of susceptibility clearly distinguishes compensated antiferromagnetic interactions from uncompensated interactions(ferrimagnetic, and ferromagnetic); the former yield a positive deviation from the Curie-Weiss model while the later show a negative deviation from the

Curie-Weiss model (fig. 1.9). Ferrimagnets and ferromagnets have a scaled inverse susceptibility with a value of -1 below their magnetic ordering temperatures. This representation also clearly shows frustrated interactions on the $T/|\Theta_{CW}|$ axis where frustrated materials order when $T/|\Theta_{CW}| \ll 1$. We illustrate the effect of this representation in the systems $Mg_{1-x}Cu_xCr_2O_4$ as shown in fig 1.9.

1.4 Characterization techniques

Polycrystalline samples of magnetic oxide spinels were structurally characterized by variable-temperature high-resolution synchrotron x-ray diffraction at beamline 11BM of the Advanced Photon Source at Argonne National Laboratory. The high intensity and energy of x-rays at the synchrotron combined with recently installed facilities that enable variable-temperature measurements have led to important findings regarding the nature of spin-lattice coupling in magnetic oxides. X-rays are particularly well suited for studying the nuclear structure because magnetic scattering is absent. Resolving structure from single crystal diffraction can be challenging when twinning occurs, but such effects are not encountered when studying the structure of polycrystalline materials.

The crystal structure of a material determines the x-ray diffraction peak posi-

tions and intensities. Constructive interference of diffracted x-rays occurs when the path difference of radiation from planes separated by a distance (d), satisfies equation 1.6. For a fixed wavelength (λ), a family of planes (hkl) will diffract x-rays at particular angles $(2\,\theta)$. The lattice determines the angles of the diffracted x-rays while the basis of atoms determines the intensity of diffraction peaks.

For integer n:

$$2d_{\text{hkl}} \sin\theta = n\lambda. \tag{1.6}$$

A diffraction pattern is a map of the reciprocal lattice of the crystal. In reciprocal space, the diffraction condition is met when the change in wave vector $(\Delta\mathbf{k})$ of the diffracted x-ray is equal to a reciprocal lattice vector $(\mathbf{G})$ as shown in equation 1.7.

$$\Delta\mathbf{k} = \mathbf{G} \tag{1.7}$$

The amplitude of the scattered wave is proportional to the volume integral of the electron density of a diffracting element as specified in equation 1.8. $n(\mathbf{r})$ is the local electron density.

$$F = \int dV\, n(\mathbf{r}) \text{exp}(-i\Delta\mathbf{k}\cdot\mathbf{r}) \tag{1.8}$$

Ultimately the structure factor, which describes the scattering of radiation in a crystal, takes the general form shown in equation 1.9 where f_j is the atomic form factor. The atomic form factor depends on the number of electrons and the scattering angle. At small angles, f_j is equal to the number of electrons of an atom, however, this initial value of f_j decays with increase in angle.

$$S_{\mathbf{G}} = \sum_j f_j \exp(-i\mathbf{G} \cdot \mathbf{r}) \tag{1.9}$$

We employ a least-squares refinement approach developed by Hugo Rietveld to analyze x-ray powder diffraction data.[38] This technique models the height, width, and position of diffraction peaks to a specified structural model by minimizing the differences between the model and the data. Prior to performing a Rietveld refinement the details of the structural model must be provided, these include: space group, lattice parameters, atom types and positions, atom occupancies, and thermal displacement parameters. During the refinement, these structural parameters are relaxed to fit the structural model to the diffraction patten. The effects of instrumental parameters on the diffraction pattern are handled by selecting the appropriate peak profile, specifying the x-ray wavelength, and refining the sample displacement during a Rietveld refinement. In addition to using x-ray scattering to study the average structure of materials

from Bragg scattering, we have also performed total neutron scattering to understand short-range correlations in Jahn-Teller active spinels. Diffuse scattering, which is often modeled as a simple background during average structure studies, contains information about local atomic correlations.

Magnetic properties of the studied spinel oxides were determined from susceptibility measurements. Temperature-dependent and field-dependent susceptibility measurements can distinguish the nature of magnetism in materials, be it antiferromagnetic, ferromagnetic, diamagnetic, or paramagnetic. Evolution of magnetism from antiferromagnetism in $MgCr_2O_4$ to ferrimagnetism in $CuCr_2O_4$ is presented in fig. 1.9. The number of spins in each magnetic ion can also be determined from fitting the susceptibility in the paramagnetic regime to the Curie-Weiss equation (equations 1.1 and 1.2). We use a Magnetic Properties Measurement System with a superconducting quantum interference device (SQUID) magnetometer. During a measurement, the vibrations of a magnetic sample change the magnetic flux intersecting the superconducting detection coils. A change in current that is proportional to the change in magnetic flux is induced in the detection coils. This current couples inductively to the SQUID, which provides a voltage output that is proportional to the magnetic moment of the sample.

We perform heat capacity measurements to study entropy changes during

structural and magnetic phase transformations. We use a Physical Properties Measurement System, which employs a thermal relaxation technique to measure the heat capacity of materials. This method is ideal when studying small sample sizes and when measuring heat capacity at low temperatures. Thermal relaxation methods measure a relaxation time τ which is related to heat capacity as shown in equation 1.10. C is the heat capacity while κ is the thermal conductivity of the sample.

$$\tau \approx C/\kappa \tag{1.10}$$

During a thermal relaxation heat capacity measurement, a sample is placed on a platform which is equipped with a thermometer and a heater. The sample platform is coupled to a thermal reservoir. This system can be modeled as a sample connected to the platform though a thermal link κ_2 and a platform linked to the thermal reservoir by another thermal link κ_1. The thermal relaxation measurement geometry is illustrated in fig.1.10 (a). Once the entire system is in thermal equilibrium, a heat pulse with power P_0 is applied for a period ($t_1 - t_0$) until temperature T_1 is achieved. When the heater power is removed, the temperature decays to T_0 with a time constant τ_1. In the limit where κ_2 is negligible, τ_1 is related to sample (C_s) and platform (C_p) heat capacities by

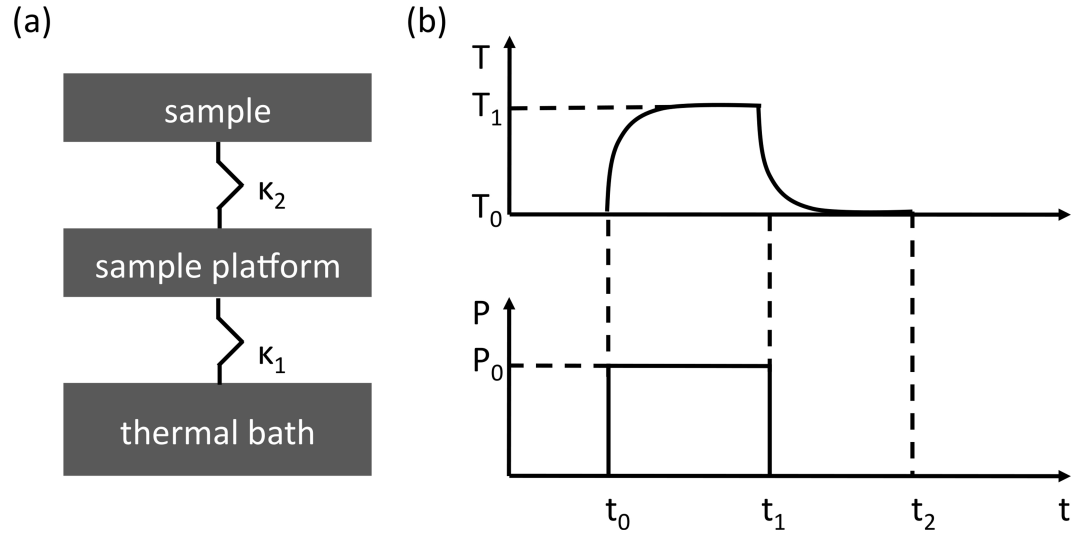

Figure 1.10: (a) The configuration during a thermal relaxation heat capacity measurement. (b) When carrying out a heat capacity measurement, the system is first thermally equilibrated, then a power pulse P_0 is applied to the system until it attains the temperature T_1. The power is then turned off and the system temperature decays with a characteristic time constant τ_1 which is proportional to the sample and platform heat capacities. κ_1 and κ_2 are the thermal conductivity values of the thermal links between the sample, platform, and thermal reservoir.

equation 1.11. Figure 1.10 (b) illustrates the thermal relaxation approach to measuring heat capacity.

$$\tau_1 \approx (C_p + C_s)/\kappa_1 \tag{1.11}$$

We employ an Andeen Hagerling capacitance bridge to measure the dielectric properties of magnetic spinels. The capacitance bridge is connected by coaxial cables to the sample, which is placed in a Physical Properties Measurement

System to access variable-temperature and variable-field conditions. During capacitance measurements, the unknown capacitor is placed in a circuit of other known components. The balance of impedances in the circuit is used to determine the unknown capacitance.

1.5 Overview

Spinels accommodate diverse cations on the tetrahedral and octahedral sites yielding a large spinel palette as illustrated in fig. 1.11. The compositional diversity of spinels combined with the presence of competing spin and orbital interactions make this structural family a rich playground for understanding the physics of transition metal oxides. This thesis will examine the Cr-B-site spinels $MgCr_2O_4$, $ZnCr_2O_4$, $NiCr_2O_4$, and $CuCr_2O_4$. We will show that by only varying the identity of A-site cation, these compositions exhibit ferrimagnetism, antiferromagnetism, frustrated antiferromagnetism, Jahn-Teller effects, spin-Jahn-Teller effects, and magnetodielectric coupling. We will also examine magnetostructural coupling in the normal spinel Mn_3O_4.

The present work will address the following objectives:

1. Show that long-range spin ordering in the spinels ACr_2O_4 (A = Mg, Zn,

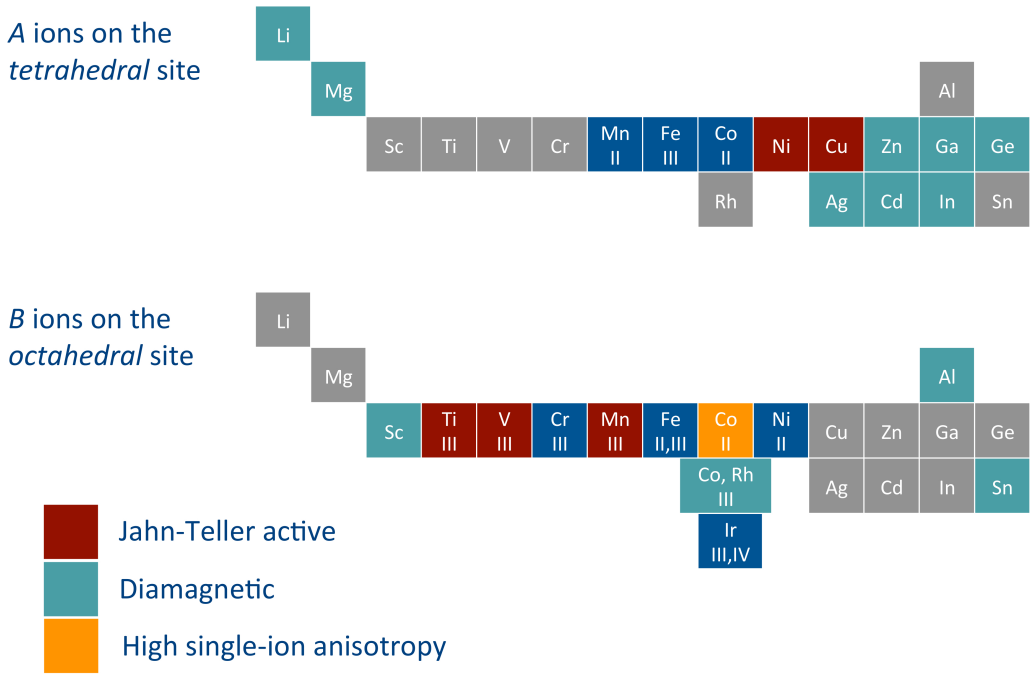

Figure 1.11: Compositional diversity in spinel oxides. A wealth of phenomena such as Jahn-Teller activity, spin frustration, and single-ion anisotropy are observed in this family of compounds.

Ni, Cu) and Mn_3O_4 is accompanied by distortions in average structure. Our results of magnetostructural coupling in $NiCr_2O_4$ and $CuCr_2O_4$ are the very first demonstrations of spin-lattice coupling in these materials.

2. Employ high-resolution synchrotron x-ray diffraction to resolve the complete crystallographic description of several magnetic spinel oxides.

3. We study the effect of dilute A site spins on the structural ground states of the frustrated systems $MgCr_2O_4$ and $ZnCr_2O_4$. We show that the spin-

Jahn-Teller effect in these systems is completely suppressed even when only 10 $\%$ of the non-magnetic A site spins are substituted by magnetic cations. On the contrary, the substitution of only 10$\%$ Jahn-Teller active cations on the non-magnetic A sites of $MgCr_2O_4$ and $ZnCr_2O_4$ induce Jahn-Teller distortions above the Néel temperatures of these spinels without breaking spin frustration.

4. We present detailed studies of emergent properties in the magnetic phases of these spinels. Specifically, we describe magnetodielectric coupling in $NiCr_2O_4$.

5. We also describe the evolution of magnetic properties in the solid solution $Mg_{1-x}Cu_xCr_2O_4$.

Impact: The understanding of the low temperature structures of magnetic oxide spinels will guide the development of structure-property relations in these materials and enhance the understanding of the properties of these spinels in the magnetic state. Our studies of the structures of the frustrated spinels $MgCr_2O_4$ and $ZnCr_2O_4$ provide insights into the ground states of frustrated systems. We present a detailed description of magnetodielectric coupling in $NiCr_2O_4$. Finally, we describe the evolution of structure and magnetism in the frustrated spinels $MgCr_2O_4$ and $ZnCr_2O_4$ due to the substitution of spins on the non-magnetic A

site.

Chapter 2

Spin-induced symmetry breaking in orbitally ordered $NiCr_2O_4$ and $CuCr_2O_4$

At room temperature, the normal oxide spinels $NiCr_2O_4$ and $CuCr_2O_4$ are tetragonally distorted and crystallize in the $I4_1/amd$ space group due to cooperative Jahn-Teller ordering driven by the orbital degeneracy of tetrahedral Ni^{2+} (t_2^4) and Cu^{2+} (t_2^5). Upon cooling, these compounds undergo magnetic or-

[1]The contents of this chapter have substantially appeared in reference [14]: M. R. Suchomel, D. P. Shoemaker, L. Ribaud, M. C. Kemei, and R. Seshadri, Spin−induced symmetry breaking in orbitally ordered $NiCr_2O_4$ and $CuCr_2O_4$ *Phys. Rev. B* **86** 0544061 (2012), © 2012 American Physical Society.

dering transitions; interactions being somewhat frustrated for $NiCr_2O_4$ but not for $CuCr_2O_4$. We employ variable-temperature high-resolution synchrotron X-ray powder diffraction to establish that at the magnetic ordering temperatures there are further structural changes, which result in both compounds distorting to an orthorhombic structure consistent with the $Fddd$ space group. $NiCr_2O_4$ exhibits additional distortion, likely within the same space group, at a yet-lower transition temperature of $T = 30$ K. The tetragonal to orthorhombic structural transition in these compounds appears to primarily involve changes in NiO_4 and CuO_4 tetrahedra.

2.1 Introduction

Strong coupling between spin, lattice, and orbital degrees of freedom in functional transition metal oxide compounds results in rich behavior such as the tendency for cooperative Jahn-Teller[39] and spin-Peierls distortions.[40] Such coupling between the different degrees of freedom enables multifunctionality as observed in multiferroics $R\mathrm{MnO}_3$(R = heavy rare earth).[41, 42] In these systems, manipulation of one property can influence another, exemplified by the electric field control of magnetic polarization in $HoMnO_3$[43]. Seeking out such strong links between distinct degrees of freedom represents a powerful strategy

in the search for new multifunctional systems, and affords unique opportunities for a deeper understanding of these interactions.[32, 44]

One such frequently studied interaction is magnetostructural coupling in geometrically frustrated antiferromagnets [45, 46] where a structural distortion lifts the large ground state degeneracy allowing long range magnetic order.[31, 47] However, frustration-driven magnetostructural coupling is not expected in the ferrimagnetic spinels with the formula $A\mathrm{Cr_2O_4}$ where A is a magnetic cation. This is a consequence of the magnetic A-O-$\mathrm{Cr^{3+}}$ interaction usually being collectively stronger than the frustrated interactions between the $\mathrm{Cr^{3+}}$. Furthermore, Jahn-Teller activity of the A site cation can cause tetragonal distortions that should further alleviate frustration in the $\mathrm{Cr^{3+}}$ sublattice. Nonetheless, previous structural, thermodynamic, and magnetic studies of $\mathrm{NiCr_2O_4}$[48, 49] report a coupled magnetic and structural transition, and infrared spectroscopy measurements suggest concurrent magnetic and structural transitions in $\mathrm{CuCr_2O_4}$.[50]

Structural transitions at the magnetic ordering temperatures have been observed in numerous transition metal oxide antiferromagnets such as $\mathrm{Cr_2O_3}$,[51] MnO,[52, 53] FeO,[52, 53] CoO,[52, 53] and NiO.[52, 53] Cubic to rhombohedral transformations are found in MnO, FeO, and NiO, while CoO undergoes a cubic to tetragonal transition. The rhombohedral lattice constants of $\mathrm{Cr_2O_3}$

change at its antiferromagnetic ordering temperature. Two mechanisms of magnetostructural coupling have been suggested in these compounds based on neutron and X-ray diffraction measurements. Li has suggested that magnetostructural coupling in NiO, MnO, CoO, and FeO is driven by magnetostriction,[54] where anisotropy arises from the selection of a magnetic ordering axis and drives the magnetocrystalline deformation. Smart and Greenwald alternatively proposed that distortions in the above binary oxides are caused by exchange striction, which is the displacement of interacting ions to strengthen exchange coupling thus modifying the underlying lattice.[52] The relations between crystal distortions and exchange interactions are challenging to identify. For example, it is difficult to find a unique solution to certain magnetic scattering patterns.[53, 54]

Here, we determine the low temperature structures of $NiCr_2O_4$ and $CuCr_2O_4$ across the transitions associated with magnetic ordering using high resolution synchrotron powder X-ray diffraction. These compounds are fully-ordered and stoichiometric normal cubic spinels with the space group $Fd\bar{3}m$ at temperatures above 320 K[55, 56] for $NiCr_2O_4$ and 853 K[18, 56] for $CuCr_2O_4$.[57] Cr^{3+} $3d^3$ preferentially populates the octahedral sites because of the strong crystal field stabilization of the half occupied nondegenerate t_{2g} states and empty e_g states, while Ni^{2+} $3d^8$ and Cu^{2+} $3d^9$ are found on the tetrahedral sites.[39] The tetra-

hedral crystal field around Ni^{2+} $3d^8$ and Cu^{2+} $3d^9$ in the cubic phase results in fully occupied low energy e levels and triply degenerate t_2 levels rendering this structure potentially unstable.[58, 59] A cooperative lattice distortion – from cubic to tetragonal symmetry – lifts the orbital degeneracy in $NiCr_2O_4$ at 320 K[49, 55, 60] and in $CuCr_2O_4$ at 853 K.[18, 60] There had been a debate in the literature concerning the ambient temperature structure of $CuCr_2O_4$. Using neutron diffraction data, Prince postulated that the noncentrosymmetric space group $I\bar{4}2d$ was a better structural fit than $I4_1/amd$.[61] More recently, Dollase and O'Neill showed no statistically significant advantage to using the $I\bar{4}2d$ structural model over the centrosymmetric structure $I4_1/amd$.[62] In the tetragonal structure of $CuCr_2O_4$, CuO_4 tetrahedra are compressed toward a square planar configuration thus lifting orbital degeneracy. [39] The tetragonal structure of $NiCr_2O_4$ is known to crystallize in the space group $I4_1/amd$ with elongated NiO_4 tetrahedra.[63] Previous work has also shown further distortion of tetragonal $NiCr_2O_4$ to an orthorhombic phase, which occurs at the magnetic transition temperature $T_N = 60$ K and has been observed in thermodynamic, X-ray diffraction, and magnetic studies.[48, 49]

Noncollinear ferrimagnetism that is not described by the Néel model is observed in both $NiCr_2O_4$ and $CuCr_2O_4$. Tomiyasu and Kagomiya describe a magnetic structure comprising of a ferrimagnetic component and an antiferromag-

netic component in $NiCr_2O_4$.[49, 64] These authors used neutron scattering to show that the antiferromagnetic component orders at $T = 31\,K$ while the ferrimagnetic component orders at $T = 74\,K$. A saturation magnetization moment of $0.3\,\mu_B$ *per* formula unit has been reported for $NiCr_2O_4$.[64] Neutron scattering studies on $CuCr_2O_4$ suggest a magnetic structure comprising of two canted Cr^{3+} sublattices with a net moment, and Cu^{2+} sublattice that couples antiferromagnetically to the net moment of the Cr^{3+} sublattices below $T_N = 135\,K$.[56, 60, 61] The magnetic moment of $CuCr_2O_4$ in this structure is $0.5\,\mu_B$ *per* formula unit.

Given this prior evidence of concurrent magnetic and structural transitions in $NiCr_2O_4$[48, 49] and $CuCr_2O_4$[50], there is a clear need for further exploration of these compounds. In this study, we employ high-resolution temperature-dependent powder X-ray diffraction, magnetic susceptibility, and heat capacity measurements to investigate magnetostructural coupling in $NiCr_2O_4$ and $CuCr_2O_4$. This is the first observation by X-ray powder diffraction of the tetragonal to orthorhombic structural distortion of $CuCr_2O_4$ at the ferrimagnetic ordering temperature. We also reveal for the first time X-ray diffraction evidence of further symmetry lowering in orthorhombic $NiCr_2O_4$ at the second magnetic transition $T = 30\,K$. These results affirm strong magnetostructural coupling can also occur in spinels that are not expected to be frustrated. This new under-

standing of coupling between spin and lattice degrees of freedom in $NiCr_2O_4$ and $CuCr_2O_4$ suggests that these compounds are promising magnetodielectrics, and provides considerable motivation for further investigation of magnetostructural coupling in related spinel compounds.

2.2 Methods

$NiCr_2O_4$ was prepared by dissolving stoichiometric amounts of $Ni(NO_3)_2{\cdot}6H_2O$ and $Cr(NO_3)_3{\cdot}9H_2O$ in deionized water. The nitrate solution was heated to evaporate the solvent, leaving a precipitate that was ground and calcined at 1000° C for 24 hours. A dark green powder of $NiCr_2O_4$ was obtained. Black shiny single crystals of $CuCr_2O_4$ were prepared following the flux method described by Ye *et al.*[18] $K_2Cr_2O_7$ was used as a reactive flux that partly decomposes to Cr_2O_3 at $\sim$ 700 K. ye *et al.* propose that the reduction of Cr^{6+} into Cr^{3+} plays an important role in stabilizing the oxidation state of Cu^{2+} during the synthesis of $CuCr_2O_4$. [18] $K_2Cr_2O_7$ acts both as a flux and a source of Cr_2O_3. A 20 g mixture of 17.8% mass CuO (Sigma Aldrich 98%) and 82.2% mass $K_2Cr_2O_7$ (Fisher 99%) with 0.2 g Bi_2O_3 as a second flux was prepared. The mixture was ground using an agate mortar and pestle, placed in a covered platinum crucible, heated to 800° C with a ramp of 100°C/h, held for

24 h, and slowly cooled to ambient temperature at 15°C/h. After the reaction, black crystals of $CuCr_2O_4$ were collected and washed in boiling water. It should be noted that more conventional solid state preparation yielded samples with significantly broader linewidths in the synchrotron X-ray diffraction profile, potentially obscuring the ability to fully characterize the low-temperature structure. High-resolution ($\Delta Q/Q \leq 2 \times 10^{-4}$) synchrotron X-ray powder diffraction data were recorded on beamline 11-BM at the Advanced Photon Source (APS), Argonne National Laboratory. [65] Scans were collected using a 2Θ step size of 0.001° with $\lambda = 0.413441$ Å for $NiCr_2O_4$ and $\lambda = 0.413263$ Å for $CuCr_2O_4$ in a closed-flow helium cryostat over the temperature range 7 K to 300 K. The sample was in direct contact with the helium exchange gas during data collection, and was spun at 5 Hz to improve powder averaging. Structural models of $NiCr_2O_4$ and $CuCr_2O_4$ were fit to the diffraction data using the Rietveld refinement method as implemented in the EXPGUI/GSAS software program.[66, 67] Crystal structures were visualized using the program VESTA.[68] In each composition, a single small impurity phase was observed in the powder diffraction data, and quantitatively fit using the Rietveld method. The $NiCr_2O_4$ sample was determined to have a 0.5 wt.-% of Cr_2O_3, and the $CuCr_2O_4$ sample a 1.1 wt.-% CuO impurity.

Magnetic susceptibility measurements on powder samples were performed

using a Quantum Design MPMS 5XL superconducting quantum interference device (SQUID) magnetometer. Heat capacity measurements were collected on pellets of 50% mass silver and 50% mass sample using a Quantum Design Physical Properties Measurement System. The pellets were prepared by grinding equal amounts of silver and sample in an agate mortar and pestle followed by pressing at $\sim$ 330 MPa. Apiezon N grease was used to enhance thermal coupling between the sample and the stage. The heat capacity of the Apiezon N grease and silver were collected separately and subtracted from the measured heat capacity.

2.3 Results and Discussion

2.3.1 Magnetism

Three magnetic transitions are observed in the temperature dependent magnetic susceptibility of $NiCr_2O_4$ (Fig. 2.1). A high temperature transition occurs at 310 K where cooperative Jahn-Teller distortions lift the orbital degeneracy in $NiCr_2O_4$ and lower the structural symmetry from cubic ($Fd\bar{3}m$) to tetragonal ($I4_1/amd$) [Fig. 2.1 (a)]. Weak, compensated magnetic interactions occur at 310 K, as illustrated by the scaled inverse susceptibility of $NiCr_2O_4$ (Fig. 2.2).

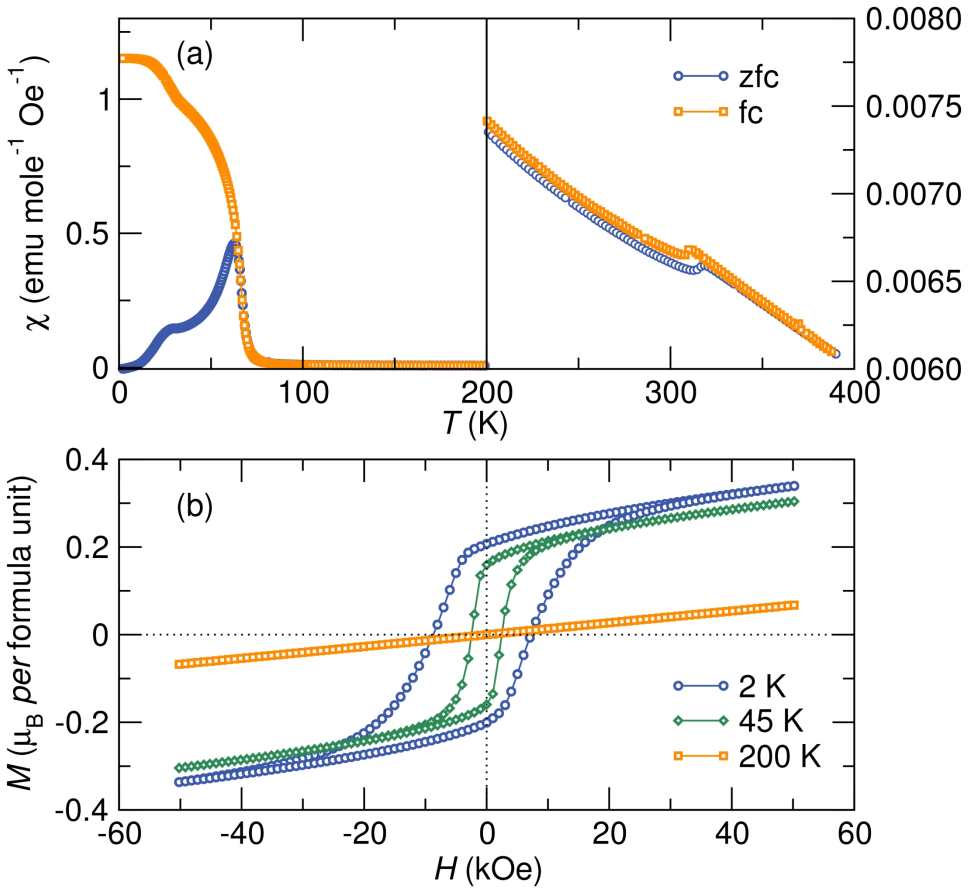

Figure 2.1: Magnetic measurements of the spinel $NiCr_2O_4$. (a) Zero field cooled and field cooled temperature dependent magnetic susceptibility measured under a 1000 Oe DC field show three anomalies at 310 K, 65 K and 30 K. $NiCr_2O_4$ displays little change in the magnetism at 310 K, and is seen to order ferrimagnetically at 65 K, with an additional change in the magnetic structure at 30 K. (b) The isothermal field dependent magnetization measured above the magnetic ordering temperature shows paramagnetic behavior. At 2 K, the coercive field and saturation magnetization are significantly larger than what is observed at 45 K. Reproduced with permission from reference [14], © 2012 American Physical Society.

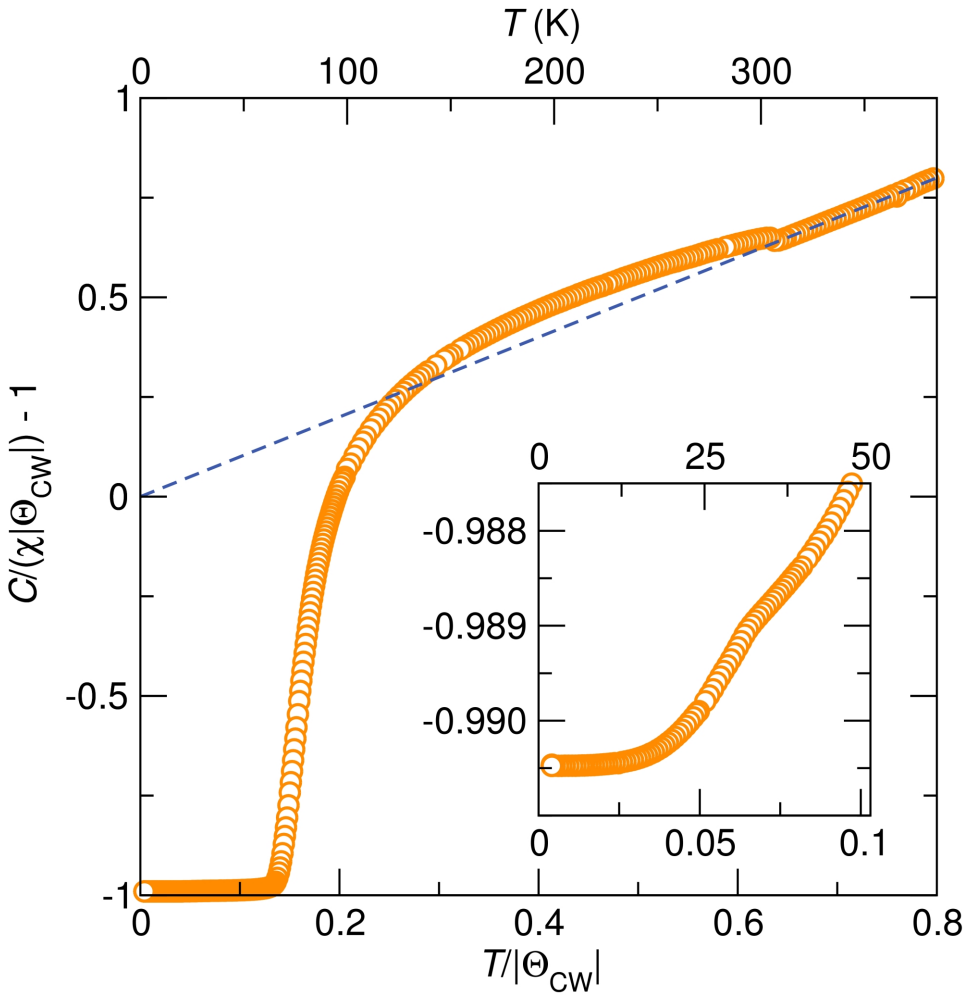

Figure 2.2: Normalized inverse magnetic susceptibility of $NiCr_2O_4$ showing ideal Curie Weiss paramagnetism above 310 K. Weak compensated interactions arise at 310 K and persist to about 65 K below which strong uncompensated interactions dominate. The subtle magnetic transition at 30 K is shown in the inset. Reproduced with permission from reference [14], © 2012 American Physical Society.

The scaling is carried out by recasting the Curie-Weiss equation using:[37]

$$\frac{C}{\chi|\Theta_{CW}|} + \text{sgn}(\Theta_{CW}) = \frac{T}{|\Theta_{CW}|} \tag{2.1}$$

The linear dependence of the magnetization on the applied field at 200 K [Fig. 2.1(b)] suggests that $NiCr_2O_4$ is mainly paramagnetic down to 65 K where there is a transition to a ferrimagnetic state [Fig. 2.1(a)]. The normalized inverse magnetic susceptibility trace shows the development of strong uncompensated magnetic correlations at 65 K (Fig. 2.2). A small coercive field and saturation magnetization is observed in the field dependent magnetization of $NiCr_2O_4$ at 45 K [Fig. 2.1(b)] in agreement with the onset of ferrimagnetic order. Tomiyasu and Kagomiya attribute the magnetic transition at 65 K in $NiCr_2O_4$ to the ordering of the longitudinal ferrimagnetic component of $NiCr_2O_4$.[64] At 30 K, another anomaly is observed in both zero field cooled (ZFC) and field cooled (FC) measurements of the temperature dependent magnetic susceptibility [Fig. 2.1(a)] as well as in the scaled inverse susceptibility (Fig. 2.2) of $NiCr_2O_4$. Below 30 K, an increase in the coercive field and the saturation magnetization of $NiCr_2O_4$ is observed [Fig. 2.1(b)]. Previous neutron diffraction measurements of $NiCr_2O_4$ attribute this anomaly to the ordering of the antiferromagnetic component of $NiCr_2O_4$.[64]

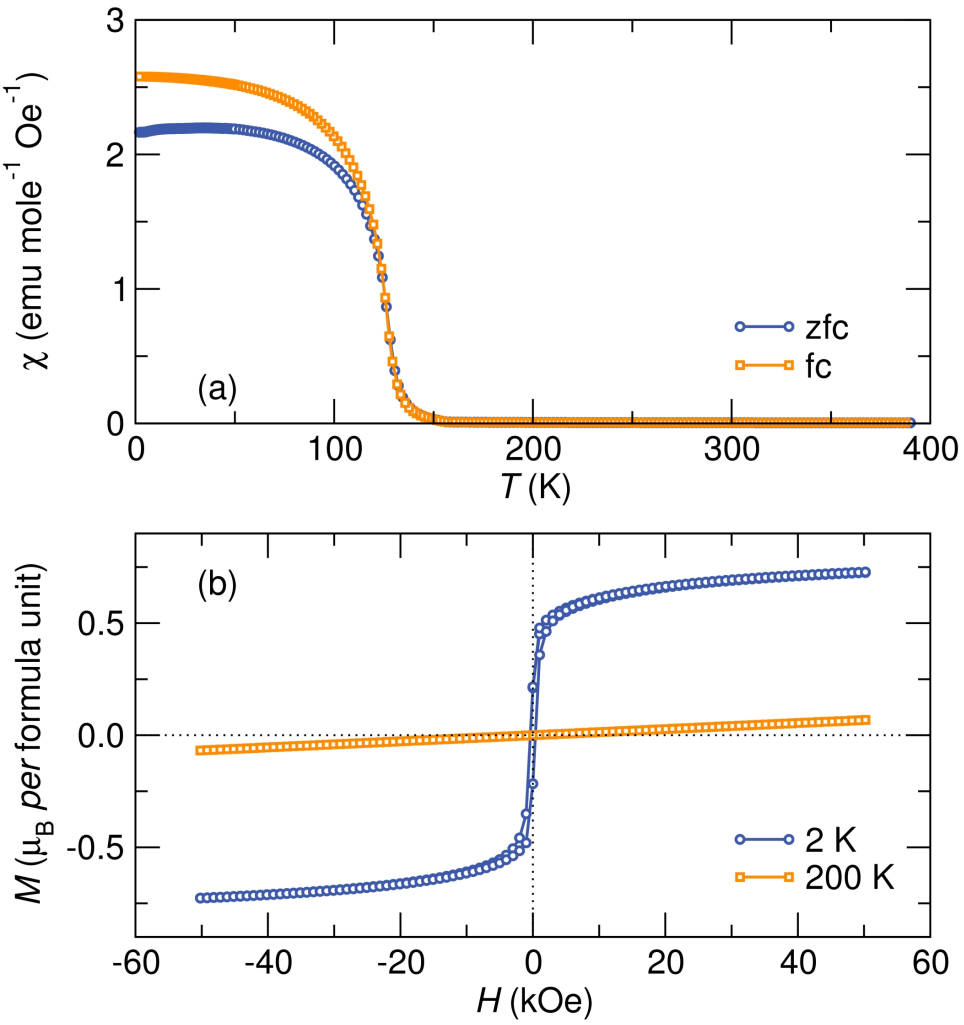

Figure 2.3: Magnetic measurements of the spinel $CuCr_2O_4$. (a) Magnetic susceptibility as a function of temperature under a 1000 Oe DC field shows an increase in susceptibility at the magnetic ordering temperature ≈130 K in both zero field cooled and field cooled measurements. This is a paramagnetic to ferrimagnetic transition. (b) Isothermal field dependent magnetization measured above (200 K) and below (2 K) the magnetic ordering temperature. Reproduced with permission from reference [14], © 2012 American Physical Society.

The temperature dependent magnetic susceptibility of $CuCr_2O_4$ shows a rapid increase at 130 K where there is a paramagnetic to ferrimagnetic transition [Fig. 2.3(a)]. The ZFC susceptibility exhibits a reduced low temperature saturation value when compared to the FC susceptibility data illustrating domain behavior. A linear dependence of magnetization with applied field occurs before the onset of magnetic order while a magnetization trace with a coercive field of 380 Oe and a saturation magnetization of 0.725 μ_B is measured at 2 K. The measured saturation magnetization of $CuCr_2O_4$ is in good agreement with that of the triangular magnetic structure observed previously using neutron powder diffraction.[61]

The Curie-Weiss (CW) equation $\chi = C/(T - \Theta_{CW})$ is applied to paramagnetic regimes of $NiCr_2O_4$ and $CuCr_2O_4$ yielding an effective moment (μ_{eff}) of 6.53 μ_B *per* formula unit for $NiCr_2O_4$ and 4.27 μ_B *per* formula unit for $CuCr_2O_4$. The expected μ_{eff} of $NiCr_2O_4$ is 6.16 μ_B *per* formula unit of $NiCr_2O_4$. This value is slightly smaller that the experimentally determined value of 6.53 μ_B *per* formula unit obtained from fitting the paramagnetic regime to the Curie-Weiss model, implying a small orbital contribution to the measured moment. The expected μ_{eff} of 5.74 μ_B *per* formula unit of $CuCr_2O_4$ is much larger than the experimental value suggesting the likely presence of magnetic correlations in the paramagnetic regime.[36] The Weiss temperature (Θ_{CW}) of $NiCr_2O_4$ is

-487 K while that of $CuCr_2O_4$ is -147 K. The frustration index ($|\Theta_{CW}|/T_N$) of $NiCr_2O_4$ is about 7.8 and that of $CuCr_2O_4$ is 1.1 indicating that $NiCr_2O_4$ is the more frustrated compound. The negative sign of Θ_{CW} coupled with the low saturation magnetization observed in isothermal field dependent measurements is consistent with noncollinear ferrimagnetic ordering in $NiCr_2O_4$ and $CuCr_2O_4$.

The magnetic transitions of $CuCr_2O_4$ and $NiCr_2O_4$ are strongly coupled to the lattice. All magnetic changes in $NiCr_2O_4$ are accompanied by structural transitions. The known Jahn-Teller cubic to tetragonal structural distortion in $NiCr_2O_4$ at 310 K causes a small change in the temperature dependent magnetization [Fig. 2.1(a)].[48] Ishibashi and Yasumi reported further distortion from tetragonal to orthorhombic symmetry at the onset of ferrimagnetic order (T_N = 65 K).[48] We observe this tetragonal to orthorhombic crystal distortion occurring concurrently with the onset of ferrimagnetic order in $NiCr_2O_4$ in Fig. 2.4. A low temperature anomaly at T = 30 K, has been observed in magnetic susceptibility and heat capacity measurements of $NiCr_2O_4$ however, there is no prior report of a concurrent structural distortion. [48, 49] In the current study, using high-resolution X-ray powder diffraction, we find evidence for a structural distortion at T = 30 K, as described in detail in a later section. Similarly, an orthorhombic distortion of the already Jahn-Teller distorted tetragonal $CuCr_2O_4$ occurs concurrently with ferrimagnetic ordering at 130 K (Fig. 2.5). This transi-

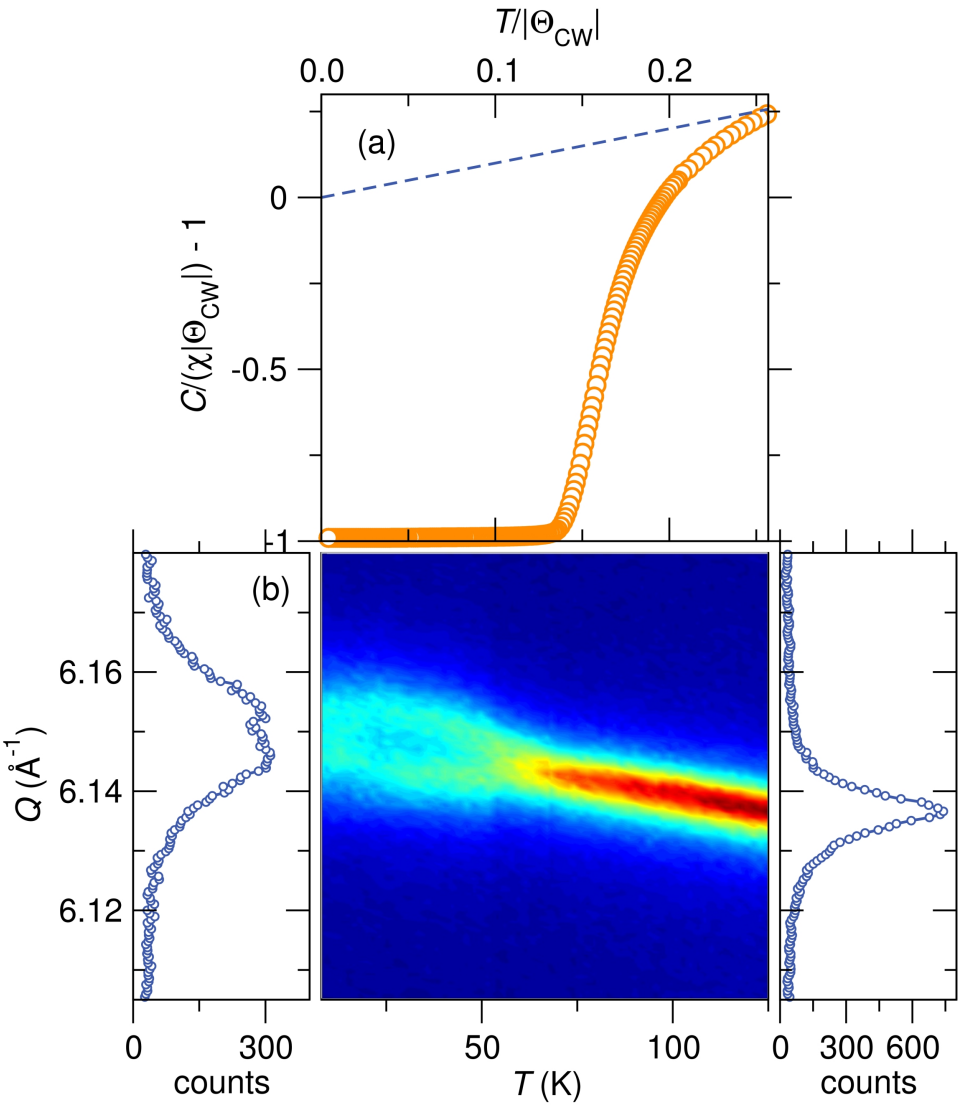

Figure 2.4: Magnetostructural coupling in $NiCr_2O_4$. (a) $NiCr_2O_4$ orders ferrimagnetically at $T_N = 65$ K, where the normalized inverse magnetic susceptibility deviates negatively from ideal Curie-Weiss paramagnetic behavior. (b) A structural transition occurs at the ferrimagnetic ordering temperature seen from the splitting of the tetragonal 440 diffraction peak into 080 and 800 orthorhombic peaks. Below 30 K, a subtle peak narrowing and intensity change is coincident with anomalies in magnetic and specific heat measurements. 125 K and 7 K diffraction patterns are shown to the right and left of the central panel. During this structural transition, the 440 reflection splits in the Q range 10^{-2}Å well within the instrumental resolution of 10^{-4}Å. Reproduced with permission from reference [14], © 2012 American Physical Society.

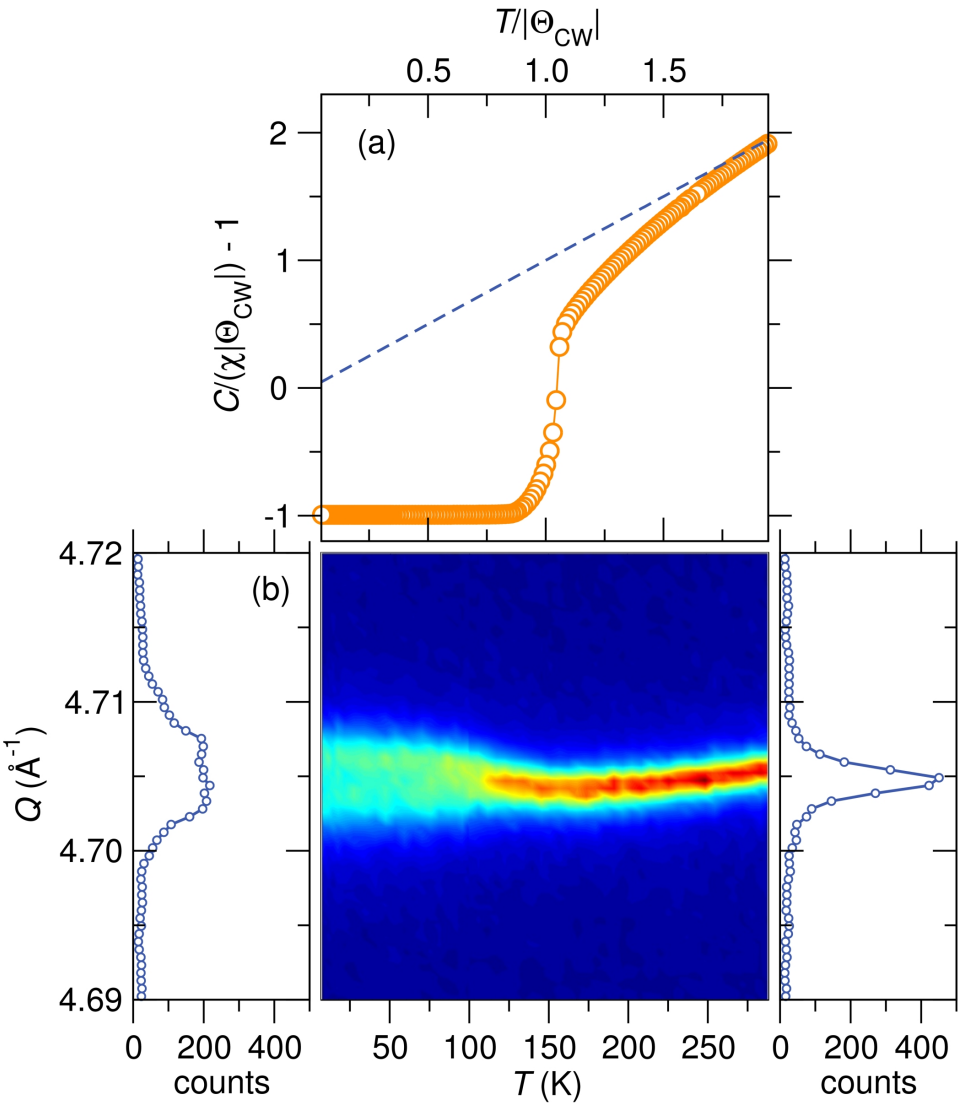

Figure 2.5: Magnetostructural coupling in $CuCr_2O_4$. (a) Long-range ferrimagnetic order occurs at $T_N = 130$ K in $CuCr_2O_4$ where the normalized inverse magnetic susceptibility of $CuCr_2O_4$ deviates negatively from ideal Curie-Weiss behavior (b) Concurrent with the onset of magnetic order is a structural transition seen in the splitting of the tetragonal 322 reflection into orthorhombic 206 and 260 reflections. Diffraction patterns at 288 K and 7 K are shown to the right and left of the central plot respectively. This structural distortion result in reflection splitting in the Q range 10^{-2}Å well within the instrumental resolution of 10^{-4}Å. Reproduced with permission from reference [14], © 2012 American Physical Society.

Table 2.1: Structural parameters of $NiCr_2O_4$ obtained from Rietveld refinement of high-resolution synchrotron X-ray diffraction data collected at temperatures above and below the orthorhombic distortion temperature.

	$NiCr_2O_4$	
	Orthorhombic	Tetragonal
T	10 K	100 K
Space group	$Fddd$	$I4_1/amd$
Setting	origin 2	origin 2
Z	8	4
a (Å)	8.18139(5)	5.79029(2)
b (Å)	8.16699(4)	5.79029(2)
c (Å)	8.56786(4)	8.54639(4)
Vol/Z (Å^3)	71.5601(6)	71.6346(4)
Ni/Cu	$8a$ (1/8, 1/8 1/8)	$4a$ (0, 1/4, 3/8)
U_{iso} (10^2 Å^2)	0.01(1)	0.13(1)
Cr	$16d$ (1/2, 1/2, 1/2)	$8d$ (0,0,0)
U_{iso} (10^2 Å^2)	0.01(1)	0.019(1)
O	$32h$ (x, y, z)	$16h$ $(0, y, z)$
	x 0.2561(2)	x 0
	y 0.2589(2)	y 0.5152(2)
	z 0.2683(1)	z 0.2322(2)
U_{iso} (10^2 Å^2)	0.03(2)	0.16(2)
χ^2	3.85	4.15
R_p (%)	6.25	7.06
R_{wp} (%)	8.39	9.41

tion in $CuCr_2O_4$, not previously noted in structural or diffraction studies, is observed here using variable-temperature high-resolution synchrotron X-ray powder diffraction performed on a sample of crushed single-crystals.

Table 2.2: Structural parameters of $CuCr_2O_4$ obtained from Rietveld refinement of high-resolution synchrotron X-ray diffraction data collected at temperatures above and below the orthorhombic distortion temperature.

	$CuCr_2O_4$	
	Orthorhombic	Tetragonal
T	10 K	298 K
Space group	$Fddd$	$I4_1/amd$
Setting	origin 2	origin 2
Z	8	4
a (Å)	7.71271(2)	6.03277(1)
b (Å)	8.53611(2)	6.03277(1)
c (Å)	8.54357(2)	7.78128(1)
Vol/Z (Å^3)	70.3098(3)	70.7986(2)
Ni/Cu	$8a$ (1/8, 1/8 1/8)	$4a$ (0, 1/4, 3/8)
U_{iso} (10^2 Å^2)	0.08(1)	0.67(1)
Cr	$16d$ (1/2, 1/2, 1/2)	$8d$ (0,0,0)
U_{iso} (10^2 Å^2)	0.07(1)	0.29(1)
O	$32h$ (x, y, z)	$16h$ $(0, y, z)$
	0.2446(1)	0
	0.2675(2)	0.5364(1)
	0.2675(2)	0.2526(1)
U_{iso} (10^2 Å^2)	0.06(2)	0.55(1)
χ^2	2.31	3.84
R_p (%)	7.50	8.96
R_{wp} (%)	8.39	6.65

2.3.2 Crystal structure

The ambient temperature structure of both compounds can be indexed in the tetragonal centrosymmetric space group $I4/amd$. At 298 K, $NiCr_2O_4$ is still undergoing the Jahn-Teller driven cubic-tetragonal transition and better structural parameters of the tetragonal phase are obtained at 100 K. Structural parameters obtained from Rietveld refinement of 100 K diffraction data for $NiCr_2O_4$and 298 K diffraction data for $CuCr_2O_4$ to the space group $I4/amd$ are shown in Table 2.1 and Table 2.2. These parameters are in good agreement with previous reports.[55, 63]

Magnetic ordering drives further structural distortions in $NiCr_2O_4$ and $CuCr_2O_4$.[48, 50] The low symmetry structures of $NiCr_2O_4$ and $CuCr_2O_4$ are described by the orthorhombic spacegroup $Fddd$. $Fddd$ is a maximal nonisomorphic subgroup of $I4_1/amd$ and is derived from the parent $Fd\bar{3}m$ by loss of all threefold rotation axes and part of the twofold screw axes. Rietveld refinement fits of 10 K diffraction data to the orthorhombic space group $Fddd$ for both $NiCr_2O_4$ and $CuCr_2O_4$ are shown in Fig. 2.6. Symmetry lowering in $NiCr_2O_4$ and $CuCr_2O_4$ is demonstrated by the splitting of certain high symmetry diffraction peaks as illustrated in Fig. 2.6 (c) and (f). The current work is the first description of the orthorhombic $Fddd$ structure for $CuCr_2O_4$. In $NiCr_2O_4$,

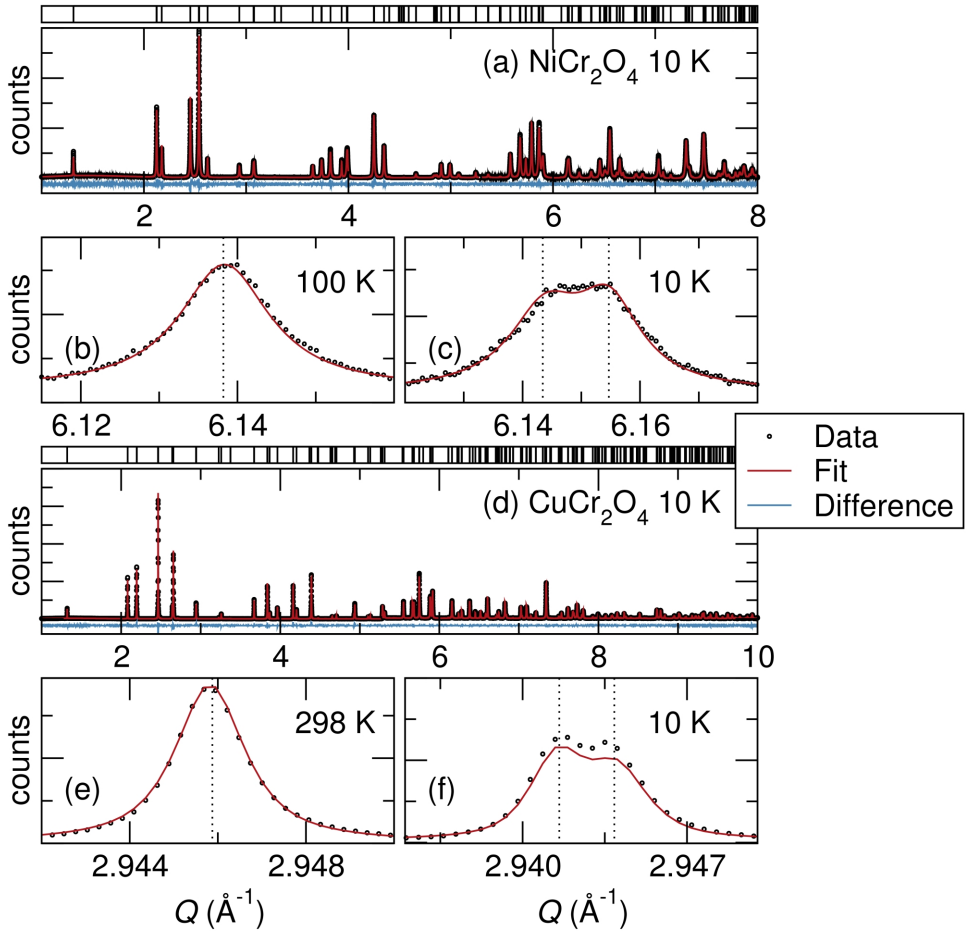

Figure 2.6: High resolution synchrotron powder X-ray diffraction of $NiCr_2O_4$ and $CuCr_2O_4$. (a) The low temperature diffraction pattern of $NiCr_2O_4$ is indexed to the orthorhombic space group $Fddd$. The lowering of average crystal symmetry in $NiCr_2O_4$ from tetragonal to orthorhombic symmetry is illustrated by the splitting of the (b) tetragonal (440) reflection into (c) orthorhombic 800 and 080 reflections. (d) Like $NiCr_2O_4$, the low temperature diffraction data of $CuCr_2O_4$ is indexed to the orthorhombic space group $Fddd$ which is evident in the splitting of (e) (220) tetragonal reflections into (f) 004 and 040 orthorhombic reflections. Structural models are fit to the X-ray powder diffraction patterns using the Rietveld refinement method. Reproduced with permission from reference [14], © 2012 American Physical Society.

variable-temperature synchrotron X-ray diffraction measurements show additional structural changes below 30 K, in concurrence with anomalies in specific heat and susceptibility measurements of $NiCr_2O_4$ reported both here and previously in the literature. This low temperature structural change of $NiCr_2O_4$ is discussed in detail in a later subsection.

Changes in structural symmetry are reflected in the temperature dependence of lattice parameters. At 310 K there is a cubic to tetragonal transition in $NiCr_2O_4$ that splits the cubic a lattice constant into tetragonal a and c lattice parameters [Fig. 2.7 (a) and (b)]. Below 310 K, the tetragonal $NiCr_2O_4$ distortion grows, with an increasing c and a decreasing a lattice constant (plotted as $\sqrt{2}a$). Below 65 K, magnetic ordering occurs concurrently with a transition to orthorhombic symmetry. The tetragonal a lattice parameter of $NiCr_2O_4$ diverges into distinct orthorhombic a and b lattice constants [Fig. 2.7(b)]. At 30 K, a slope change clearly visible in the a and c lattice parameters [Fig. 2.7] matches anomalies in other property measurements as will be discussed later. $CuCr_2O_4$ is already tetragonal at ambient temperature due to cooperative Jahn-Teller ordering at 853 K. The tetragonal lattice constants of $CuCr_2O_4$ diverge below 300 K with c decreasing and the a lattice constant [plotted as $\sqrt{2}a$ in Fig. 2.8(a)] increasing, resulting in an enhanced tetragonal distortion with decreasing temperature. Below 130 K, where an orthorhombic distortion occurs concurrently with the

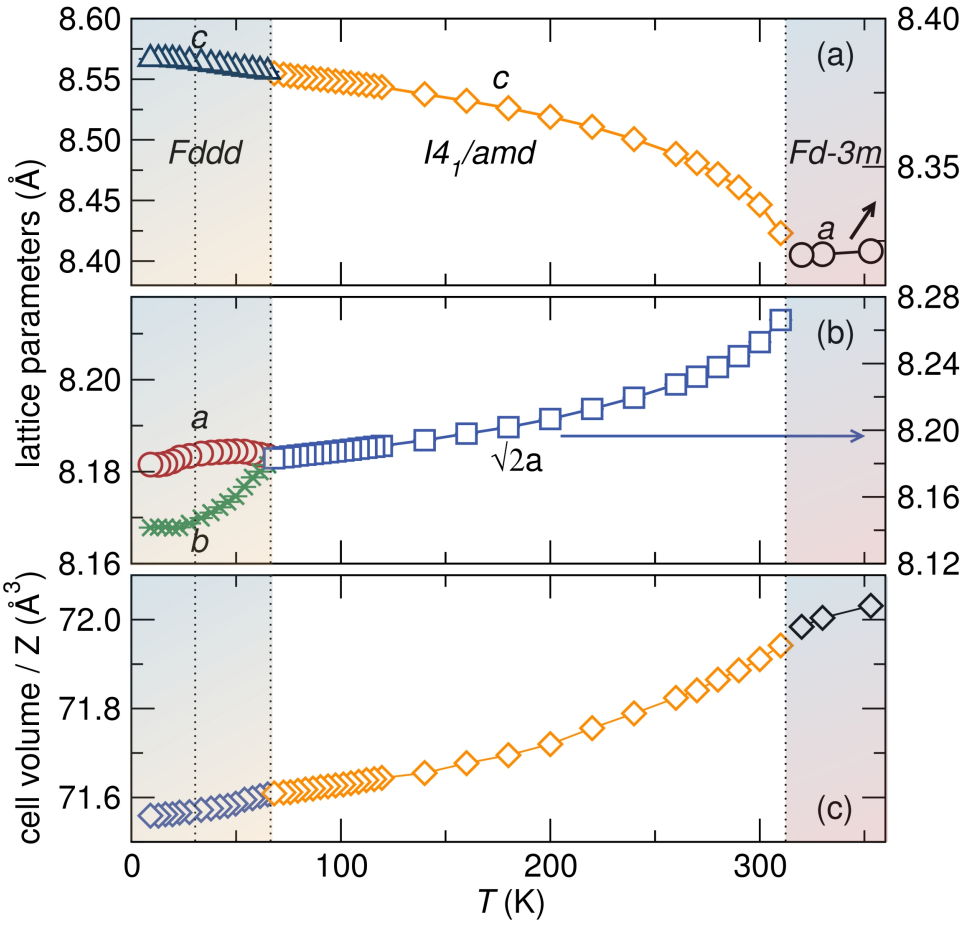

Figure 2.7: Changes in lattice parameters as a function of temperature in $NiCr_2O_4$. (a) A cubic to tetragonal structural transition occurs at 310 K where the a lattice constant of the cubic phase diverges into a and c lattice parameters of the tetragonal phase. The a lattice constant of the tetragonal cell is multiplied by $\sqrt{2}$ to clearly follow trends in the lattice parameters of $NiCr_2O_4$. In the tetragonal phase, the a parameter decreases (b) while c increases (a) with decreasing temperature. At 65 K, a tetragonal to orthorhombic structural distortion occurs resulting in three distinct lattice constants as shown in (a) and (b). (c) Variation of the cell volume normalized by the number of formula units(Z) in each cell. A further structural distortion of orthorhombic $NiCr_2O_4$ occurs at 30 K where there is a slight discontinuity of the lattice parameters (a) and (b) and cell volume (c); this is highlighted by the dashed line at $T = 30$ K. In (a), (b) and (c) the error bars are smaller than the data symbols. Reproduced with permission from reference [14], © 2012 American Physical Society.

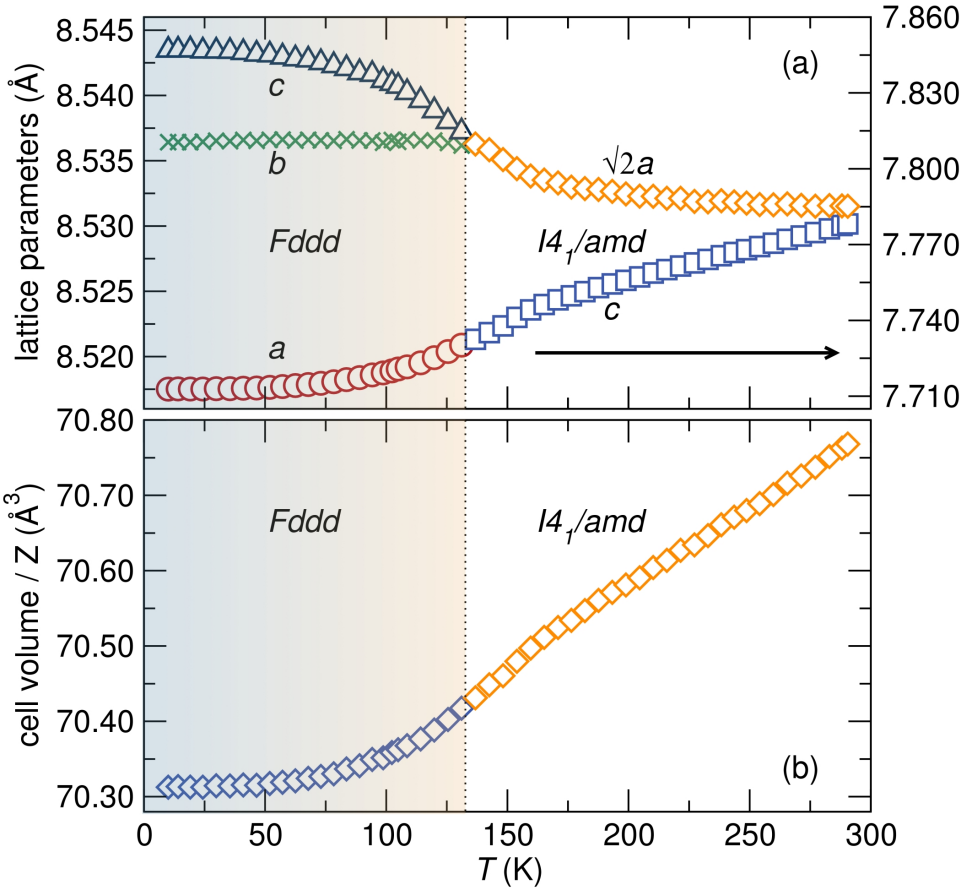

Figure 2.8: (a) The thermal evolution of lattice parameters of $CuCr_2O_4$ reveals a tetragonal $I4_1/amd$ to orthorhombic $Fddd$ structural transition at $\sim$ 130 K. The tetragonal a lattice parameter has been multiplied by $\sqrt{2}$ to match the low temperature b and c lattice values of the orthorhombic $Fddd$ cell. (b) Temperature dependence of the cell volume normalized by the number of formula units (Z) in each cell shows a steady decrease with temperature. In both (a) and (b), the error bars are smaller than the data symbols. Reproduced with permission from reference [14], © 2012 American Physical Society.

onset of ferrimagnetic order [Fig. 2.8(a)], distinct a, b, and c orthorhombic lattice constants emerge. The orthorhombic lattice constants continue to diverge from 130 K to the lowest temperatures measured as indicated in Fig. 2.8(a). The structural change due to orbital ordering in $NiCr_2O_4$ at 310 K results in a discontinuity of the normalized cell volume indicating a first order phase transition. In contrast, in the low temperature tetragonal to orthorhombic phase transitions in $NiCr_2O_4$ and $CuCr_2O_4$ the continuous slope of the normalized cell volume through the magnetostructural transition indicates a second order phase transition [Fig. 2.7(c) and 2.8 (b)].

Structural changes in $NiCr_2O_4$ and $CuCr_2O_4$ originate from deformations of NiO_4 and CuO_4 polyhedra. In a perfect tetrahedron, all bond lengths are equal and all O-Cation-O angles are 109.5°. Ideal NiO_4 tetrahedra are observed in the cubic $NiCr_2O_4$ structure above 310 K [Fig. 2.9 (a) and (b)]. Orbital ordering results in a distorted tetrahedron with a single Ni-O bond distance, but two O-Ni-O angles [Fig. 2.9 (a) and (b)] in the tetragonal phase. Below 65 K, the orthorhombic structure preserves a single Ni-O bond length, but splits the O-Ni-O angles into three distinct O-Ni-O angles in the NiO_4 tetrahedra [Fig. 2.9 (a) and (b)]. These distortions in Ni-O bond lengths and O-Ni-O bond angles result in an elongation of NiO_4 tetrahedra. At ambient temperature, CuO_4 tetrahedra are already significantly distorted with two different O-Cu-O angles and a single Cu-O

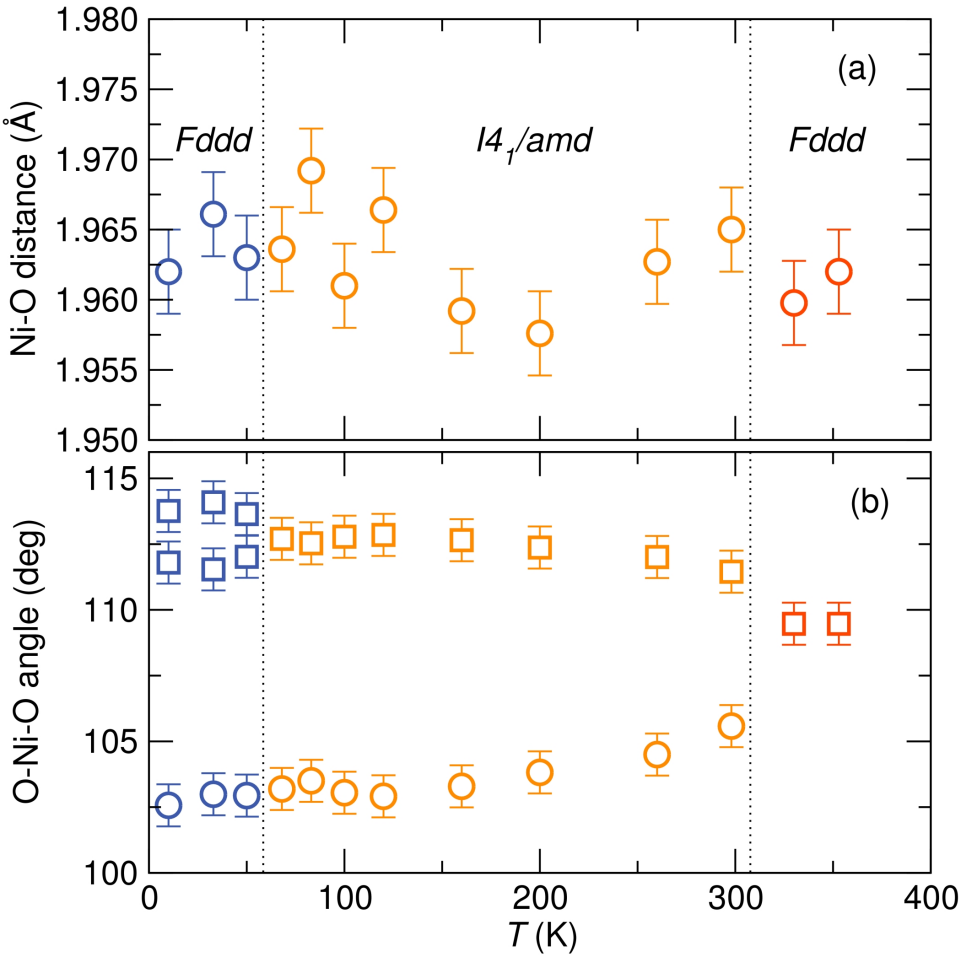

Figure 2.9: The variation in NiO_4 polyhedra as a function of temperature. (a) The Ni-O bond length remains relatively constant in all the structural phases (b) The single O-Ni-O angle of the cubic phase separates into a larger angle and a smaller angle in the tetragonal phase. Below the orthorhombic transition, there are three distinct O-Ni-O angles. Reproduced with permission from reference [14], © 2012 American Physical Society.

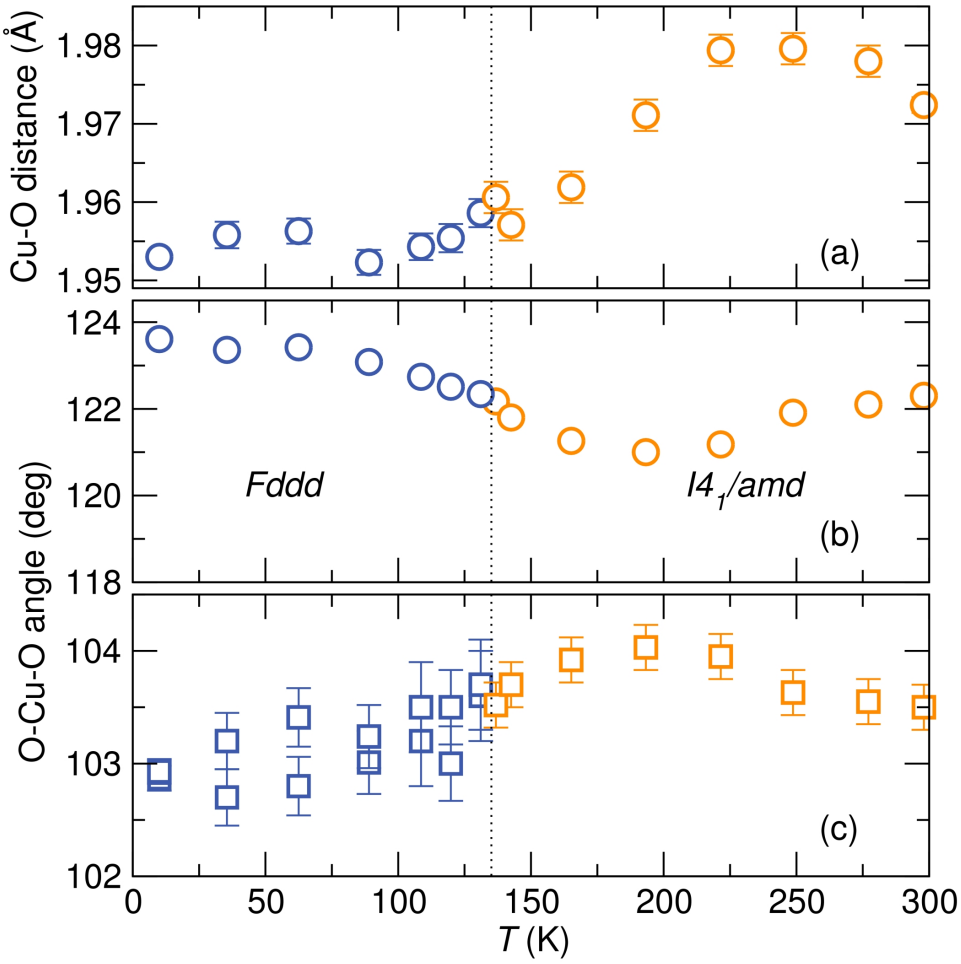

Figure 2.10: Changes in the CuO_4 polyhedra as a function of temperature (a) There is an overall decrease in the Cu-O bond distance, (b) an increase in the larger O-Cu-O angle, and (c) a decrease in the smaller O-Cu-O angle coupled with a splitting of this angle. These trends are obtained from Rietveld refinement of synchrotron X-ray diffraction data. Reproduced with permission from reference [14], © 2012 American Physical Society.

bond distance. With decrease in temperature and the onset of the orthorhombic structural transition, we note a decrease in Cu-O bond lengths [Fig. 2.10(a)], an increase in the larger O-Cu-O angle [Fig. 2.10(b)] and a decrease in the smaller O-Cu-O angle [Fig. 2.10(c)]. The two smaller O-Cu-O angles divide into two. The overall effect of these structural changes is a flattening of the CuO_4 polyhedra toward a square planar configuration. The differences in the distortion of the CuO_4 and NiO_4 tetrahedra are apparent in the average low temperature structures of $NiCr_2O_4$ and $CuCr_2O_4$ shown in Fig. 2.11.

2.3.3 Heat capacity

There are several interesting features in the heat capacity of $NiCr_2O_4$ and $CuCr_2O_4$ that occur concurrently with magnetic and structural transformations in these compounds. Klemme and Miltenburg report three anomalies in the heat capacity of $NiCr_2O_4$ occurring at 310 K, 75 K, and 30 K.[49] Our heat capacity measurements over the temperature range $3\,\mathrm{K} \leq T \leq 200\,\mathrm{K}$ for $NiCr_2O_4$ show two anomalies at 65 K and 30 K [Fig. 2.12(a)]. The Jahn-Teller cubic-tetragonal structural distortion of $NiCr_2O_4$ causes the anomaly in heat capacity at 310 K reported by Klemme and Miltenburg.[49] The transition into a ferrimagnetic ordered state [Fig. 2.4(a)] that occurs concurrently with a structural

change [Fig. 2.4(b)] results in the change in entropy that we observe at 65 K and was reported by Klemme and Miltenburg to occur at $T = 75$ K. Klemme and Miltenburg also reported an additional anomaly in specific heat at 30 K; Ishibashi and Yasumi noted a change in magnetic susceptibility at this temperature. [48, 49] We observe this anomaly in the heat capacity of $NiCr_2O_4$ at 30 K and attribute it to an additional change in the magnetic [Fig. 2.12(b)] and crystal structure [Fig. 2.4(b)] as will be discussed in section D of this paper.

There are two anomalies in the specific heat of $CuCr_2O_4$ at 130 K and 155 K [Fig. 2.12(c)]. The anomaly at 130 K is coincident with ferrimagnetic [Fig. 2.12(d)] and tetragonal-orthorhombic [Fig. 2.5(b)] phase transitions in the compound. The transition into the orthorhombic ferrimagnetic state in $CuCr_2O_4$ occurs through an intermediate step with signatures in Fisher heat capacity and specific heat measurements at 155 K [Fig. 2.12 (c) and (d)].[69] Slight structural effects accompany this second transition as shown in Fig. 2.8(b) where there is a subtle inflection point of the evolution of cell volume with temperature. Further characterization of this intermediate change in the magnetism of $CuCr_2O_4$ at about 155 K requires careful investigation in future study.

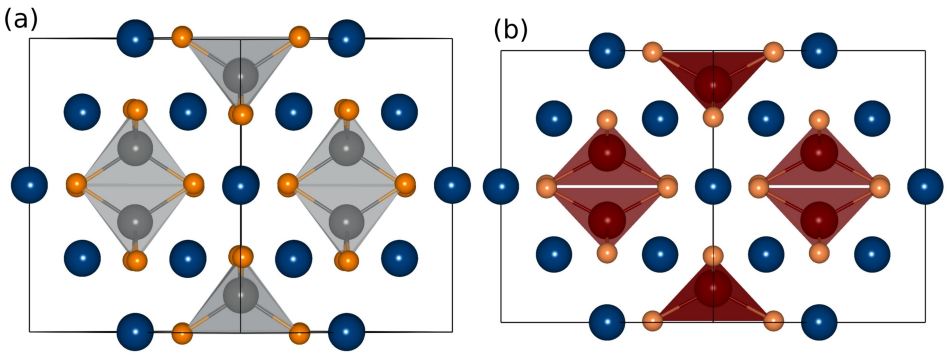

Figure 2.11: Low temperature (10 K) orthorhombic crystal structures of (a)$NiCr_2O_4$ projected down the [101] direction and (b)$CuCr_2O_4$ projected down the [011] direction. Ni(grey) and Cu(red) are tetrahedrally coordinated by oxygen (orange). Chromium is shown in blue. The elongation of NiO_4 tetrahedra along with the compression of CuO_4 polyhedra is clearly seen in the low temperature average structures. Reproduced with permission from reference [14], © 2012 American Physical Society.

2.3.4 Further magnetostructural transitions of $NiCr_2O_4$ at 30 K

During the ferrimagnetic transition of $NiCr_2O_4$, a simultaneous cooperative crystal distortion from tetragonal to orthorhombic symmetry occurs as reported by Ishibashi and Yasumi.[48, 64] We observe this magnetostructural transition in $NiCr_2O_4$ at $T = 65$ K (Fig. 2.4,2.7). Magnetic susceptibility measurements by Ishibashi and Yasumi show yet another low temperature magnetic transition in $NiCr_2O_4$ at $T = 31$ K that was reported by Tomitasu and Kagomiya as corresponding to the ordering of the antiferromagnetic component of the magnetic structure of $NiCr_2O_4$. Klemme and Miltenburg also observed a change in en-

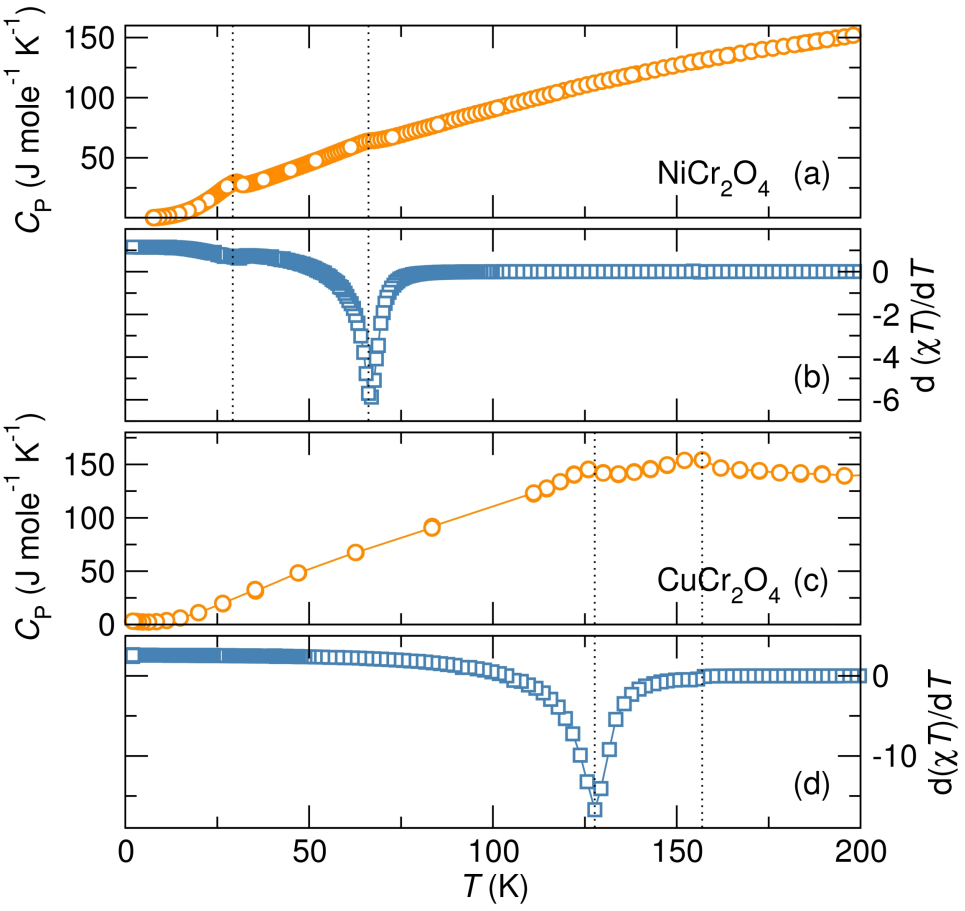

Figure 2.12: Entropy changes in $NiCr_2O_4$ and $CuCr_2O_4$ resulting from structural and magnetic transformations. (a) The heat capacity of $NiCr_2O_4$ shows two anomalies at 65 K and 30 K. (b) Fisher heat capacity of $NiCr_2O_4$ indicating release of magnetic entropy occurring at the same temperatures where changes in specific heat are observed. (c) $CuCr_2O_4$ also shows two transitions in the heat capacity at 155 K and 130 K. Concurrent with these changes in heat capacity of $CuCr_2O_4$ are variations in magnetic structure as illustrated by Fisher heat capacity shown in (d). Reproduced with permission from reference [14], © 2012 American Physical Society.

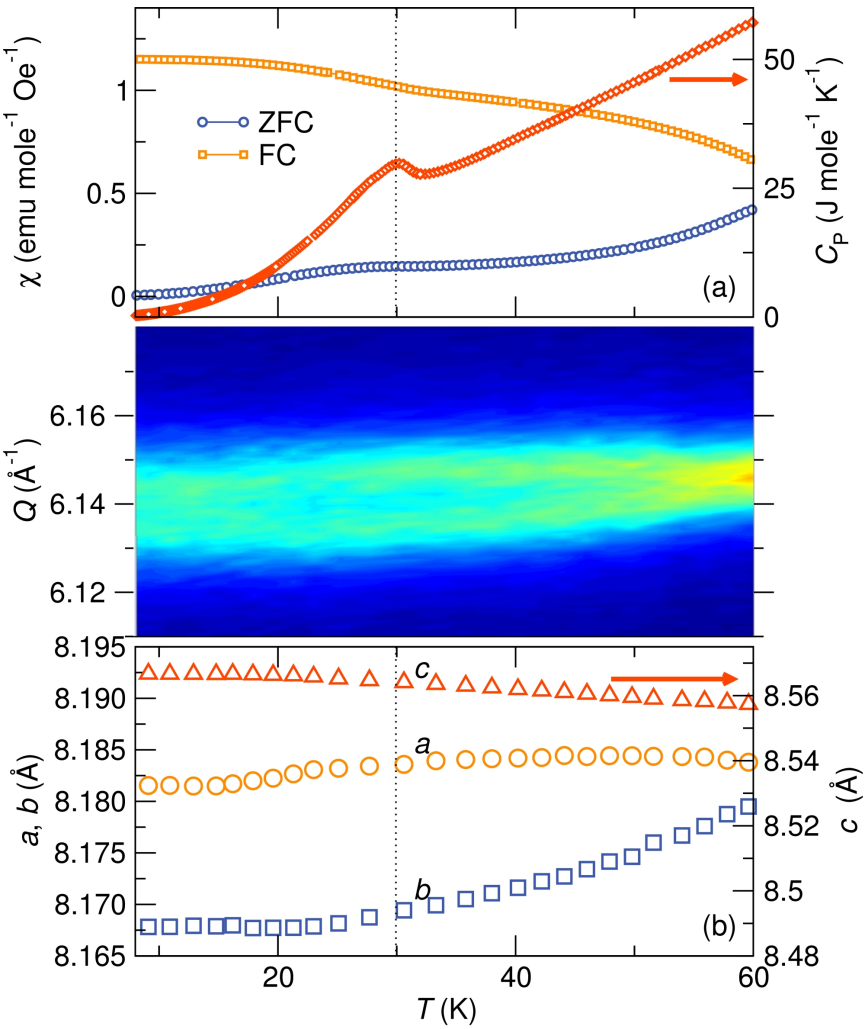

Figure 2.13: Changes in magnetic order and heat capacity of $NiCr_2O_4$ at $T = 30$ K are accompanied by a structural change. (a) Zero field cooled and field cooled temperature dependent magnetic susceptibility measurements of $NiCr_2O_4$ show a change in magnetic order at $T = 30$ K. Concurrent with this transition in magnetism is a change in entropy indicated by the anomaly in heat capacity. The central panel tracks changes in intensity of the orthorhombic 080 and 800 reflections at $T = 30$ K illustrating that a structural change takes place at $T = 30$ K. (c) This structural change is also reflected in the temperature dependent lattice constants of $NiCr_2O_4$ which vary at this temperature. The structural distortion above occurs in the Q range 10^{-2}Å within the instrumental resolution of 10^{-4}Å. Reproduced with permission from reference [14], © 2012 American Physical Society.

tropy at this temperature[49], however, no changes of the average structure of $NiCr_2O_4$ have been observed at $T = 31$ K. [48, 64] Our measurements reveal similar anomalies in the magnetism and specific heat measurements of $NiCr_2O_4$ [Fig. 2.13(a)] at $T = 30$ K. Furthermore, we observe a slight change in average structure at this temperature. The central panel in Fig. 2.13(b) tracks a $NiCr_2O_4$ Bragg diffraction peak as a function of temperature and shows a distinct peak narrowing and intensity change below 30 K. Likewise, the $Fddd$ lattice parameters obtained from Rietveld analysis of the variable temperature diffraction data Fig. 2.7 show a clear change in slope near 30 K [Fig. 2.13(b)]. However, no evidence for a further change of $NiCr_2O_4$ symmetry (*eg.* to monoclinic) below 30 K is found in these high-resolution powder diffraction data. This is the first report of a structural effect concurrent with reported anomalies in heat capacity and magnetic measurements, and will be further examined in future studies.

2.4 Conclusions

Structural changes occur concurrently with magnetic phase transitions in $NiCr_2O_4$ and $CuCr_2O_4$. We have resolved details of the crystal structure of the low temperature phase of $NiCr_2O_4$ and $CuCr_2O_4$ in the orthorhombic space group $Fddd$ and present the first structural description of orthorhom-

bic $CuCr_2O_4$. We find that the magnetic transition at 30 K in $NiCr_2O_4$ is also accompanied by further, subtle structural anomaly. Pronounced elongation of NiO_4 tetrahedra, and compression of CuO_4 tetrahedra toward a square planar configuration drive the distortions into the orthorhombic phase in these compounds. As postulated by Smart and Greenwald, we suggest that multiple exchange coupling pathways in the distorted orthorhombic structure are likely to be the reason behind the strong magnetostructural coupling observed in these compounds.[52] We anticipate that this study will inspire further investigation of such coupling in ferrimagnetic spinels.

Chapter 3

Magnetodielectric coupling in the spinel $NiCr_2O_4$

The spinel $NiCr_2O_4$ is characterized using dielectric and high magnetic field measurements. The trends in the magnetodielectric response fall into three clear temperature regimes corresponding to known magnetic and structural transitions. Above the Néel temperature, weak magnetic field dependence of the dielectric constant is observed with no hysteresis. Below the Néel temperature but above 30 K, a dependence of the dielectric constant on the magnetic

[1]The contents of this chapter have substantially appeared in reference [70]: T. D. Sparks, M. C. Kemei, P. T. Barton, R. Seshadri, E.−D. Mun, and V. Zapf, Magnetocapacitance as a sensitive probe of magnetostructural changes in $NiCr_2O_4$, *Phys. Rev. B* **89** 0244051 (2014)

field is observed and hysteresis develops resulting in so called butterfly loops. Below 30 K, magnetodielectric hysteresis is enhanced. Magnetodielectric hysteresis mirrors magnetic hysteresis suggesting that spin-spin interactions are the mechanism for the magnetodielectric effect in $NiCr_2O_4$. We show that below 40 kOe, the field-dependent permittivity scales linearly with the squared magnetization as described by the Ginzburg-Landau theory. At high fields however, the magnetization continues to increase while the dielectric constant saturates. Magnetodielectric measurements of $NiCr_2O_4$ suggest an additional, previously unobserved transition at 20 K. Subtle changes in magnetism and structure at 20 K, suggest the completion of ferrimagnetic ordering and the spin driven structural distortion. We demonstrate that magnetocapacitance is a sensitive probe of magnetostructural distortion and provide the first high-field measurements of $NiCr_2O_4$.

3.1 Introduction

Coupling of spin and charge in insulating materials can give rise to magnetodielectric effects which enable the control of magnetic polarization using an electric field, or conversely, the reversal of electric polarization by a magnetic field. However, few technologies based on the magnetodielectric effect in in-

sulators have been realized due to the small magnitude of induced magnetic or electric polarization, weak coupling between charge and spin, and the low-temperatures where magnetodielectric coupling often arises. In the last decade, intense effort has been devoted to understanding how magnetism that breaks spatial-inversion symmetry can induce ferroelectricity in so-called type-two multiferroics, especially in the $REMnO_3$ systems.[71, 72] More recently, room temperature magnetodielectricity due to complex spin ordering has been observed in hexaferrites.[71, 73] Electric field control of four different magnetodielectric states in the hexaferrite $Ba_{0.52}Sr_{2.48}Co_2Fe_{24}O_{41}$ reveals new opportunities for the next-generation of memory devices based on magnetodielectric materials.[74]

Advancing the understanding of known magnetodielectric compounds is an important challenge that will guide the design of future multiferroic materials. The normal spinel $NiCr_2O_4$ is a known magnetodielectric that was first reported by Mufti $et\,al.$[55, 75] $NiCr_2O_4$ crystallizes in the cubic space group $Fd\bar{3}m$ above 310 K.[55] Ni^{2+} ions have the degenerate electronic configuration $e^4\,t_2^4$ in tetrahedral coordination while non-degenerate Cr^{3+} e_g^3 prefer to occupy octahedral sites. Below 310 K, orbital degeneracy on tetrahedral Ni^{2+} drives cooperative Jahn-Teller distortion of $NiCr_2O_4$ resulting in the lowering of average structural symmetry from cubic $Fd\bar{3}m$ to tetragonal $I4_1/amd$.[39, 76] This tetrahedral distortion results in the elongation of NiO_4

tetrahedra and $c/a > 1$. Magneto-structural coupling drives further distortion of $NiCr_2O_4$ from tetragonal symmetry to orthorhombic symmetry at the Néel temperature ($T_N \sim$65 K).[14, 48] A second distortion within the orthorhombic structure takes place at $T = 30$ K where anomalies in magnetic susceptibility and heat capacity are observed.[14, 49, 64, 76]

Neutron diffraction studies by Kagomiya and Tomiyasu show that the ordering of the longitudinal ferrimagnetic component of $NiCr_2O_4$ occurs at 60 K and this is followed by the ordering of the transverse antiferromagnetic components at 30 K.[64] Neutron scattering reveals four Cr^{3+} B sublattices, that give rise to a net moment of 2.69 μ_B along the [100] direction, this moment is compensated by the net A sublattice moment of 3.0 μ_B resulting in an overall moment of 0.31 μ_B per formula unit of $NiCr_2O_4$.[64] Detailed heat capacity measurements by Klemme and Miltenburg show three anomalies: at 310 K due to Jahn-Teller ordering, near 70 K and at 29 K due to magneto-structural coupling.[49] Mufti $et\,al.$ have reported changes in the slope of the dielectric constant of $NiCr_2O_4$ at 75 K and 31 K; they also show magnetic field dependence of the dielectric constant of $NiCr_2O_4$.[75] Following this initial work, Maignan $et\,al.$ measured a polarization of 13 μC m^{-2} in the ferrimagnetic state of $NiCr_2O_4$.[77] Polarization in the ferrimagnetic state of the related spinels $FeCr_2O_4$ and $CoCr_2O_4$ has also been observed.[78]

Here, we present a carefully study of the temperature and magnetic field-dependence of polycrystalline $NiCr_2O_4$, revealing three temperature regimes that describe the trends in magnetocapacitance. We provide the first high-field magnetization measurements of the spinel $NiCr_2O_4$ at various temperatures. We describe the correlations between spin-spin interactions and the dielectric constant of $NiCr_2O_4$. We demonstrate the linear correlation between the field-dependent squared magnetization and the changes in dielectric permittivity at low fields. We also discuss the multiferroic properties of $NiCr_2O_4$ in the context of recent studies of magnetostructural coupling in $NiCr_2O_4$ showing that variations in magnetocapacitance occur concurrently with changes in structure and spin configuration.[14] We illustrate the sensitivity of magnetocapacitance measurements to magnetostructural changes in $NiCr_2O_4$ by revealing an unreported anomaly at 20 K. Incorporating detailed magnetic and structural studies, we investigate the origin of the anomaly at 20 K. We conclude that the 20 K anomaly corresponds to the completion of structural and magnetic ordering.

3.2 Methods

Phase pure powders of $NiCr_2O_4$ were prepared from stoichiometric amounts of NiO and Cr_2O_3 that were ground, pelletized, and annealed at 800 $^\circ$ for 12

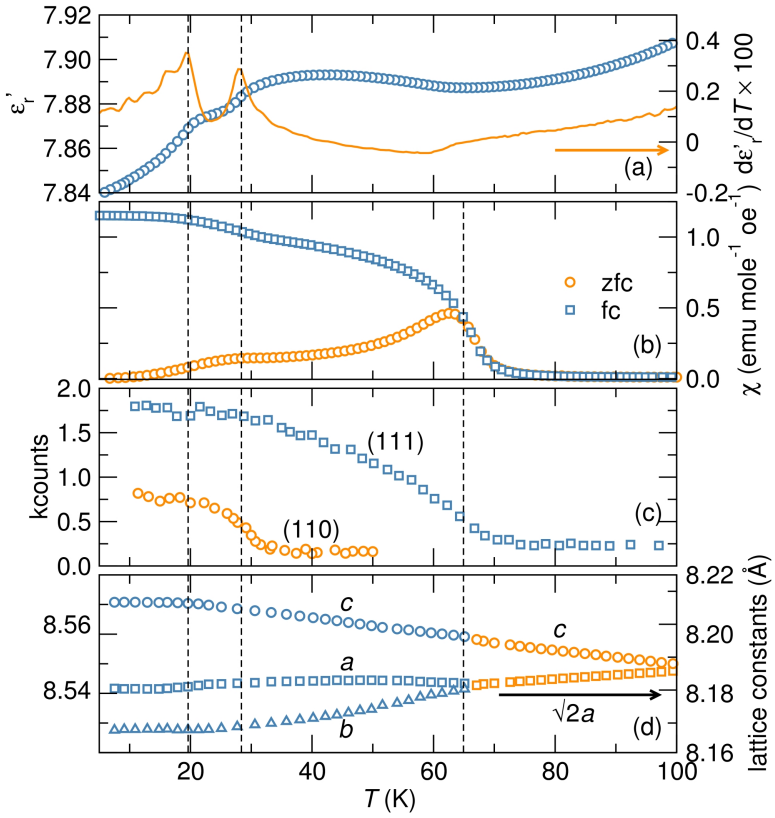

Figure 3.1: Magnetostructural and magnetodielectric coupling in $NiCr_2O_4$. (a) Temperature-dependent dielectric permittivity measurements of $NiCr_2O_4$ collected at 20 kHz, shows anomalies near 30 K and 20 K. The anomaly at 20 K has not been previously observed. The derivative of the dielectric permittivity as a function of temperature shows maxima near 20 K and 30 K. (b) Zero field cooled (ZFC) and field cooled (FC) temperature-dependent magnetic susceptibility of $NiCr_2O_4$ reveal the onset of ferrimagnetic order at 65 K where the ZFC and FC curves diverge. At 30 K, another change in the magnetic structure occurs. We note that below 20 K, the ZFC and FC curves saturate. Neutron diffraction studies of $NiCr_2O_4$ reported by Tomiyasu and Kagomiya are shown in (c).[64] The fundamental (111) reflection increases in intensity below 65 K while the superlattice (110) reflection increases in intensity below 30 K. The neutron reflections attain stable values below 20 K. (d) Lattice parameters of $NiCr_2O_4$ as a function of temperature; the tetragonal to orthorhombic transition occurs at 65 K followed by further structural change at 30 K within the orthorhombic $Fddd$ spacegroup. Below 20 K, the lattice constants plateau. Reproduced with permission from reference [70], © 2014 American Physical Society.

hours. Sample pellets were reground, repelletized, and annealed at 1100 $^\circ$ for 24 hours. Structural characterization was performed using high-resolution ($\Delta Q/Q \leq 2 \times 10^{-4}$) synchrotron X-ray powder diffraction at the Advanced Photon Source, Argonne National Laboratory. Powder patterns were fit to the crystal structure using the Rietveld refinement method as implemented in the EXPGUI/GSAS program.[66, 67] Magnetic susceptibility measurements were performed using a Quantum Design (QD) Magnetic Property Measurement System. High field magnetization was measured using an extraction magnetometer in a capacitor-bank-driven 65 Tesla pulsed-field magnet at the National High Magnetic Field Laboratory Pulsed-Field Facility at Los Alamos National Laboratory.[79] Samples for magnetocapacitance measurements were spark plasma sintered at 1200 K under a load of 6 kN for 10 minutes with a very fast heating and cooling cycle. Spark plasma sintering was used to achieve high densities ensuring the collection of highly reliable dielectric measurements. Densified pellets were annealed in air to 1100 K for 3 hours to ensure stoichiometric $NiCr_2O_4$ is recovered following slight reduction during the spark plasma sintering process. Laboratory Cu$K\alpha$ X-ray diffraction performed on annealed spark plasma sintered pellets show that stoichiometric $NiCr_2O_4$ is obtained.

Dielectric measurements as a function of temperature and applied magnetic field were carried out using an Andeen-Hagerling AH2700A capacitance bridge

connected via shielded coaxial cables to a sample located within a QD Dynacool Physical Property Measurement System. Coplanar faces of a cylindrical sample 9.5 mm in diameter were polished and coated with conducting epoxy to enable the connection of electrical contacts. The sample was 2.3 mm thick. Capacitance measurements were collected at several frequencies continuously as the temperature or magnetic field was varied at 3 K/min or 150 Oe/s respectively.

3.3 Results

Synchrotron X-ray powder diffraction of $NiCr_2O_4$ collected at 100 K shows that the prepared sample is well modeled by the tetragonal space group $I4_1/amd$ with lattice parameters a = 5.79183(2) Å and c = 8.53835(5) Å. The lattice parameters reported here are in good agreement with values reported in the literature.[14] Oxygen atoms are described by the general positions $x = 0$, $y = 0.5129(2)$, and $z = 0.2329(1)$ while Ni^{2+} and Cr^{3+} occupy special positions (0,$\frac{1}{4}$,$\frac{3}{8}$) and (0,0,0) respectively.

Temperature-dependent dielectric measurements of $NiCr_2O_4$ show anomalies at 20 K and 30 K with clear maxima in the derivative of the dielectric permittivity as a function of temperature [Fig. 3.1 (a)]. A shallow minimum

of the temperature-dependent dielectric permittivity is observed at 65 K with no clear feature in the derivative of the dielectric permittivity with respect to temperature [Fig. 3.1 (a)]. The temperature-dependent dielectric measurements suggests that phase transitions occur at 20 K and 30 K, where there are clear maxima in the derivative of the dielectric permittivity with respect to temperature, while magnetostriction may play a role in the slight changes in the dielectric permittivity of $NiCr_2O_4$ at 65 K. The dielectric permittivity anomalies correlate well with structural and magnetic transitions in $NiCr_2O_4$. Ferrimagnetic ordering occurs near 65 K as shown by divergence of zero-field cooled and field cooled temperature-dependent susceptibility measurements shown in Fig. 3.1 (b). In agreement with the susceptibility studies, neutron diffraction studies by Tomiyasu and Kagomiya show the enhancement of the fundamental (111) reflections below 65 K due to the ordering of the longitudinal ferrimagnetic component of $NiCr_2O_4$ [Fig. 3.1 (c)].[64] Further change in the magnetic structure occurs at 30 K where another anomaly in the temperature-dependent susceptibility is observed [Fig. 3.1 (b)] and (110) superlattice reflections emerges in neutron scattering studies as a result of ordering of the transverse antiferromagnetic component of $NiCr_2O_4$ [Fig. 3.1 (c)].[64] Magnetic ordering in $NiCr_2O_4$ is strongly coupled to structure as reported by Suchomel $et\,al.$[14] At 65 K, ferrimagnetic ordering is accompanied by a tetragonal $I4_1/amd$ to

orthorhombic $Fddd$ structural distortion [Fig. 3.1 (d)]. Further change in magnetic ordering at 30 K also occurs concurrently with further structural distortion of $NiCr_2O_4$ within the orthorhombic $Fddd$ spacegroup [Fig. 3.1 (d)].

At 20 K, a clear anomaly is observed in magnetodielectric measurements of $NiCr_2O_4$[Fig. 3.1 (a)]. Re-evaluation of temperature-dependent magnetic susceptibility, neutron reflection intensities, and lattice constants reveals signatures of structural and magnetic changes at 20 K (Fig. 3.1). Notably, following the magnetostructural transition at 20 K, all the temperature-dependent structural and magnetic parameters attain steady values below 20 K. These trends in neutron intensity, magnetic susceptibility and lattice parameters suggest that magnetic and structural ordering in $NiCr_2O_4$ occurs over a wide temperature range, between 65 K and 20 K, finally reaching completion at 20 K. This finding of the continuous change in spin and lattice structure between 65 K and 20 K is facilitated by high precision magnetocapacitance measurements. The observation of a dielectric phase transition at 20 K that is accompanied by subtle changes in magnetism and structure of $NiCr_2O_4$ demonstrates that magnetocapacitance measurements are extremely sensitive to subtle magnetic and structural changes in functional materials.

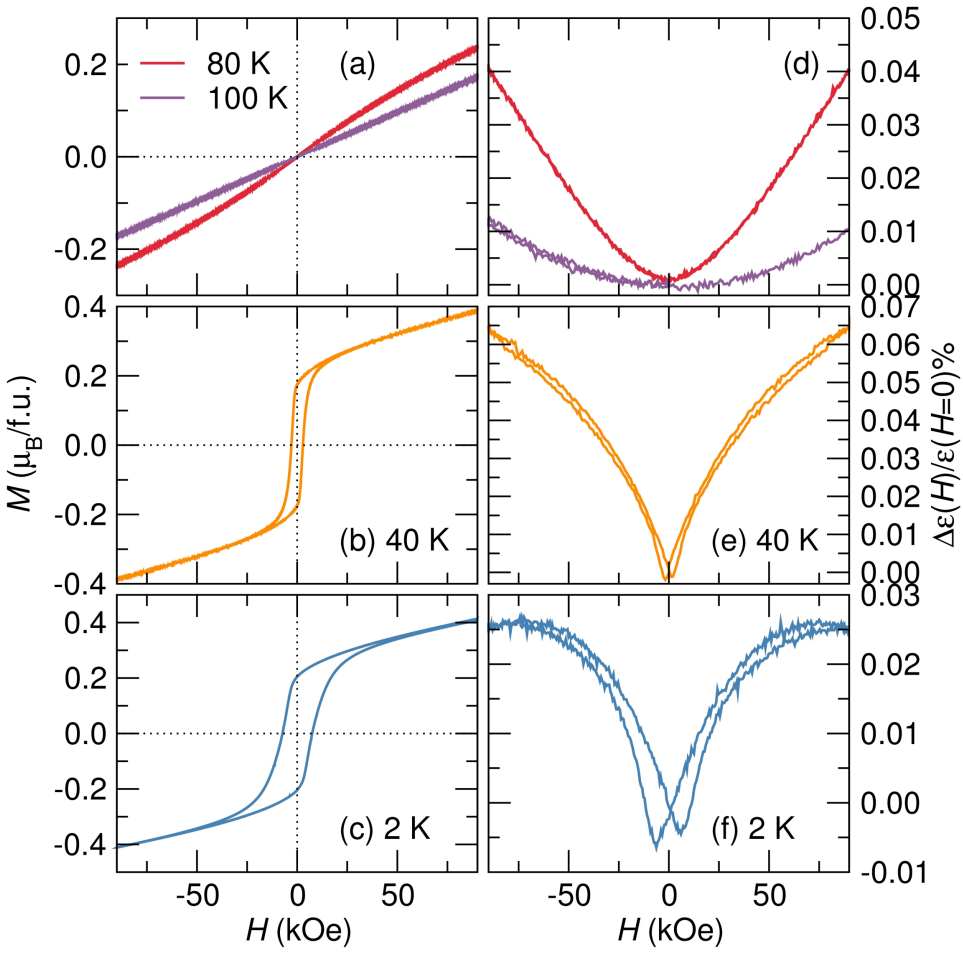

Figure 3.2: Magnetization and magnetodielectric trends in $NiCr_2O_4$. Field-dependent magnetization measurements collected at (a) $\geq$ 80 K, (b) 40 K and (c) 2 K are shown alongside percentage changes in the dielectric permittivity in a varying magnetic field measured at (d) $\geq$ 80 K, (e) 40 K, and (f) 2 K. Above the Néel temperature, there is a weak dependence of the magnetization and the field-dependent dielectric constant on the applied field and no hysteresis [(a) and (d)]. Below the Néel temperature, slight hysteresis is observed in both field-dependent magnetization and dielectric measurements [(b) and (e)]. Below the second magnetic transition of 30 K, hysteresis is further enhanced in both magnetization and dielectric measurements. Field-dependent magnetization measurements collected at 2 K (b) and 40 K (c) show the suppression of hysteresis above 5 T. Reproduced with permission from reference [70], © 2014 American Physical Society.

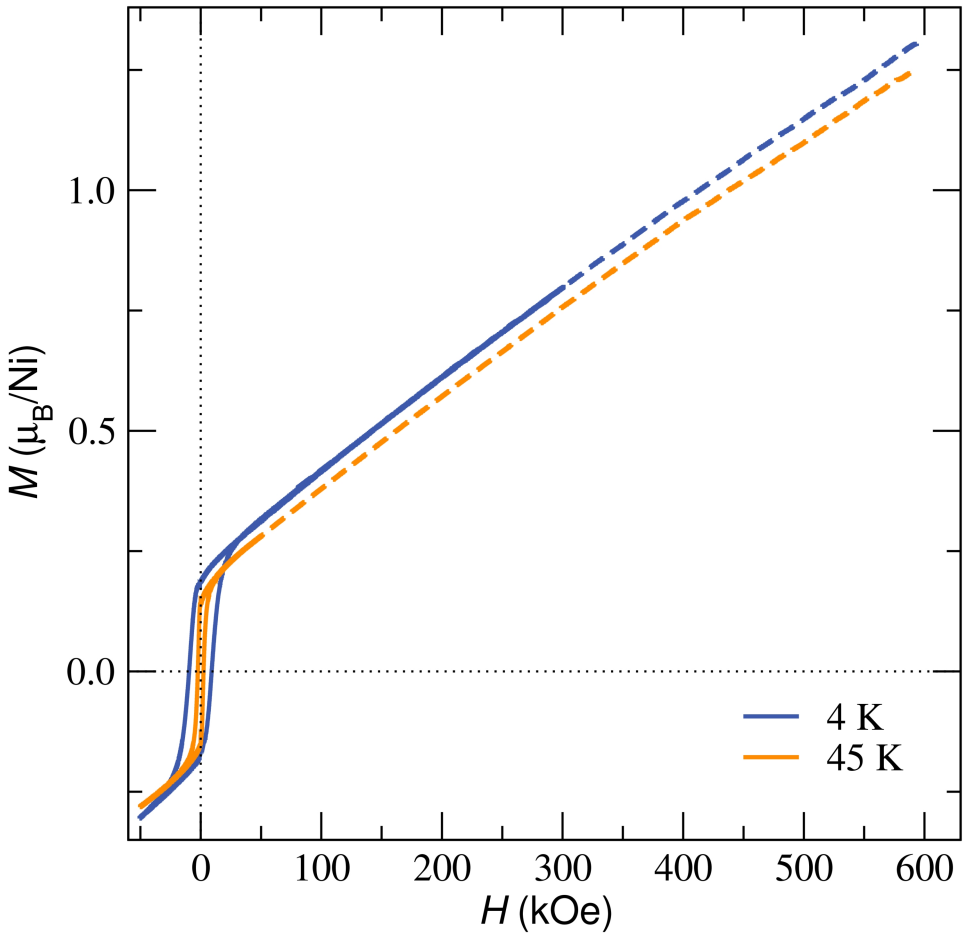

Figure 3.3: High field magnetization measurements of $NiCr_2O_4$ at 45 K and 4 K reveal a linear increase in magnetization with increase in field upto 60 T. Reproduced with permission from reference [70], © 2014 American Physical Society.

There is a linear dependence of the magnetization on the applied field above the Néel temperature as shown in Fig. 3.2 (a). Coercivity develops below the ferrimagnetic ordering temperature of $NiCr_2O_4$ [Fig. 3.2 (b)]. Further enhancement of the coercivity occurs below the second magnetic ordering temperature of 30 K as illustrated in Fig. 3.2 (c). The highest coercivity of $\sim$8.3 kOe is observed near 2 K. High field magnetization studies performed at 4 K and at 45 K reveal a suppression of hysteresis and a linear increase of magnetization above 2.5 T [Fig. 3.3]. At 4 K and 60 T, the magnetization of $NiCr_2O_4$ is about 1.6 μB per formula unit. This magnetization value is 2.4 μ_B less than the expected value for a collinear ferrimagnetic configuration in $NiCr_2O_4$ suggesting that the magnetic structure of $NiCr_2O_4$ reported by Kagomiya and Tomiyasu, which consists of longitudinal and transverse magnetic sublattices, persists to high fields with slight canting of spins contributing to the linear enhancement of the magnetization with field.[64]

When ferrimagnetic interactions are present in $NiCr_2O_4$, the dielectric permittivity exhibits a dependence on the applied magnetic field. Isothermal field dependent dielectric permittivity measurements show a parabolic dependence on the applied field near T_N. Further below T_N, a distinct dependence of the dielectric permittivity, with a sharp minimum near $H = 0$ Oe and significant in-

crease with applied magnetic field emerges. The trends in the isothermal field-dependent dielectric measurements are well described by three temperature regimes [Fig. 3.2 (d), (e), and (f)]. Above $\sim$80 K [Fig. 3.2 (d)], there is a very weak dependence of the dielectric permittivity on the applied field as shown by the field-dependent permittivity measured at 100 K. In the temperature range 30 K$<T<$80 K [Fig. 3.2 (e)], $\Delta\varepsilon(H)/\varepsilon(H=0)$% reaches the maximum value observed in $NiCr_2O_4$ of 0.065 % and hysteresis develops. The dependence of the dielectric constant on the applied field when $T \leq$30 K becomes weaker while significant hysteresis emerges in the field-dependent dielectric response [Fig. 3.2 (f)]. As we discuss below, the trends in the three regimes follow closely the field dependence of the squared magnetization. The very subtle feature in the dielectric permittivity near 65 K suggests magnetostriction may play a role in the observed field dependence of the dielectric permittivity in the temperature regime 30 K$<T<$80 K.

To ensure that the observed magnetodielectric response in $NiCr_2O_4$ is not merely due to magnetoresistance (Maxwell-Wagner effects) we examine the field dependence of the dissipation factor. [80] Catalan has shown that magnetoresistive effects have signatures in the dielectric loss. The dissipation factor, shown in the bottom panel of Fig. 3.4, remains constant in a varying magnetic field while the dielectric permittivity is dependent on the applied field indicating

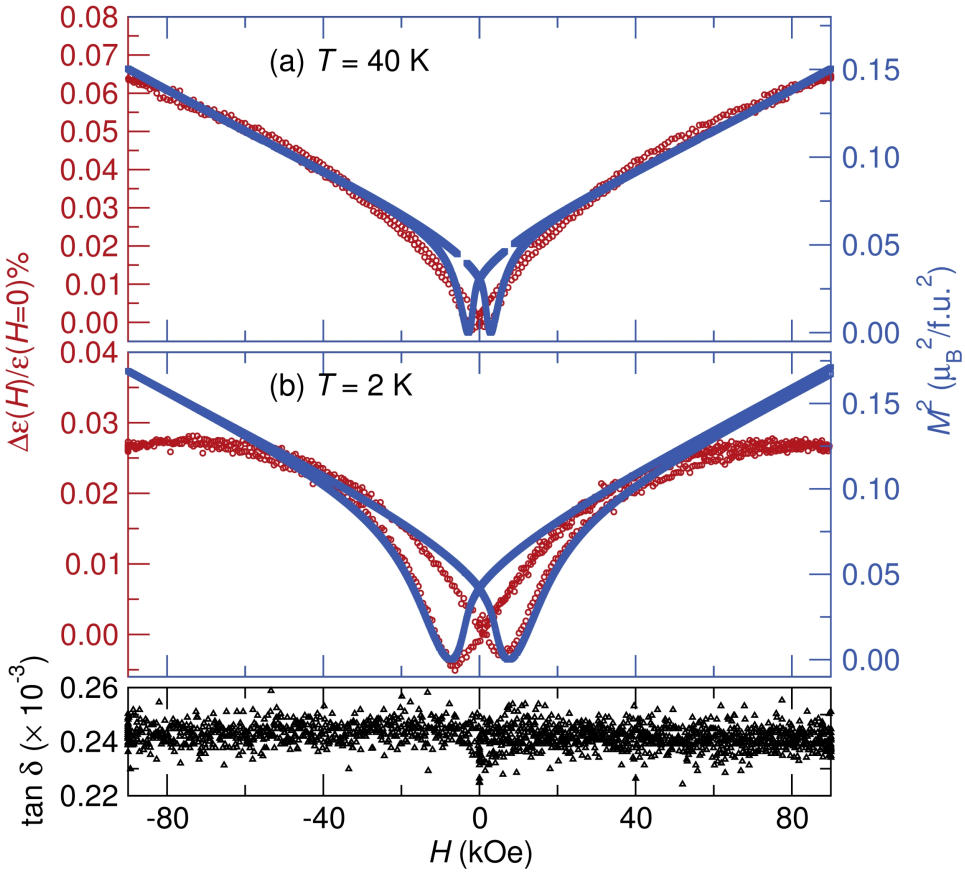

Figure 3.4: The squared field-dependent magnetization plotted against the field-dependent dielectric permittivity measurements collected at (a) 40 K and (b) 2 K. Field-dependent changes in the dielectric constant correlate with trends in the field-dependent squared magnetization at low fields. The bottom panel shows that the dissipation factor is independent of the applied field. The loss was measured at 2 K. Reproduced with permission from reference [70], © 2014 American Physical Society.

intrinsic magnetocapacitance in $NiCr_2O_4$ (Fig. 3.4).[80]

3.4 Discussion

The dielectric anomaly near 30 K occurs concurrently with changes in magnetic structure [Fig. 3.1 (a), (b), and (c)].[64] This correlation supposes that magnetic perturbations couple to the dielectric constant of $NiCr_2O_4$. The coupling between spin-spin correlations and phonons in $NiCr_2O_4$ is not surprising in light of the recent work of Suchomel $et\,al.$ which shows lattice distortions occurring concomitantly with magnetic ordering [Fig. 3.1 (d)].[14] Similar spin-phonon mediated magnetodielectric coupling has been reported for the magnetodielectrics Mn_3O_4,[81] $SeCuO_3$,[82] and $TeCuO_3$.[82]

Changes in the squared magnetization in the presence of an applied field depict the trends in magnetodielectric hysteresis at low fields as shown in Fig. 3.4 (a) and (b). The relative changes in dielectric permittivity in a changing magnetic field trace the squared magnetization below 5 T (Fig. 3.4). Above 5 T and near 2 K, the squared magnetization continues to increase with field while the relative change in dielectric permittivity saturates [Fig. 3.4 (b)]. The agreement between the squared magnetization and the changes in dielectric constant at low fields illustrate that the magnetodielectric coupling term $\gamma P^2 M^2$ of the

Ginzburg-Landau theory for second-order phase transitions (Equation 3.1) is the most significant in $NiCr_2O_4$ as was earlier proposed by Mufti $et\,al.$[72, 75] In the thermodynamic potential Φ expanded to include only second order terms as shown in Equation 3.1, α, α', and γ are temperature-dependent magnetodielectric coupling coefficients, M and P are the magnetization and polarization respectively, and E and H are the electric and magnetic fields respectively. The electric permittivity can be derived from the second partial derivative of the thermodynamic potential with respect to polarization as indicated in equation 3.2. These expressions yield a linear relationship between ϵ and M^2 as shown in equation 3.4. We find that this spin mediated magnetodielectric coupling is most significant at low fields. Field dependent dielectric measurements and the squared magnetization were interpolated over the field range $0\,\text{kOe} \leq H \leq 90\,\text{kOe}$. A linear relationship between $\Delta\epsilon(H)$ and $M^2(H)$ is observed when $10\,\text{kOe} \leq H \leq 50\,\text{kOe}$ as illustrated in Fig. 3.5. Above 50 kOe, the magnetization continues to increase with the applied field while the dielectric permittivity plateaus [Fig. 3.5].

$$\Phi = \Phi_0 + \alpha P^2 - PE + \alpha' M^2 - MH + \gamma P^2 M^2 \tag{3.1}$$

$$\frac{1}{\chi_e} = \frac{\partial^2 \Phi}{\partial P^2} = 2\alpha + 2\gamma M^2 \tag{3.2}$$

$$\epsilon = \chi_e + 1 = \frac{1}{2\alpha + 2\gamma M^2} + 1 \tag{3.3}$$

$$\epsilon \approx 1 + \frac{1}{2\alpha}(1 - \frac{\gamma}{\alpha} M^2) \tag{3.4}$$

The magnetodielectric response, particularly the field dependence of capacitance, yields unique insight to subtle structural distortions in $NiCr_2O_4$. The details of the structural change at 30 K in $NiCr_2O_4$ are not known beyond a slight change in temperature-dependent lattice constants resulting from the elongation of NiO_4 tetrahedra. Nevertheless, the increased magnitude in magnetodielectric hysteresis could possibly suggest a cation off-centering that was not observed in previous structural studies. Polarization measurements by Maignan *et al.* have demonstrated that $NiCr_2O_4$ is indeed a multiferroic with polarization that develops near the Néel temperature and continues to increase until 20 K where it approaches a steady value.[77]

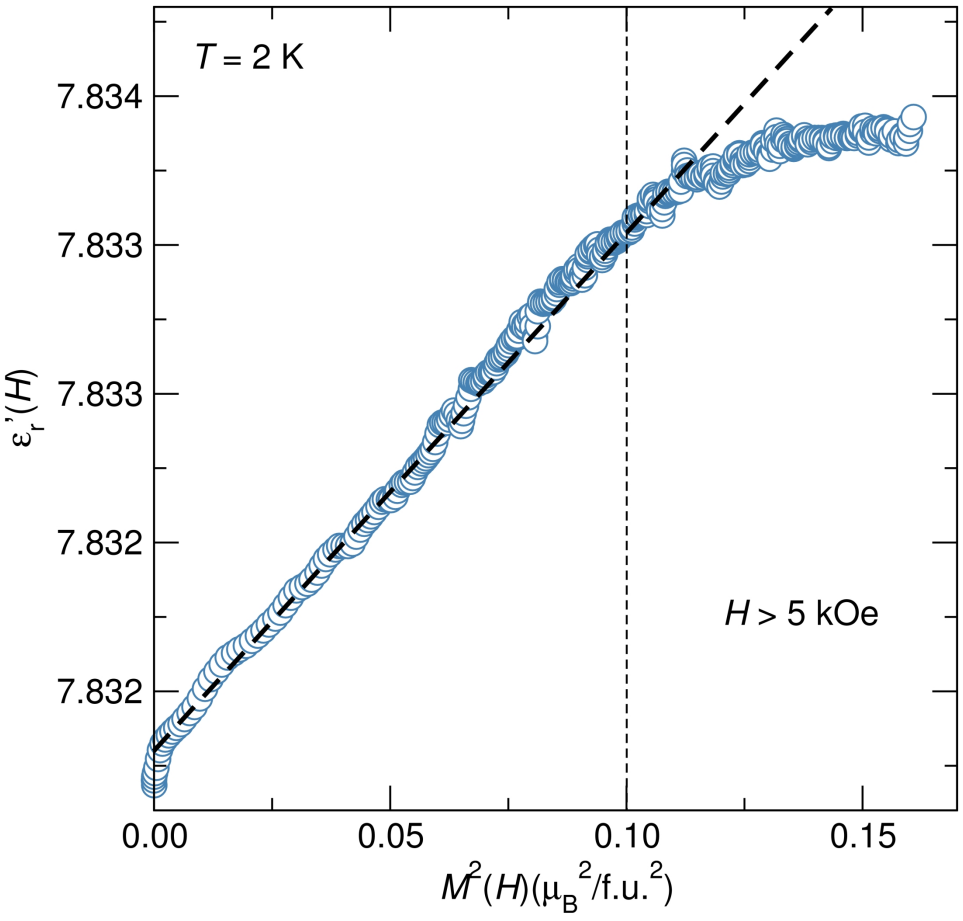

Figure 3.5: A linear relationship is observed between the measured $\epsilon(H)$ plotted against $M^2(H)$ for 10 kOe $\leq H \leq$ 50 kOe near 2 K. Reproduced with permission from reference [70], © 2014 American Physical Society.

3.5 Conclusion

In summary, the magnetodielectric response of dense, single phase $NiCr_2O_4$ samples was measured as a function of field and temperature. The largest magnetodielectric hysteresis was observed in the $Fddd$ phase below 30 K while the largest $\Delta\varepsilon(H)/\varepsilon(H = 0)\% = 0.06\%$, was also observed in the $Fddd$ phase but in the temperature range 30 K $\leq$ T $\leq$ 65 K. We discuss magnetocapacitance in the context of recently reported magnetostructural coupling in $NiCr_2O_4$. We demonstrate the coupling of the spin-spin correlation function to the dielectric constant of $NiCr_2O_4$ which results in three temperature regimes with varying trends in magnetocapacitance. We show the linear correlation between the field induced changes in dielectric permittivity and the squared magnetization in $NiCr_2O_4$ below 50 kOe. We report a 20 K anomaly in $NiCr_2O_4$ that is evident in magnetodielectric measurements and has subtle features in structural and magnetic order parameters. The features in temperature dependent magnetic susceptibility and lattice parameters of $NiCr_2O_4$ at 20 K suggest the completion of spin and structural transformations. We show that magnetocapacitance is a sensitive probe of magnetostructural coupling in $NiCr_2O_4$. We present high-field magnetization studies of the spinel $NiCr_2O_4$ which show a linearly increasing magnetization upto 60 T at 45 K and 4 K.

Chapter 4

Crystal structures of spin-Jahn-Teller–ordered $MgCr_2O_4$ and $ZnCr_2O_4$

Magnetic ordering in the geometrically frustrated magnetic oxide spinels $MgCr_2O_4$ and $ZnCr_2O_4$ is accompanied by a structural change that helps relieve the frustration. Analysis of high-resolution synchrotron X-ray scattering reveals that the low-temperature structures are well described by a two-phase model

[1]The contents of this chapter have substantially appeared in reference [1]: M. C. Kemei, P. T. Barton, S. L. Moffitt, M. W. Gaultois, J. A. Kurzman, R. Seshadri, M. R. Suchomel, and Y.−I. Kim, Crystal structures of spin-Jahn-Teller–ordered $MgCr_2O_4$ and $ZnCr_2O_4$, *J. Phys.: Condens. Matter* **25** 3260011 (2013)

of tetragonal $I4_1/amd$ and orthorhombic $Fddd$ symmetries. The Cr_4 tetrahedra of the pyrochlore lattice are distorted at these low-temperatures, with the $Fddd$ phase displaying larger distortions than the $I4_1/amd$ phase. The spin-Jahn-Teller distortion is approximately one order of magnitude smaller than is observed in first-order Jahn-Teller spinels such as $NiCr_2O_4$ and $CuCr_2O_4$. In analogy with $NiCr_2O_4$ and $CuCr_2O_4$, we further suggest that the precise nature of magnetic ordering can itself provide a second driving force for structural change.

4.1 Introduction

Degenerate ground states, commonly known to occur in amorphous, glassy and spin frustrated compounds, are fertile grounds for the realization of novel phenomena such as zero energy excitations. [8] The properties of liquid ground states, for example the precise nature of excitations and the explicit ground state configurations, are not well known. Spin frustrated systems are ideal models for investigating such behavior. Antiferromagnetically coupled spins on the pyrochlore Cr sublattice of ACr_2O_4 spinels, where A is non-magnetic cation, are geometrically frustrated and they show spin liquid states over a wide temperature range facilitating studies of these highly degenerate ground states.

The highly degenerate spin liquid states of ACr$_2$O$_4$ spinels can order at low temperature in conjunction with a lattice distortion, in a manner sometimes referred to as spin-Jahn-Teller ordering.[24, 83] Despite extensive studies of the spin-Jahn-Teller phases of ACr$_2$O$_4$ spinels, there is little agreement on the full description of the low-temperature structures of MgCr$_2$O$_4$ and ZnCr$_2$O$_4$.[31, 84] At room temperature, ACr$_2$O$_4$ are cubic spinels in the space group $Fd\overline{3}m$, provided the A ions are non-magnetic. A cations occupy tetrahedral sites while Cr^{3+} with spin $S = 3/2$ populate octahedral sites. These are normal spinels: Cr^{3+} shows a strong preference for the octahedral site.[39] Magnetic frustration in ACr$_2$O$_4$ spinels is known to decrease from A = Zn to Mg to Cd to Hg with the respective spinels showing Weiss intercepts Θ_{CW} of -390 K,[46] -346 K,[25, 46] -71 K,[46] and -32 K[34, 46] and spin-Jahn-Teller ordering temperatures (T_N) of $\approx$12.7 K,[28] $\approx$12.5 K,[24] $\approx$7.8 K,[27, 33, 85] and $\approx$5.8 K[34].

Several low-temperature nuclear structures have been proposed for ACr$_2$O$_4$ spinels. X-ray diffraction studies reveal $Fddd$ symmetry in the spin-Jahn-Teller phase of HgCr$_2$O$_4$.[34] A tetragonal $I4_1/amd$ structure of MgCr$_2$O$_4$ was identified in low-temperature synchrotron X-ray[86] and neutron powder diffraction studies.[28] A tetragonal distortion has also been observed in the antiferromagnetic phase of CdCr$_2$O$_4$, identified by Aguilar *et al.* using infrared spectroscopy,[85] and by Chung and co-workers from elastic and inelastic neu-

tron scattering studies.[33] The low-temperature structure of $CdCr_2O_4$ was assigned to the $I4_1/amd$ space group as reported by Lee *et al.* from synchrotron X-ray and neutron scattering studies of single crystals.[31] In the same report, single crystals of $ZnCr_2O_4$ were reported to adopt the tetragonal $I\bar{4}m2$ space group below the Néel temperature.[31] However, X-ray powder diffraction by Kagomiya *et al.* suggested, without describing the complete structure, that at low-temperatures $ZnCr_2O_4$ is modelled by the orthorhombic space group $Fddd$.[84] Recent electron-spin resonance studies of single crystal $ZnCr_2O_4$ by Glazkov *et al.* showed that tetragonal and orthorhombic distortions coexist in the Néel phase of $ZnCr_2O_4$.[87]

We report coexisting tetragonal $I4_1/amd$ and orthorhombic $Fddd$ symmetries in the spin-Jahn-Teller phases of $MgCr_2O_4$ and $ZnCr_2O_4$, observed using high-resolution synchrotron X-ray powder diffraction. Phase coexistence is suggested for the first time in these materials from diffraction studies. This is the first complete description of the spin-Jahn-Teller structures of the important frustrated compounds $MgCr_2O_4$ and $ZnCr_2O_4$. We provide all structural details including the atom positions in both the tetragonal and orthorhombic phases of these systems. This new understanding of the structural ground states of $MgCr_2O_4$ and $ZnCr_2O_4$ is pivotal for theoretical studies and interpretation of excitations in the spin-Jahn-Teller phases of these compounds.

4.2 Experimental details

$MgCr_2O_4$ was prepared by calcination of appropriate solution mixtures of the nitrates $Mg(NO_3)_2{\cdot}6H_2O$ and $Cr(NO_3)_3{\cdot}9H_2O$ at 1000 °C for 10 hours. $ZnCr_2O_4$ and $CdCr_2O_4$ were prepared by solid-state methods from ZnO, CdO, and Cr_2O_3 powders. Samples were annealed in the temperature range 800 °C to 1100 °C. A separate $ZnCr_2O_4$ sample was prepared in a Pt crucible by heating ZnO in an excess $K_2Cr_2O_7$ flux at 800 °C for 24 hours, followed by cooling at 15 °C/h to room temperature. Samples were structurally characterized by high-resolution($\Delta Q/Q \leq 2 \times 10^{-4}$) synchrotron X-ray powder diffraction at temperatures between 6 K and 295 K. These measurements were performed at beamline 11-BM of the Advanced Photon Source, Argonne National Laboratory. Structural models were refined against diffraction data using the Rietveld method as implemented in the EXPGUI/GSAS software program.[66, 67] Atom positions for the low-symmetry structures were obtained using the internet-server tool ISODISPLACE.[88] Crystal distortions were analyzed using the program VESTA.[68] Magnetic properties were characterized using a Quantum Design MPMS 5XL superconducting quantum interference device (SQUID). Heat capacity measurements were performed using a Quantum Design Physical Properties Measurement System.

Table 4.1: Magnetic parameters of $A\mathrm{Cr_2O_4}$ spinels

	T_N (K)	Θ_{CW} (K)	$f = \frac{\lvert\Theta_{CW}\rvert}{T_N}$	μ_{exp} (μ_B)	μ_{calc} (μ_B)
$\mathrm{MgCr_2O_4}$	12.9	−368	29	5.4	5.47
$\mathrm{ZnCr_2O_4}$	12.3	−288	23	5.2	5.47
$\mathrm{CdCr_2O_4}$	7.86	−69.7	8.9	5.3	5.47

4.3 Results and Discussion

At room temperature, the prepared $A\mathrm{Cr_2O_4}$ spinels are homogeneous compounds in the space group $Fd\bar{3}m$ as shown in Figure 4.1. $\mathrm{MgCr_2O_4}$ has a cubic lattice constant of 8.33484(8) Å and it contains a 3.0 wt.% $\mathrm{Cr_2O_3}$ impurity. We study two samples of $\mathrm{ZnCr_2O_4}$; one sample, labelled $\mathrm{ZnCr_2O_4}$ c, is prepared by solid-state routes [Figure 4.1 (b)] while the other, labelled $\mathrm{ZnCr_2O_4}$ x, is prepared through a self-limiting flux approach [Figure 4.1 (c)]. In the later, the $\mathrm{K_2Cr_2O_7}$ flux decomposes to yield $\mathrm{Cr_2O_3}$ which reacts with available $\mathrm{Zn^{2+}}$ species to form $\mathrm{ZnCr_2O_4}$. The solid-state $\mathrm{ZnCr_2O_4}$ sample is phase pure and has a lattice constant of 8.32765(8) Å while the flux-prepared $\mathrm{ZnCr_2O_4}$ sample has a lattice parameter of 8.331945(19) Å and contains very small impurities that are almost undetectable in Figure 4.1 (c). The lattice parameters of all the compounds studied here are $\approx 0.1\%$ larger than those of stoichiometric compounds.[29] We discuss the effects of stoichiometry on the properties of these materials later in the manuscript.

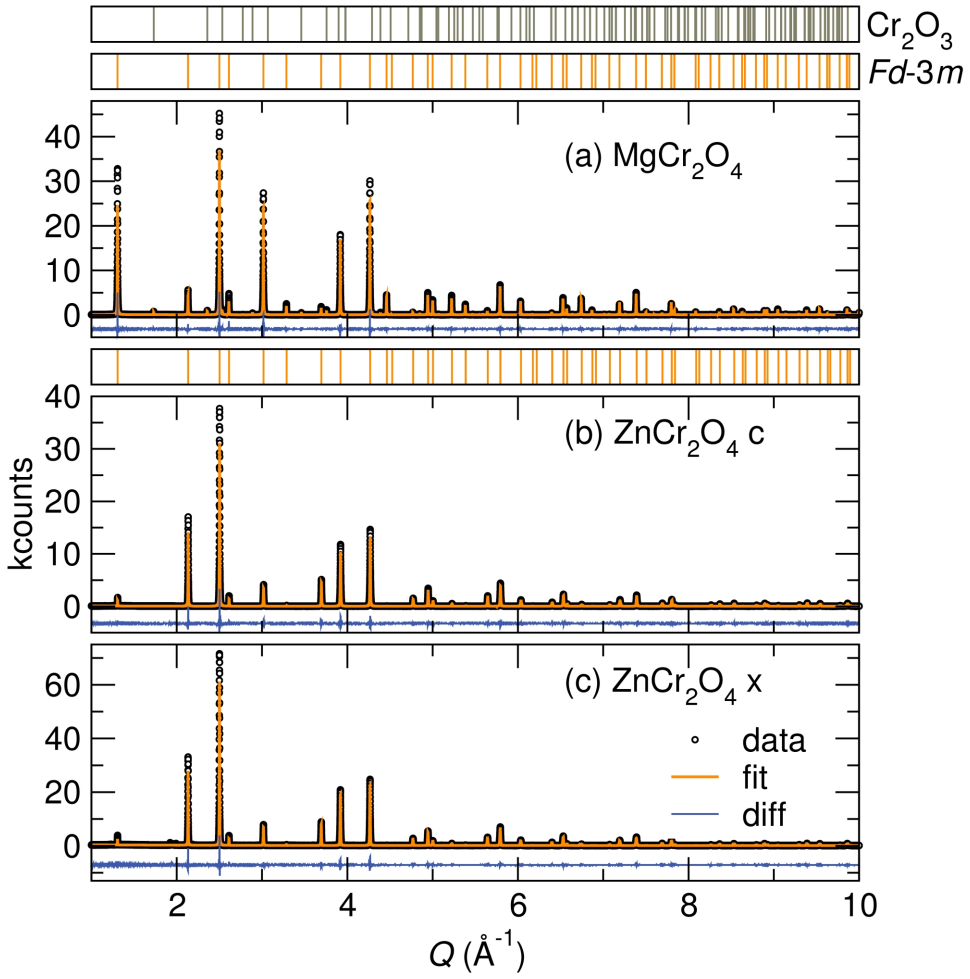

Figure 4.1: Room temperature high-resolution synchrotron X-ray powder diffraction of $MgCr_2O_4$ and $ZnCr_2O_4$. (a) Rietveld refinement of $MgCr_2O_4$ to the $Fd\bar{3}m$ cubic space group. The sample has a 3.0 wt. % Cr_2O_3 impurity. (b) $ZnCr_2O_4$ prepared through a solid-state route (sample labelled $ZnCr_2O_4$ c) and (c) using a $K_2Cr_2O_7$ flux (sample labelled $ZnCr_2O_4$ x) are also indexed to the cubic $Fd\bar{3}m$ space group. The solid-state sample (denoted as $ZnCr_2O_4$ c) is phase pure while the flux approach sample (denoted as $ZnCr_2O_4$ x) features small unidentified impurities. Reproduced with permission from reference [1] © 2013 IOP Publishing Ltd.

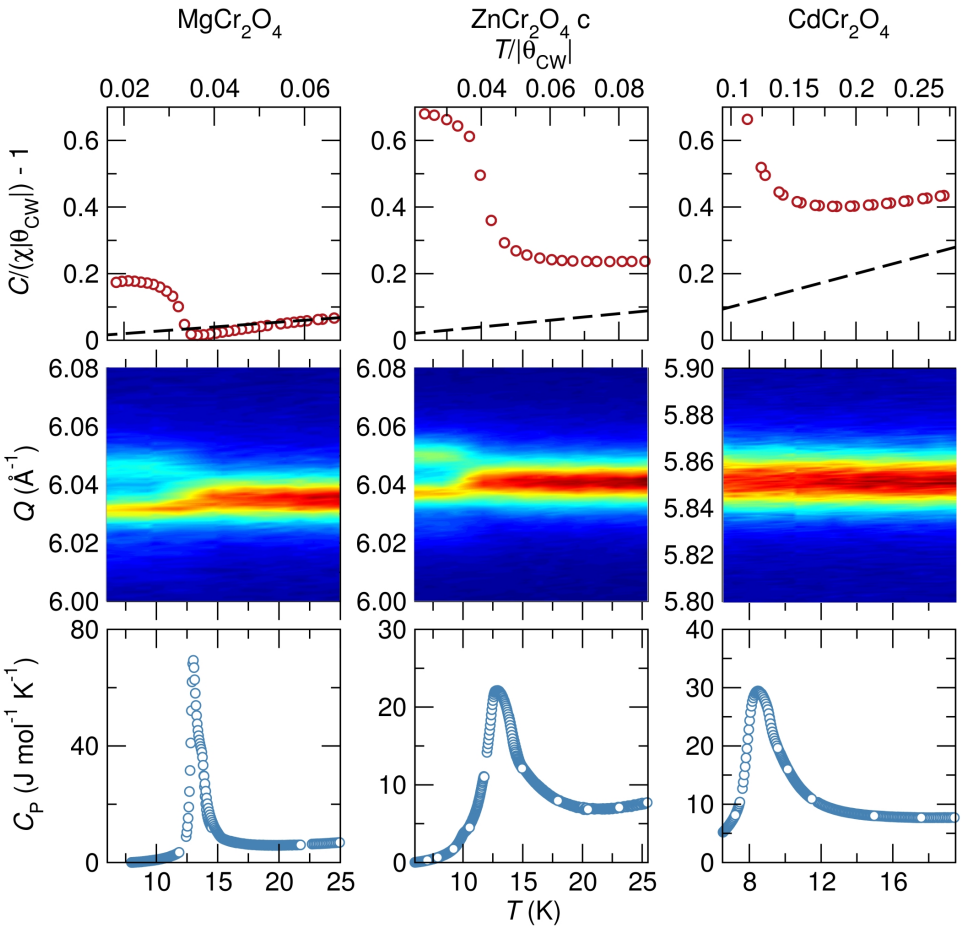

Figure 4.2: Spin-Jahn-Teller distortions in $A\mathrm{Cr_2O_4}$ spinels. The top panel shows the scaled inverse field-cooled susceptibility. The dashed black line models ideal paramagnetism. $\mathrm{MgCr_2O_4}$ and $\mathrm{ZnCr_2O_4}$ were measured under a 1000 Oe field while $\mathrm{CdCr_2O_4}$ was measured in 6000 Oe. Antiferromagnetic order is suppressed to low temperatures in $\mathrm{MgCr_2O_4}$ ($T_N = 12.9\,\mathrm{K}$), $\mathrm{ZnCr_2O_4}$ ($T_N = 12.3\,\mathrm{K}$), and $\mathrm{CdCr_2O_4}$ ($T_N = 7.86\,\mathrm{K}$). The splitting of high-symmetry cubic diffraction peaks into several low-symmetry peaks shows the onset of spin-driven structural distortions(middle panel). $\mathrm{CdCr_2O_4}$ shows a subtle structural distortion that is indicated by a slight decrease in intensity and increase in width of the high-symmetry peak. The bottom panel shows the change in entropy at the Néel temperature. Reproduced with permission from reference [1] © 2013 IOP Publishing Ltd.

Scaled inverse field-cooled susceptibilities of $A\mathrm{Cr_2O_4}$ as described by the recast Curie–Weiss equation are shown in the top panel of Fig. 4.2. Antiferromagnetic ordering occurs when $T/\Theta_{CW} \ll 1$, indicating geometrically frustrated spin interactions (top axis scale of Fig. 4.2). Slight antiferromagnetic spin correlations are observed above T_N in $\mathrm{ZnCr_2O_4}$ and $\mathrm{CdCr_2O_4}$. We define T_N as the temperature at which $d\chi_{ZFC}/dT$ is maximized. The magnetic properties of the samples presented here are tabulated in Table 4.1. Experimental magnetic moments of these compounds are within error of the calculated effective moment of 5.47 μ_B (Table 4.1). There is a ≈0.3 K thermal hysteresis between the zero-field-cooled and field-cooled temperature dependent susceptibilities of the $A\mathrm{Cr_2O_4}$ spinels. We observe a Θ_{CW} of −288 K for $\mathrm{ZnCr_2O_4}$ which is consistent with the earlier work by Melot *et al.*[37] but is lower than other $|\Theta_{CW}|$ values reported in the literature.[25, 28] The lower $|\Theta_{CW}|$ value could be due to slight off-stoichiometry in $\mathrm{ZnCr_2O_4}$. The magnetic ordering transitions of $A\mathrm{Cr_2O_4}$ spinels are associated with changes in entropy (Figure 4.2) and this agrees well with the earlier work of Klemme *et al.* [89, 90] $\mathrm{ZnCr_2O_4}$ and $\mathrm{CdCr_2O_4}$ have smooth heat capacity anomalies while $\mathrm{MgCr_2O_4}$ has a sharp anomaly with a shoulder feature that could indicate that its structural and magnetic transitions occur at slightly different temperatures.

The cubic $Fd\bar{3}m$ (800) diffraction peak of $\mathrm{MgCr_2O_4}$ and $\mathrm{ZnCr_2O_4}$ splits

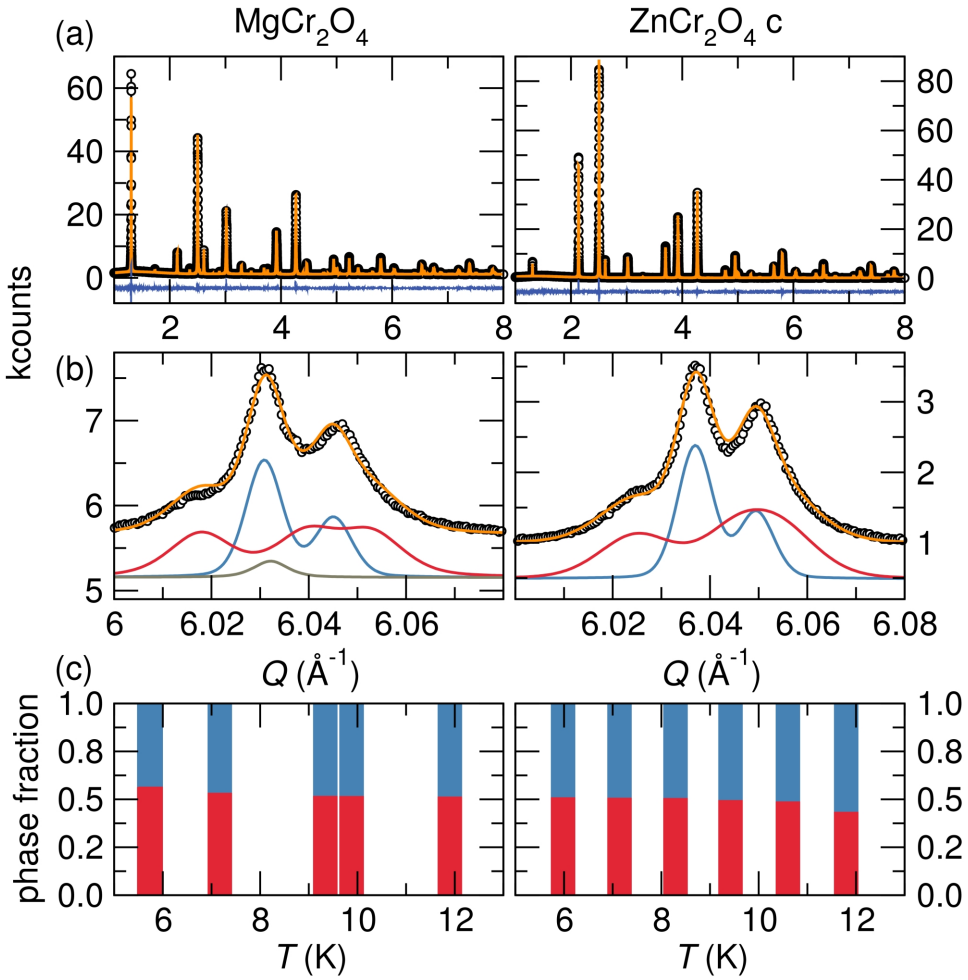

Figure 4.3: Low-temperature diffraction and Rietveld refinement of $MgCr_2O_4$ (left panel) and $ZnCr_2O_4$ c (right panel). (a) High-resolution synchrotron X-ray powder patterns collected at ≈6 K and indexed to a two-phase model of tetragonal $I4_1/amd$ and orthorhombic $Fddd$ symmetries [Data (black), combined $I4_1/amd$ and $Fddd$ fit (orange), difference (blue)]. (b) The high-symmetry (800) peak splits into several $I4_1/amd$ and $Fddd$ reflections. The $I4_1/amd$ and $Fddd$ fits have been offset from the data for clarity. [$I4_1/amd$ (blue), $Fddd$ (red), and Cr_2O_3 impurity (grey)] (c) Nearly equal amounts of $I4_1/amd$ (blue) and $Fddd$ (red) phases coexist below T_N; the $Fddd$ phase fraction increases slightly with decreasing T. Reproduced with permission from reference [1] © 2013 IOP Publishing Ltd.

Table 4.2: The low-temperature structures of $MgCr_2O_4$ and $ZnCr_2O_4$ as determined from Rietveld refinement of high-resolution synchrotron X-ray powder diffraction data. All atomic parameters were allowed to vary during the structural refinement except for isotropic thermal parameters that are constrained to be the same for both low-temperature phases. Tabulated coherence lengths are determined from Scherrer analysis of well resolved peaks. This is the lower limit of crystallite size and assumes that all peak broadening is due to crystallite size.

	$MgCr_2O_4$	$ZnCr_2O_4$ c	$ZnCr_2O_4$ x
T (K)	5.7	5.4	6.9
λ (Å)	0.413393	0.413399	0.413331
space group	$I4_1/amd$	$I4_1/amd$	$I4_1/amd$
Z	4	4	4
a (Å)	5.89351(2)	5.88753(1)	5.88919(2)
c (Å)	8.31503(7)	8.30895(4)	8.31703(5)
Vol (Å^3)	288.809(2)	288.013(2)	288.456(2)
Mg/Zn	$(0,\frac{3}{4},\frac{1}{8})$	$(0,\frac{3}{4},\frac{1}{8})$	$(0,\frac{3}{4},\frac{1}{8})$
Cr	$(0,0,\frac{1}{2})$	$(0,0,\frac{1}{2})$	$(0,0,\frac{1}{2})$
O	0	0	0
	0.5240(3)	0.5250(4)	0.5196(5)
	0.7391(2)	0.7379(4)	0.7387(5)
wt. frac.	0.42(0)	0.43(0)	0.39(0)
coherence length(nm)	69.9	74.5	
space group	$Fddd$	$Fddd$	$Fddd$
Z	8	8	8
a (Å)	8.3041(2)	8.3012(1)	8.3059(9)
b (Å)	8.3228(2)	8.3144(1)	8.3247(8)
c (Å)	8.3526(2)	8.3430(1)	8.3415(0)
Vol (Å^3)	577.279(6)	575.830(5)	576.758(4)
Mg/Zn	$(\frac{1}{8},\frac{1}{8},\frac{1}{8})$	$(\frac{1}{8},\frac{1}{8},\frac{1}{8})$	$(\frac{1}{8},\frac{1}{8},\frac{1}{8})$
Cr	$(\frac{1}{2},\frac{1}{2},\frac{1}{2})$	$(\frac{1}{2},\frac{1}{2},\frac{1}{2})$	$(\frac{1}{2},\frac{1}{2},\frac{1}{2})$
O	0.26130(4)	0.26466(4)	0.26092(3)
	0.26135(4)	0.25722(7)	0.26639(5)
	0.26093(2)	0.26193(5)	0.26015(3)
wt. frac.	0.55(0)	0.57(0)	0.61(0)
coherence length(nm)	40.4	35.6	
Mg/Zn U_{iso}	0.00290(1)	0.00254(5)	0.00305(4)
Cr U_{iso}	0.00167(4)	0.00074(5)	0.00164(4)
O U_{iso}	0.00115(1)	0.00458(2)	0.00321(2)
χ^2	2.903	3.673	1.709
R_{wp}	0.0331	0.0582	0.0823

into several low-symmetry peaks (Figure 4.2). $CdCr_2O_4$ on the other hand, while displaying some peak broadening, remains well modeled by the high-temperature $Fd\bar{3}m$ space group even at 6.9 K (Figure 4.2). Rietveld fits to the low-temperature synchrotron X-ray powder diffraction data of $MgCr_2O_4$ and $ZnCr_2O_4$ using structural models reported in the literature[28, 31, 84, 86] resulted in regions of poorly fit intensity. Similarly, the low-symmetry structures $F222$, $C2/c$, and $I2/a$ could not model the data well. Group-subgroup relations of the space group $Fd\bar{3}m$ yield the lower-symmetry groups $I4_1/amd$ and $Fddd$. Individually, neither of these structural models can reproduce the intensities and peak splittings observed in our low-temperature diffraction patterns of $MgCr_2O_4$ and $ZnCr_2O_4$. However, we find that the diffraction data can be well described by a two-phase model combining both tetragonal $I4_1/amd$ and orthorhombic $Fddd$ structures [Fig. 4.3(a)]. This refinement yields chemically reasonable and stable isotropic thermal displacement parameters for both phases (Table 4.2). In Fig. 4.3(b), the low-temperature peak splitting of the cubic $Fd\bar{3}m$ (800) reflection is de-convoluted into contributions from the $I4_1/amd$ and $Fddd$ phases. Nearly equal fractions of the two phases coexist in the low-temperature nuclear structures of $MgCr_2O_4$ and $ZnCr_2O_4$ [Figure 4.3(c)]. Employing the Thompson-Cox-Hastings pseudo-voigt profile function, we observe a slight increase of the $Fddd$ phase fraction with a decrease in temperature below T_N for both $MgCr_2O_4$

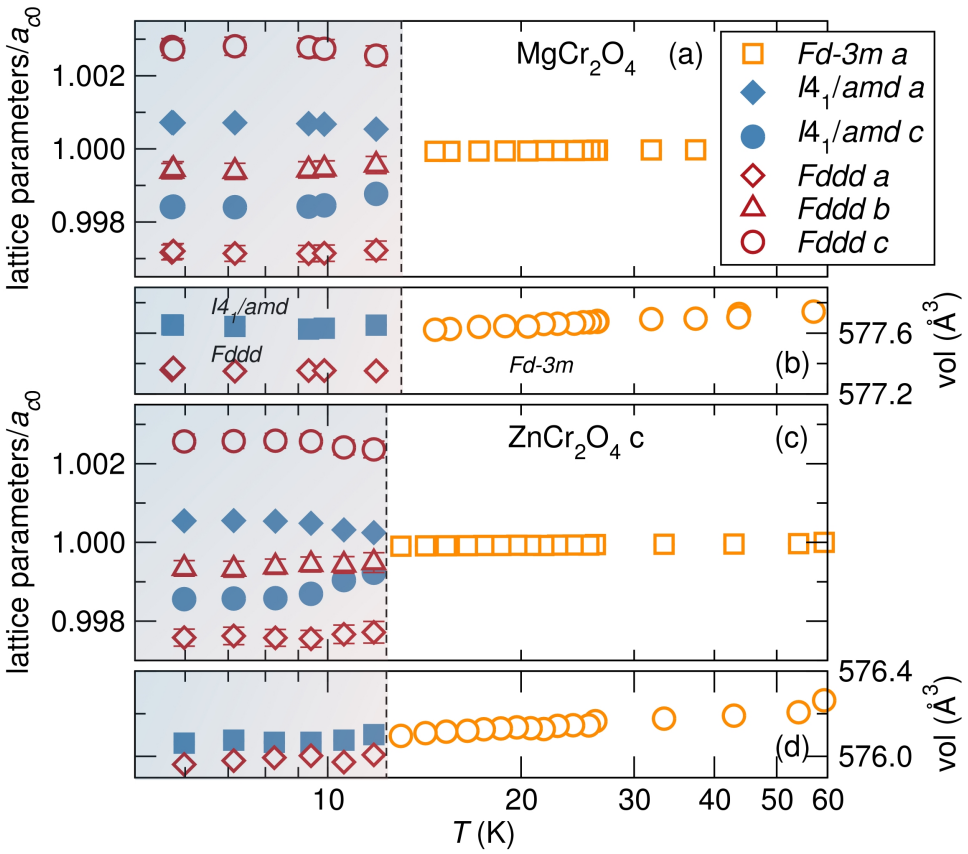

Figure 4.4: Temperature evolution of lattice parameters in $MgCr_2O_4$ and $ZnCr_2O_4$ through their magnetostructural distortions. The cubic lattice constants of $MgCr_2O_4$ (a) and $ZnCr_2O_4$ (c) separate into $I4_1/amd$ and $Fddd$ lattice constants at $T_N = 12.9$ K and $T_N = 12.3$ K respectively. The lattice parameters of $MgCr_2O_4$ are normalized by the lattice constant at 57.1 K ($a_{c0} = 8.32871$ Å) while the lattice constants of $ZnCr_2O_4$ are normalized by the lattice constant at 59.3 K ($a_{c0} = 8.3216$ Å). The $I4_1/amd$ lattice constants have been multiplied by $\sqrt{2}$. The $Fddd$ phases of $MgCr_2O_4$ (b) and $ZnCr_2O_4$ (d) have smaller volumes compared to the $I4_1/amd$ phases. In some cases, error bars are smaller than the data symbols. Reproduced with permission from reference [1] © 2013 IOP Publishing Ltd.

and $ZnCr_2O_4$. While the estimated standard deviations suggest rather accurate phase fractions (Table 4.2), separate refinements employing different profile functions show variations of up to 10%. Scherrer analysis of de-convoluted $I4_1/amd$ and $Fddd$ peaks shown in Fig. 4.3(b) yield larger coherence lengths in the tetragonal phases ($\sim$ 70nm) of $MgCr_2O_4$ and $ZnCr_2O_4$ compared with the orthorhombic phases ($\sim$ 40nm). Williamson–Hall analysis yields larger room temperature crystallite sizes of 118 nm in $MgCr_2O_4$ and 200 nm in $ZnCr_2O_4$. This suggests that the larger $Fd\bar{3}m$ domains split at low temperature into smaller domains of coexisting $I4_1/amd$ and $Fddd$ phases which coexist down to the lowest temperatures studied (Table 4.2).

We have also examined a $ZnCr_2O_4$ sample prepared using a $K_2Cr_2O_7$ flux to explore the effect of sample preparation conditions. High-resolution synchrotron X-ray diffraction measurements carried out at 7 K reveal that it is also described by a combination of both $I4_1/amd$ and $Fddd$. There are subtle differences in the low-temperature phase composition of the flux-prepared sample. The flux-prepared sample has a slightly higher $Fddd$ phase fraction compared with the solid-state $ZnCr_2O_4$ sample (Table 4.2). Coexistence of $I4_1/amd$ and $Fddd$ phases in the spin-Jahn-Teller phases of both flux prepared and solid state $ZnCr_2O_4$ demonstrates that phase coexistence is independent of sample preparation methods.

The $Fd\bar{3}m$ lattice parameter of $MgCr_2O_4$ and $ZnCr_2O_4$ splits abruptly into two $I4_1/amd$ and three $Fddd$ lattice constants at T_N, as shown in Fig. 4.4(a) and (c) respectively. The evolution of lattice parameters of the flux-prepared $ZnCr_2O_4$ sample follows a similar trend. The $Fddd$ a and c parameters of $MgCr_2O_4$ and $ZnCr_2O_4$ show the greatest distortion from cubic symmetry. The smaller cell volume of the $Fddd$ phase of each compound compared to its $I4_1/amd$ counterpart, suggests that $Fddd$ is the lower energy structure. $MgCr_2O_4$ and $ZnCr_2O_4$ undergo a first-order structural transition at T_N indicated by the change in slope of the cell volume [Figure 4.4(b) and (d)], the onset of a two-phase regime [Figure 4.3(b)], and the release of entropy (Figure 4.2).

Cr_4 tetrahedra of $MgCr_2O_4$ and $ZnCr_2O_4$ are distorted below T_N. We compute a tetrahedral distortion index of Cr_4 tetrahedra, $D = 1/n \sum_{i=1}^{n} |l_i - \bar{l}|/\bar{l}$, where l_i is the ith Cr-Cr bond distance and $\bar{l}$ is the average Cr-Cr bond distance.[91] A larger D is seen for the $Fddd$ phases of $MgCr_2O_4$ and $ZnCr_2O_4$ in comparison to the $I4_1/amd$ phases [Figure 4.5(a), (b), and (c)]. Similarly, we compute an angle variance of Cr_4 tetrahedra, $\sigma^2 = 1/(m-1) \sum_{i=1}^{m} (\phi_i - \phi_0)^2$, where ϕ_0 is the ideal tetrahedron angle of 109.47°, ϕ_i is the measured angle, and m is (the number of faces of a tetrahedron)$\times$ 3/2.[68, 92] A greater angle variance occurs in the orthorhombic phases of $MgCr_2O_4$ and $ZnCr_2O_4$ rather

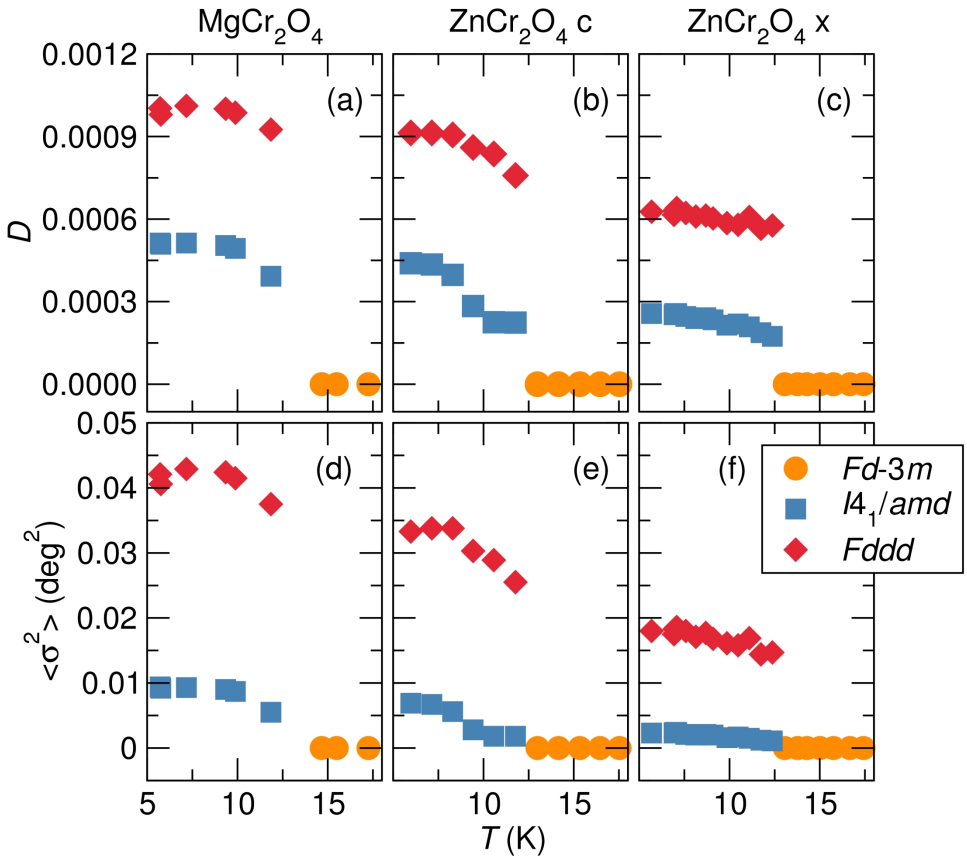

Figure 4.5: Distortion of Cr_4 tetrahedra in the spin-Jahn-Teller phases of $MgCr_2O_4$ and $ZnCr_2O_4$. At 12.9 K and 12.3 K, Cr-Cr bond distance distortions occur in $MgCr_2O_4$ (a) and $ZnCr_2O_4$ (b) and (c). Bond distance distortions are indicated by the distortion index (D). (b) Similarly angle variance (σ^2) shows that Cr_4 angles are distorted below T_N in $MgCr_2O_4$ (d) and $ZnCr_2O_4$ (e) and (f). c denotes the solid-state polycrystalline $ZnCr_2O_4$ sample while x denotes the $ZnCr_2O_4$ sample prepared using a $K_2Cr_2O_7$ flux. Distortions of Cr_4 tetrahedra are suppressed in flux-prepared $ZnCr_2O_4$ compared to the solid-state $ZnCr_2O_4$ sample. Reproduced with permission from reference [1] © 2013 IOP Publishing Ltd.

than in the tetragonal phases [Figure 4.5(d), (e), and (f)]. The $ZnCr_2O_4$ sample prepared from a $K_2Cr_2O_7$ flux has less distortion of its Cr_4 tetrahedra compared with the solid-state $ZnCr_2O_4$ compound (Figure 4.5). The differences in distortion of the two $ZnCr_2O_4$ samples is likely due to higher strain effects in the $K_2Cr_2O_7$ flux prepared sample. Of the two compounds studied, Cr_4 tetrahedra are more distorted in $MgCr_2O_4$ than in $ZnCr_2O_4$.

The lattice parameters and magnetic properties of $MgCr_2O_4$ and $ZnCr_2O_4$ are sensitive to stoichiometry.[29] Lattice constants of $MgCr_2O_4$ and $ZnCr_2O_4$ reported in the literature show a large distribution with the most stoichiometric compounds showing the smallest lattice parameters.[12, 28, 29, 37, 46, 84, 86, 93] Our samples are slightly non-stoichiometric with lattice parameters $\approx 0.1\%$ larger than those of stoichiometric compounds.[29] There appears to be a correlation between stoichiometry and the extracted Θ_{CW} values. Stoichiometric compounds of $ZnCr_2O_4$ yield Θ_{CW} values of ≈ -400 K[29, 46] while slightly off-stoichiometric compounds have Θ_{CW} values of ≈ -288 K as reported here. The effect of stoichiometry on the low-temperature nuclear structures of $MgCr_2O_4$ and $ZnCr_2O_4$ should be examined. We anticipate that stoichiometric samples will show one or both of the low-symmetry structures reported here.

The spin-Jahn-Teller distortion of $MgCr_2O_4$ and $ZnCr_2O_4$ resembles martensitic phase transitions, which are displacive solid-solid transitions. Much like

martensitic phase transformations, the spin-Jahn-Teller distortions of $MgCr_2O_4$ and $ZnCr_2O_4$ are induced by varying temperature, involve changes in crystal symmetry without a change in chemical composition, and show hysteresis. Volume changes between the parent and product phases of $MgCr_2O_4$ and $ZnCr_2O_4$, that occur at the spin-Jahn-Teller distortion temperature, could induce strains that result in the coexistence of multiple phases.

It is important to consider whether a single low-symmetry space group could model the data. Our refinements using $F222$, $C2/c$, or $I2/a$ were unable to generate the observed peak separations. Analysis of the Cr_4 tetrahedra distortions shows that the $Fddd$ phase is more distorted than the $I4_1/amd$ phase. Additionally, the $Fddd$ phase fraction increases slightly with a decrease in temperature below T_N. The combination of these two effects would be challenging to describe using a single low-symmetry structural model. Further, the two-phase $I4_1/amd$ and $Fddd$ model is robust against changes in sample preparation conditions.

Phase coexistence following a phase transition is not unusual. Compositional inhomogeneity contributes to multiple low-temperature phases in $Nd_{0.5}Sr_{0.5}MnO_3$.[94] Similarly, complex phase behavior featuring three coexisting phases occurs in the relaxor-ferroelectric systems $Pb(Mg,Nb,Ti)O_3$ due to internal strain, and are proposed to be intrinsic to the system.[95] Distortion from

$Fd\bar{3}m$ to $I4_1/amd$ symmetry, driven by orbital ordering, occurs in the related spinel compounds $NiCr_2O_4$ and $CuCr_2O_4$. This is followed by further distortion to $Fddd$ symmetry due to magnetostructural coupling.[14] The magnetostructural distortions of $NiCr_2O_4$ and $CuCr_2O_4$ are of the same order of magnitude as the structural distortions we observe in $MgCr_2O_4$ and $ZnCr_2O_4$. We make the suggestion that while tetragonal distortion alone may be sufficient to lift spin degeneracy in $MgCr_2O_4$ and $ZnCr_2O_4$, magnetostructural coupling could drive further distortion from tetragonal to orthorhombic symmetry.

4.4 Conclusion

In summary, we report coexisting $I4_1/amd$ and $Fddd$ phases in the spin-Jahn-Teller structures of $MgCr_2O_4$ and $ZnCr_2O_4$. Nearly equal phase fractions of the $I4_1/amd$ and the $Fddd$ phase coexist below T_N. The tetragonal phases have larger coherence lengths than the orthorhombic phases. We make comparisons between the spin-Jahn-Teller phase transitions of $MgCr_2O_4$ and $ZnCr_2O_4$ and martensitic phase transitions. We propose that two mechanisms, spin frustration and magnetostructural coupling, could potentially give rise to the observed structural phase coexistence in $MgCr_2O_4$ and $ZnCr_2O_4$. We note that temperature-dependent heat capacity measurements of $MgCr_2O_4$ show two fea-

tures that likely correspond to a slight separation in temperature of the structural and magnetic phase transitions.

The hallmark of a frustrated system is a highly degenerate ground state configuration. The manifold of degenerate ground states is susceptible to slight perturbations that often give rise to emergent behavior. Examples of novel properties include the observation of zero energy excitations in the degenerate ground state of $ZnCr_2O_4$.[8] This work presents new insights into the ground state nuclear structures of $MgCr_2O_4$ and $ZnCr_2O_4$. This new understanding of the crystal structure of the canonically frustrated systems $MgCr_2O_4$ and $ZnCr_2O_4$ has important consequences for theoretical studies of these systems and the interpretation of excitations in the spin-Jahn-Teller–ordered phases of these compounds.

Chapter 5

Structural ground states of $(A, A')\mathbf{Cr_2O_4}$(A=Mg, Zn; A' = Co, Cu) spinel solid solutions: Spin-Jahn-Teller and Jahn-Teller effects

[1]The contents of this chapter have substantially appeared in reference [96]: M. C. Kemei, S. L. Moffitt, L. E. Darago, R. Seshadri, M. R. Suchomel, D. P. Shoemaker, K. Page, and J. Siewenie, Structural ground states of $(A, A')Cr_2O_4$(A=Mg, Zn; A' = Co, Cu) spinel solid solutions: Spin-Jahn-Teller and Jahn-Teller effects, *Phys. Rev. B* **89** 174411 (2014),

We examine the effect of small amounts of magnetic substituents in the A sites of the frustrated spinels $MgCr_2O_4$ and $ZnCr_2O_4$. Specifically we look for the effects of spin and lattice disorder on structural changes accompanying magnetic ordering in these compounds. Substitution of Co^{2+} on the non-magnetic Zn^{2+} site in $Zn_{1-x}Co_xCr_2O_4$ where $0 < x \leq 0.2$ completely suppresses the spin-Jahn-Teller distortion of $ZnCr_2O_4$ although these systems remain frustrated, and magnetic ordering occurs at very low temperatures of $T < 20$ K. On the other hand, the substitution of Jahn-Teller active Cu^{2+} for Mg^{2+} and Zn^{2+} in $Mg_{1-x}Cu_xCr_2O_4$ and $Zn_{1-x}Cu_xCr_2O_4$ where $0 < x \leq 0.2$ induce Jahn-Teller ordering at temperatures well above the Néel temperatures of these solid solutions, and yet spin interactions remain frustrated with long-range magnetic ordering occurring below 20 K without any further lattice distortion. The Jahn-Teller distorted solid solutions $Mg_{1-x}Cu_xCr_2O_4$ and $Zn_{1-x}Cu_xCr_2O_4$ adopt the orthorhombic $Fddd$ structure of ferrimagnetic $CuCr_2O_4$. Total neutron scattering studies of $Zn_{1-x}Cu_xCr_2O_4$ suggest that there are local AO_4 distortions in these Cu^{2+}-containing solid solutions at room temperature and that these distortions become cooperative when average structure distortions occur. Magnetism evolves from compensated antiferromagnetism in $MgCr_2O_4$ and $ZnCr_2O_4$ to uncompensated antiferromagnetism with substitution of magnetic cations on the non-magnetic cation sites of these frustrated compounds. The sharp heat ca-

pacity anomalies associated with the first-order spin-Jahn-Teller transitions of $MgCr_2O_4$ and $ZnCr_2O_4$ become broad in $Mg_{1-x}Cu_xCr_2O_4$, $Zn_{1-x}Co_xCr_2O_4$, and $Zn_{1-x}Cu_xCr_2O_4$ when $x > 0$. We present a temperature-composition phase diagram summarizing the structural ground states and magnetic properties of the studied spinel solid solutions.

5.1 Introduction

Triangular lattice topologies are at the center of complex ground states in functional oxides as has been shown in the charge ordered triangular metallic $AgNiO_2$ where charge ordering rather than a Jahn-Teller distortion lifts orbital degeneracy[97] and in geometrically frustrated spin systems such as $ZnCr_2O_4$ where magnetic ordering is accompanied by a lattice distortion.[8] The ground states of the canonical spin frustrated systems ACr_2O_4 (A = Mg,[1, 27, 28, 86] Zn,[1, 8, 25, 84] Cd,[27, 33, 85] and Hg[34]) have been extensively explored. To understand the degenerate ground states of ACr_2O_4 spinels, the effect of spin disorder on the magnetic properties of these systems has been investigated; spin disorder is introduced by substituting magnetic ions on the non-magnetic A sublattice of these materials.[36, 37, 98] Similarly, the effect of low concentrations of magnetic vacancies on the Cr sublattice of $ZnCr_{2(1-x)}Ga_{2x}O_4$ has been

studied showing that the freezing temperature of these systems for small x is independent of the spin vacancy concentration.[99] However, the effect of spin and lattice disorder on the structural ground states of the canonical frustrated systems $MgCr_2O_4$ and $ZnCr_2O_4$ has so far not been studied.

Here, we study magnetic ordering and correlated or uncorrelated structural changes in $MgCr_2O_4$ and $ZnCr_2O_4$ when low concentrations of magnetic cations are substituted on the non-magnetic A site. $MgCr_2O_4$ and $ZnCr_2O_4$ are ideal candidates for the present study as they are: (i) Strongly frustrated with expected ordering temperatures of about 400 K yet suppressed antiferromagnetic ordering occurs below 15 K.[29] (ii) Their structural and magnetic ground states are strongly coupled with a lattice distortion occurring concomitantly with antiferromagnetic ordering.[1, 8, 86] (iii) Finally, Cr^{3+} $3d^3$ strongly prefers the octahedral site where it has a non-degenerate electronic configuration thus enabling compositional variation only on the tetrahedral A site. The effect of spin disorder on the structural ground states of $ZnCr_2O_4$ is investigated by substituting magnetic Co^{2+} with a tetrahedral ionic radius of 0.58 Å for Zn^{2+} which has an ionic radius of 0.6 Å in tetrahedral coordination.[100] The similarity in ionic radii between Co^{2+} and Zn^{2+} minimizes the effects of lattice distortion while allowing us to probe the effect of dilute A site spins on the structural ground states of $ZnCr_2O_4$. Jahn-Teller active Cu^{2+} with an ionic radii of 0.57 Å is introduced

to the A sites of $MgCr_2O_4$ and $ZnCr_2O_4$ to study the effect of both structural and spin disorder on the structural ground states of these systems.[100] Mg^{2+} has a Shannon-Prewitt ionic radius of 0.57 Å in tetrahedral coordination.[100]

This study is enabled by variable-temperature high-resolution synchrotron X-ray diffraction, which is a powerful tool for investigating the coupling of spin and lattice degrees of freedom in magnetic oxides. For example, it has been used to show that exchange striction drives further distortions to orthorhombic symmetry in the already Jahn-Teller distorted tetragonal spinels $NiCr_2O_4$ and $CuCr_2O_4$.[14] Similarly, high-resolution synchrotron X-ray diffraction revealed phase coexistence in the spin-Jahn-Teller phases of $MgCr_2O_4$ and $ZnCr_2O_4$.[1] Barton *et al.* have also shown a spin-driven rhombohedral to monoclinic structural distortion in $Co_{10}Ge_3O_{16}$.[101]

We show that $\geq 10\%$ Co^{2+} ions on the Zn^{2+} site of $ZnCr_2O_4$ suppress the structural distortion that accompanies antiferromagnetic ordering in $ZnCr_2O_4$. We also find that concentrations $\geq 10\%$ of Jahn-Teller active Cu^{2+} on the Mg^{2+} site of $MgCr_2O_4$ and on the Zn^{2+} site of $ZnCr_2O_4$ induce average structure distortions at temperatures above the magnetic ordering temperature. The Jahn-Teller average structure distortion in $Mg_{1-x}Cu_xCr_2O_4$ and $Zn_{1-x}Cu_xCr_2O_4$ occurs at higher temperatures with increase in x. Despite the lattice distortions in $Mg_{1-x}Cu_xCr_2O_4$ and $Zn_{1-x}Cu_xCr_2O_4$ when $x \geq 0.1$, magnetic interactions re-

main frustrated and no further average structure distortions are observed at the Néel temperature. The Jahn-Teller distorted systems $Mg_{1-x}Cu_xCr_2O_4$ and $Zn_{1-x}Cu_xCr_2O_4$ when $x \geq 0.1$, are orthorhombic in the space group $Fddd$. In all the studied solid solutions, magnetism evolves from frustrated antiferromagnetism to glassy uncompensated antiferromagnetism.

5.2 Methods

Powder samples of $Zn_{1-x}Co_xCr_2O_4$, $Mg_{1-x}Cu_xCr_2O_4$, and $Zn_{1-x}Cu_xCr_2O_4$ were prepared using solid state preparation methods. The samples $Mg_{1-x}Cu_xCr_2O_4$ were prepared from stoichiometric solution mixtures of the nitrates $Mg(NO_3)_2.6H_2O$, $Cu(NO_3)_2.6H_2O$, and $Cr(NO_3)_3.9H_2O$. The nitrate precursor was calcined at temperatures between 700 °C and 1000 °C for 10 hours as reported by Shoemaker and Seshadri.[93] Powders of $Zn_{1-x}Cu_xCr_2O_4$ were prepared from stoichiometric amounts of ZnO, CuO, and Cr_2O_3 that were ground, pressed into pellets, and calcined at 800 °C for 12 hours. These samples were reground, pressed into pellets, and annealed at 1000 °C for 48 hours followed by further annealing at 800 °C for 12 hours. Stoichiometric powders of $Zn_{1-x}Co_xCr_2O_4$ were prepared from $CoC_2O_4.2H_2O$, ZnO, and Cr_2O_3. These powders were mixed, pressed into pellets, and calcined at 800 °C for 12

hours. The samples were then reground, pressed into pellets, and annealed at 1150 °C for 12 hours followed by further annealing at 800 °C for 24 hours. Samples were structurally characterized by high-resolution ($\delta Q/Q \leq 2 \times 10^{-4}$, $\lambda = 0.413393$ Å) variable-temperature (6 K $\leq T \leq$ 300 K) synchrotron X-ray powder diffraction at beamline 11BM at the Advanced Photon Source, Argonne National Laboratory. Diffraction patterns were fit to structural models using the Rietveld method as implemented in the EXPGUI/GSAS software program.[66, 67] Crystal structures are visualized using the program VESTA. [68] Magnetic properties were measured using the Quantum Design MPMS 5XL superconducting quantum interference device (SQUID). Heat capacity measurements were performed using a Quantum Design Physical Properties Measurement System. Time-of-flight neutron scattering data was collected on the NPDF instrument at Los Alamos National Laboratory. The neutron pair distribution function (NPDF) with a maximum Q of 35 Å was processed using the PDFGETN program.[102] Least squares refinement of the NPDFs was performed using PDFGUI.[103]

5.3 Structural ground states of the spinels $Zn_{1-x}Co_xCr_2O_4$: $x \leq 0.2$

$ZnCr_2O_4$ and $CoCr_2O_4$ are normal cubic spinels in the space group $Fd\bar{3}m$ at room temperature. These systems vary significantly in their magnetic properties, primarily due to the differences in properties of the A site cations. Zn^{2+} has the closed electron configuration [Ar]$3d^{10}$ which renders it magnetically inert. Direct antiferromagnetic Cr^{3+}-Cr^{3+} interactions in the pyrochlore Cr sublattice of $ZnCr_2O_4$ give rise to geometric frustration. A spin-Jahn-Teller distortion partially lifts spin frustration in $ZnCr_2O_4$ enabling the onset of antiferromagnetic order at the Néel temperature.[8, 31, 84, 90] The nuclear structure of the spin-Jahn-Teller phase of $ZnCr_2O_4$ has been extensively studied.[1, 8, 31, 84] Recently, our group has proposed a structural model of coexisting tetragonal $I4_1/amd$ and orthorhombic $Fddd$ phases for $ZnCr_2O_4$.[1] On the other hand, Co^{2+} has the electronic configuration [Ar]$3d^7$ with three unpaired spins that interact ferrimagnetically with Cr^{3+} through Co^{2+}-O-Cr^{3+} superexchange interactions. $CoCr_2O_4$ shows complex magnetic behavior; it undergoes a magnetic phase transition from a paramagnetic state to a ferrimagnetic long-range ordered state near 94 K.[4, 64, 104] A recent report by Chang *et al.* shows long range spiral order in $CoCr_2O_4$ below 25 K with an incommensurate propagation

Table 5.1: Magnetic parameters of $Zn_{1-x}Co_xCr_2O_4$. μ_{eff} and Θ_{CW} were extracted from fitting the susceptibility in the temperature ranges 300 K $< T <$ 390 K, 250 K $< T <$ 390 K, and 200 K $< T <$ 390 K to the Curie-Weiss equation $\chi = \frac{C}{T-\Theta_{CW}}$. Reported are the mean μ_{eff} and Θ_{CW} values along with their standard deviation.

	T_N (K)	$\mu_{exp}(\mu_B)$	$\mu_{calc}(\mu_B)$	Θ_{CW}(K)
$ZnCr_2O_4$	12.3	5.06(0.01)	5.48	−277(4)
$Zn_{0.9}Co_{0.1}Cr_2O_4$	9	5.41(0.01)	5.61	−349(2)
$Zn_{0.8}Co_{0.2}Cr_2O_4$	11	5.60(0.01)	5.74	−373(4)

vector and a transition at 14 K to commensurate spiral order.[105] While no studies report a lowering of structural symmetry in $CoCr_2O_4$, ultrasound propagation measurements performed on single crystals of $CoCr_2O_4$ by Tsurkan *et al.* show a field-induced structural distortion to cubic symmetry at high magnetic fields.[106] $CoCr_2O_4$ exhibits spin charge coupling; the onset of incommensurate spiral order in $CoCr_2O_4$ is accompanied by a change in the dielectric constant.[4, 75] In addition, the dielectric constant shows magnetic field dependence below 95 K. [75] We examine the changes in structural ground states of $ZnCr_2O_4$ when 10% and 20% Co^{2+} cations are substituted on the non-magnetic Zn^{2+} site.

At room temperature, the prepared compounds $Zn_{1-x}Co_xCr_2O_4$ where $x \leq 0.2$ are cubic spinels in the space group $Fd\bar{3}m$ (Fig. 5.1 and Tables 5.4 and 5.5). The similarity in the tetrahedral ionic radii of Co^{2+} and Zn^{2+} allows the entire solid solution $Zn_{1-x}Co_xCr_2O_4$ to retain cubic $Fd\bar{3}m$ symmetry at room

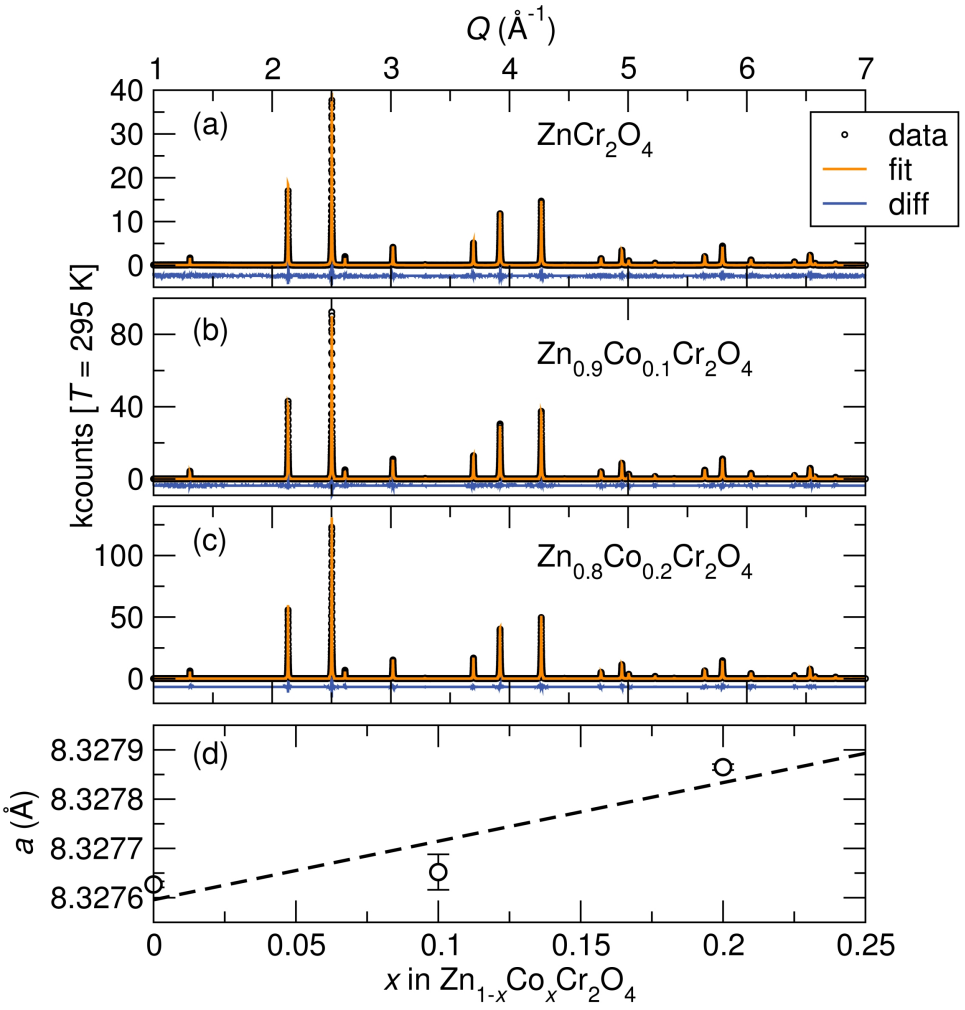

Figure 5.1: Room temperature synchrotron X-ray diffraction of the compounds (a) $ZnCr_2O_4$, (b) $Zn_{0.9}Co_{0.1}Cr_2O_4$, and (c) $Zn_{0.8}Co_{0.2}Cr_2O_4$. All samples are well described in the cubic space group $Fd\bar{3}m$ and no impurity peaks are observed. (d) A unit cell expansion occurs with substitution of Co^{2+} for Zn^{2+} in $Zn_{1-x}Co_xCr_2O_4$. The dashed line is a linear fit to the lattice parameters of $Zn_{1-x}Co_xCr_2O_4$. Reproduced with permission from reference [96], © 2014 American Physical Society.

temperature.[37] Despite the smaller ionic radius of Co^{2+}, a unit cell expansion occurs with substitution of Co^{2+} for Zn^{2+} in $Zn_{1-x}Co_xCr_2O_4$. The observed unit cell expansion has been previously reported and is attributed to higher cation-cation repulsion with increasing substitution of the more ionic Co^{2+} for Zn^{2+} in $Zn_{1-x}Co_xCr_2O_4$.[37]

Figure 5.2 shows the scaled inverse susceptibility of the systems $Zn_{1-x}Co_xCr_2O_4$. This representation is selected because it clearly differentiates compensated interactions from uncompensated interactions.[37] Compensated interactions yield a positive deviation of the inverse scaled susceptibility from the paramagnetic model while uncompensated interactions result in a negative deviation of the inverse scaled susceptibility from the Curie−Weiss model. Antiferromagnetic interactions of the geometrically frustrated spinel $ZnCr_2O_4$ [Fig 5.2 and Fig.5.3 (a)] evolve to uncompensated antiferromagnetic interactions in $Zn_{0.8}Co_{0.2}Cr_2O_4$ [Fig 5.2 and Fig. 5.3 (c)]. An increase in the number of magnetic interactions is expected in $Zn_{1-x}Co_xCr_2O_4$ with increase in x. Accordingly, Curie−Weiss fitting in the paramagnetic regime of $Zn_{1-x}Co_xCr_2O_4$ yields an increasing Θ_{CW} with x (Table 5.1). Similarly, the expected increase in effective moment with Co^{2+} substitution is also observed (Table 5.1). When spins are substituted on the non-magnetic A sites of ACr_2O_4 spinels at concentrations greater than 20%, spin frustration is lifted.[36, 37, 98] However, at dilute A site

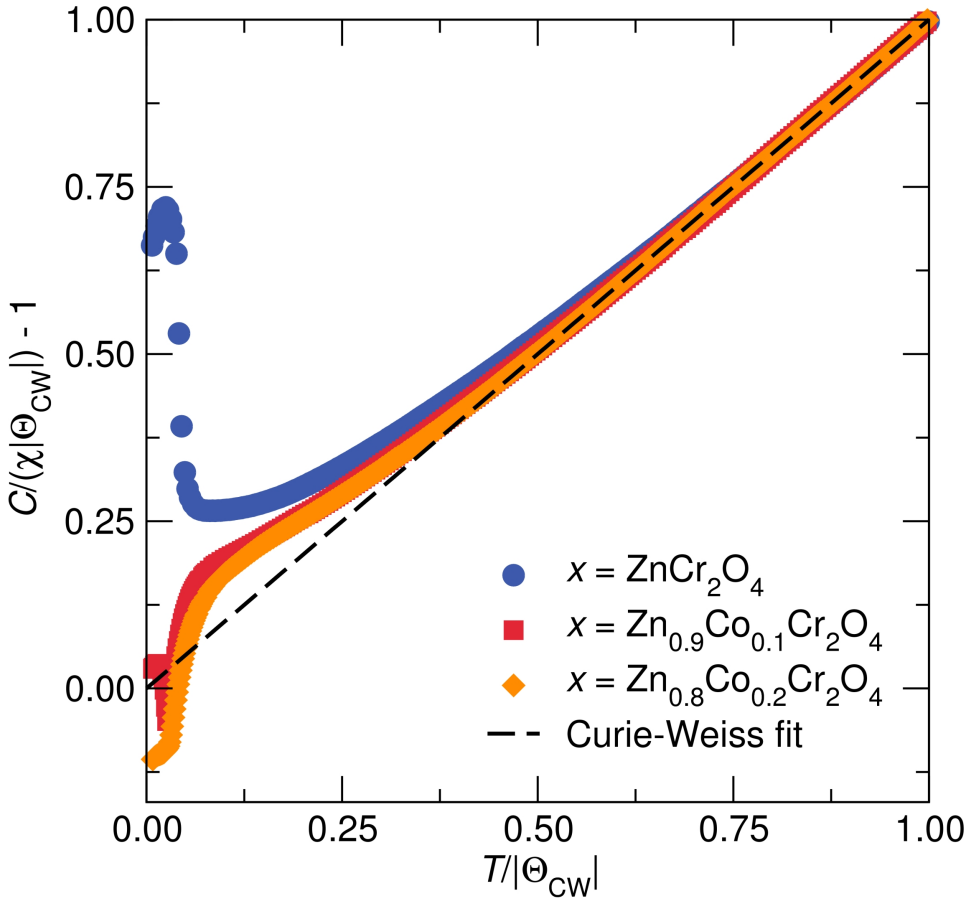

Figure 5.2: The inverse scaled temperature-dependent susceptibility of the spinels $Zn_{1-x}Co_xCr_2O_4$ are shown along with the Curie–Weiss model. Magnetism evolves from compensated antiferromagnetism in $ZnCr_2O_4$ to uncompensated antiferromagnetism in $Zn_{0.8}Co_{0.2}Cr_2O_4$. The Curie–Weiss fit was modeled to the susceptibility in the temperature range $200\,\mathrm{K} < T < 390\,\mathrm{K}$. Reproduced with permission from reference [96], © 2014 American Physical Society.

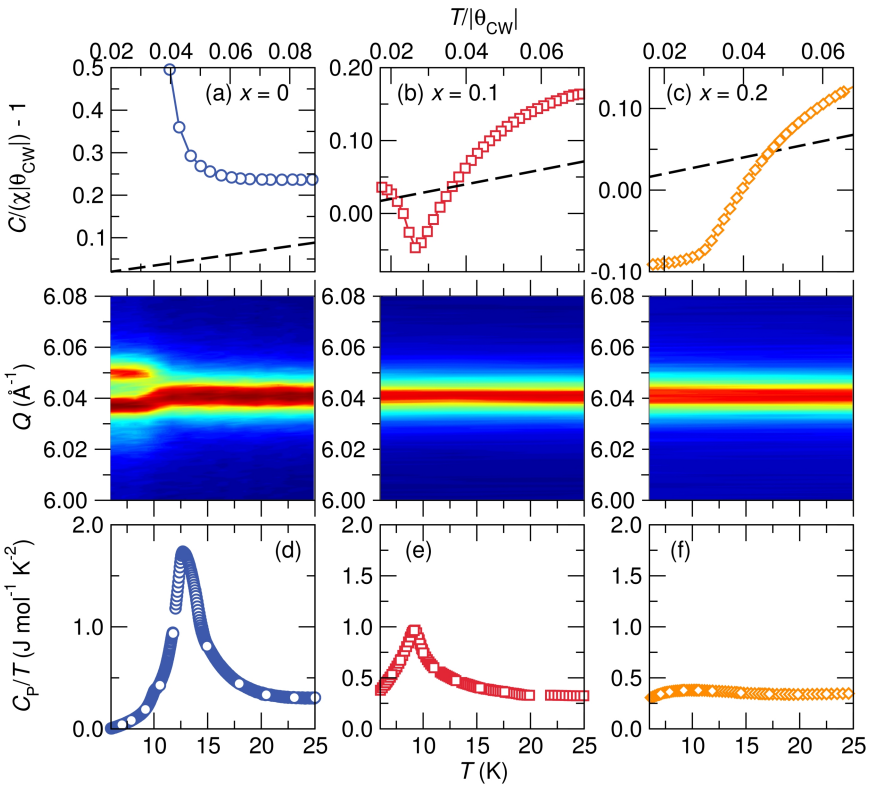

Figure 5.3: Suppression of the spin-Jahn-Teller distortion in $Zn_{1-x}Co_xCr_2O_4$ with increase in x. (a) Inverse scaled magnetic susceptibility as a function of temperature for (a) $ZnCr_2O_4$, (b) $Zn_{0.9}Co_{0.1}Cr_2O_4$, and (c) $Zn_{0.8}Co_{0.2}Cr_2O_4$ measured in a 1000 Oe field. The dashed black line is the paramagnetic model which describes the data in the paramagnetic regime where spins are disordered. Compensated antiferromagnetic interactions of $ZnCr_2O_4$ shown by the positive deviation of the inverse susceptibility from the Curie–Weiss model become uncompensated with the introduction of Co^{2+} in place of Zn^{2+} as illustrated by negative deviation of the susceptibility of $Zn_{0.8}Co_{0.2}Cr_2O_4$ from the paramagnetic model. The middle panel shows variable-temperature high-resolution X-ray powder diffraction of the cubic (800) reflection. Geometric frustration in $ZnCr_2O_4$ drives the lattice distortion shown by the splitting of the (800) reflection at the Néel temperature (12.3 K) of $ZnCr_2O_4$. The spin-Jahn-Teller distortion of $ZnCr_2O_4$ is suppressed even when only 10% Co^{2+} cations are substituted for Zn^{2+}. (d) The sharp heat capacity anomaly observed at the spin-Jahn-Teller distortion temperature of $ZnCr_2O_4$ is suppressed in $Zn_{0.9}Co_{0.1}Cr_2O_4$ (e) and strongly suppressed in $Zn_{0.8}Co_{0.2}Cr_2O_4$ (f). Reproduced with permission from reference [96], © 2014 American Physical Society.

spin concentrations, disorder in the spin interactions has been shown to further suppress magnetic ordering. [36, 37, 98] Due to the disorder in spin interactions, magnetic ordering in $Zn_{0.9}Co_{0.1}Cr_2O_4$ and $Zn_{0.8}Co_{0.2}Cr_2O_4$ occurs at lower temperatures compared to $ZnCr_2O_4$ (Table 5.1).

Antiferromagnetic order in $ZnCr_2O_4$ occurs concurrently with a structural distortion (middle panel of Fig. 5.3). The structural ground state of $ZnCr_2O_4$ has been extensively investigated and a recent report from our group shows that the spin-Jahn-Teller phase of $ZnCr_2O_4$ is best described by the combination of tetragonal $I4_1/amd$ and orthorhombic $Fddd$ space groups.[1, 31, 84] While $ZnCr_2O_4$ exhibits a clear lattice distortion at the Néel temperature, the cubic $Fd\bar{3}m$ (800) reflection for samples $x = 0.1$ and $x = 0.2$ shows no divergence illustrating the complete suppression of long-range structural distortion in these materials. As a result, the average nuclear structures of $Zn_{0.9}Co_{0.1}Cr_2O_4$ and $Zn_{0.8}Co_{0.2}Cr_2O_4$ near 5 K are well modeled by the cubic space group $Fd\bar{3}m$ as illustrated in Fig. 5.4. However, a clear peak broadening of the (800) reflection occurs near 5 K in $Zn_{0.9}Co_{0.1}Cr_2O_4$ and $Zn_{0.8}Co_{0.2}Cr_2O_4$ as shown in Fig. 5.4 (c) and (f) respectively. This broadening is indicative of higher strain at low temperatures that can result from local distortions in these materials. The structural parameters of $Zn_{0.9}Co_{0.1}Cr_2O_4$ and $Zn_{0.8}Co_{0.2}Cr_2O_4$ are tabulated in Tables 5.4 and 5.5.

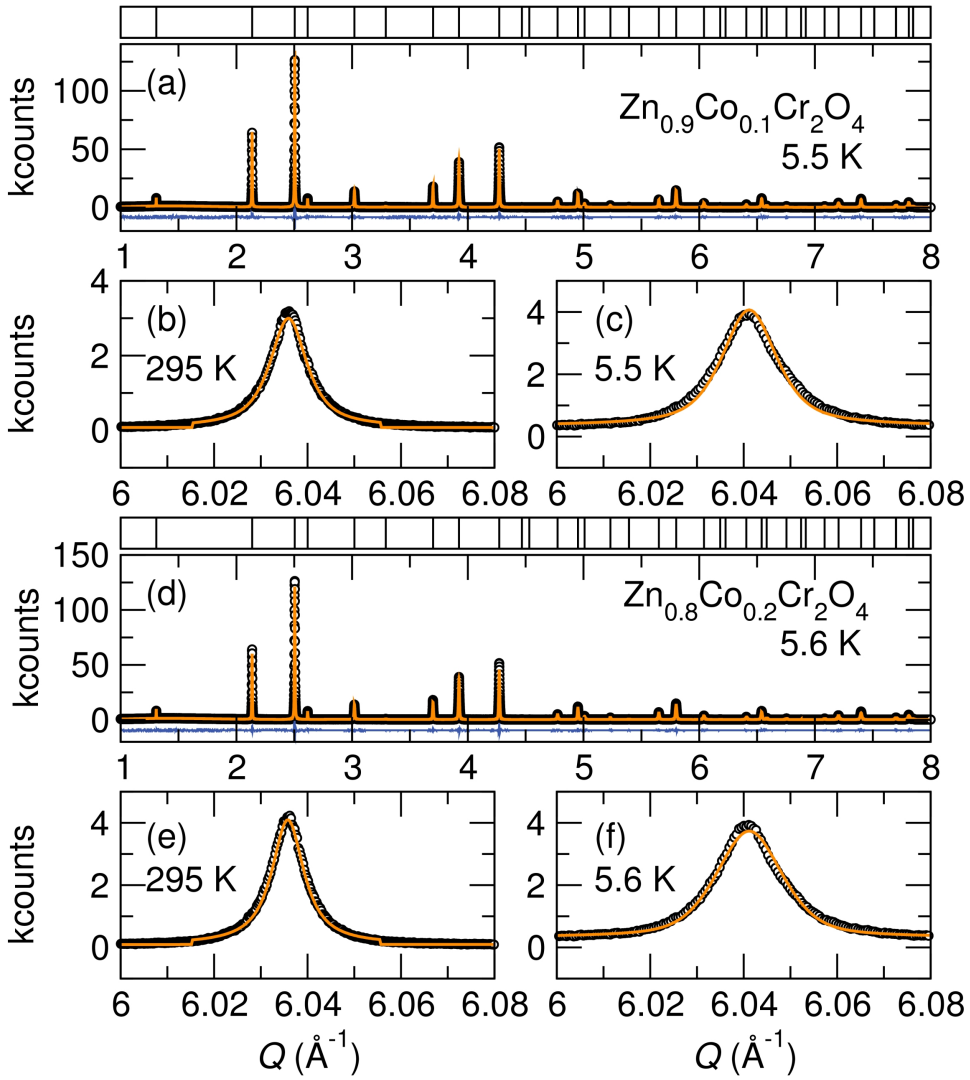

Figure 5.4: Low temperature synchrotron X-ray diffraction of (a) $Zn_{0.9}Co_{0.1}Cr_2O_4$, and (d) $Zn_{0.8}Co_{0.2}Cr_2O_4$ modeled to the cubic space group $Fd\bar{3}m$. The (800) reflections of $Zn_{0.9}Co_{0.1}Cr_2O_4$ and $Zn_{0.8}Co_{0.2}Cr_2O_4$ at room temperature are shown here in (b) and (e) respectively and near 5 K in (c) and (f) respectively. A broadening of the (800) reflection is observed at low temperature in $Zn_{0.9}Co_{0.1}Cr_2O_4$ and $Zn_{0.8}Co_{0.2}Cr_2O_4$. Reproduced with permission from reference [96], © 2014 American Physical Society.

The spin-Jahn-Teller distortion of $ZnCr_2O_4$ yields a sharp heat capacity anomaly at T_N [Fig. 5.3 (d)]. This heat capacity anomaly is slightly suppressed in $Zn_{0.9}Co_{0.1}Cr_2O_4$ and it becomes very broad in $Zn_{0.8}Co_{0.2}Cr_2O_4$ [Fig. 5.3 (e) and (f)]. The suppression of the heat capacity anomalies in $Zn_{0.9}Co_{0.1}Cr_2O_4$ and $Zn_{0.8}Co_{0.2}Cr_2O_4$ shows that these systems host residual spin and structural disorder.

We have shown the differences in structural ground state when $\geq 10\%$ of Co^{2+} are substituted on the non-magnetic A site of $ZnCr_2O_4$. The structural distortion that accompanies magnetic ordering in $ZnCr_2O_4$ is completely suppressed even for only 10% Co^{2+} substitution in $Zn_{0.9}Co_{0.1}Cr_2O_4$. This suggests that random Co-O-Cr superexchange interactions in $Zn_{1-x}Co_xCr_2O_4$, partially break the spin ground state degeneracy of these systems, allowing the onset of a magnetic ground state without the need for a long range structural distortion. It is also plausible that random Co-O-Cr superexchange interactions could be disrupting the coherency of Cr-Cr exchange coupling paths thus inhibiting spin-Jahn-Teller distortions in $Zn_{0.9}Co_{0.1}Cr_2O_4$ and $Zn_{0.8}Co_{0.2}Cr_2O_4$. Small substitutions of Co^{2+} for Mg^{2+} will likely suppress the Spin-Jahn-Teller distortion of $MgCr_2O_4$; this is supported by the similar structural effects of Cu^{2+} substitutions for Mg^{2+} and Zn^{2+} in $MgCr_2O_4$ and $ZnCr_2O_4$ as discussed in the following sections.

5.4 Structural ground states of the spinels $Mg_{1-x}Cu_xCr_2O_4$: $x \leq 0.2$

We examine the effect of both spin and lattice disorder on the spin-Jahn-Teller ground state of $MgCr_2O_4$ by substituting $\geq 10\%$ of Jahn-Teller active Cu^{2+} for Mg^{2+}. At room temperature the normal spinels $MgCr_2O_4$ and $CuCr_2O_4$ have different structural ground states; $MgCr_2O_4$ is cubic while $CuCr_2O_4$ is tetragonal. The tetragonal structure of $CuCr_2O_4$ results from cooperative Jahn-Teller ordering of CuO_4 tetrahedra at $T = 853$ K.[18] $MgCr_2O_4$ is a frustrated antiferromagnet, and its transition to an ordered magnetic state at $T_N = 12.9$ K is accompanied by a structural distortion.[28, 86] The spin-Jahn-Teller distorted phase of $MgCr_2O_4$ had been previously described by the tetragonal $I4_1/amd$ structure,[28, 86] but we have recently shown that this system consists of coexisting tetragonal $I4_1/amd$ and orthorhombic $Fddd$ phases.[1] $CuCr_2O_4$ is ferrimagnetic, with magnetic Cu^{2+} and Cr^{3+} sublattices contributing to a non-collinear magnetic structure where two canted Cr^{3+} sublattices yield a magnetic moment that is partially compensated by the Cu^{2+} sublattice at $T_N = 135$ K.[61] In addition to the high temperature Jahn-Teller driven cubic-tetragonal phase transition, $CuCr_2O_4$ undergoes yet another structural distortion from tetragonal $I4_1/amd$ to orthorhombic $Fddd$ symmetry near 130 K due to magnetostructural

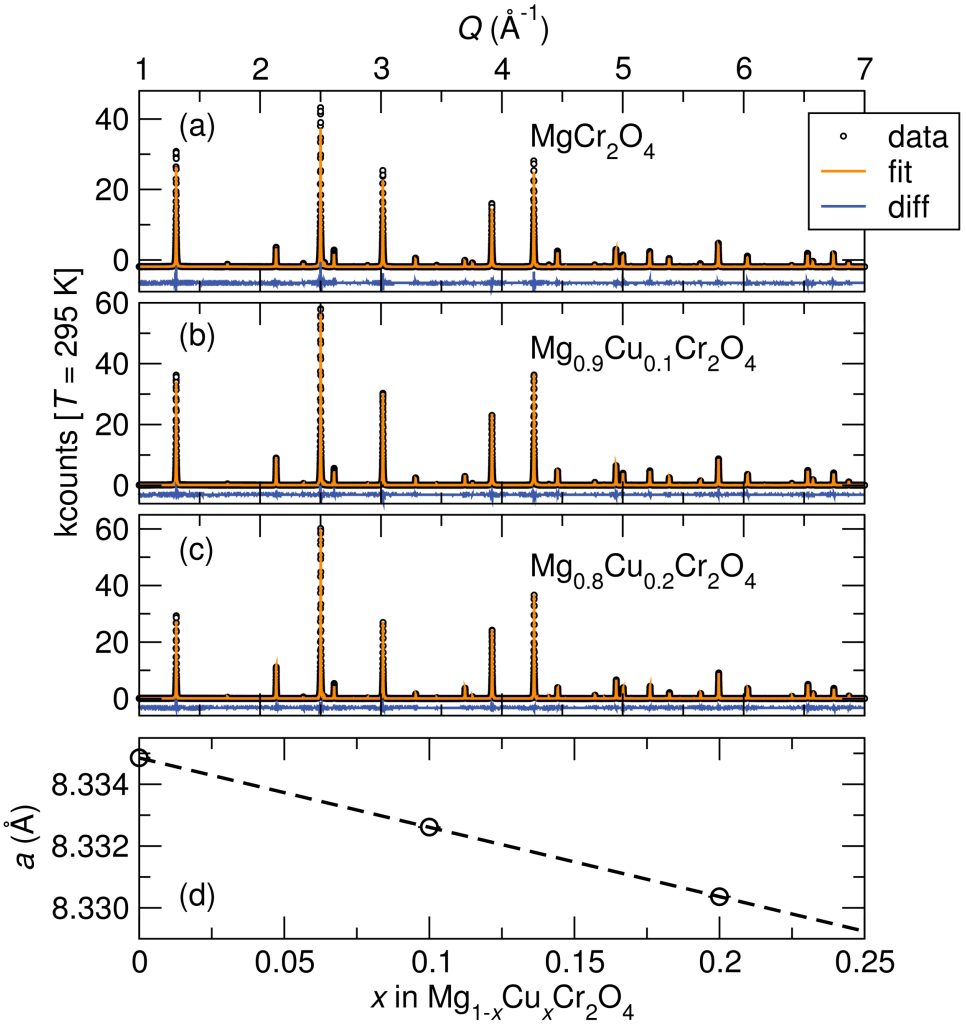

Figure 5.5: Rietveld refinement of room temperature high resolution synchrotron X-ray powder diffraction of (a) $MgCr_2O_4$ (b) $Mg_{0.9}Cu_{0.1}Cr_2O_4$ and (c) $Mg_{0.8}Cu_{0.2}Cr_2O_4$ to the cubic space group $Fd\bar{3}m$. All samples show a very small Cr_2O_3 impurity with concentrations $< 1\%$ in all samples. (d) The cubic lattice constant in $Mg_{1-x}Cu_xCr_2O_4$ decreases linearly with increase in Cu^{2+} concentration. Error bars are smaller than data symbols. Reproduced with permission from reference [96], © 2014 American Physical Society.

Table 5.2: Magnetic parameters of $Mg_{1-x}Cu_xCr_2O_4$. μ_{eff} and Θ_{CW} were extracted from fitting the susceptibility in the temperature ranges 300 K $< T <$ 390 K, 250 K $< T <$ 390 K, and 200 K $< T <$ 390 K to the Curie-Weiss equation $\chi = \frac{C}{T-\Theta_{CW}}$. Reported are the mean μ_{eff} and Θ_{CW} values along with their standard deviation.

	T_N (K)	$\mu_{exp}(\mu_B)$	$\mu_{calc}(\mu_B)$	Θ_{CW}(K)
$MgCr_2O_4$	12.9	5.21(0.03)	5.47	−357(7)
$Mg_{0.9}Cu_{0.1}Cr_2O_4$	11	5.34(0)	5.50	−361(1)
$Mg_{0.8}Cu_{0.2}Cr_2O_4$	15	5.3(0.01)	5.53	−334(3)

coupling.[14]

The prepared spinel solid solutions $Mg_{1-x}Cu_xCr_2O_4$ where $x \leq 0.2$ are cubic with the space group $Fd\bar{3}m$ at room temperature [Fig. 5.5 (a), (b), and (c)]. While tetrahedral Mg^{2+} and Cu^{2+} have identical Shannon-Prewitt ionic radii, we observe a lattice contraction with increase in Cu^{2+}, following Vegard's law [Figure 5.5 (d)]. This decrease in lattice constant with Cu^{2+} substitution is consistent with the earlier work by Shoemaker and Seshadri[93] and with the smaller pseudocubic cell volume of $CuCr_2O_4$ (566.38 Å^3)[14] compared with that of $MgCr_2O_4$(579.017 Å) at room temperature.[1] The structural parameters of $Mg_{1-x}Cu_xCr_2O_4$ for $x = 0.1$ and 0.2 at 300 K are tabulated in Tables. 5.6 and 5.7.

The evolution of magnetism in $Mg_{1-x}Cu_xCr_2O_4$ where $x \leq 0.2$, is similar to that observed in $Zn_{1-x}Co_xCr_2O_4$; frustrated antiferromagnetism in $MgCr_2O_4$ evolves to uncompensated antiferromagnetism in $Mg_{0.8}Cu_{0.2}Cr_2O_4$[Fig. 5.6 and

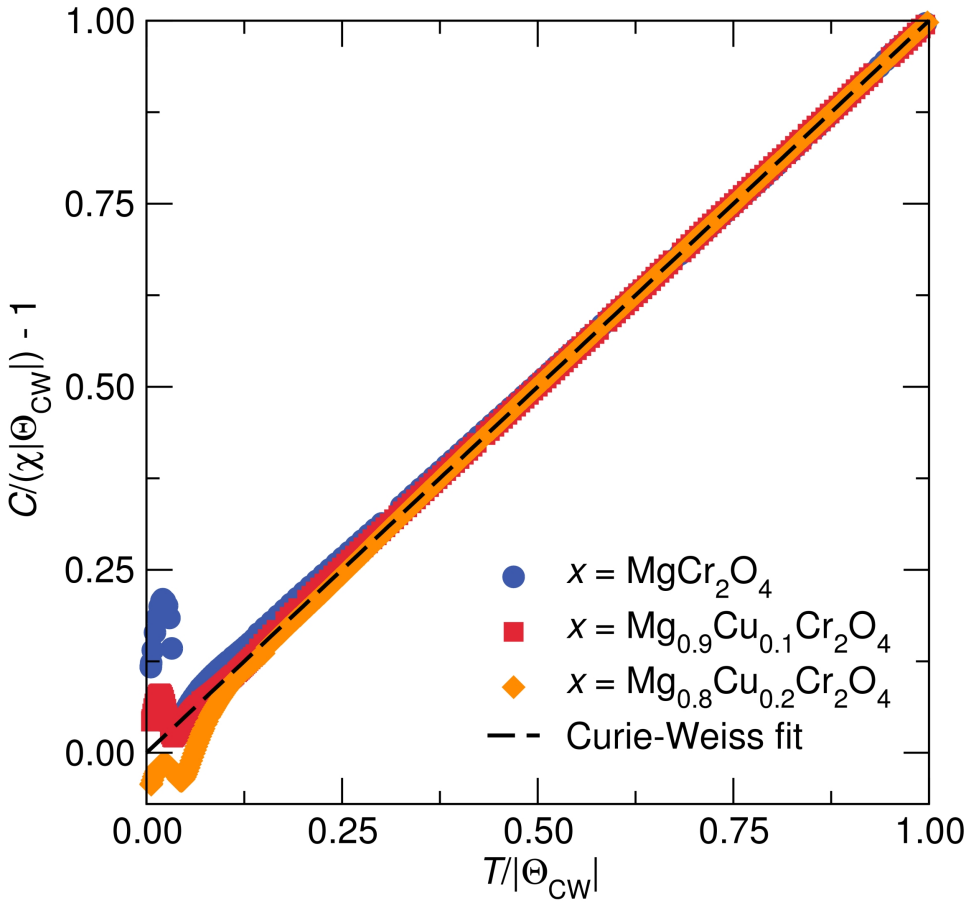

Figure 5.6: The inverse scaled temperature-dependent susceptibility of the spinels $Mg_{1-x}Cu_xCr_2O_4$ are shown along with the Curie−Weiss fits that were modeled in the temperature range $200\,\mathrm{K} < T < 390\,\mathrm{K}$. Compensated antiferromagnetism in $MgCr_2O_4$ evolves to uncompensated antiferromagnetism in $Mg_{0.8}Cu_{0.2}Cr_2O_4$. Reproduced with permission from reference [96], © 2014 American Physical Society.

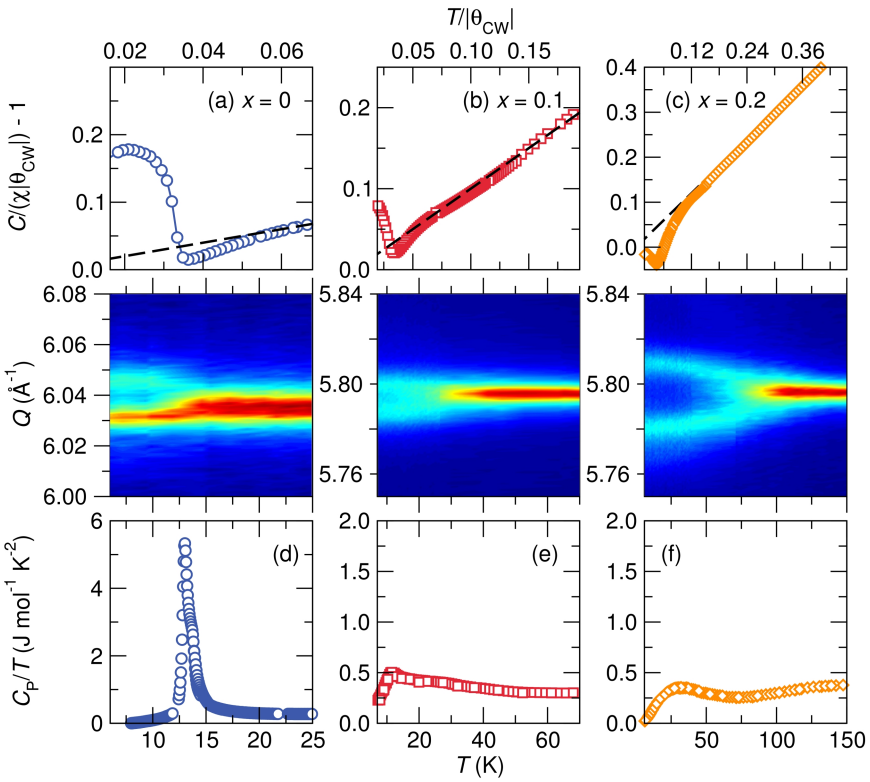

Figure 5.7: Spin-Jahn-Teller and Jahn-Teller ordering in $Mg_{1-x}Cu_xCr_2O_4$. The top panel shows the scaled inverse susceptibility of $MgCr_2O_4$ (a), $Mg_{0.9}Cu_{0.1}Cr_2O_4$ (b) and $Mg_{0.8}Cu_{0.2}Cr_2O_4$ (c) measured in a 1000 Oe field. Compensated antiferromagnetic interactions in $MgCr_2O_4$ (a) and $Mg_{0.9}Cu_{0.1}Cr_2O_4$ (b) evolve to uncompensated antiferromagnetic interactions in $Mg_{0.8}Cu_{0.2}Cr_2O_4$ (c). Geometric frustration of spins in $MgCr_2O_4$ drives a structural distortion at $T_N = 12.9$ K that is indicated by the splitting of the high symmetry (800) reflection. Cooperative Jahn-Teller ordering spurs average structure distortions in $Mg_{0.9}Cu_{0.1}Cr_2O_4$ at $T \sim 35$ K and $Mg_{0.8}Cu_{0.2}Cr_2O_4$ at $T \sim 110$ K. The structural distortions in $Mg_{0.9}Cu_{0.1}Cr_2O_4$ and $Mg_{0.8}Cu_{0.2}Cr_2O_4$ are decoupled from the magnetism and no further structural distortions occur near the Néel temperature of these compounds although they exhibit spin frustration. (d) There is a sharp heat capacity anomaly at the Néel temperature of $MgCr_2O_4$ with a shoulder feature plausibly indicating a slight separation in temperature of the magnetic and structural transitions. (e) $Mg_{0.9}Cu_{0.1}Cr_2O_4$ shows a broad heat capacity anomaly with a kink at T_N. (f) Similarly, $Mg_{0.8}Cu_{0.2}Cr_2O_4$ shows a broad heat capacity peak in the temperature range $6\,\text{K} \leq T \leq 80\,\text{K}$. Reproduced with permission from reference [96], © 2014 American Physical Society.

Fig. 5.7 (a), (b), and (c)]. The positive deviation of the inverse scaled susceptibility from the paramagnetic model in $MgCr_2O_4$ and $Mg_{0.9}Cu_{0.1}Cr_2O_4$ illustrates that antiferromagnetic interactions are compensated in these materials [Fig. 5.7 (a) and (b)]. Further substitution of Cu^{2+} cations for Mg^{2+} yields uncompensated antiferromagnetic interactions that result in the negative deviation of the inverse scaled susceptibility from the Curie−Weiss model below the Néel temperature as observed in $Mg_{0.8}Cu_{0.2}Cr_2O_4$ [Fig. 5.7 (c)]. Antiferromagnetic ordering in $Mg_{0.9}Cu_{0.1}Cr_2O_4$ occurs at a lower temperature than in $MgCr_2O_4$ due to dilute $J_{Cu-O-Cr}$ couplings interfering with J_{Cr-Cr} couplings (Table 5.2). However, the increase in Cu^{2+} concentration in $Mg_{0.8}Cu_{0.2}Cr_2O_4$ yields a higher magnetic ordering temperature and this is consistent with the findings that sufficient magnetic A site spins lift frustration in geometrically frustrated ACr_2O_4 spinels.[36, 37, 98] Curie−Weiss fitting in the paramagnetic regime of $Mg_{1-x}Cu_xCr_2O_4$ yields a slight increase in the effective moment of $Mg_{0.9}Cu_{0.1}Cr_2O_4$ and a weakening of the overall strength of magnetic interactions shown by the decrease in the magnitude of Θ_{CW} (Table 5.2). Weaker antiferromagnetic interactions with Cu^{2+} substitution are attributed to the effects of spin disorder due to dilute A site spins. The decrease in Θ_{CW} in $Mg_{1-x}Cu_xCr_2O_4$ with increase in x contrasts with the increase in Θ_{CW} in $Zn_{1-x}Co_xCr_2O_4$ with increase in x; this difference is attributed to the higher spin of Co^{2+} $3d^7$ $s = \frac{3}{2}$

compared to Cu^{2+} $3d^9$ $s = \frac{1}{2}$. The higher spin of Co^{2+} contributes to stronger magnetic interactions in $Zn_{1-x}Co_xCr_2O_4$.

Structural distortions are observed in all compounds $Mg_{1-x}Cu_xCr_2O_4$ when $x \leq 0.2$. The spin-Jahn-Teller distortion of $MgCr_2O_4$ is illustrated by the splitting of the (800) reflection to several low temperature peaks (Leftmost middle panel of Fig. 5.7). While degeneracy in spin ground states drives the structural distortion in $MgCr_2O_4$, degeneracy in the orbital configurations of tetrahedral Cu^{2+} drive Jahn-Teller distortions in $Mg_{0.9}Cu_{0.1}Cr_2O_4$ and $Mg_{0.8}Cu_{0.2}Cr_2O_4$ at 35 K and 110 K respectively. The middle panel of figure 5.7 shows the splitting of the coincident (731) and (553) reflections in $Mg_{0.9}Cu_{0.1}Cr_2O_4$ and $Mg_{0.8}Cu_{0.2}Cr_2O_4$. The Jahn-Teller distortion increases with Cu^{2+} concentration as shown by the larger separation between the low-temperature reflections of $Mg_{0.8}Cu_{0.2}Cr_2O_4$ and the onset of this distortion at higher temperature in this compound. We note that magnetic transitions do not accompany the structural distortions of $Mg_{0.9}Cu_{0.1}Cr_2O_4$ and $Mg_{0.8}Cu_{0.2}Cr_2O_4$. The Jahn-Teller phases of $Mg_{0.9}Cu_{0.1}Cr_2O_4$ and $Mg_{0.8}Cu_{0.2}Cr_2O_4$ are well modeled by the orthorhombic $Fddd$ structure (Fig. 5.8) that is ascribed to $CuCr_2O_4$ following its magnetostructural distortion.[14] An important difference between $CuCr_2O_4$ and these systems studied here is that the orthorhombic structure of $CuCr_2O_4$ occurs due to magnetostructural coupling[14] while the orthorhombic structure of

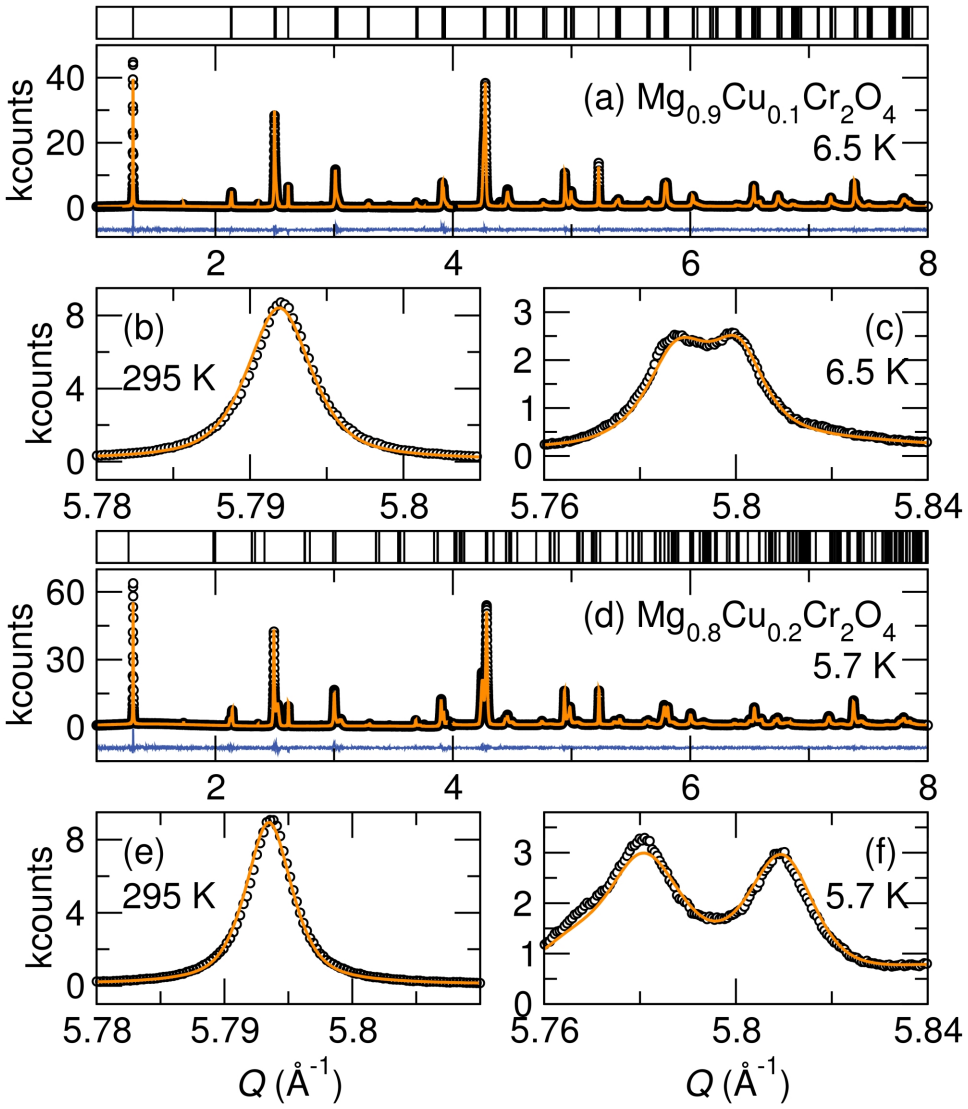

Figure 5.8: Low temperature structures of (a) $Mg_{0.9}Cu_{0.1}Cr_2O_4$ and (d) $Mg_{0.8}Cu_{0.2}Cr_2O_4$ indexed to the orthorhombic $Fddd$ structure. Data is shown in black, the structural model in orange and the difference between the structural model and the data is in blue. Below the respective Jahn-Teller ordering temperatures of $Mg_{0.9}Cu_{0.1}Cr_2O_4$ and $Mg_{0.8}Cu_{0.2}Cr_2O_4$, the coincident (731) and (553) reflections shown in (b) and (c) split into several reflections as shown in (c) and (f). Reproduced with permission from reference [96], © 2014 American Physical Society.

$Mg_{0.9}Cu_{0.1}Cr_2O_4$ and $Mg_{0.8}Cu_{0.2}Cr_2O_4$ occurs in the paramagnetic regime driven primarily by cooperative Jahn-Teller ordering.

The spin-Jahn-Teller distortion of $MgCr_2O_4$ results in a sharp heat capacity anomaly with a slight shoulder feature [Fig. 5.7 (d)]. The shoulder feature is likely due to a slight separation in temperature of the magnetic and structural changes. The onset of heat capacity changes in $Mg_{0.9}Cu_{0.1}Cr_2O_4$ and $Mg_{0.8}Cu_{0.2}Cr_2O_4$ occur at high temperatures where structural changes begin and they persist to low temperatures where magnetic ordering occurs [Fig. 5.7 (e) and (f)].

While the substitution of Co^{2+} for Zn^{2+} suppresses spin-Jahn-Teller distortion in $ZnCr_2O_4$, $\geq 10\%$ substitution of Jahn-Teller active Cu^{2+} for Mg^{2+} induces structural distortions in $Mg_{0.9}Cu_{0.1}Cr_2O_4$ and $Mg_{0.8}Cu_{0.2}Cr_2O_4$ at temperatures above the magnetic ordering temperatures of these compounds. The structural distortions in $Mg_{0.9}Cu_{0.1}Cr_2O_4$ and $Mg_{0.8}Cu_{0.2}Cr_2O_4$ affect the pyrochlore Cr sublattice; while there is only one Cr-Cr bond length at room temperature in the cubic phases of these systems, there are three Cr-Cr bond lengths in the orthorhombic phases of these materials. Surprisingly, spin interactions remain frustrated in $Mg_{0.9}Cu_{0.1}Cr_2O_4$ and $Mg_{0.8}Cu_{0.2}Cr_2O_4$ with magnetic ordering occurring below 18 K despite the presence of distortions in the pyrochlore Cr sublattice of these materials at temperatures above their Néel temperatures. No fur-

ther structural distortions are observed in $Mg_{0.9}Cu_{0.1}Cr_2O_4$ and $Mg_{0.8}Cu_{0.2}Cr_2O_4$ near the Néel temperature.

5.5 Structural ground states of the spinels $Zn_{1-x}Cu_xCr_2O_4$: $x \leq 0.2$

We examine the effect of Cu^{2+} substitutions for Zn^{2+} on the spin-Jahn-Teller distortion of $ZnCr_2O_4$. All prepared samples $Zn_{1-x}Cu_xCr_2O_4$ where $x \leq 0.2$ are cubic spinels in the space group $Fd\bar{3}m$ at room temperature as shown in Fig 5.9. Like in the solid solutions $Mg_{1-x}Cu_xCr_2O_4$, the substitution of Cu^{2+} for Zn^{2+} results in a steady decrease of the lattice constant [Fig 5.9 (d)]. This lattice decrease is in good agreement with the smaller cell volume of $CuCr_2O_4$(566.38 Å^3)[14] at room temperature compared to $ZnCr_2O_4$(577.520 Å^3).[1] The structural parameters of $Zn_{1-x}Cu_xCr_2O_4$ are tabulated in Tables 5.8 and 5.8.

Compensated antiferromagnetic interactions in $ZnCr_2O_4$ and $Zn_{0.9}Cu_{0.1}Cr_2O_4$ illustrated by the positive deviation of the inverse scaled susceptibility from the Curie−Weiss model evolve to uncompensated antiferromagnetic interactions in $Zn_{0.8}Cu_{0.2}Cr_2O_4$ where the inverse scaled susceptibility

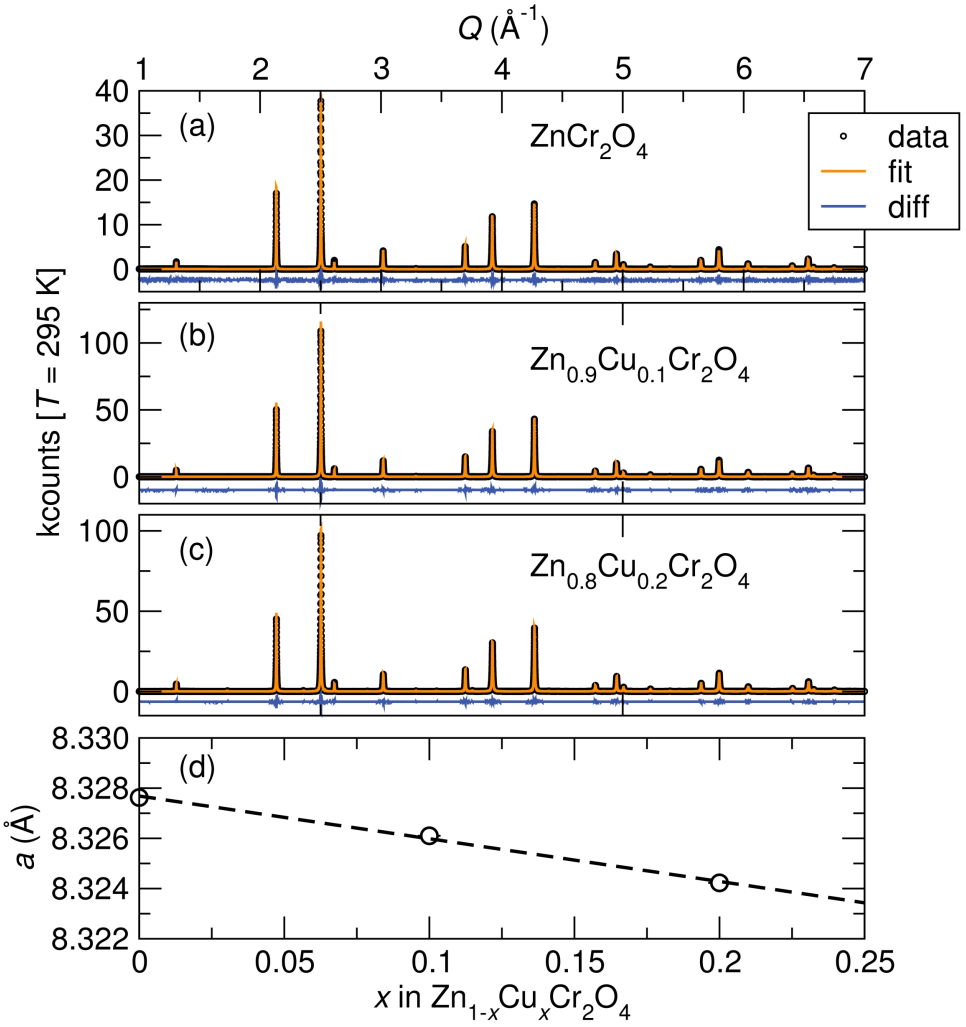

Figure 5.9: High resolution synchrotron X-ray powder diffraction of the systems (a) $ZnCr_2O_4$ (b) $Zn_{0.9}Cu_{0.1}Cr_2O_4$ and (c) $Zn_{0.8}Cu_{0.2}Cr_2O_4$ measured at room temperature. All compounds are well indexed by the cubic space group $Fd\bar{3}m$. (d) A linear decrease of the cubic lattice constant occurs with Cu^{2+} substitution for Zn^{2+}. Error bars are smaller than data symbols. Reproduced with permission from reference [96], © 2014 American Physical Society.

Table 5.3: Magnetic parameters of $Zn_{1-x}Cu_xCr_2O_4$. μ_{eff} and Θ_{CW} were extracted from fitting the susceptibility in the temperature ranges $300\,K < T < 390\,K$, $250\,K < T < 390\,K$, and $200\,K < T < 390\,K$ to the Curie-Weiss equation $\chi = \frac{C}{T-\Theta_{CW}}$. Reported are the mean μ_{eff} and Θ_{CW} values along with their standard deviation.

	T_N (K)	$\mu_{exp}(\mu_B)$	$\mu_{calc}(\mu_B)$	Θ_{CW}(K)
$ZnCr_2O_4$	12.3	5.06(0.02)	5.47	−277(4)
$Zn_{0.9}Cu_{0.1}Cr_2O_4$	11	4.89(0.02)	5.50	−237(4)
$Zn_{0.8}Cu_{0.2}Cr_2O_4$	16	5.03(0.02)	5.53	−276(6)

deviates negatively from the paramagnetic model [Fig. 5.10]. The onset of magnetic ordering in $Zn_{0.9}Cu_{0.1}Cr_2O_4$ occurs at lower temperatures than in $ZnCr_2O_4$ due to disorder arising from dilute A site spins while $Zn_{0.8}Cu_{0.2}Cr_2O_4$ shows the highest ordering temperature of the studied $Zn_{1-x}Cu_xCr_2O_4$ compounds (Table 5.3). A slight decrease in the effective moment is observed with Cu^{2+} substitution in $ZnCr_2O_4$ and this is attributed to the presence of short range spin interactions in the paramagnetic regime contributing to the underestimation of the effective moment (Table 5.3). As observed in $Mg_{1-x}Cu_xCr_2O_4$, a decrease in the magnitude of Θ_{CW} occurs in $Zn_{1-x}Cu_xCr_2O_4$ with increase in x suggesting that dilute Cu^{2+} substitutions weaken the overall strength of magnetic interactions in $MgCr_2O_4$ and $ZnCr_2O_4$.

Geometric spin frustration drives a lattice distortion at the antiferromagnetic ordering temperature of $ZnCr_2O_4$ while Jahn-Teller distortion of tetrahedral Cu^{2+} in $Zn_{1-x}Cu_xCr_2O_4$ drive structural distortions in $Zn_{0.9}Cu_{0.1}Cr_2O_4$ and

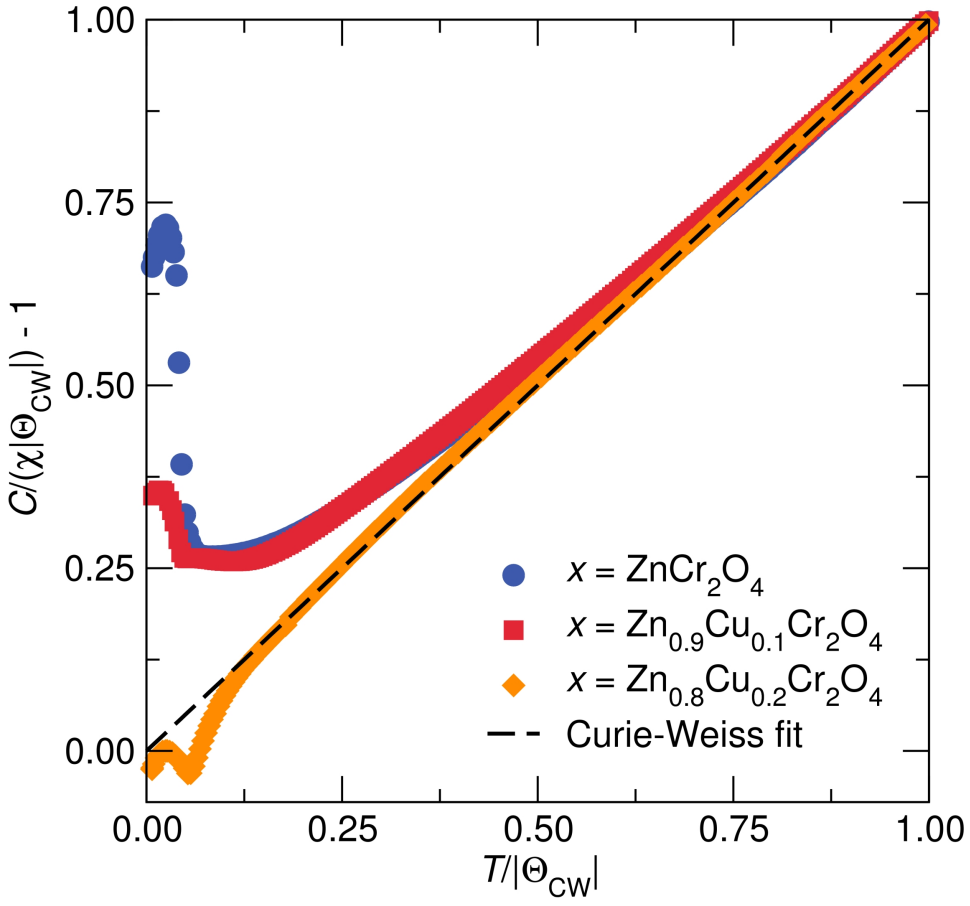

Figure 5.10: The inverse scaled temperature-dependent susceptibility of the spinels $Zn_{1-x}Cu_xCr_2O_4$ are shown along with the Curie–Weiss model. Compensated antiferromagnetism in $ZnCr_2O_4$ evolves to uncompensated antiferromagnetism in $Zn_{0.8}Cu_{0.2}Cr_2O_4$. The Curie–Weiss fit was modeled to the temperature range $200\,\mathrm{K} < T < 390\,\mathrm{K}$. Reproduced with permission from reference [96], © 2014 American Physical Society.

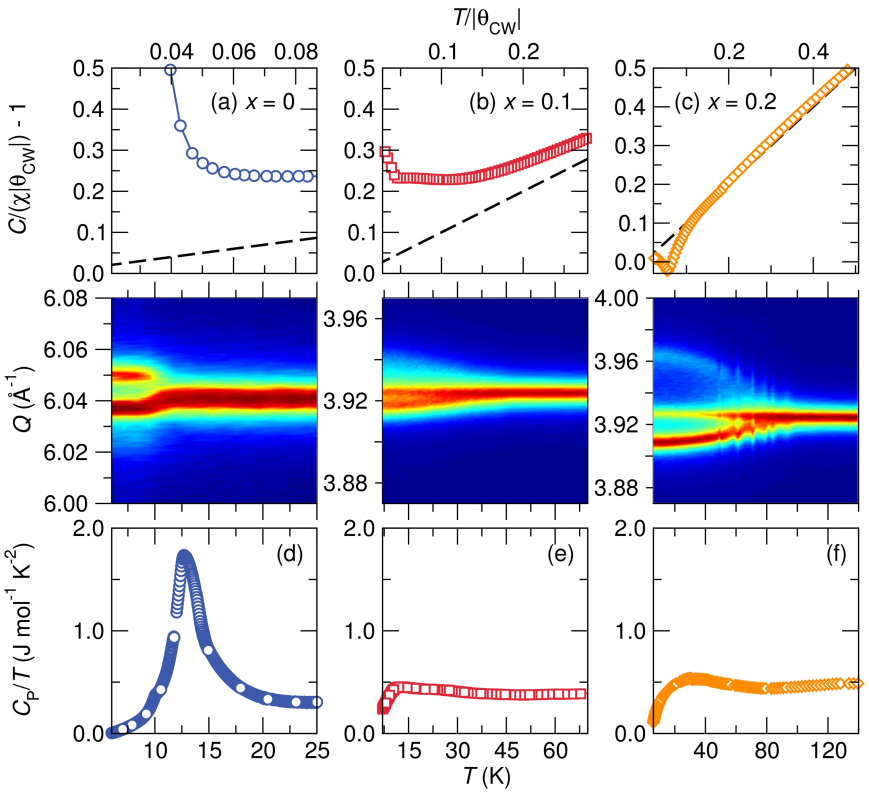

Figure 5.11: Spin-Jahn Teller and Jahn-Teller distortions in $Zn_{1-x}Cu_xCr_2O_4$. The top panel shows inverse scaled susceptibility measurements of $Zn_{1-x}Cu_xCr_2O_4$ measured under a 1000 Oe field. Compensated antiferromagnetism is observed in $ZnCr_2O_4$ (a) and $Zn_{0.9}Cu_{0.1}Cr_2O_4$ (b) below the Néel temperature while $Zn_{0.8}Cu_{0.2}Cr_2O_4$ (c) shows uncompensated antiferromagnetism. A lattice distortion accompanies magnetic ordering in $ZnCr_2O_4$ as shown by the splitting of the high symmetry (800) reflection at the Néel temperature. Jahn-Teller active Cu^{2+} on the A sites of $Zn_{0.9}Cu_{0.1}Cr_2O_4$ and $Zn_{0.8}Cu_{0.2}Cr_2O_4$ drive lattice distortions at approximately 45 K and 110 K respectively, where the coincident (511) and (333) reflections split into several low temperature reflections. There is a large heat capacity anomaly at the spin-Jahn-Teller distortion temperature of $ZnCr_2O_4$ (d). Broad heat capacity anomalies are observed in $Zn_{0.9}Cu_{0.1}Cr_2O_4$ (e) and $Zn_{0.8}Cu_{0.2}Cr_2O_4$ (f) over the temperature range where structural and magnetic changes occur. The line features in the variable temperature data of sample $Zn_{0.8}Cu_{0.2}Cr_2O_4$ are due to slight temperature fluctuations during the measurement. Reproduced with permission from reference [96], © 2014 American Physical Society.

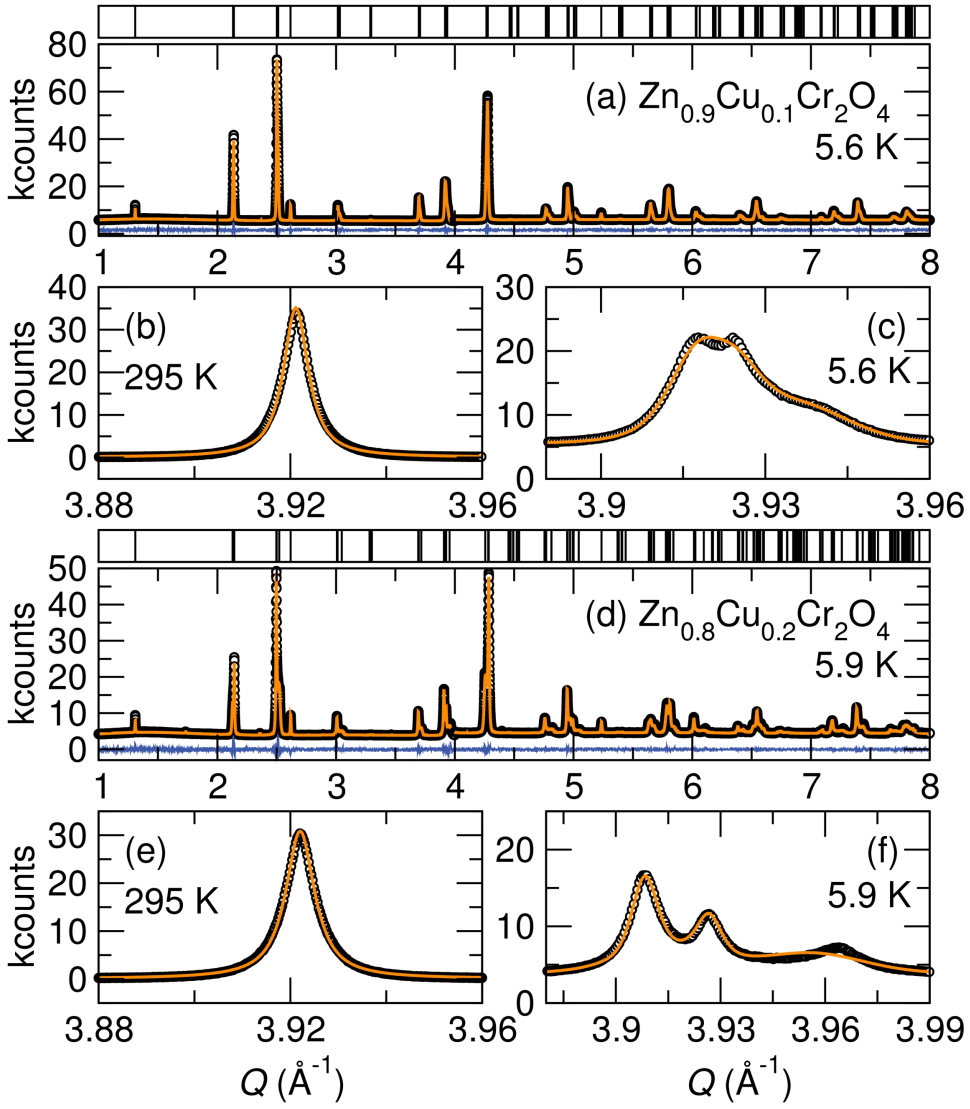

Figure 5.12: Synchrotron powder diffraction patterns of $Zn_{0.9}Cu_{0.1}Cr_2O_4$ (a) and $Zn_{0.8}Cu_{0.2}Cr_2O_4$ (d) collected near 6 K and indexed to the orthorhombic space group $Fddd$. Data is shown in black, the model is in orange while the difference is in blue. The high temperature coincident cubic $Fd\bar{3}m$ reflections (511) and (333) shown in (b) for $Zn_{0.9}Cu_{0.1}Cr_2O_4$ and in (e) for $Zn_{0.8}Cu_{0.2}Cr_2O_4$ are split at lower temperatures following the cubic to orthorhombic lattice distortion. These low temperature reflections as indexed to the orthorhombic $Fddd$ structure are shown in (c) and (f) for $Zn_{0.9}Cu_{0.1}Cr_2O_4$ and $Zn_{0.8}Cu_{0.2}Cr_2O_4$ respectively. Reproduced with permission from reference [96], © 2014 American Physical Society.

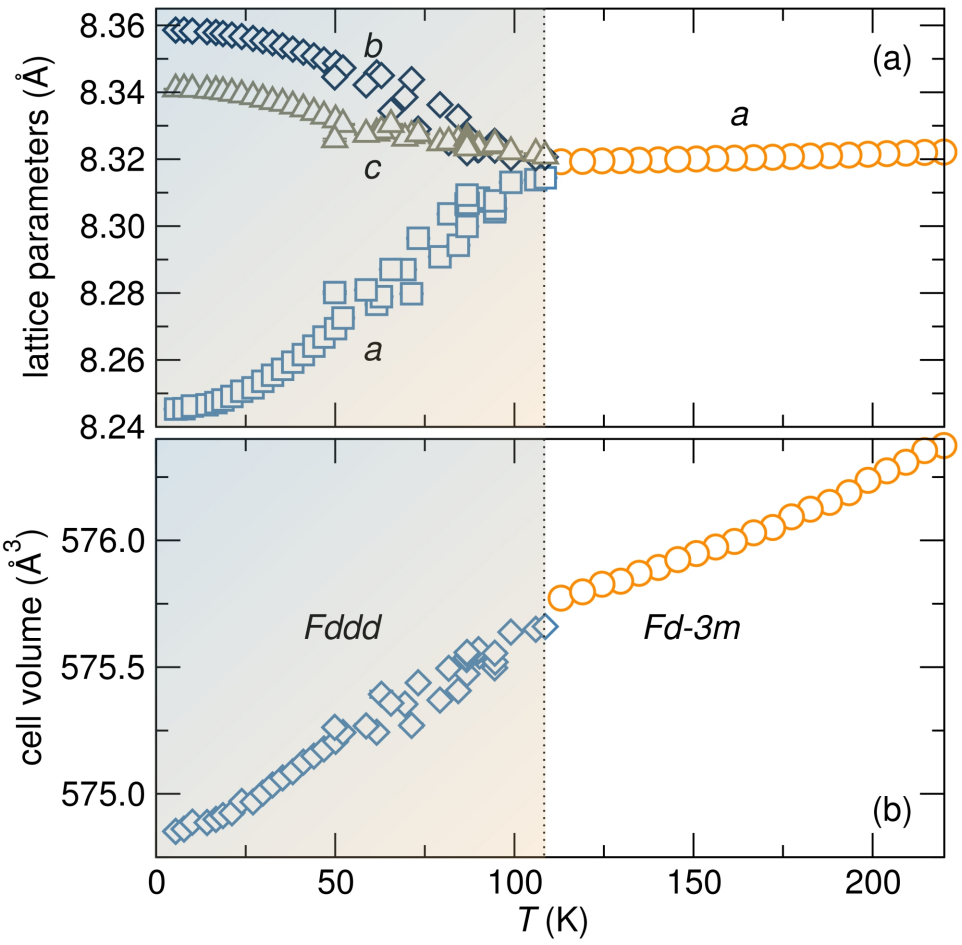

Figure 5.13: (a) The evolution of lattice parameters of $Zn_{0.8}Cu_{0.2}Cr_2O_4$ as a function of temperature revealing a structural distortion at 110 K where three orthorhombic $Fddd$ lattice constants emerge from the cubic $Fd\bar{3}m$ lattice constant. (b) There is a slight change in slope in the temperature dependent cell volume of $Zn_{0.8}Cu_{0.2}Cr_2O_4$ at the structural distortion temperature. Error bars obtained from Rietveld refinement are smaller than data symbols and do not incorporate uncertainities in the temperature. The scatter in the data near the structural distortion temperature is due to slight temperature variations during the measurement. Reproduced with permission from reference [96], © 2014 American Physical Society.

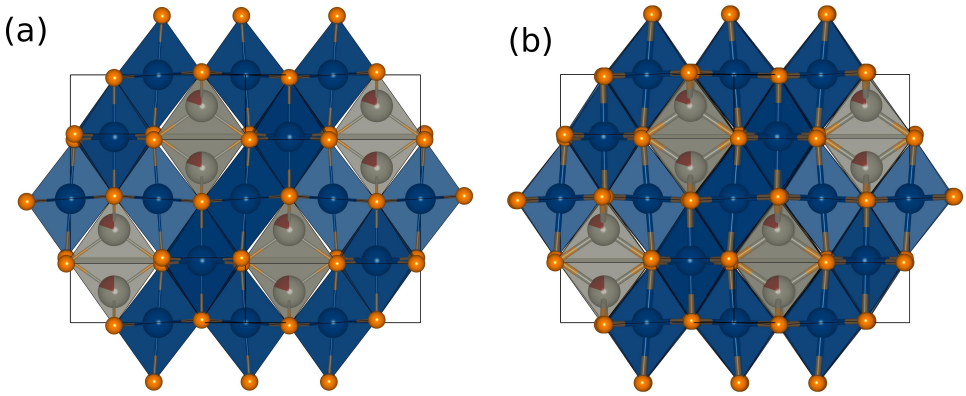

Figure 5.14: The spinel structure of $Zn_{0.8}Cu_{0.2}Cr_2O_4$ in the cubic $Fd\bar{3}m$ phase near 300 K and in the orthorhombic $Fddd$ phase near 6 K are shown in (a) and (b) respectively. Edge sharing CrO_6(blue) octahedra are corner connected to $(Zn/Cu)O_4$(grey) tetrahedra. The shared (Zn/Cu) atomic site is shown in grey(Zn atomic fraction) and dark red(Cu atomic fraction). The ideal tetrahedral angle of 109.54° observed in the cubic phase(a) of $Zn_{0.8}Cu_{0.2}Cr_2O_4$ is distorted to two angles of 111.898° and 105.99° in the orthorhombic phase(b); the $(Zn/Cu)O_4$(grey) tetrahedra appear more flattened in the orthorhombic phase(b) filling the tetrahedral voids between the CrO_6 octahedra while small gaps can be seen between the$(Zn/Cu)O_4$(grey) tetrahedra and the CrO_6(blue) octahedra in the cubic phase(a) of $Zn_{0.8}Cu_{0.2}Cr_2O_4$. Reproduced with permission from reference [96], © 2014 American Physical Society.

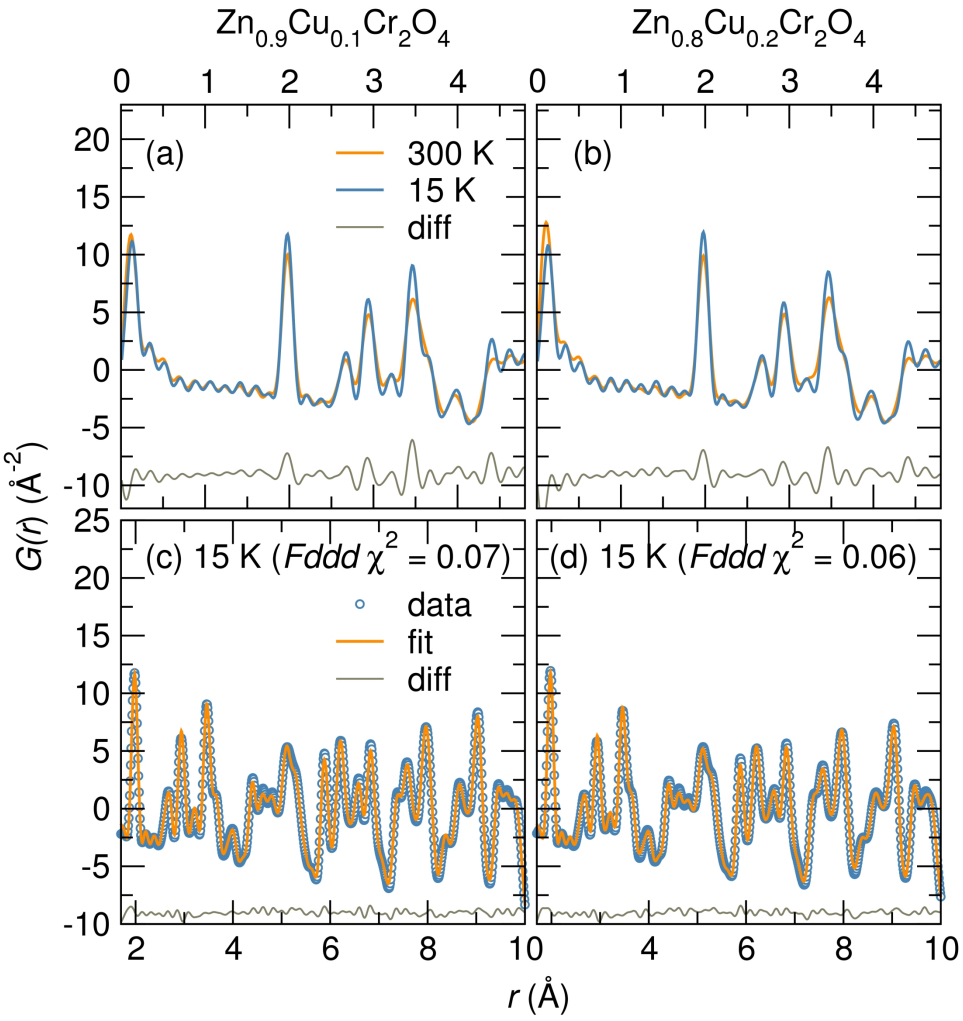

Figure 5.15: Pair distribution functions for $Zn_{0.9}Cu_{0.1}Cr_2O_4$ (a) and $Zn_{0.8}Cu_{0.2}Cr_2O_4$ (b) measured at 300 K and 15 K show that the local structure varies slightly from room temperature to low temperature. The low r region is shown in (a) and (b) to point out the slight increase in intensity of the pair distribution function at low temperature. The difference between the 15 K and the 300 K pair distribution functions is shown at the bottom. Least squares refinement of the pair distribution functions of these compounds at 15 K are well modeled by the $Fddd$ structure as shown in (c) and (d). Reproduced with permission from reference [96], © 2014 American Physical Society.

$Zn_{0.8}Cu_{0.2}Cr_2O_4$ at 45 K and 110 K respectively (middle panel of Fig. 5.11). The lattice distortions of $Zn_{0.9}Cu_{0.1}Cr_2O_4$ and $Zn_{0.8}Cu_{0.2}Cr_2O_4$ are shown by the divergence of the coincident (511) and (333) reflections at the respective distortion temperatures of these materials (Fig. 5.11). The structural changes of $Zn_{0.9}Cu_{0.1}Cr_2O_4$ and $Zn_{0.8}Cu_{0.2}Cr_2O_4$ are decoupled from antiferromagnetic ordering (Table 5.3), nonetheless there is a change in slope of the inverse susceptibility of these systems at the structural distortion temperatures. Jahn-Teller distortion is enhanced in $Zn_{1-x}Cu_xCr_2O_4$ with increase in Cu^{2+} content, occurring at higher temperatures and involving larger lattice distortions (Fig. 5.11). Like in $Mg_{1-x}Cu_xCr_2O_4$, the Jahn-Teller phases of $Zn_{0.9}Cu_{0.1}Cr_2O_4$ [Fig. 5.12 (a)] and $Zn_{0.8}Cu_{0.2}Cr_2O_4$ [Fig. 5.12 (d)] are well modeled by the orthorhombic $Fddd$ space group. The complete structural descriptions of these compounds at room temperature and near 6 K are tabulated in Tables 5.8 and 5.9.

The large heat capacity anomaly of $ZnCr_2O_4$ at the spin-Jahn-Teller distortion temperature [Fig. 5.11 (d)] evolves into a broad transition in $Zn_{0.9}Cu_{0.1}Cr_2O_4$ [Fig. 5.11 (e)] and $Zn_{0.8}Cu_{0.2}Cr_2O_4$ [Fig. 5.11 (f)] over the temperature range were structural and magnetic changes take place.

We further explore the structural distortions of $Zn_{0.8}Cu_{0.2}Cr_2O_4$ by performing sequential Rietveld refinements from the high temperature cubic phase to the low temperature orthorhombic phase. The cubic lattice constant diverges

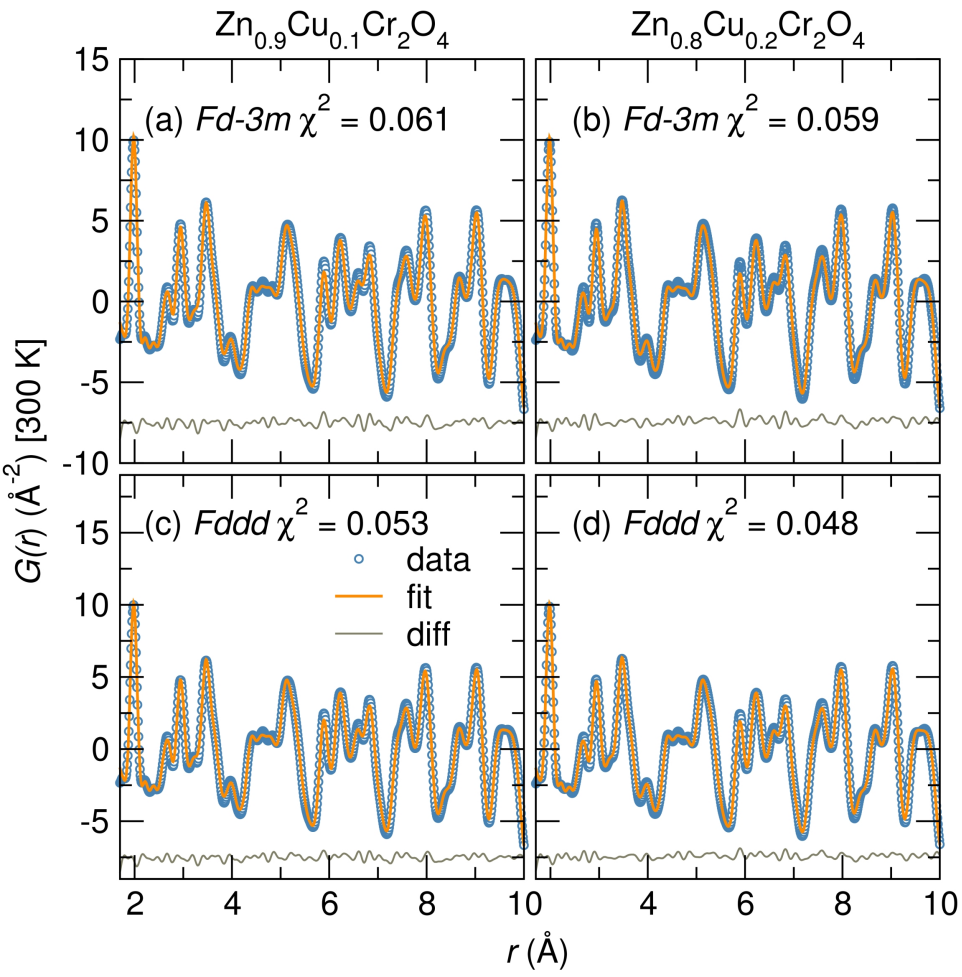

Figure 5.16: Least squares refinement of the pair distribution function of $Zn_{0.9}Cu_{0.1}Cr_2O_4$ and $Zn_{0.8}Cu_{0.2}Cr_2O_4$ collected at 300 K are indexed to the cubic $Fd\bar{3}m$ structure[(a) and (b)] and to the orthorhombic $Fddd$ structure[(c) and (d)]. A smaller difference curve and slightly better χ^2 parameters are obtained when the orthorhombic model is applied to the room temperature data suggesting that dynamic Jahn-Teller distortion may be present at ambient temperature that becomes static at the Jahn-Teller distortion temperatures of these compounds. Reproduced with permission from reference [96], © 2014 American Physical Society.

into three independent orthorhombic lattice parameters at 110 K [Fig. 5.13 (a)]. The a lattice constant decreases steeply with temperature while the b and c lattice constants increase. The orthorhombic distortion increases with decrease in temperature. The fluctuations in the orthorhombic lattice parameters when $50\,\mathrm{K} < T < 110\,\mathrm{K}$ are due to slight temperature variations. Although the structural distortions of $Mg_{1-x}Cu_xCr_2O_4$ and $Zn_{1-x}Cu_xCr_2O_4$ occur primarily due to the Jahn-Teller activity of tetrahedral Cu^{2+}, there is a distinct difference in the distortions observed in the spinel solid solutions compared to the spinel $CuCr_2O_4$. Jahn-Teller distortion in $CuCr_2O_4$ occurs near 853 K and involve a cubic $Fd\bar{3}m$ to tetragonal $I4_1/amd$ lattice distortion.[18] Magnetostructural coupling drives further structural distortion in $CuCr_2O_4$ from tetragonal $I4_1/amd$ to orthorhombic $Fddd$ symmetry.[14] In the solid solutions $Mg_{1-x}Cu_xCr_2O_4$ and $Zn_{1-x}Cu_xCr_2O_4$, we observe a cubic $Fd\bar{3}m$ to orthorhombic $Fddd$ distortion, completely bypassing the tetragonal $I4_1/amd$ structure observed in $CuCr_2O_4$ and the lattice distortions occur without the onset of magnetic ordering. The different character of distortion in $Mg_{1-x}Cu_xCr_2O_4$ and $Zn_{1-x}Cu_xCr_2O_4$ compared to $CuCr_2O_4$ is attributed to poor connectivity between CuO_4 tetrahedra. Dilute randomly distributed CuO_4 tetrahedra in the solid solutions results in average distortions in all axes of the unit cell and hence these systems adopt orthorhombic symmetry in the Jahn-Teller phases. Group-subgroup relations show that

structural distortion from cubic $Fd\bar{3}m$ to orthorhombic $Fddd$ symmetry goes through an intermediate tetragonal $I4_1/amd$ space group. It is plausible that the Jahn-Teller ordering systems $Mg_{1-x}Cu_xCr_2O_4$ and $Zn_{1-x}Cu_xCr_2O_4$ quickly go through the tetragonal $I4_1/amd$ structure before adopting the orthorhombic structure. A similar cubic $Fd\bar{3}m$ to orthorhombic $Fddd$ lattice distortion driven by charge ordering has been observed in the cathode spinel material $LiMn_2O_4$ near room temperature.[107]

The $Zn_{0.8}Cu_{0.2}Cr_2O_4$ unit cell contracts with decrease in temperature as reflected in Fig. 5.13 (b). There is a slight change in slope of the unit cell volume at the structural distortion temperature. This small change in slope of the cell volume at 110 K and the broad heat capacity anomaly of $Zn_{0.8}Cu_{0.2}Cr_2O_4$ suggest that it undergoes a second-order structural distortion.

The AO_4 tetrahedra of the cubic phase of $Zn_{0.8}Cu_{0.2}Cr_2O_4$ are distorted in the orthorhombic phase. Specifically, a single A-O distance is preserved while two distinct O-A-O bond angles of 111.898° and 105.99° emerge from the ideal tetrahedral angle 109.47° of the cubic phase. The overall effect of these angle distortions in $Zn_{0.8}Cu_{0.2}Cr_2O_4$ is a compression of the tetrahedra. This is illustrated in Fig. 5.14 (a) where the ideal AO_4 tetrahedra of the cubic phase leave small voids in the surrounding CrO_6 network while the flattened AO_4 tetrahedra of the orthorhombic phase completely fill the tetrahedral voids [Fig.

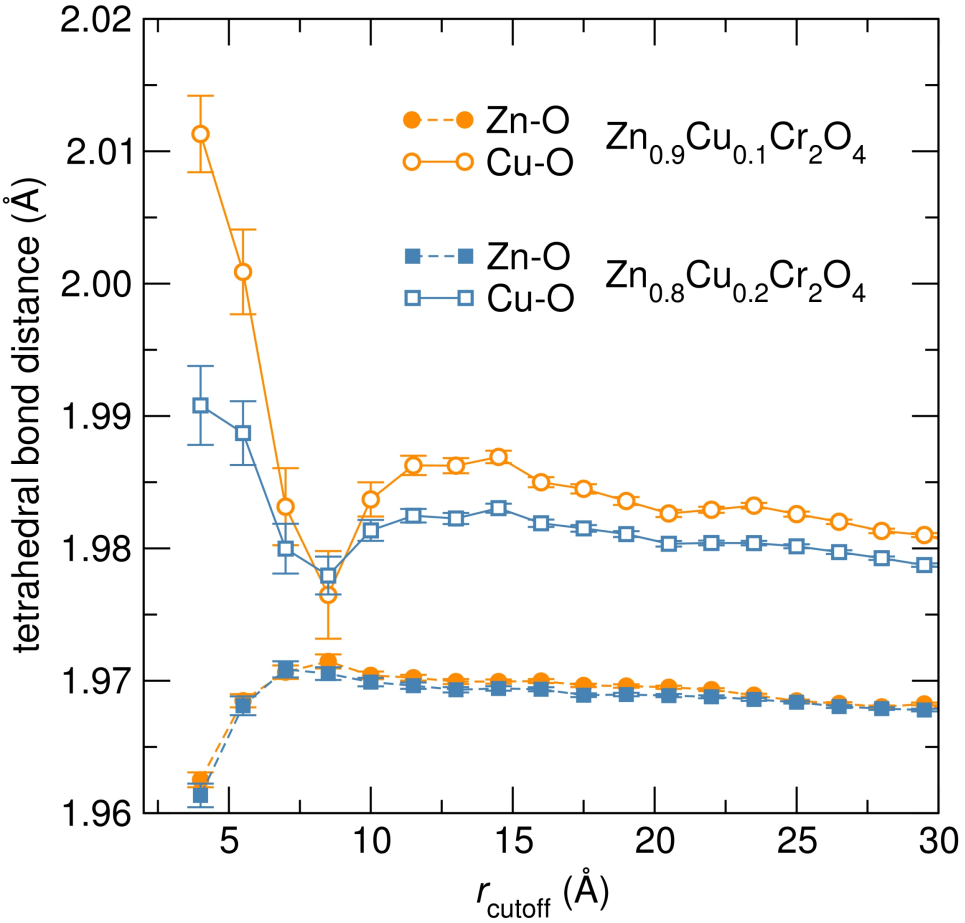

Figure 5.17: Least squares refinement of the 300 K pair distribution function of $Zn_{0.9}Cu_{0.1}Cr_2O_4$ and $Zn_{0.8}Cu_{0.2}Cr_2O_4$ to a two phase model of $ZnCr_2O_4$ and $CuCr_2O_4$ shows that the environment around Zn^{2+} varies from that around Cu^{2+} at low r as shown by the different Zn-O and Cu-O bond lengths of the ZnO_4 and CuO_4 tetrahedra. The phase fractions of the $ZnCr_2O_4$ model are 90% for $Zn_{0.9}Cu_{0.1}Cr_2O_4$ and 80% for $Zn_{0.8}Cu_{0.2}Cr_2O_4$. The differences in Zn-O and Cu-O bond lengths of the AO_4 tetrahedra are smaller at high r. Reproduced with permission from reference [96], © 2014 American Physical Society.

5.14(b)]. The compression of AO_4 tetrahedra is similar to the flattening of CuO_4 tetrahedra in the orthorhombic phase of $CuCr_2O_4$.[14] The AO_4 distortions of $Zn_{0.8}Cu_{0.2}Cr_2O_4$ distort the surrounding CrO_6 matrix. Three distinct Cr-O bond distances and O-Cr-O bond angles emerge in the orthorhombic phase of $Zn_{0.8}Cu_{0.2}Cr_2O_4$ compared to the cubic phase where there are no bond length or bond angle distortions. The distortions of the Cr sublattice in $Mg_{1-x}Cu_xCr_2O_4$ and $Zn_{1-x}Cu_xCr_2O_4$ do not lift spin degeneracy and magnetic ordering in these materials still takes place below 20 K (Table 5.2 and 5.3).

Real space structural descriptions of $Zn_{1-x}Cu_xCr_2O_4$ for $x > 0$ give insights as to the nature of the Jahn-Teller distortions in these compounds. There are differences in the pair distribution functions of $Zn_{0.9}Cu_{0.1}Cr_2O_4$ and $Zn_{0.8}Cu_{0.2}Cr_2O_4$ collected at room temperature and at 15 K as shown in Fig. 5.15 (a) and (b). The differences are mainly in the intensity of atom pair correlations; at low temperature, the distribution functions have slightly higher intensity than at room temperature where atomic vibrations broaden the pair distribution function [Fig. 5.15 (a) and (b)]. The low temperature average structural model, orthorhombic $Fddd$, describes the local structure of $Zn_{0.9}Cu_{0.1}Cr_2O_4$ and $Zn_{0.8}Cu_{0.2}Cr_2O_4$ at 15 K [Fig. 5.15 (c) and (d)].

Combined average and local structure studies can distinguish whether Jahn-Teller distortions occur spontaneously at the average structure distortion tem-

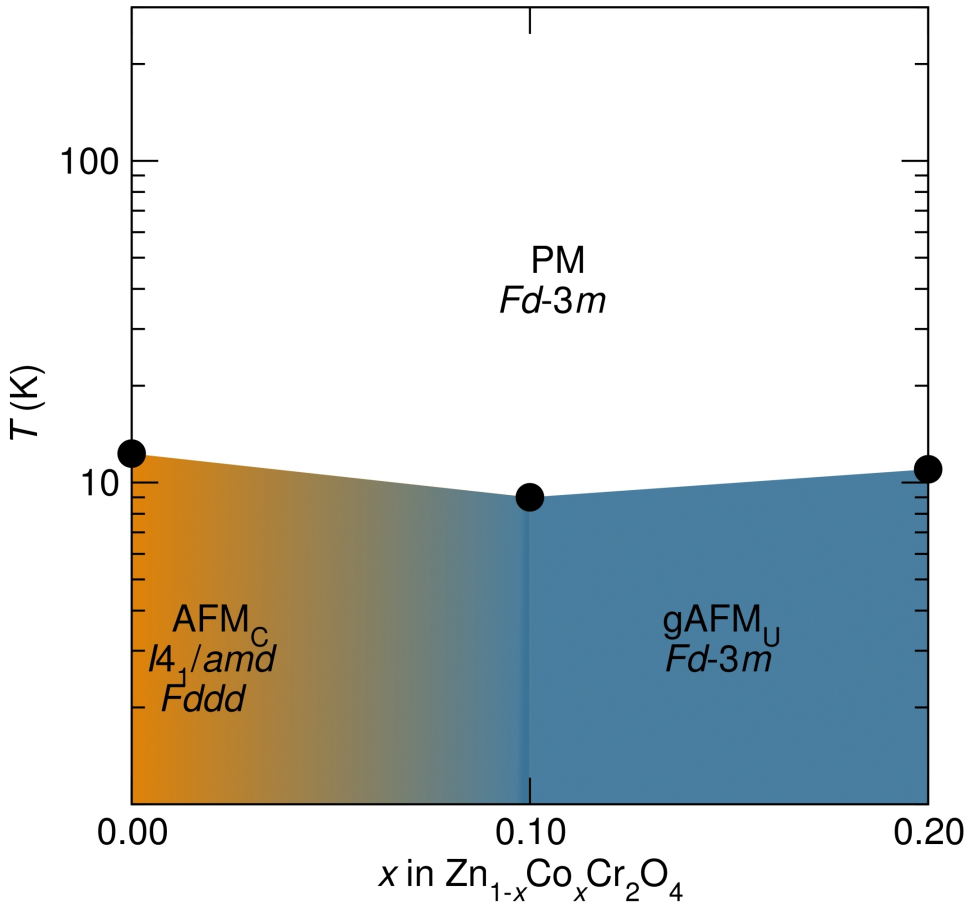

Figure 5.18: Temperature-composition phase diagram of the spinel solid solution $Zn_{1-x}Co_xCr_2O_4$. At high temperatures the spinels $Zn_{1-x}Co_xCr_2O_4$ where $x \leq 0.2$ are paramagnetic(PM) and cubic in the space group $Fd\bar{3}m$. Magnetism evolves from frustrated compensated antiferromagnetism (AFM_C) in $ZnCr_2O_4$ to glassy uncompensated antiferromagnetism ($gAFM_U$) when x=0.2. We have recently reported that tetragonal $I4_1/amd$ and orthorhombic $Fddd$ structures coexist in the spin-Jahn-Teller phase of $ZnCr_2O_4$.[1] Reproduced with permission from reference [96], © 2014 American Physical Society.

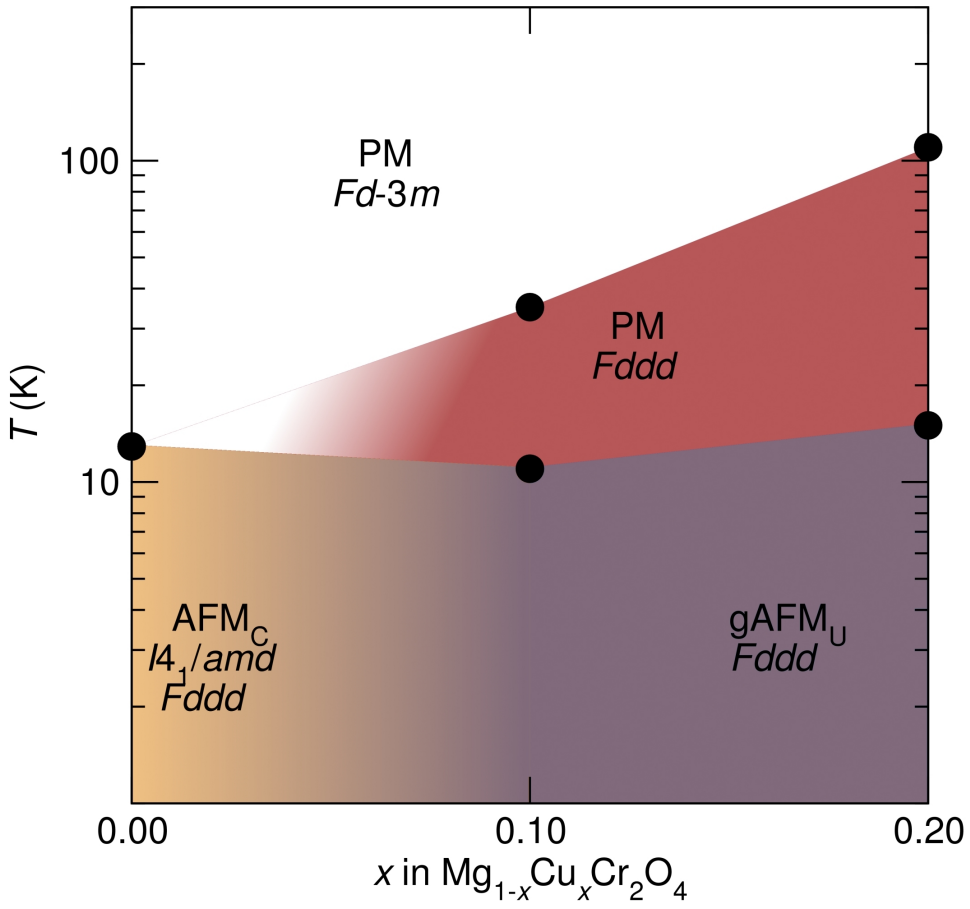

Figure 5.19: Temperature-composition phase diagrams of the spinel solid solution $Mg_{1-x}Cu_xCr_2O_4$. At high temperatures all systems $Mg_{1-x}Cu_xCr_2O_4$ where $x \leq 0.2$ are paramagnetic(PM) and cubic in the space group $Fd\bar{3}m$. Magnetism evolves from frustrated compensated antiferromagnetism (AFM_C) in $MgCr_2O_4$ to glassy uncompensated antiferromagnetism ($gAFM_U$) when x=0.2. A transition from cubic $Fd\bar{3}m$ to orthorhombic $Fddd$ symmetry occurs in $Mg_{1-x}Cu_xCr_2O_4$ when $x \geq 0.1$ due to Jahn-Teller distortions of tetrahedral CuO_4. We have recently reported that tetragonal $I4_1/amd$ and orthorhombic $Fddd$ structures coexist in the spin-Jahn-Teller phase of $MgCr_2O_4$.[1] Reproduced with permission from reference [96], © 2014 American Physical Society.

peratures of $Zn_{0.9}Cu_{0.1}Cr_2O_4$ and $Zn_{0.8}Cu_{0.2}Cr_2O_4$ or whether local distortions of CuO_4 tetrahedra persist in the cubic phases of these materials with these distortions becoming cooperative at the Jahn-Teller distortion temperature. In Figure 5.16 we model the room temperature pair distribution functions of $Zn_{0.9}Cu_{0.1}Cr_2O_4$ (a) and $Zn_{0.8}Cu_{0.2}Cr_2O_4$ (b) to the cubic average structure model $Fd\bar{3}m$ and to the Jahn-Teller distorted orthorhombic $Fddd$ structure. At room temperature, the cubic $Fd\bar{3}m$ fit yields slightly larger goodness-of-fit parameters compared to the lower symmetry $Fddd$ fits [Fig. 5.16 (c) and (d)]. The better description of the local structure of these compounds at room temperature by the lower symmetry structural model suggests that local CuO_4 distortions are present in the cubic phases of $Zn_{0.9}Cu_{0.1}Cr_2O_4$ and $Zn_{0.8}Cu_{0.2}Cr_2O_4$ and that these distortions become cooperative at the respective Jahn-Teller distortion temperatures of these systems. The presence of local distortions at room temperature in $Zn_{0.9}Cu_{0.1}Cr_2O_4$ and $Zn_{0.8}Cu_{0.2}Cr_2O_4$ is further corroborated by least squares refinements of the pair distribution functions to a structural model of two cubic phases assigned to either $ZnCr_2O_4$ or $CuCr_2O_4$[Fig. 5.17]. Structural models consisting of stoichiometrically weighted end-member structures have been previously successfully employed to describe the pair distribution function of the frustrated spinel $CoAl_{1.6}Ga_{0.4}O_4$ at low r.[108] In the two phase refinement, the $ZnCr_2O_4$ and $CuCr_2O_4$ structural models are scaled to corre-

late with the mole fractions of Zn^{2+} and Cu^{2+} and only the lattice parameters and Zn^{2+}/Cu^{2+} thermal parameters are allowed to vary. There is a difference in the Zn-O and Cu-O bond lengths in the two phases at low r_{cutoff} for both $Zn_{0.9}Cu_{0.1}Cr_2O_4$ and $Zn_{0.8}Cu_{0.2}Cr_2O_4$ and this difference decreases at high r_{cutoff} (Fig. 5.17). This suggests that there are local distortions in $Zn_{0.9}Cu_{0.1}Cr_2O_4$ and $Zn_{0.8}Cu_{0.2}Cr_2O_4$ that are best modeled by differentiating the environment around Zn^{2+} and Cu^{2+}. As one examines the pair distribution functions to higher r_{cutoff}, these local distortions are averaged out becoming less apparent as observed by the smaller difference in A-O bond lengths of $ZnCr_2O_4$ and $CuCr_2O_4$. At room temperature, the CuO_4 tetrahedra of $CuCr_2O_4$ are significantly compressed[14] with an angle variance of 94.2619 deg.^{2} while ZnO_4 tetrahedra in $ZnCr_2O_4$ are in an ideal configuration.[29] The discrepancies in Zn-O and Cu-O bond distances at low r in $Zn_{0.9}Cu_{0.1}Cr_2O_4$ and $Zn_{0.8}Cu_{0.2}Cr_2O_4$ are due to the strong Jahn-Teller tendency of tetrahedral Cu^{2+} compared to non-Jahn-Teller Zn^{2+} which have a closed electron shell configuration. The presence of local distortions in $Zn_{0.9}Cu_{0.1}Cr_2O_4$ and $Zn_{0.8}Cu_{0.2}Cr_2O_4$ is in good agreement with total scattering studies of the spinels $Mg_{1-x}Cu_xCr_2O_4$ by Shoemaker and Seshadri that show more distortions of the local CuO_4 environments compared to MgO_4 environments in this spinel solid solution.[93]

Cu^{2+} substitution on the non-magnetic A sites of $MgCr_2O_4$ and $ZnCr_2O_4$

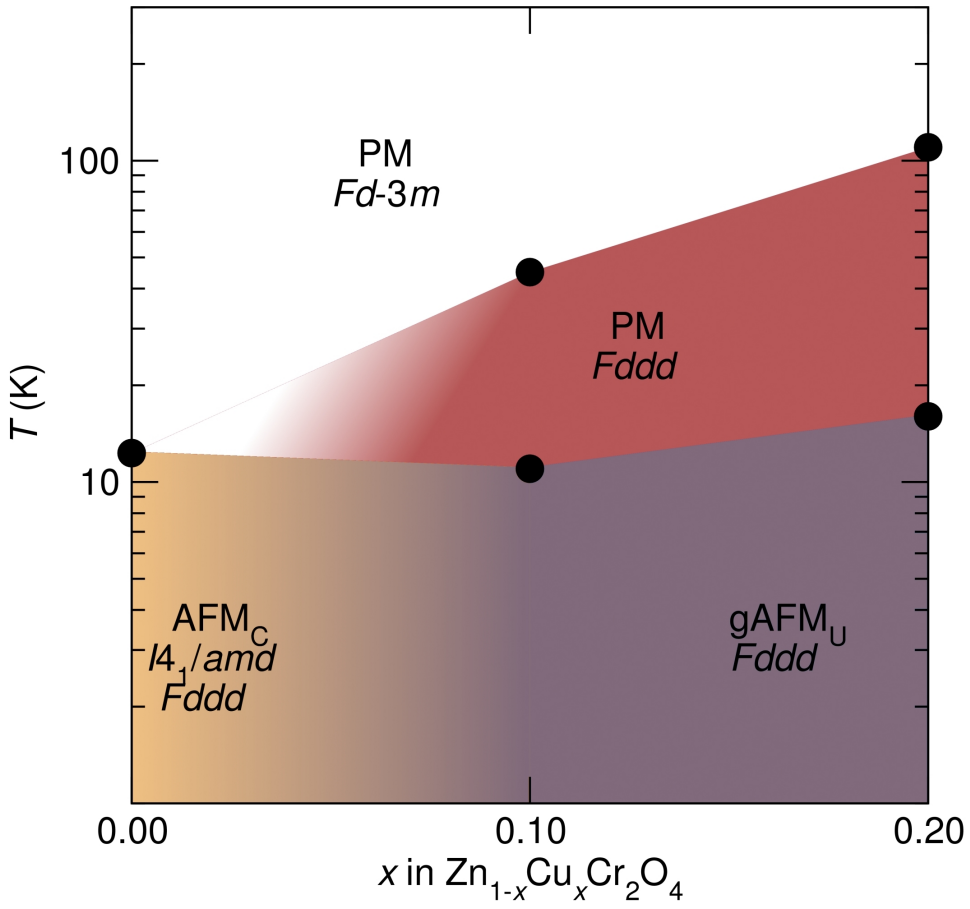

Figure 5.20: Temperature-composition phase diagrams of the spinel solid solution $Zn_{1-x}Cu_xCr_2O_4$. At high temperatures all systems $Zn_{1-x}Cu_xCr_2O_4$ where $x \leq 0.2$ are paramagnetic(PM) and cubic in the space group $Fd\bar{3}m$. Magnetism evolves from frustrated compensated antiferromagnetism (AFM_C) in $ZnCr_2O_4$ to glassy uncompensated antiferromagnetism ($gAFM_U$) when $x = 0.2$. A transition from cubic $Fd\bar{3}m$ to orthorhombic $Fddd$ symmetry occurs in $Zn_{1-x}Cu_xCr_2O_4$ when $x \geq 0.1$ due to Jahn-Teller distortions of tetrahedral CuO_4. We have recently reported that tetragonal $I4_1/amd$ and orthorhombic $Fddd$ structures coexist in the spin-Jahn-Teller phase of $ZnCr_2O_4$.[1] Reproduced with permission from reference [96], © 2014 American Physical Society.

has very similar effects on the structure and magnetic properties of the resulting solid solutions. Average structure distortions due to Jahn-Teller ordering of CuO_4 tetrahedra occur in $Mg_{1-x}Cu_xCr_2O_4$ and $Zn_{1-x}Cu_xCr_2O_4$ without accompanying long-range magnetic ordering. The distortions of CuO_4 tetrahedra are present in the cubic phases of $Zn_{1-x}Cu_xCr_2O_4$ when $x \geq 0.1$ and become cooperative at the Jahn-Teller distortion temperature where average structure distortions are observed. The Jahn-Teller distorted phases are described by the orthorhombic $Fddd$ space group. The degeneracy of Cr-Cr bond distances is broken when average structure distortions occur in $Mg_{1-x}Cu_xCr_2O_4$ and $Zn_{1-x}Cu_xCr_2O_4$, however, antiferromagnetic interactions remain largely frustrated with magnetic ordering occurring below 20 K. We contrast the propensity for Jahn-Teller distortions compared with spin-Jahn-Teller distortion in the systems $Mg_{1-x}Cu_xCr_2O_4$ and $Zn_{1-x}Cu_xCr_2O_4$ where only few Cu^{2+} cations drive Jahn-Teller distortions while these small concentrations of magnetic ions on the non-magnetic A sites of these materials completely suppress spin-Jahn-Teller distortion. The evolution of structure and magnetism in the solid solutions $Zn_{1-x}Co_xCr_2O_4$, $Mg_{1-x}Cu_xCr_2O_4$, and $Zn_{1-x}Cu_xCr_2O_4$ are summarized in the phase diagrams presented in figs. [5.18, 5.19, 5.20].

5.5.1 Conclusions

We report the effect of magnetic A site substitutions on spin and structural ordering in $MgCr_2O_4$ and $ZnCr_2O_4$. We contrast the effect of Co^{2+} $3d^7$ substitutions in $Zn_{1-x}Co_xCr_2O_4$ with Cu^{2+} $3d^9$ substitutions in $Mg_{1-x}Cu_xCr_2O_4$ and $Zn_{1-x}Cu_xCr_2O_4$. Substitution of magnetic cations for non-magnetic cations can lead to composition inhomogeneities due to the differences in orbital occupation in these cations. Rietveld refinement of high resolution synchrotron X-ray powder diffraction of the solid solutions $Zn_{1-x}Co_xCr_2O_4$, $Mg_{1-x}Cu_xCr_2O_4$, and $Zn_{1-x}Cu_xCr_2O_4$ shows that these materials are homogeneous; at room temperature they are all well described by the cubic $Fd\bar{3}m$ space group. These solid solutions follow Vegard's law, this further illustrates the homogeneous incorporation of magnetic cations. Co^{2+} $3d^7$ substitution in $Zn_{1-x}Co_xCr_2O_4$ induces spin disorder that suppresses the spin-Jahn-Teller distortion of $ZnCr_2O_4$. On the other hand, spin and lattice disorder due to Cu^{2+} $3d^9$ substitutions in $Mg_{1-x}Cu_xCr_2O_4$ and $Zn_{1-x}Cu_xCr_2O_4$ induce Jahn-Teller distortions in the paramagnetic phases of these compounds yet antiferromagnetic interactions in these systems remain frustrated with long-range magnetic ordering occurring below 20 K with no accompanying structural transformations. In other words, the Jahn-Teller active Cu^{2+} ions decouple structural and magnetic ordering, even when only substi-

tuted in small amounts. The low-temperature nuclear structure of Cu^{2+} substituted $MgCr_2O_4$ and $ZnCr_2O_4$ is orthorhombic $Fddd$. Analysis of distortions in $Zn_{0.8}Cu_{0.2}Cr_2O_4$ indicate a flattening of AO_4 tetrahedra in the orthorhombic phase. Total neutron scattering studies of $Zn_{1-x}Cu_xCr_2O_4$ suggest that AO_4 are likely distorted locally at room temperature with these distortions becoming cooperative where average structure distortions are observed. Addition of magnetic Co^{2+} and Cu^{2+} induce uncompensated antiferromagnetic interactions in $Zn_{1-x}Co_xCr_2O_4$, $Mg_{1-x}Cu_xCr_2O_4$, and $Zn_{1-x}Cu_xCr_2O_4$. Compounds with dilute A site spins have broad heat capacity features suggesting remanent disorder in these materials. We find that spin-Jahn-Teller ordering is extremely sensitive to spin disorder while Jahn-Teller ordering is robust, and occurs even when only few Jahn-Teller active cations are substituted into the spinel structure.

Table 5.4: Structural parameters of $Zn_{0.9}Co_{0.1}Cr_2O_4$ obtained from Rietveld refinement of high-resolution synchrotron powder X-ray diffraction collected at 295 K and near 6 K and modeled to the cubic space group $Fd\bar{3}m$.

	$Zn_{0.9}Co_{0.1}Cr_2O_4$	
Temperature (K)	5.5	295
Setting	origin 2	origin 2
Z	8	8
a(Å)	8.32037(2)	8.327641(1)
Vol/ (Å^3)	576.008(4)	577.519(3)
Zn/Co	$8a$ (1/8, 1/8 1/8)	$8a$ (1/8, 1/8, 1/8))
U_{iso} (10^2 Å^2)	0.24(1)	0.389(5)
Cr	$16d$ (1/2, 1/2, 1/2)	$16d$ (1/2, 1/2, 1/2)
U_{iso} (10^2 Å^2)	0.196(9)	0.213(4)
O	$32h$ (x, y, z)	$32e$ (x, x, x)
	x 0.2612(1)	x 0.26205(4)
U_{iso} (10^2 Å^2)	0.54(3)	0.32(1)
χ^2	15.73	5.263
R_p(%)	8.10	9.12
R_{wp}(%)	10.12	11.54

Table 5.5: Structural parameters of $Zn_{0.8}Co_{0.2}Cr_2O_4$ obtained from Rietveld refinement of high-resolution synchrotron powder X-ray diffraction collected at 295 K and near 6 K and modeled to the cubic space group $Fd\bar{3}m$.

	$Zn_{0.8}Co_{0.2}Cr_2O_4$	
Temperature (K)	5.6	295
Setting	origin 2	origin 2
Z	8	8
a(Å)	8.32038(1)	8.327868(5)
Vol/ (Å^3)	576.009(2)	577.566(1)
Zn/Co	$8a$ (1/8, 1/8 1/8)	$8a$ (1/8, 1/8, 1/8)
U_{iso} (10^2 Å^2)	0.128(7)	0.398(5)
Cr	$16d$ (1/2, 1/2, 1/2)	$16d$ (1/2, 1/2, 1/2)
U_{iso} (10^2 Å^2)	0.145(6)	0.230(4)
O	$32h$ (x, y, z)	$32e$ (x, x, x)
	0.26208(7)	0.26221(5)
U_{iso} (10^2 Å^2)	0.35(2)	0.360(1)
χ^2	6.976	7.434
R_p(%)	7.54	9.33
R_{wp}(%)	9.43	12.56

Table 5.6: Structural parameters of $Mg_{0.9}Cu_{0.1}Cr_2O_4$ obtained from Rietveld refinement of high-resolution synchrotron powder X-ray diffraction collected at 295 K and near 6 K.

	$Mg_{0.9}Cu_{0.1}Cr_2O_4$	
	Orthorhombic	Cubic
Temperature (K)	6.5	295
Space group	$Fddd$	$Fd\bar{3}m$
Setting	origin 2	origin 2
Z	8	8
a(Å)	8.293741(1)	8.332613(3))
b(Å)	8.335834(1)	8.332613(3)
c(Å)	8.3488(5)	8.332613(3)
Vol/ (Å^3)	577.196(4)	578.554(1)
Mg/Cu	$8a$ (1/8, 1/8 1/8)	$8a$ (1/8, 1/8, 1/8))
U_{iso} (10^2 Å^2)	0.384(2)	0.651(7)
Cr	$16d$ (1/2, 1/2, 1/2)	$16d$ (1/2, 1/2, 1/2)
U_{iso} (10^2 Å^2)	0.17(9)	0.321(3)
O	$32h$ (x, y, z)	$32e$ (x, x, x)
	x 0.26284(2)	x 0.26161(3)
	y 0.25845(3)	y 0.26161(3)
	z 0.262891(2)	z 0.26161(3)
U_{iso} (10^2 Å^2)	0.144(2)	0.651(7)
Cr_2O_3 wt%	0.89(8)	0.89(8)
χ^2	4.37	2.550
R_p(%)	6.7	5.98
R_{wp}(%)	9.16	8.12

Table 5.7: Structural parameters of $Mg_{0.8}Cu_{0.2}Cr_2O_4$ obtained from Rietveld refinement of high-resolution synchrotron powder X-ray diffraction collected at 295 K and near 6 K.

	$Mg_{0.8}Cu_{0.2}Cr_2O_4$	
	Orthorhombic	Cubic
Temperature (K)	5.7	295
Space group	$Fddd$	$Fd\bar{3}m$
Setting	origin 2	origin 2
Z	8	8
a(Å)	8.231110(8)	8.330362(3)
b(Å)	8.360256(9)	8.330362(3)
c(Å)	8.373391(5)	8.330362(3)
Vol/ (Å^3)	576.208(4)	578.085(1)
Mg/Cu	$8a$ (1/8, 1/8 1/8)	$8a$ (1/8, 1/8, 1/8)
U_{iso} (10^2 Å^2)	0.371(2)	0.696(7)
Cr	$16d$ (1/2, 1/2, 1/2)	$16d$ (1/2, 1/2, 1/2)
U_{iso} (10^2 Å^2)	0.102(1)	0.344(3)
O	$32h$ (x, y, z)	$32e$ (x, x, x)
	0.260090(1)	0.26170(4)
	0.260627(2)	0.26170(4)
	0.263825(2)	0.26170(4)
U_{iso} (10^2 Å^2)	0.25(0)	0.59(1)
Cr_2O_3 wt%	0.87(7)	0.87(7)
χ^2	6.81	2.571
R_p(%)	6.29	6.23
R_{wp}(%)	8.14	8.15

Table 5.8: Structural parameters of $Zn_{0.9}Cu_{0.1}Cr_2O_4$ obtained from Rietveld refinement of high-resolution synchrotron powder X-ray diffraction collected at 295 K and near 6 K.

	$Zn_{0.9}Cu_{0.1}Cr_2O_4$	
	Orthorhombic	Cubic
Temperature (K)	5.6	295
Space group	$Fddd$	$Fd\bar{3}m$
Setting	origin 2	origin 2
Z	8	8
a(Å)	8.328150(7)	8.326102(6)
b(Å)	8.335862(5)	8.326102(6))
c(Å)	8.289697(5)	8.326102(6)
Vol/ (Å^3)	575.490(3)	577.199(1)
Zn/Cu	$8a$ (1/8, 1/8 1/8)	$8a$ (1/8, 1/8, 1/8))
U_{iso} (10^2 Å^2)	0.309(8)	0.453(5)
Cr	$16d$ (1/2, 1/2, 1/2)	$16d$ (1/2, 1/2, 1/2)
U_{iso} (10^2 Å^2)	0.297(8)	0.247(4)
O	$32h$ (x, y, z)	$32e$ (x, x, x)
	x 0.2577(3)	x0.262013(48)
	y 0.2642(3)	y0.262013(48)
	z 0.2628(2)	z0.262013(48)
U_{iso} (10^2 Å^2)	0.329(21)	0.393(14)
Cr_2O_3 wt%	0.326(35)	0.259(23)
χ^2	4.494	7.035
R_p(%)	2.52	8.66
R_{wp}(%)	3.49	11.98

Table 5.9: Structural parameters of $Zn_{0.8}Cu_{0.2}Cr_2O_4$ obtained from Rietveld refinement of high-resolution synchrotron powder X-ray diffraction collected at 295 K and near 6 K.

	$Zn_{0.8}Cu_{0.2}Cr_2O_4$	
	Orthorhombic	Cubic
Temperature (K)	5.9	295
Space group	$Fddd$	$Fd\bar{3}m$
Setting	origin 2	origin 2
Z	8	8
a(Å)	8.244895(8)	8.324225(5)
b(Å)	8.358441(5)	8.324225(5)
c(Å)	8.3409(1)	8.324225(5)
Vol/ (Å^3)	574.809(5)	576.808(1)
Zn/Cu	$8a$ (1/8, 1/8 1/8)	$8a$ (1/8, 1/8, 1/8)
U_{iso} (10^2 Å^2)	0.281(13)	0.465(3)
Cr	$16d$ (1/2, 1/2, 1/2)	$16d$ (1/2, 1/2, 1/2)
U_{iso} (10^2 Å^2)	0.254(13)	0.247(3)
O	$32h$ (x, y, z)	$32e$ (x, y, z)
	0.260315(184)	0.261980(33)
	0.266652(262)	0.261980(33)
	0.257599(340)	0.261980(33)
U_{iso} (10^2 Å^2)	0.304(33)	0.465(3)
Cr_2O_3 wt%	1.05(15)	1.18(0)
χ^2	7.808	3.249
R_p(%)	3.81	6.32
R_{wp}(%)	5.85	8.33

Chapter 6

Structural change and phase coexistence upon magnetic ordering in the magnetodielectric spinel Mn_3O_4

Cooperative Jahn-Teller ordering is well-known to drive the cubic $Fd\bar{3}m$ to tetragonal $I4_1/amd$ structural distortion in Mn_3O_4 at 1170 °C. Further structural distortion occurs in Mn_3O_4 upon magnetic ordering at 42 K. Employing high-resolution variable-temperature synchrotron x-ray diffraction we show that

tetragonal $I4_1/amd$ and orthorhombic $Fddd$ phases coexist, with nearly equal fractions, below the Néel temperature of Mn_3O_4. Significant variation of the orthorhombic a and b lattice constants from the tetragonal a lattice constant is observed. Structural phase coexistence in Mn_3O_4 is attributed to large strains due to the lattice mismatch between the tetragonal $I4_1/amd$ and the orthorhombic $Fddd$ phases. Strain tensors determined from Rietveld refinement show a highly strained matrix of the $I4_1/amd$ phase that accommodates the nucleated orthorhombic $Fddd$ phase in the phase coexistence regime. A comparison of the deformation observed in Mn_3O_4 to structural deformations of other magnetic spinels shows that phase coexistence may be a common theme when structural distortions occur below 50 K.

6.1 Introduction

Phase coexistence is a recurring theme that has been extensively investigated in perovskite manganese oxides displaying colossal magnetoresistance.[109] Phase separation of charge ordered insulating (antiferromagnetic) and metallic (ferromagnetic) phases has been observed in the manganites (La,Pr,Ca)MnO_3.[110, 111] Competing double exchange mechanisms and Jahn-Teller-like electron-lattice coupling have been proposed to explain the coexis-

tence of multiple phases.[110, 111] Chemical disorder has also been invoked to explain microscale structural phase separation.[112, 113] However, generalizations in describing the mechanisms of phase coexistence are often insufficient in describing all aspects of these phenomena prompting continued interest in these materials.[114] Here, we encounter structural phase coexistence below the Néel temperature of the spinel Mn_3O_4.

Mn_3O_4 (the mineral hausmanite) consists of edge sharing MnO_6 octahedra that are corner connected to MnO_4 tetrahedra. It is a cubic spinel in the space group $Fd\bar{3}m$ above 1170 °C. Mn_3O_4 undergoes a cooperative Jahn-Teller distortion below 1170 °C due to orbital degeneracy of the e_g^1 states of Mn^{3+} cations that occupy the octahedral sites. Jahn-Teller ordering of the octahedral e_g states stabilizes the z^2 orbital by elongating the MnO_6 octahedral units resulting in tetragonal $I4_1/amd$ symmetry below 1170 °C.[16, 115] Mn_3O_4 is a paramagnet above the Néel temperature (T_N) = 41 K, below T_N, it adopts a non-collinear magnetic structure that consists of ferromagnetically coupled Mn^{2+} cations along the (010) direction and two Mn^{3+} sub-lattices with a net moment that couples antiferromagnetically to the magnetization of Mn^{2+} cations. A transition to an incommensurate spiral configuration occurs at 39 K, followed by a transition to commensurate spiral order below 33 K.[116] Commensurate spiral spin ordering in Mn_3O_4 is described by an orthorhombic magnetic unit

cell, which is twice the size of the chemical tetragonal unit cell.[116] Magnon excitations in ferrimagnetic Mn_3O_4 have been recently investigated by Gleason *et al.*[**?**] Magnetism in Mn_3O_4 couples to its dielectric properties. Consequently, dielectric anomalies are observed near the magnetic transition temperatures. In addition, magnetic field control of the dielectric constant below T_N has also been demonstrated.[81, 117]

While Jahn-Teller ordering yields a high temperature cubic-tetragonal distortion in Mn_3O_4 ,[16, 115] spin ordering drives further lattice distortions in this spinel.[118] Kim *et al.* reported a transition from tetragonal to monoclinic symmetry in single crystal Mn_3O_4 at the commensurate spiral ordering temperature ($T \sim 33$ K) under zero applied fields.[118] In a subsequent report, Kim and coauthors proposed that the low temperature structure of Mn_3O_4 is orthorhombic in the space group $Fddd$.[119] Similarly, Chung *et al.* have recently reported orthorhombic instabilities in Mn_3O_4.[120] While these initial efforts clearly illustrate a structural transformation in ferrimagnetic Mn_3O_4, the complete low-temperature structure of Mn_3O_4 remains unresolved and is the focus of the present work. Extensive studies of the magnetostructural phases of Mn_3O_4 by Kim and coauthors show that in the presence of large magnetic fields, the structural distortion occurs at higher temperatures in the incommensurate spiral magnetic phase. Remarkably, a spin disordered phase can be stabilized

in Mn_3O_4 near 0 K when intermediate fields are applied parallel to the $(1\bar{1}0)$ direction. Here, applied fields transverse to the magnetic ordering direction frustrate spin ordering resulting in disordered spins far below the magnetic ordering temperature.[118] Kim $et\,al.$ have also shown an increase in the Néel temperature under pressure to temperatures as high as 54 K.[119]

We present here, a complete description of the low-temperature nuclear structure of Mn_3O_4 finding that tetragonal $I4_1/amd$ and orthorhombic $Fddd$ phases coexist in ferrimagnetic Mn_3O_4. The orthorhombic $Fddd$ phase is spontaneously nucleated at the Néel temperature and its phase fraction increases slightly, attaining a maximum of about 55% near 8 K. The evolution of the unit cell volume as a function of temperature indicates a distortion in both the tetragonal $I4_1/amd$ and orthorhombic $Fddd$ phases below 42 K. Distortions in both low temperature tetragonal and orthorhombic phases are corroborated by detailed studies of polyhedra distortions which show deformations in both of these phases. In the orthorhombic phase, MnO_6 octahedra show elongation of equatorial Mn-O bonds while the MnO_4 tetrahedra show a decrease in the Mn-O bond length. Conversely, the distorted tetragonal phase shows shortened Mn-O equatorial bonds in the MnO_6 octahedra and elongated Mn-O bonds in the MnO_4 tetrahedra. We examine the role of strain in stabilizing coexisting tetragonal and orthorhombic phases in ferrimagnetic Mn_3O_4 and make comparisons

of the structural distortion of Mn_3O_4 to those of other magnetic spinels. The complexities in understanding the variations of structural deformations in magnetic spinels are highlighted. The complete structural description of this spinel is pivotal to unraveling the complex ground states of this material. These results necessitate a reinvestigation of the magnetic structure of Mn_3O_4, which was resolved considering only the tetragonal nuclear structure below the Néel temperature.

6.2 Methods

Polycrystalline Mn_3O_4 was prepared from a $MnC_2O_4{\cdot}2H_2O$ precursor. The oxalate was decomposed at 600 °C for 3 hrs. The precursor powder was then ground, pelletized, and annealed at 1000 °C for 24 hrs and water quenched. Variable-temperature (7.5 K – 450 K) high-resolution ($\delta Q/Q \leq 2\times10^{-4}$, $\lambda = 0.41394$ Å) synchrotron x-ray powder diffraction was performed at beamline 11BM of the Advanced Photon Source, Argonne National Laboratory and the ID31 beamline ($\lambda = 0.39985$ Å) of the European Synchrotron Radiation Facility. Variable temperature measurements were collected on heating with a temperature scan rate of 0.8 K/min and an x-ray pattern was collected every 3 minutes. Diffraction patterns were fit to crystallographic models using

the EXPGUI/GSAS software program.[67**?**] Crystal structures were visualized using the program VESTA.[**?**] Density measurements of a powder sample of Mn_3O_4 were performed on a MicroMetrics AccuPyc II 1340 pycnometer. A sample cup with a volume of 0.1 cm^3 was filled with Mn_3O_4 powder with a mass of 93.1 mg during the density measurement. Temperature-dependent and field-dependent magnetic measurements were performed using the Quantum Design (QD) MPMS 5XL superconducting quantum interference device (SQUID). Heat capacity measurements were collected using a QD Physical Properties measurement system. Mn_3O_4 pellets for dielectric measurements were spark plasma sintered at 1000 °C under a 6 kN load for 3 minutes. Prior to measuring dielectric properties, the spark plasma sintered pellet was annealed at 1000 °C for 12 hrs, quenched, and characterized by x-ray diffraction to ensure that stoichiometric Mn_3O_4 was retained. Dielectric measurements were performed on a pellet with a diameter of 9.51 mm and a thickness of 2.28 mm whose cylindrical faces were coated by conducting epoxy. Dielectric properties were measured by an Andeen-Hagerling AH2700A capacitance bridge connected to the sample by shielded coaxial cables. The sample was placed in a QD Dynacool Physical Properties measurement system which provides a variable temperature and variable field environment when carrying out dielectric measurements.

6.3 Results and Discussion

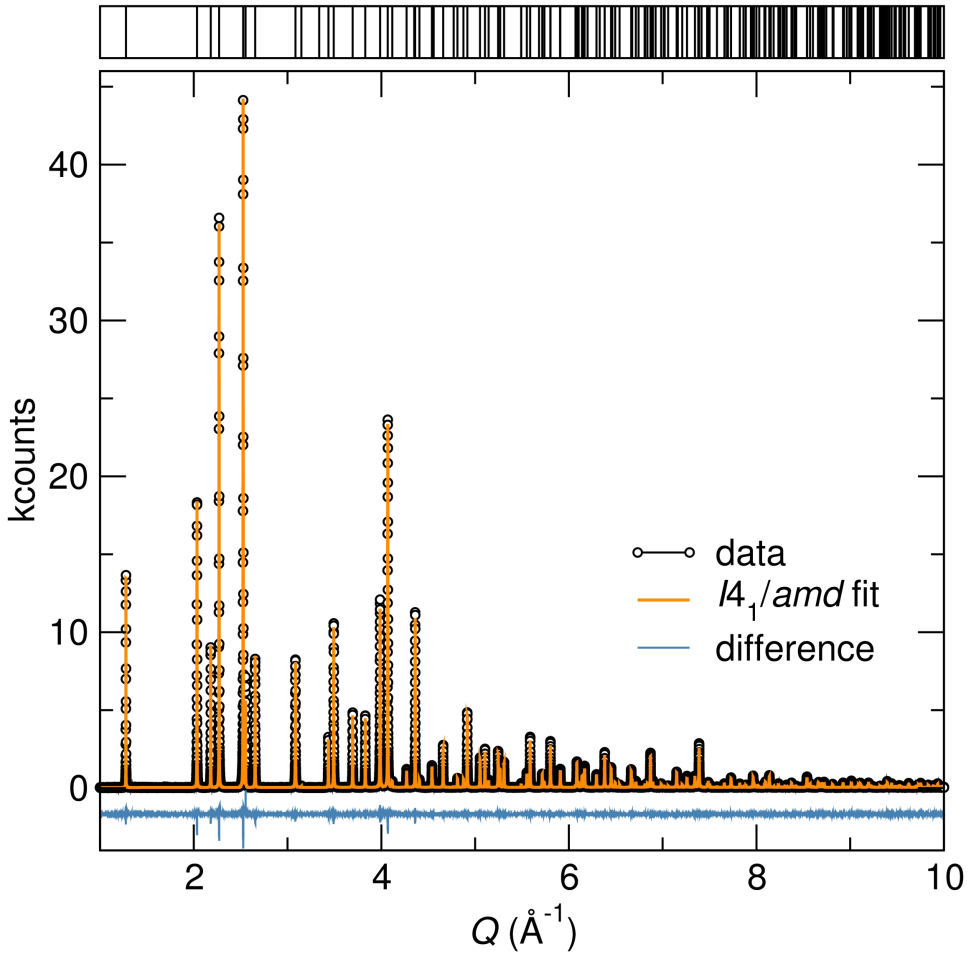

Figure 6.1: The room temperature synchrotron diffraction pattern of Mn_3O_4 modeled to the tetragonal $I4_1/amd$ structure.

At room temperature Mn_3O_4, is a tetragonal spinel in the space group $I4_1/amd$. The synchrotron x-ray diffraction pattern measured at 298 K and modeled to the space group $I4_1/amd$ is illustrated in fig. 6.1. Rietveld refinement of the diffraction pattern yields lattice constants $a = 5.76289(2)$ Å and

$c = 9.46885(1)$ Å with a $c/a\sqrt{2}$ of 1.16 in good agreement with values from the literature.[121, 122] Goodness of fit parameters χ^2, R_{wp}, and R_p of 2.354, 10.23 %, and 8.11 % respectively are obtained from the refinement. Valence bond sums computed using room temperature bond lengths show that Mn_3O_4 is a normal spinel with tetrahedral and octahedral valence states of 2.01 and 3.02 respectively.

A broad transition from a paramagnetic to a ferrimagnetic state, which is characteristic of polycrystalline Mn_3O_4 ,[81] occurs near $T_N = 42$ K. At T_N, a separation between the zero-field cooled and field cooled curves develops and is enhanced with decrease in temperature [fig. 6.2 (a)]. While a single broad magnetic transition is observed in the temperature-dependent susceptibility, the magnetic structure of Mn_3O_4 is extremely rich, featuring a transition to a collinear magnetic structure at 42 K followed by the onset of an incommensurate magnetic spiral at 39 K, and finally a commensurate spiral magnetic state occurs below 33 K.[116, 123] Each of these transitions is observed in heat capacity and capacitance measurements as discussed later in the manuscript. Curie-Weiss fitting in the temperature range $500\,\text{K} < T < 600\,\text{K}$ yields a Θ_{CW} of 663 K in good agreement with prior work [fig. 6.2 (b)].[122, 123] Comparison between the expected Curie-Weiss ordering temperature and T_N results in a significant frustration index of 15.8. This illustrates that frustration may play a role

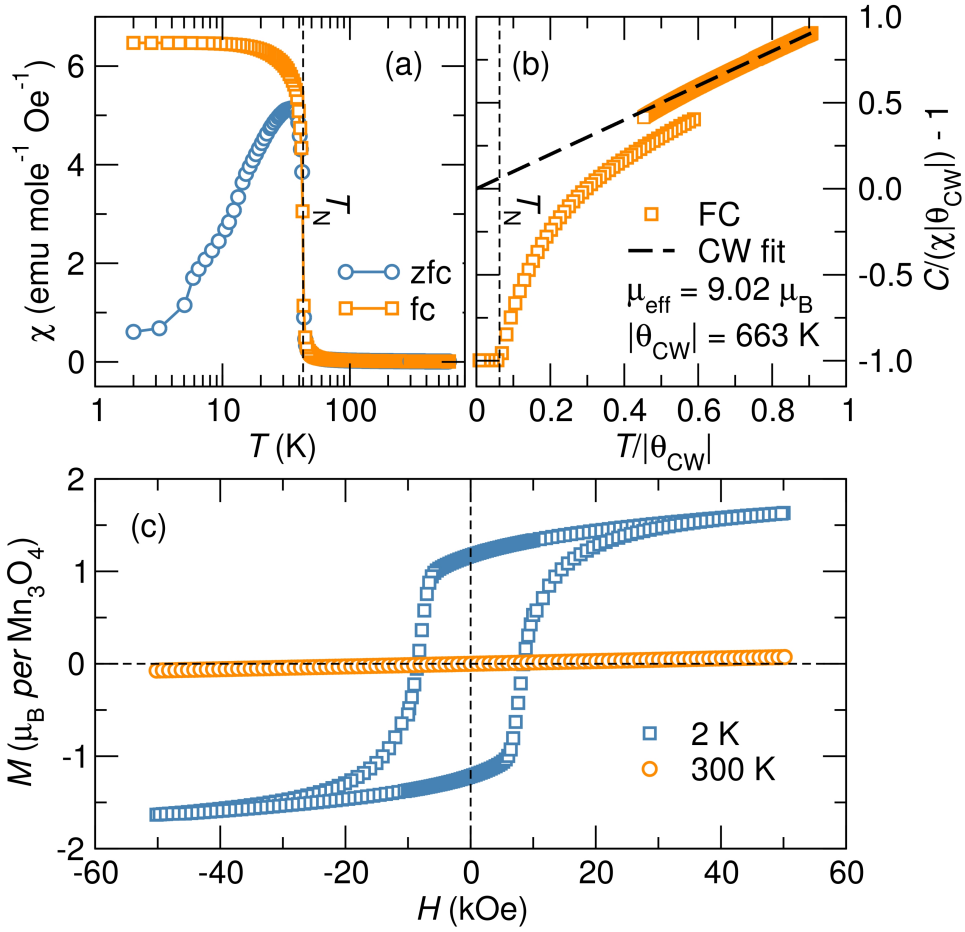

Figure 6.2: (a) Temperature dependent magnetic susceptibility measurements of Mn_3O_4 performed in a 1000 Oe field show a deviation of the zero-field cooled susceptibility from the field cooled susceptibility below the Néel temperature $T_N = 42$ K. (b) Curie-Weiss fitting in the temperature range $500\,\text{K} < T < 600\,\text{K}$ yields an effective moment of $9.02\,\mu_B$ and an expected ordering temperature $|\theta_{CW}| = 663$ K. High-temperature and low-temperature susceptibility measurements were conducted on different instruments and instrumental variations yield the slight offset between the low-temperature and high-temperature susceptibility that is negligible in plot (a) but emphasized in the $1/\chi$ scaling of plot (b). (c) Field-dependent magnetization shows paramagnetic behavior above the Néel temperature of Mn_3O_4 and ferrimagnetic behavior below T_N with a saturation magnetization of $1.63\,\mu_B$ and a coercive field of 8.5 kOe when $H =$ 50 kOe and $T = 2$ K.

in the magnetism of Mn_3O_4. The Curie-Weiss fit also yields an effective moment of 9.02 μ_B which is congruent with the expected effective moment of 9.11 μ_B computed from the spin-only effective moments of Mn^{2+} and Mn^{3+} which are 5.92 μ_B and 4.9 μ_B respectively. Short-range correlations cause deviations of the inverse susceptibility from the Curie-Weiss model above the Néel temperature as illustrated in fig.6.2 (b).

The weak linear increase in magnetization with field in the paramagnetic phase evolves to a hysteretic magnetization in ferrimagnetic Mn_3O_4 [fig. 6.2 (c)]. A saturation magnetization of 1.63 μ_B and a coercive field of 8.5 kOe are measured at 50 kOe and 2 K. A collinear ferrimagnetic state in Mn_3O_4 would yield a saturation magnetization of 3 μ_B/formula unit, however, the measured saturation moment of 1.63 μ_B is consistent with the reported spiral magnetic structure of Mn_3O_4 near 2 K.[116] Mn_3O_4 exhibits significant anisotropy with an easy axis along the (001) direction, which yields a spontaneous magnetization of 1.85 μ_B in single crystalline samples.[124] However, a slightly decreased value of the spontaneous magnetization is expected in polycrystalline materials due to the random alignment of Mn_3O_4 grains.[81, 124]

Spin ordering in Mn_3O_4 leads to changes in entropy that are illustrated in fig. 7.6. Variations in magnetic structure give rise to distinct heat capacity anomalies at 42.5 K, 40 K, and 34.5 K under zero-field conditions. The largest change in en-

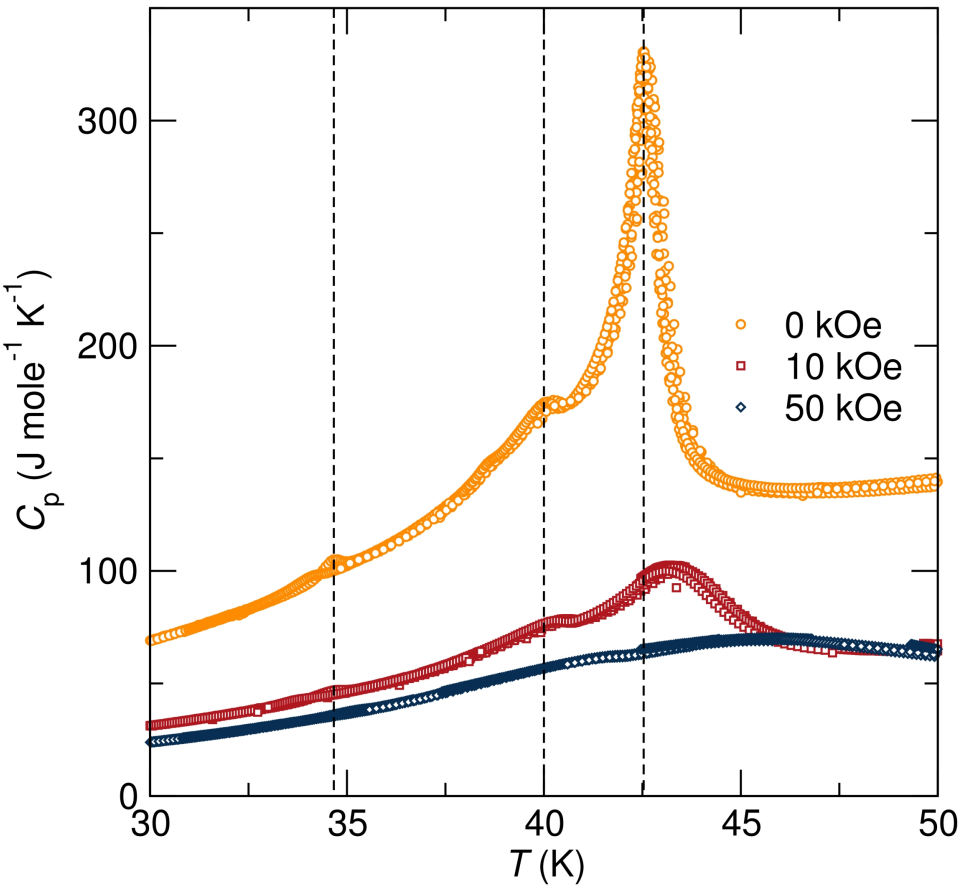

Figure 6.3: Heat capacity measurements of Mn_3O_4 show three anomalies associated with changes in magnetic structure at 42.5 K, 40 K, and 34.5 K. These transitions are evident under zero field conditions but they become suppressed and shifted to higher temperatures in the presence of a magnetic field.

tropy occurs at 42 K where the highest heat capacity peak is observed. Entropy changes in Mn_3O_4 depend on the applied magnetic field, with large fields suppressing the heat capacity transitions. At 10 kOe field, heat capacity peaks are broad but still visible at the transition temperatures and the 42.5 K peak shifts to a higher temperature, $T_N =$ 43.2 K. Pronounced suppression of the heat capacity transitions is evident at 50 kOe. The trend in the field-dependent heat capacity reported here, namely, the suppression of heat capacity anomalies and the shift to higher temperatures is in agreement with the work of Kim $et\,al.$, which reports an increase in T_N in the presence of a field and complete suppression of the onset of magnetic order when a magnetic field is applied along certain crystallographic directions.[118, 119]

Mn_3O_4 is a known magnetodielectric.[81, 117] Figure 6.4 (a) shows anomalies in the dielectric constant occurring in close proximity to spin ordering transition temperatures at 45 K, 39 K, and 36 K. The dielectric constant shows no frequency dependence and this illustrates the intrinsic nature of magnetodielectric coupling in the studied Mn_3O_4 sample. A frequency dependent dielectric constant would indicate that magnetoresistive effects are contributing to magnetodielectric coupling. We also note the presence of dielectric anomalies above 45 K[fig 6.4 (a)], which could be linked to short-range spin correlations in the temperature range $T_N < T < |\Theta_{CW}|$. The origin of the dielectric changes above

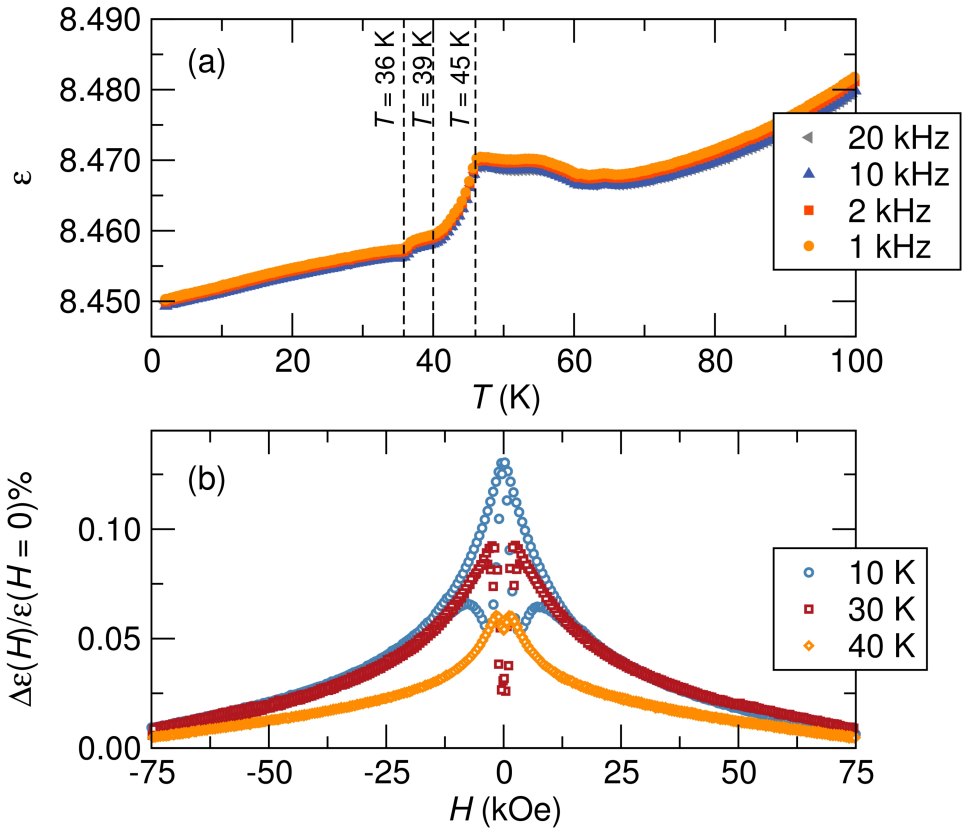

Figure 6.4: Magnetodielectric coupling in Mn_3O_4. (a) The dielectric constant as a function of temperature shows three anomalies at 36 K, 39 K, and 45 K which are in close proximity to spin ordering transitions. (b) A magnetic field can modulate the dielectric constant below T_N. The changes in the dielectric constant in the presence of a magnetic field increase with decrease in temperature.

T_N should be further investigated. The dielectric constant exhibits strong field dependence below T_N [fig.6.4 (b)]. The field dependence of the dielectric constant increases with decrease in temperature.

The onset of long-range magnetic order in Mn_3O_4 occurs concurrently with a structural distortion. Figure 6.5 (a) and (b) show spin and entropy changes occurring concurrently near 42 K. Figure 6.5 (c) also shows x-ray diffraction evidence of structural changes in Mn_3O_4 occurring simultaneously near 42 K. A splitting of the tetragonal $I4_1/amd$ (321) reflection to several peaks below 42 K is clearly demonstrated by variable-temperature high-resolution synchrotron x-ray diffraction [Fig. 6.5 (c)]. The emergence of new diffraction peaks below 42 K indicates an average structure distortion. This study of polycrystalline Mn_3O_4 shows that the magnetostructural distortion occurs near 42 K [fig. 6.5 (c)] while earlier studies of single crystal Mn_3O_4 have reported a 33 K magnetostructural distortion under zero-field conditions and a 39 K spin-drive structural transition in the presence of an applied magnetic field.[118, 119] The difference in the transition temperature is attributed to varying strain effects in polycrystalline versus single crystal samples; large strains in single crystal samples could suppress the onset of the structural transition. In addition, the cooling and heating rates of the sample during a structural study are also expected to influence the structural distortion temperature.

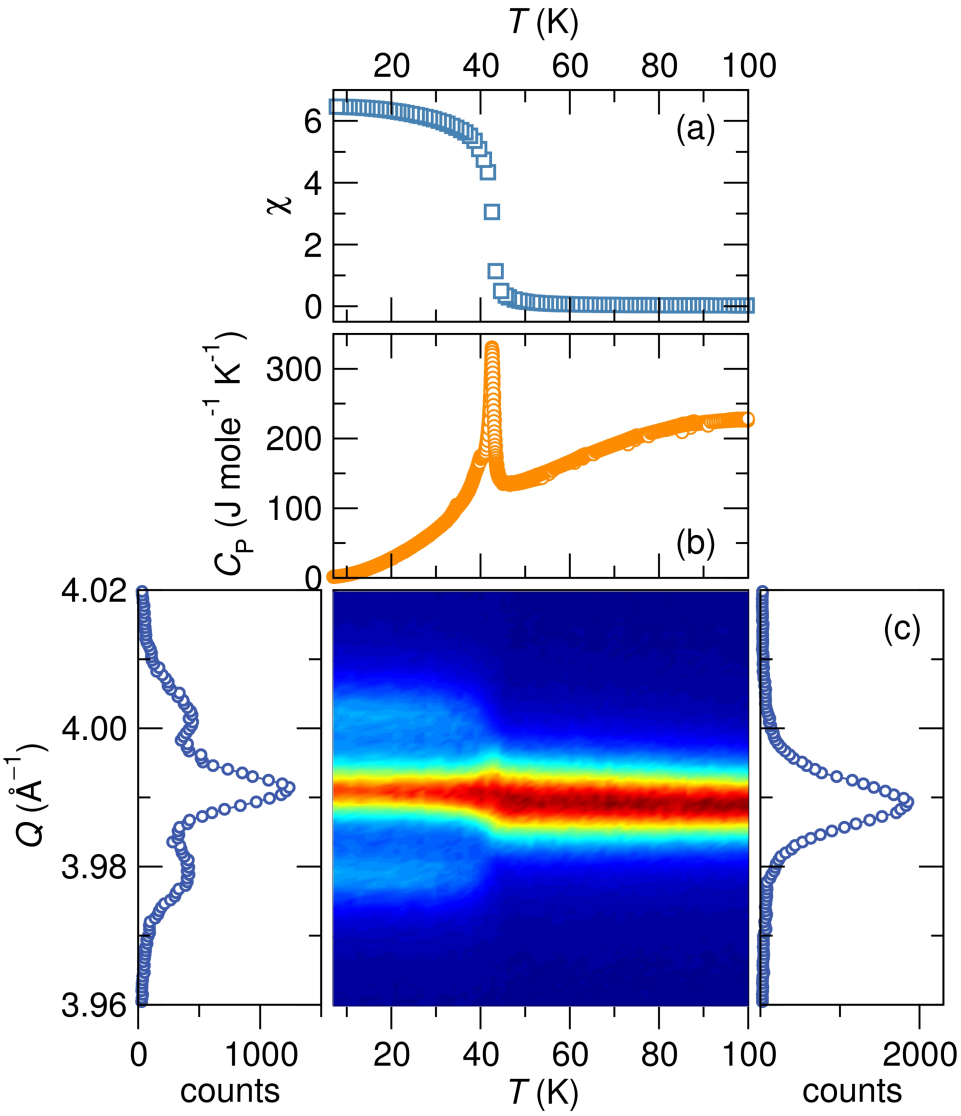

Figure 6.5: Concurrent magnetic and structural ordering in Mn_3O_4. (a) Field-cooled magnetic susceptibility in units of emu mole^{-1} Oe^{-1} and (b) zero-field cooled heat capacity measurements show the onset of long-range ferrimagnetic order in Mn_3O_4 near 42 K. (c) A structural distortion occurs concomitantly with the onset of ferrimagnetic order in Mn_3O_4 at 42 K where variable-temperature high-resolution synchrotron x-ray diffraction shows a splitting of the high temperature tetragonal (321) reflection. While there is a decrease in intensity of the tetragonal (321) reflection in the low temperature phase, we note that it coexists with the emergent peaks to the lowest temperatures studied.

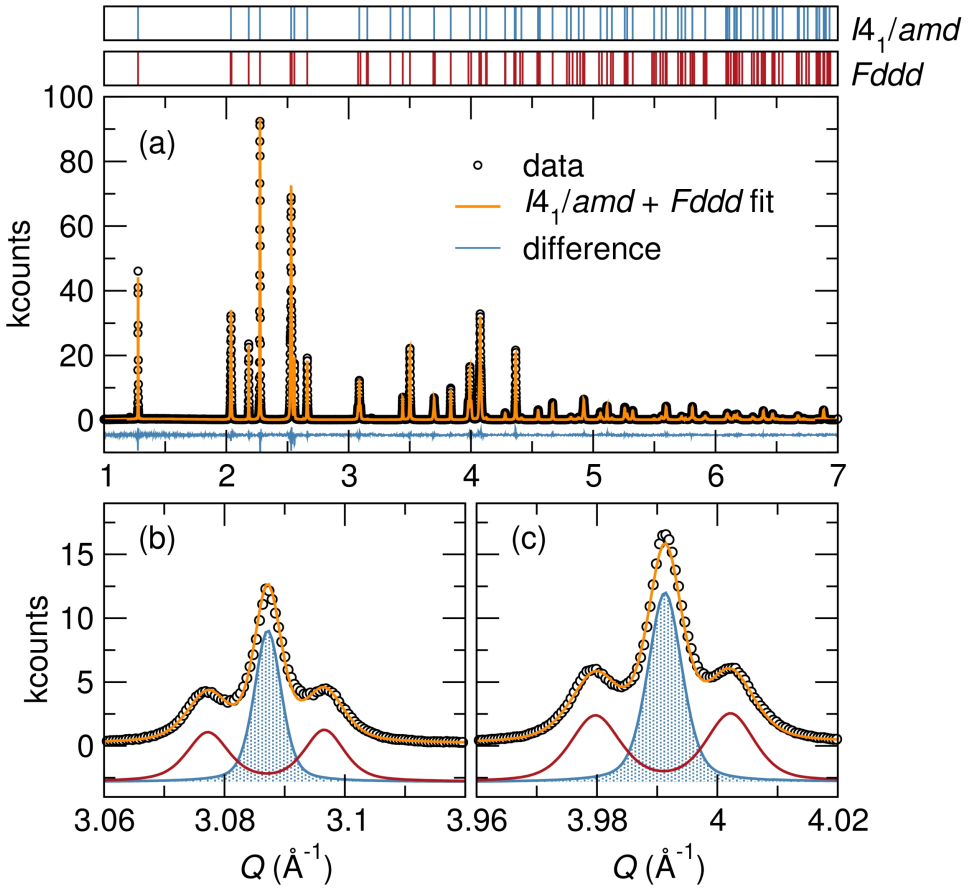

Figure 6.6: (a) The 8.2 K synchrotron x-ray diffraction pattern of Mn_3O_4 modeled to a structure of coexisting tetragonal $I4_1/amd$ and orthorhombic $Fddd$ structures. (b) The tetragonal $I4_1/amd$ (220) reflection splits into three reflections consisting of the tetragonal reflection and the orthorhombic $Fddd$ reflections (040) and (400). (c) In a similar way, tetragonal (321) reflection splits giving rise to the orthorhombic $Fddd$ (511) and (151) reflections.

Table 6.1: Structural parameters of Mn_3O_4 at 8.2 K. Mn_3O_4 is described by coexisting tetragonal $I4_1/amd$ and orthorhombic *Fddd* phases.

Coexisting $I4_1/amd$ and *Fddd* phases in Mn_3O_4	
Temperature (K)	8.2
Space group	$I4_1/amd$
Setting	origin 2
Z	4
a(Å)	5.75638(1)
c(Å)	9.44393(4)
Vol/(Å^3)	312.934(1)
Mn^{2+}	$4a$ (0, 1/4, 7/8)
Mn^{3+}	$8d$ (0, 1/2, 1/2)
O	$16h$ $(0, y, z)$
	y 0.47153(21)
	z 0.25952(20)
Mn^{2+} U_{iso} (10^{-2} Å^2)	1.406(17)
Mn^{3+} U_{iso} (10^{-2} Å^2)	1.379(14)
O U_{iso} (10^{-2} Å^2)	1.509(31)
Wt. frac.	0.44(6)
Space group	*Fddd*
Setting	origin 2
Z	8
a(Å)	8.11602(5)
b(Å)	8.16717(5)
c(Å)	9.44209(5)
Vol/(Å^3)	625.869(4)
Mn^{2+}	$8a$ (1/8, 1/8, 1/8)
Mn^{3+}	$16d$ (1/2, 1/2, 1/2)
O	$32h$ (x, y, z)
	x 0.48709(16)
	y 0.48690(16)
	z 0.25853(21)
Mn^{2+} U_{iso} (10^{-2} Å^2)	1.251(19)
Mn^{3+} U_{iso} (10^{-2} Å^2)	1.208(15)
O U_{iso} (10^{-2} Å^2)	1.454(33)
Wt. frac.	0.56(6)
χ^2	3.206
R_p(%)	5.46
R_{wp}(%)	6.82

The precise structural description of Mn_3O_4 in the ferrimagnetic state is so far unknown. We find that Mn_3O_4 undergoes a phase transformation from tetragonal $I4_1/amd$ symmetry to a phase coexistence regime consisting of both tetragonal $I4_1/amd$ and orthorhombic $Fddd$ phases. Figure 6.6 (a) shows the 8.2 K diffraction pattern of Mn_3O_4 modeled by tetragonal $I4_1/amd$ and orthorhombic $Fddd$ phases. Structural parameters and goodness of fit parameters obtained from Rietveld refinement are tabulated in Table 6.1. Small goodness of fit parameters along with the agreement between the model and the data illustrates that coexisting tetragonal and orthorhombic phases characterize ferrimagnetic Mn_3O_4. No single phase low symmetry solution could be obtained to model the low temperature structure of Mn_3O_4. A closer look at some of the diffraction reflections that split below the Néel temperature is presented in Fig. 6.6 (b) where the tetragonal (220) reflection coexists with orthorhombic (040) and (400) reflections. Similarly, fig. 6.6 (c) shows the coexistence of the tetragonal (321) and the orthorhombic (511) and (151) reflections. The orthorhombic $Fddd$ space group is a subgroup of the tetragonal space group $I4_1/amd$, and it has been shown to describe structural ground states of the Jahn-Teller active spinels $NiCr_2O_4$ and $CuCr_2O_4$.[14] Magnetostructural phase transitions leading to complex structural ground states are an emerging theme in magnetic spinels; a recent report from our group shows structural phase coexistence in $MgCr_2O_4$

and $ZnCr_2O_4$.[1]

The low-temperature structures coexist with nearly equal fractions below T_N. Weight fractions of 50.4 % and 49.6 % for the $I4_1/amd$ and $Fddd$ phases respectively are measured near T_N. With decrease in temperature below T_N, the orthorhombic phase fraction increases slightly attaining a maximum value of 56 % near 8 K. Scherrer analysis reveals that large crystallite sizes with dimensions $> 10\mu m$ are observed in the high temperature and low temperature tetragonal phases while smaller domain sizes of about 690 nm characterize the orthorhombic phase. The simple Scherrer model of crystallite size analysis neglects instrumental broadening, therefore, the sizes obtained are the minimum values.

At the magnetostructural ordering temperature of Mn_3O_4, orthorhombic $Fddd$ lattice constants emerge and coexist with tetragonal $I4_1/amd$ lattice constants (Fig. 6.7). The orthorhombic a and b lattice constants derive from the tetragonal a lattice parameter. A ≈ 0.3 % compression of the orthorhombic a axis and a ≈ 0.33 % elongation of the orthorhombic b axis relative to the tetragonal a lattice constant are measured [Fig. 6.7 (a)]. The continuous decrease of the tetragonal c axis that occurs above 42 K, is disrupted at T_N where the orthorhombic c axis emerges with values ≈ 0.02 % smaller relative to the tetragonal c axis [Fig. 6.7 (b)]. The temperature-dependence of the unit cell volume

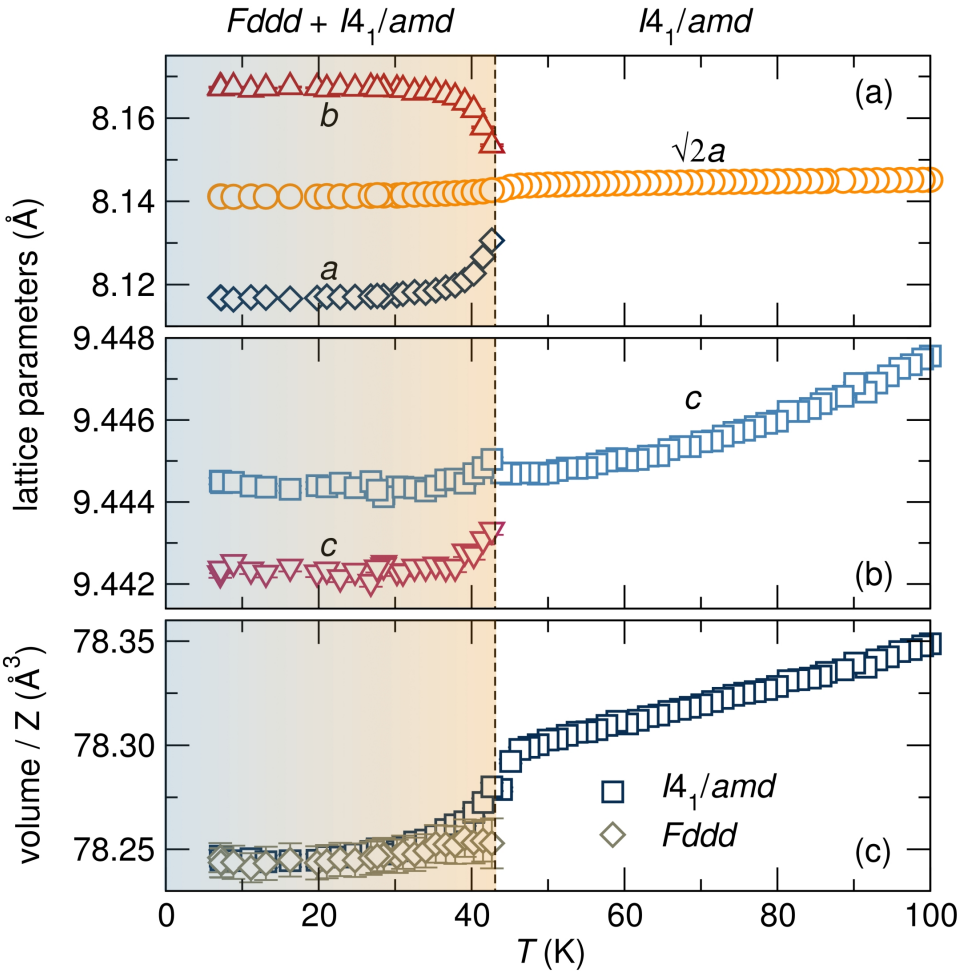

Figure 6.7: Temperature-dependence of the structural parameters of Mn_3O_4. (a) Variation of the tetragonal a lattice constant of Mn_3O_4 with temperature shows the emergence of a compressed orthorhombic a lattice constant and an elongated orthorhombic b lattice constants below 42 K. (b) The tetragonal c lattice constant decreases with temperature to 42 K, below which the orthorhombic c lattice constant, which has a decreased value, emerges. (c) A linear decrease in the unit cell volume is observed above 42 K. At 42 K, a discontinuous decrease in cell volume is observed in both the tetragonal $I4_1/amd$ and orthorhombic $Fddd$ phases.

shows a discontinuous decrease below 42 K [Fig. 6.7 (c)]. In the Ehrenfest classification of phase transitions, first order phase transitions are characterized by a discontinuous change in the first derivative of the free energy. The discontinuous change in the cell volume of Mn_3O_4 and coexistence of two low-temperature structures suggests that this is a first order phase transition. The structural distortion of Mn_3O_4, b_{orth}/a_{tet} =1.003, is of the same order as those of other spin driven lattice distortions observed in the related spinel compounds $NiCr_2O_4$,[14] $CuCr_2O_4$,[14] $ZnCr_2O_4$,[1] and $MgCr_2O_4$.[1]

The complete crystallographic description of Mn_3O_4 enables detailed investigation of polyhedral distortions that occur following the structural distortion. The elongated MnO_6 polyhedral units of tetragonal Mn_3O_4 above T_N are described by an apical bond length of 2.275(9) Å, which is twofold degenerate and an equatorial bond length of 1.93(3) Å that is fourfold degenerate [Fig. 6.8 (a) and (b)]. Below the structural transition temperature, the apical bond length remains fairly temperature independent with small variations around the 2.275(5) Å value in both the tetragonal and orthorhombic phases[Fig. 6.8 (a)]. On the other hand, below T_N, the equatorial bond length of the tetragonal phase decreases to a length of about 1.92(5) Å while retaining its fourfold degeneracy. The equatorial Mn-O bond length of MnO_6 octahedra exhibits distortions in the orthorhombic phase that yield two Mn-O bond lengths that are about

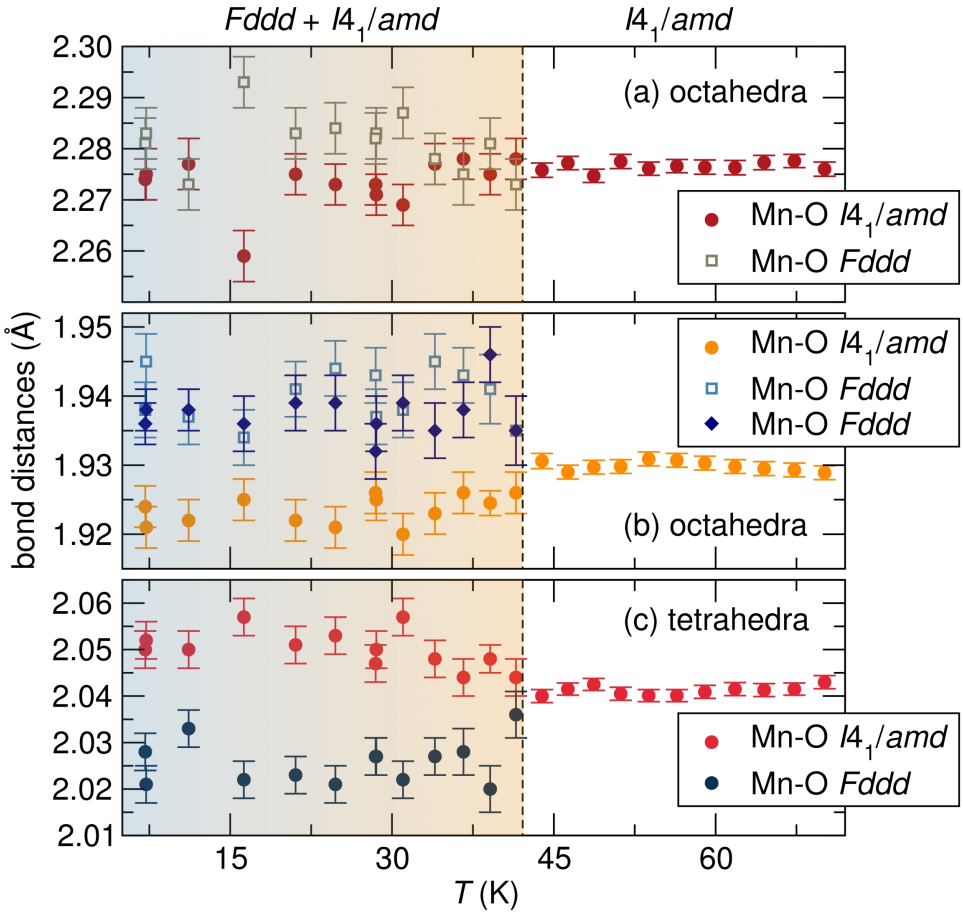

Figure 6.8: Polyhedra distortions of Mn_3O_4. (a) The axial Mn-O bond length of the MnO_6 octahedra shows relative temperature independence across the structural phase transition in both the tetragonal and orthorhombic phases. (b) The equatorial Mn-O bond length of MnO_6 octahedra in the high temperature tetragonal phase has a value of about 1.93 Å. Below the structural phase transition, this equatorial bond length is compressed in the tetragonal phase and has a value of $\approx$1.92 Å. In the orthorhombic phase, this bond length is distorted giving rise to two different equatorial bonds with lengths of about 1.94 Å. (c) Below T_N, the Mn-O bond length of the MnO_4 polyhedra increases in length in the tetragonal phase while its length decreases in the orthorhombic phase.

Table 6.2: Pseudo-Voigt with Finger-Cox-Jephcoat asymmetry(GSAS profile 3) profile microstrain terms of the various phases of Mn_3O_4 obtained from Rietveld refinement. HT denotes high temperature while LT denotes low temperature. The magnitude of the microstrain terms of the low temperature tetragonal phase are larger than those of the other phases of Mn_3O_4. These strain tensors have been plotted in an ellipsoidal representation in Fig 6.9.

Microstrain term	HT $I4_1/amd$	LT $I4_1/amd$	LT $Fddd$
L11	0.1071	-0.0257	0.1666
L22	0.159	-0.3624	0.1975
L33	0.0743	0.1071	0.0837
L12	0.1093	0.3676	-0.0481
L13	-0.0151	-0.0392	-0.0127
L23	-0.0218	-0.02115	-0.0350

1.935(5) Å long, each with twofold degeneracy [Fig. 6.8 (b)]. The high temperature tetragonal phase has a tetrahedral Mn-O bond length of 2.04 Å, this bond length increases to ≈ 2.05(3) Å in the low temperature tetragonal phase while it decreases in the orthorhombic phase to ≈ 2.025(4) Å [Fig. 6.8 (c)]. The distortions of the polyhedra in each of the low temperature structures are complementary, for instance examining the low temperature orthorhombic phase: the elongation of the equatorial bond lengths of MnO_6 octahedra are compensated by the decrease in Mn-O bond lengths of the MnO_4 tetrahedra.

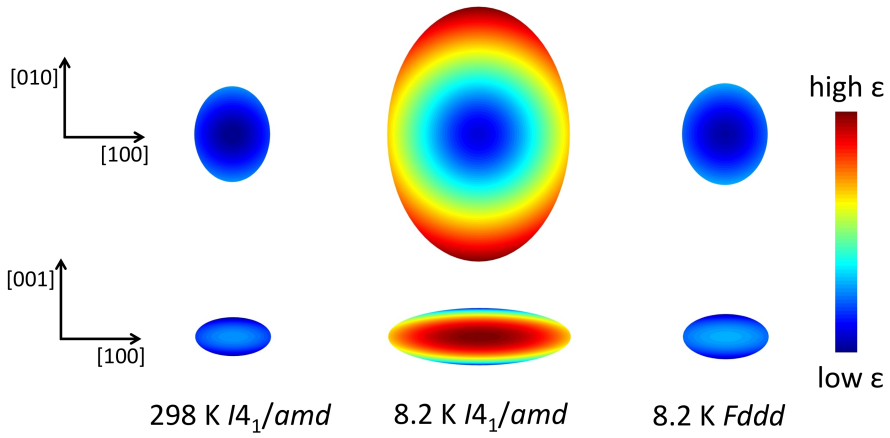

Figure 6.9: Ellipsoid representation of the second rank strain tensor of Mn_3O_4 in the various phases as determined by Rietveld refinement using the Pseudo-Voigt with Finger-Cox-Jephcoat asymmetry(GSAS profile 3) profile function. In addition to the color scale, the size of the ellipsoid scales with the magnitude of the strain. In all the phases of Mn_3O_4 , large strains are observed in the [110] plane compared to the [001] direction. The low temperature tetragonal $I4_1/amd$ phase is highly strained compared to the high temperature tetragonal phase and low temperature orthorhombic phase. The high temperature $I4_1/amd$ phase shows the lowest strains of the three phases of Mn_3O_4.

High resolution synchrotron x-ray diffraction has emerged as an important tool for characterizing the low temperature structures of magnetic materials.[1, 14, 113] However, it has been shown that chemical inhomogeneity that is present at all times, but cannot be easily detected by high resolution x-ray diffraction above the phase transition temperature, can lead to structural phase coexistence below a structural phase transition temperature.[113] In this light, we have refined the elemental occupancies of all atoms in the low temperature tetragonal and orthorhombic phases. All elements remain stoichiometric within error. The highest vacancy concentration of 1.33 $\%$ is obtained for Mn^{3+} cations in the orthorhombic phase. Nevertheless, this small vacancy concentration cannot account for $>50\,\%$ orthorhombic phase content observed below T_N. We have performed high-precision density measurements of the Mn_3O_4 sample to further investigate the stoichiometry of this material. Density measurements of the powder sample at room temperature give a density of 4.855(9) g/cm^3 which compares well with the expected density of 4.86 g/cm^3 confirming that off-stoichiometric effects are not influencing the structural phase transition of this sample.

Structural phase coexistence in Mn_3O_4 is linked to large strains at the phase transition temperature due to the lattice mismatch between the low temperature orthorhombic phase and the high temperature tetragonal phase. Figure.

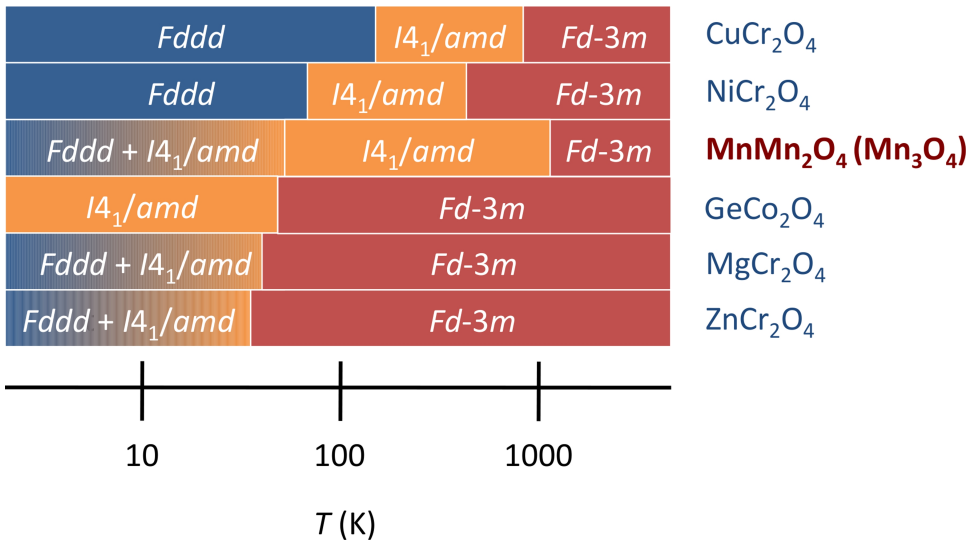

Figure 6.10: Structural distortions in spinels due to Jahn-Teller ordering and magnetostructural coupling effects. While in many instances full structural transformations occur. Phase coexistence is observed for $MgCr_2O_4$, $ZnCr_2O_4$, and Mn_3O_4. Notably phase coexistence is prevalent when structural phase transitions occur below 50 K.

6.7 shows that the orthorhombic a and b lattice constants vary by 0.3 % from those of both the high temperature and low temperature tetragonal phases. The c axis varies slightly, by 0.02 % between the $Fddd$ and $I4_1/amd$ phases. The map of the strain tensor shows a highly strained low temperature tetragonal phase (Fig. 6.9). Most of the strain is along the crystallographic a and b axes where the largest lattice mismatch between the low temperature tetragonal and orthorhombic phases is observed. The orthorhombic $Fddd$ phase also experiences slightly higher strain compared to the high temperature tetragonal phase. It is important to note the significantly smaller strain along the [001] direction,

this finding agrees well with the fairly invariant c lattice constants of the high temperature and low temperature phases. Evidence of strain stabilized structural phase coexistence in Mn_3O_4 is corroborated by the work of Suzuki and Katsufuji, who have performed strain measurements on single crystals of Mn_3O_4 observing changes in the temperature dependent strain ($\Delta L/L$) at the magnetic ordering temperatures. [117] Suzuki and Katsufuji also show larger strain effects along the [110] plane of Mn_3O_4 compared to the [001] direction.[117]

Evidence of coexisting tetragonal and orthorhombic phases is in agreement with prior studies of the hausmanite Mn_3O_4. Chung $et\,al.$ reported orthorhombic instabilities in a single crystal of Mn_3O_4 after observing subtle diffraction peak asymmetry.[120] The study by Chung $et\,al.$ essentially indicates the present of coexisting phases in Mn_3O_4 below T_N, with the tetragonal phase yielding dominant peaks and the orthorhombic phase contributing to mere peak asymmetry. Considering the work of Chung and coworkers, it is clear that large strains in a single crystal can inhibit the formation of a large phase fraction of the low temperature orthorhombic phase. The polycrystalline sample examined here along with the use of high-resolution synchrotron x-ray diffraction allows us to fully resolve the diffraction reflections of the orthorhombic $Fddd$ phase and to complete a detailed study of the structural changes taking place at low temperatures.

The structural phase transformation of Mn_3O_4 bears some of the hallmark characteristics of a martensitic phase transformation. We observe the nucleation of an orthorhombic $Fddd$ phase within the matrix of the parent $I4_1/amd$ phase. Strain energy inhibits the complete structural transformation of Mn_3O_4 to the orthorhombic phase, stabilizing a mixed phase structure. Comparable strain-mediated structural phase coexistence is reported in the manganites $Bi_{0.2}Ca_{0.8}MnO_3$ and $La_{0.275}Pr_{0.35}Ca_{0.375}MnO_3$.[125] However, it must be noted that the perovskites are usually on the verge of being metals and the inhomogeneities are frequently the result of very slightly differing levels of chemical doping, but this is not the case in Mn_3O_4 because it is stoichiometric and insulating. Examination of hysteresis effects of the structural phase transition of Mn_3O_4 are inconclusive due to slow heating and cooling rates applied during variable temperature x-ray measurements. A comparison of the magnetostructural phase transformation of Mn_3O_4 to spin-driven lattice deformations of other magnetic spinels suggests that phase coexistence likely occurs when structural deformations occur at low temperatures ($T < 50\,\mathrm{K}$) (Fig. 6.10). However, the spinel $GeCo_2O_4$ shows a full transformation from cubic to tetragonal symmetry near 22 K indicating that low temperatures do not necessarily limit full structural transformations in all spinels and perhaps the particular strains involved in the lattice deformation play a larger role in stabilizing phase coexistence.

These results call for a re-examination of the properties of Mn_3O_4 at low temperatures. For example, how do we understand spin ordering in the various low temperature phases? Further, it is important to resolve the magnetic structure of Mn_3O_4 taking into account structural phase coexistence in the ferrimagnetic phase. Since strain influences phase coexistence, it presents a new approach to controlling the magnetostructural phase transition of Mn_3O_4 to achieve a desired low temperature structure.

6.4 Conclusions

High resolution synchrotron x-ray diffraction reveals the coexistence of tetragonal $I4_1/amd$ and orthorhombic $Fddd$ below the Néel temperature of the magnetodielectric spinel Mn_3O_4. The two low temperature phases coexist in nearly equal fractions. A complete crystallographic description of Mn_3O_4 in the ferrimagnetic state is presented. Polyhedral distortions in the ferrimagnetic phase of Mn_3O_4 are described. We show that strains due to the lattice mismatch between the orthorhombic phase, which is nucleated below 42 K, and the high temperature tetragonal $I4_1/amd$ phase likely contribute to the observed phase coexistence. We propose strain as a new approach to control the properties of

Mn_3O_4 below the magnetic ordering temperature.

Chapter 7

Evolution of magnetic properties in the normal spinel solid solution $Mg_{1-x}Cu_xCr_2O_4$

We examine the evolution of magnetic properties in the normal spinel oxides $Mg_{1-x}Cu_xCr_2O_4$ using magnetization and heat capacity measurements. The end-member compounds of the solid solution series have been studied in some detail because of their very interesting magnetic behavior. $MgCr_2O_4$ is a highly

[1]The contents of this chapter have substantially appeared in reference [36]: M. C. Kemei, S. L. Moffitt, D. P. Shoemaker, and R. Seshadri, Evolution of magnetic properties in the normal spinel solid solution $Mg_{1-x}Cu_xCr_2O_4$ *J. Phys.: Condens. Matter* **24** 0460031 (2012)

frustrated system that undergoes a first order structural transition at its antiferromagnetic ordering temperature. $CuCr_2O_4$ is tetragonal at room temperature as a result of Jahn-Teller active tetrahedral Cu^{2+} and undergoes a magnetic transition at 135 K. Substitution of magnetic cations for diamagnetic Mg^{2+} on the tetrahedral *A* site in the compositional series $Mg_{1-x}Cu_xCr_2O_4$ dramatically affects magnetic behavior. In the composition range $0 \leq x \leq \approx 0.3$, the compounds are antiferromagnetic. A sharp peak observed at 12.5 K in the heat capacity of $MgCr_2O_4$ corresponding to a magnetically driven first order structural transition is suppressed even for small x. Uncompensated magnetism – with open magnetization loops – develops for samples in the x range $\approx 0.43 \leq x \leq 1$. Multiple magnetic ordering temperatures and large coercive fields emerge in the intermediate composition range $0.43 \leq x \leq 0.47$. The Néel temperature increases with increasing x across the series while the value of the Curie-Weiss Θ_{CW} decreases. A magnetic temperature-composition phase diagram of the solid solution series is presented.

7.1 Introduction

Materials with the spinel structure display a wide range of functional properties and are applied as battery electrodes [126], multiferroic materials[4, 127],

and catalytic materials.[128] In addition, spinels offer unique opportunities for the exploration of exotic magnetic phenomena.[32, 87, 129] A rich diversity of possible magnetic ground states can be found in materials with the spinel structure. These range from long range ordered ferrimagnetic states, observed in magnetite Fe_3O_4, to degenerate spin liquid states seen in systems with geometrically frustrated interactions such as $ZnCr_2O_4$.[8] In spinels with the general formula AB_2O_4, cation *A* and *B* sites can both be occupied by magnetic ions. Coupling between the various magnetic ions gives rise to a number of competing exchange pathways and a multitude of possible ground states. Additional complexity arises when antiferromagnetically coupled cations populate the pyrochlore *B* sublattice in spinels. In this configuration, geometric constraints preclude the realization of a unique ground state resulting in frustrated systems. Slight perturbations of highly degenerate spin liquid states in frustrated magnets can result in a range of novel behavior.[20, 130]

Strongly frustrated three-dimensional pyrochlore *B* sublattices occur in oxide spinels with a non-magnetic *A* site and a chromium *B* site. Cr^{3+} with a $[Ar]3d^3$ electron configuration shows a preference for the octahedral site where crystal field splitting stabilizes a half filled t_{2g} level separated in energy from an empty e_g level.[39, 131] Antiferromagnetic nearest neighbour (NN) interactions between Cr^{3+} ions populating the pyrochlore *B* sublattice cannot be fully satis-

fied. Pyrochlore sublattices with antiferromagnetically coupled spins have been shown to result in frustrated Heisenberg spin Hamiltonian expressions where NN interactions alone would not result in a single low energy state even at T = 0 K.[26, 31, 83, 132] Given the strongly frustrated Cr^{3+} sublattice, the choice of *A* site cation can profoundly affect magnetic properties in chromium oxide spinels.

Magnetic ground states depend strongly on the *A* cation in ACr_2O_4 spinels. Non-magnetic *A* site (for instance *A* = Zn, Mg, Cd) chromium oxide spinels are highly frustrated.[47] Spin-lattice coupling resolves the large ground state degeneracy by selecting a unique ordered state *via* a spin Jahn-Teller effect at the magnetic ordering temperature.[83] In magnetic *A* site spinels (for instance *A* = Co, Fe, Cu, Mn), *A*-O-Cr coupling dominates over frustrated Cr-Cr interactions and non-collinear ferrimagnetic ground states are attained.[4, 50, 61, 64, 133, 134] Understanding changes in interactions due to gradual addition of magnetic ions on the *A* site of frustrated ACr_2O_4 spinels is important. In this study, we investigate the magnetic properties of the solid solution $Mg_{1-x}Cu_xCr_2O_4$ where the end members $MgCr_2O_4$ and $CuCr_2O_4$ differ both structurally and magnetically.

The canonical geometrically frustrated spinel $MgCr_2O_4$ crystallizes in the cubic space group $Fd\bar{3}m$ at 300 K. The pyrochlore Cr^{3+} sublattice is based on a

triangular motif where antiferromagnetic NN Cr-Cr coupling is geometrically frustrated. As a result, the spins in $MgCr_2O_4$ remain disordered far below the theoretical ordering temperature ($\Theta_{CW} \approx -400\,\mathrm{K}$).[29, 135] A structural distortion lifts the spin state degeneracy of the pyrochlore Cr^{3+} sublattice at the Néel temperature (T_N) $\approx$ 12.5 K. The tetragonal space group $I4_1/amd$ has been suggested as the low symmetry crystallographic structure.[28, 86] A sharp peak in heat capacity coincident with the magnetically driven structural transition in $MgCr_2O_4$ denotes the first-order nature of this transition.[89]

The spinel $CuCr_2O_4$ is cubic above 873 K,[58, 136] with Cu^{2+} occupying tetrahedral sites and Cr^{3+} populating octahedral sites. In the cubic phase, tetrahedral crystal field splitting of the d^9 Cu^{2+} energy level results in triply degenerate high lying t_2 subshells and fully occupied low energy e_g subshells.[59] Distortion of the CuO_4 tetrahedra lifts the orbital degeneracy of the t_2 level, and when these distortions are coherent, the symmetry of $CuCr_2O_4$ is lowered from cubic $Fd\bar{3}m$ to tetragonal $I4_1/amd$.[62] Magnetic studies of $CuCr_2O_4$ show that it is ferrimagnetic at 135 K. The magnetic structure in the ordered state is triangular with Cr^{3+} in the 001 planes aligned parallel but at an angle to Cr^{3+} in adjacent planes. Cu^{2+} align antiparallel to the net moment of the Cr^{3+} sublattices forming a magnetic structure comprising triangles of spins.[61]

Previous work has investigated the local and average structural changes in

the series $Mg_{1-x}Cu_xCr_2O_4$.[93] These studies show that although local distortions occur for all Cu^{2+} substituted compositions, cooperative structural changes are dependent on x and on temperature. For example, at room temperature, compounds of the series $Mg_{1-x}Cu_xCr_2O_4$ remain cubic on average for $x < 0.43$. Tetragonal average symmetry driven by cooperative Cu^{2+} Jahn-Teller distortions appears in compositions with $x > 0.43$ at 300 K.

We study the effect of introducing magnetic, Jahn-Teller active Cu^{2+} on the non-magnetic *A* site of $MgCr_2O_4$ on magnetic frustration and on the nature of magnetic interactions. A previous study of the system $Zn_{1-x}Co_xCr_2O_4$ showed that addition of Co^{2+} on the non-magnetic Zn^{2+} site quenched frustration across the series.[37] Here, we explore changes in magnetic behavior as Jahn-Teller active tetrahedral Cu^{2+} induces lattice distortions in addition to adding magnetism on *A* site of the compounds $Mg_{1-x}Cu_xCr_2O_4$.[93] Novel properties such as intrinsic exchange bias have been shown to exist at phase boundaries.[121] We therefore closely examine the region between the antiferromagnetic and ferrimagnetic phases in $Mg_{1-x}Cu_xCr_2O_4$ for unusual phenomena.

7.2 Experimental details

Polycrystalline samples of the series $Mg_{1-x}Cu_xCr_2O_4$ (x = 0, 0.1, 0.2, 0.43, 0.47, 0.6, 0.8, and 1) were prepared through calcination of nitrate precursors as reported by Shoemaker and Seshadri.[93] The samples were structurally characterized by laboratory x-ray diffraction using a Philips X'pert diffractometer with Cu-Kα radiation. Phase purity was confirmed in selected compositions using high-resolution synchrotron powder x-ray diffraction collected at the 11-BM beamline at the Advanced Photon Source. Some of the samples have also been previously characterized by time-of-flight neutron scattering which verified that all the spinels are normal, meaning the *B* site is purely Cr^{3+}, and there is not Cr^{3+} on the *A* site. Magnetic susceptibility measurements on powder samples were performed using a Quantum Design MPMS superconducting quantum interference device (SQUID) magnetometer. In all samples, magnetization as a function of temperature was measured at a field of 0.1 T. Isothermal field dependent magnetization measurements were performed at 2 K and 5 K. A Quantum Design Physical Properties Measurement System was used to measure heat capacity at 0 T for various temperature ranges selected to accommodate the magnetic transition temperature of each sample. For the heat capacity measurements, pellets of 50 % sample mass and 50 % silver mass were prepared by

grinding and pressing at about 330 MPa. Silver was used to increase mechanical strength and thermal conductivity. The pellets were mounted on the sample stage using Apiezon N grease. The heat capacity of the grease and of silver were collected separately and subtracted to obtain the sample heat capacity.

7.3 Results and Discussion

We study the magnetic properties of the compounds $Mg_{1-x}Cu_xCr_2O_4$ using magnetic susceptibility measurements. Zero field cooled (ZFC) and field cooled (FC) magnetic susceptibility collected under a DC field of 1000 Oe as a function of temperature shows a composition dependent ordering temperature (T_N) defined as the temperature where $\mathrm{d}\chi/\mathrm{d}T$ is maximum (Figure 7.1 and Table 7.1). T_N increases with Cu^{2+} substitution. In addition to Cr^{3+}-Cr^{3+} interactions that are present in all compositions, Cu^{2+}-Cr^{3+} and Cu^{2+}-Cu^{2+} interactions occur in copper doped samples. The increase in T_N correlates well with the increase in the number of magnetic interactions. It is also likely that Cu^{2+} moments compensate some of the Cr^{3+} sublattice moments. As Cr^{3+} are compensated, the difficulty involved with satisfying antiferromagnetic interactions between spins on a pyrochlore lattice is alleviated easing frustration and allowing magnetic order at high T_N. The sample $x = 0.1$ shows a lower T_N indicating suppressed

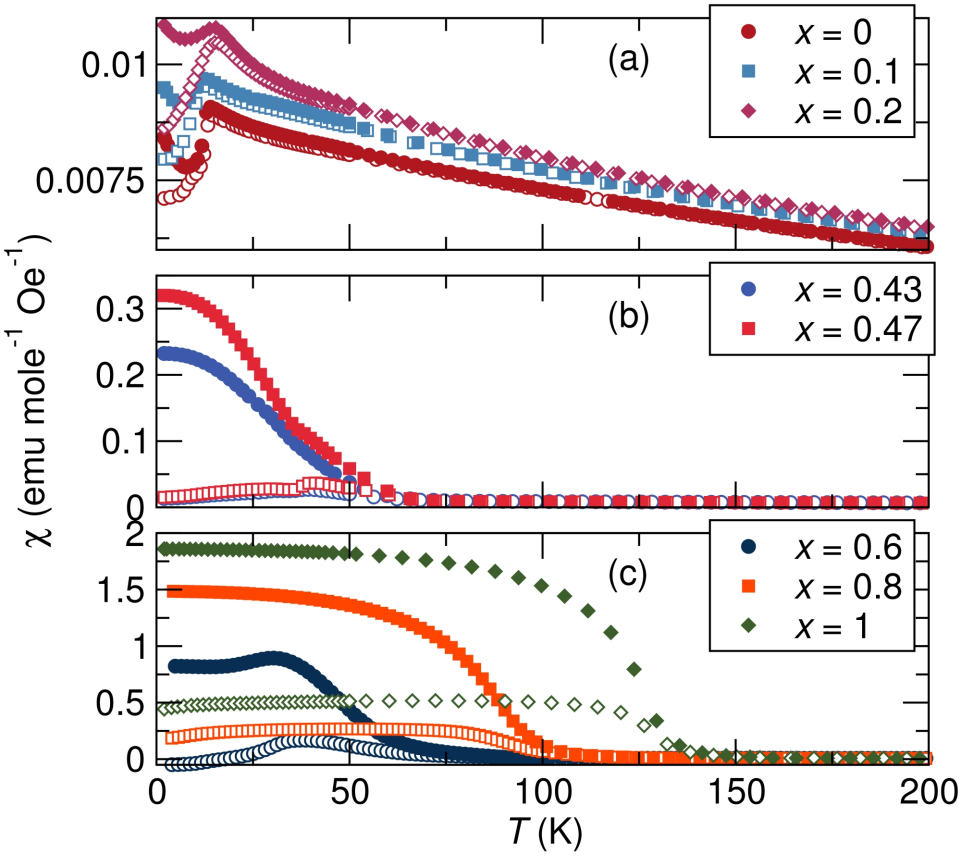

Figure 7.1: Zero-field-cooled (open symbols) and field-cooled (closed symbols) magnetic susceptibility as a function of temperature of the series $Mg_{1-x}Cu_xCr_2O_4$ under a DC fields of 0.1 T (a) samples with $x < 0.4$, (b) Samples with $0.4 < x < 0.5$, and (c) Samples $x > 0.5$. Magnetic ordering temperatures and the magnetization at low temperatures increase with x concentration. Reproduced with permission from reference [36] © 2012 IOP Publishing Ltd.

.

magnetic order for small amounts of magnetic ions on the non-magnetic A site of $MgCr_2O_4$. Concurrent structural and magnetic transitions occur in $MgCr_2O_4$ and structural studies of the compound x= 0.1 will enhance the understanding of the magnetic properties observed here. The decrease in T_N with dilute doping of magnetic cations on the *A* site of a frustrated antiferromagnet has been observed in the system $Zn_{1-x}Co_xCr_2O_4$.[37]

In samples x = 0, 0.1, and 0.2 susceptibility increases to a maximum at T_N before decreasing below T_N [Figure 7.1(c)]. This trend in both ZFC and FC data indicates dominant antiferromagnetic interactions. A sharp cusp is observed at T_N in $MgCr_2O_4$ where long range magnetic order occurs *via* a spin-driven Jahn-Teller transition.[7] This cusp broadens in samples x = 0.1 and 0.2 indicating changes in the magnetic ground state with Cu^{2+} doping. The decrease in ZFC susceptibility coupled with the increase in FC susceptibility below T_N in compositions x = 0.43, 0.47, 0.6, 0.8 and 1 [Figure 7.1(a) and (b)] demonstrates ferrimagnetic behavior. The magnitude of the low temperature susceptibility increases with Cu^{2+} content as shown in Figure 7.1.

There are two ordering temperatures in the magnetic susceptibility of There are two ordering temperatures in the magnetic susceptibility of samples x = 0.43 and x = 0.47 (Figure 7.2, Table 7.1). This suggests the presence of two different kinds of long range interactions, coexisting long range order and a

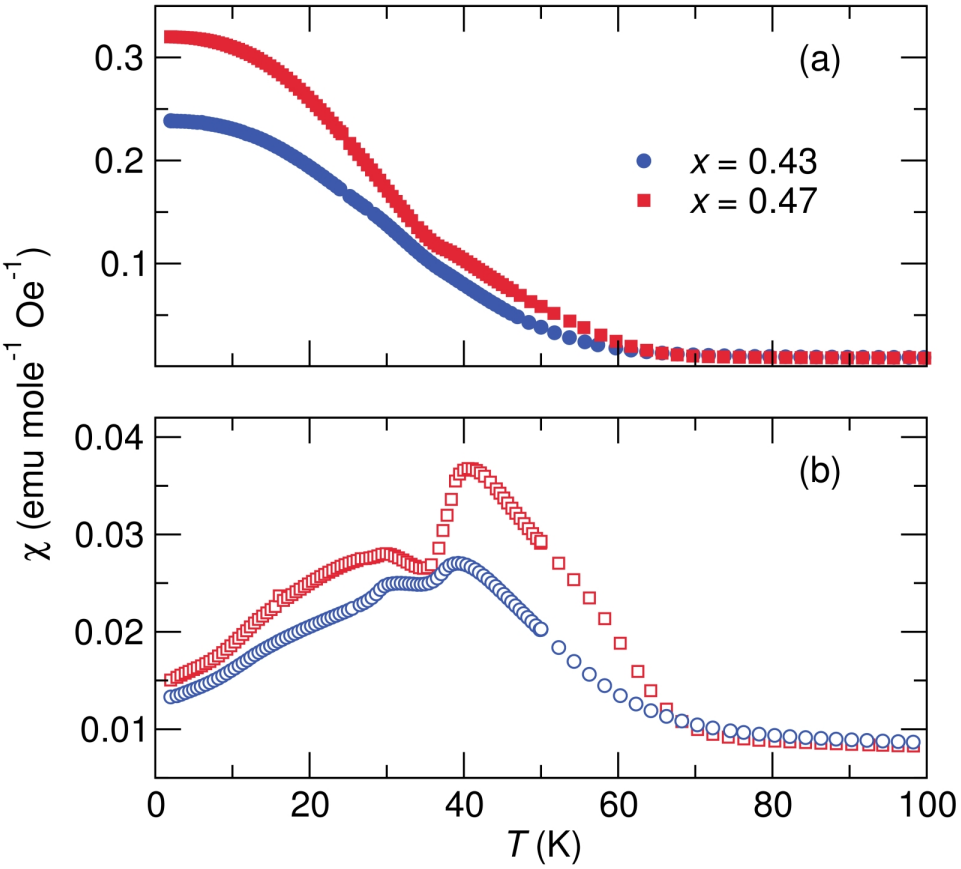

Figure 7.2: (a) Field-cooled and (b) zero-field-cooled magnetic susceptibility of the compounds with $x = 0.43$ and $x = 0.47$ showing multiple magnetic transition temperatures present in these samples. Reproduced with permission from reference [36] © 2012 IOP Publishing Ltd.

glassy state, or magnetic compensation. We find strong evidence for two distinct coexisting long range ordered states. Structural studies of these samples showed that compositions $x \leq 0.43$ have a cubic average structure at room temperature. Under similar conditions, compositions $x \geq 0.47$ showed tetragonal average symmetry. Average cubic and tetragonal symmetry was present in the range $0.43 \leq x \leq 0.47$ at 300 K. Shoemaker and Seshadri suggest that although locally CuO_4 tetrahedra are distorted for Cu^{2+} content ≤ 0.43 due to the Jahn-Teller activity of tetrahedral Cu^{2+}, the average structure remains cubic at 300 K. At $x = 0.43$, the distorted CuO_4 distribution is sufficient to cause a cooperative effect and the tetragonal phase appears.[93] Here, magnetic susceptibility studies complement structural studies well. We find that in Cu^{2+} concentrations $x \leq 0.2$, magnetism is antiferromagnetic as occurs in $MgCr_2O_4$. For x above 0.6, ferrimagnetism develops (Figure 7.1). Although addition of Cu^{2+} increases the degree of non-compensation of B site spins, the $B - B$ interaction dominates at low x values. Multiple transitions at $x = 0.43$, suggest that *A*-O-*B* coupling is sufficient to cause ferrimagnetic (Fi) long range order in addition to antiferromagnetic (AF) order. We attribute the presence of two magnetic transitions in the range $0.43 \leq x \leq 0.47$ to coexisting Fi and AF interactions. Evidence of structural phase separation in the range $0.43 \leq x \leq 0.47$ at 300 K supports the magnetic data showing two distinct yet coexisting kinds of magnetic order.[93]

For $x > 0.6$, ferrimagnetism prevails. We probe the sample $x = 0.43$ for glassy behaviour that may alternatively cause one of the two transitions observed in this sample.

Random interactions in a spin glass result in highly irreversible dynamic magnetization states well probed by ac susceptibility measurements. A common signature of glassy behavior is a frequency dependent magnetic transition temperature. Figure 7.3 shows frequency dependent susceptibility measurements of the compounds $Mg_{0.9}Cu_{0.1}Cr_2O_4$(a) and $Mg_{0.57}Cu_{0.43}Cr_2O_4$(b). The sharp cusp at T_N associated with the antiferromagnetic transition of highly frustrated systems appears at all measured frequencies for $Mg_{0.9}Cu_{0.1}Cr_2O_4$. In $Mg_{0.57}Cu_{0.43}Cr_2O_4$ a broad transition appears for all probed frequencies. The two well resolved magnetic transitions of $Mg_{0.57}Cu_{0.43}Cr_2O_4$ measured during dc zero field cooling (Figure 7.2(b)) are present in the ac measurement but they are much poorly resolved. The frequency independence of the magnetic transitions in both compounds shows little amounts of disorder in these samples. This measurements provide further evidence for coexisting ferrimagnetic and antiferromagnetic regions in the mixed composition compounds.

High temperature susceptibility data was fit to the Curie-Weiss (CW) equation (Equation 7.1) to obtain the effective paramagnetic moment (μ_{eff}) and Θ_{CW}.

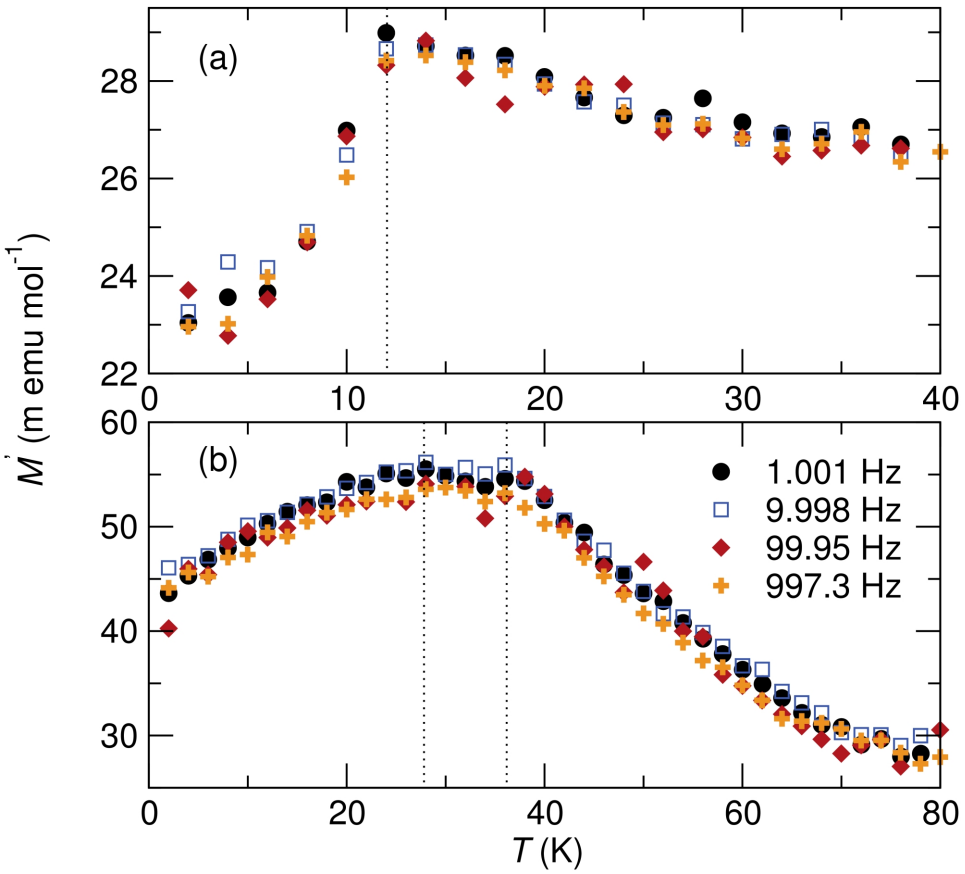

Figure 7.3: Magnetic ac susceptibility of the compounds (a) $Mg_{0.9}Cu_{0.1}Cr_2O_4$ (b) $Mg_{0.57}Cu_{0.43}Cr_2O_4$ taken with an ac field of 1 Oe under zero dc field. The magnetic ordering temperature of both compounds is frequency independent. We highlight approximate magnetic ordering temperatures. Reproduced with permission from reference [36] © 2012 IOP Publishing Ltd.

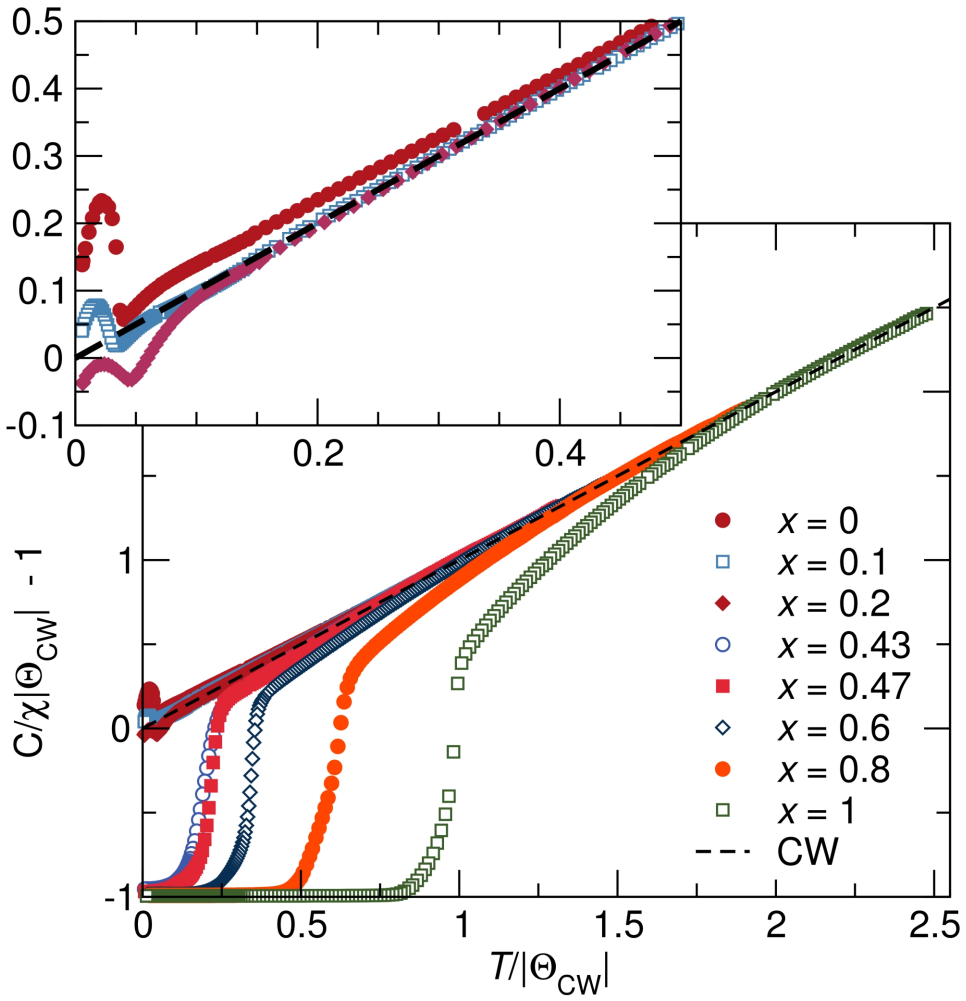

Figure 7.4: Normalized plots of inverse field-cooled magnetic susceptibility of $Mg_{1-x}Cu_xCr_2O_4$ acquired in a 0.1 T field, as a function of $T/|\Theta_{CW}|$. The black dashed line represents ideal Curie-Weiss (CW) behavior. For small x, the susceptibility follows Curie-Weiss behavior to $T \ll |\Theta_{CW}|$ and at T_N deviate positively from ideal CW behavior as seen also in the inset. Compounds with $x = 0.43$, 0.47, 0.6, 0.8, and 1 deviate negatively from ideal CW behavior at temperatures closer to $|\Theta_{CW}|$. Every other data point has been omitted for clarity. Reproduced with permission from reference [36] © 2012 IOP Publishing Ltd.

$$\chi = \frac{C}{T - \Theta_{CW}} \tag{7.1}$$

The Curie constant (C) yields an effective paramagnetic moment following the expression $\mu_{eff} = \sqrt{3K_B C/N_A}$. Θ_{CW} is a measure of the strength and nature of magnetic interactions. A plot of the scaled normalized inverse susceptibility shown by Equation 7.2 simplifies comparison of magnetic behavior in compounds where magnetic interactions evolve significantly with composition.[37]

$$\frac{C}{\chi|\Theta_{CW}|} + \text{sgn}(\Theta_{CW}) = \frac{T}{|\Theta_{CW}|} \tag{7.2}$$

Inverse susceptibility scaled according to Equation 7.2 using values obtained from Curie Weiss fits of the high temperature susceptibility data $300 \leq T \leq 390$ K are presented in Figure 7.4. Ideal CW paramagnetism occurs in all samples when $T/|\Theta_{CW}| \geq 1.5$ with the exception of $CuCr_2O_4$. In the paramagnetic regime, spins are disordered. Deviations from CW behavior denote the onset of long- or short-range interactions. Uncompensated interactions contribute to negative deviations, while compensated interactions lead to positive deviations. Compensated interactions in $MgCr_2O_4$ gradually become uncompensated with Cu^{2+} doping. On the basis of powder neutron diffraction, Prince[61] has proposed the magnetic structure of $CuCr_2O_4$ to consist of triangular ordering, where

Cr^{3+} sublattices in (001) sheets are parallel within each plane but at an angle to Cr^{3+} moments on other planes. The net moment from the Cr^{3+} sublattice is partially compensated by the Cu^{2+} sublattice. It is likely that this effect, which increases the number of uncompensated interactions, develops gradually with Cu^{2+} substitution in $MgCr_2O_4$. Negative deviations from ideal CW behaviour in $CuCr_2O_4$ when $T/|\Theta_{CW}| \geq 1$ indicate the presence of short range uncompensated interactions above T_N (Figure 7.4).

The normalized CW plot is a direct indicator of frustrated magnetism. $T_N/|\Theta_{CW}|$ is the inverse of the frustration parameter (f). The onset of long range order when $T/|\Theta_{CW}| \ll 1$ is a sign of strong frustration.[25] The canonical geometrically frustrated antiferromagnet, $MgCr_2O_4$, shows a high frustration index (Figure 7.4, Table 7.1). Surprisingly, the compound $x = 0.1$, is the most frustrated of the series despite the presence of random Cu^{2+} ions. The increase in frustration index despite the addition of small amounts of magnetic ions on the non-magnetic A site of geometrically frustrated systems has been shown in the study of $Zn_{1-x}Co_xCr_2O_4$ by Melot *et al.*[37] Magneto-structural studies of the compound $Mg_{0.9}Cu_{0.1}Cr_2O_4$ will likely shed light into the enhanced frustration index. Except for the composition $x = 0.1$, Cu^{2+} doping eases frustration in $MgCr_2O_4$ and this occurs because of the disruption of symmetric Cr^{3+}-Cr^{3+} interactions with random Cu^{2+} distribution in the doped compounds. Cu^{2+} in-

Table 7.1: Magnetic data of the series $Mg_{1-x}Cu_xCr_2O_4$. Experimental μ_{eff} and Θ_{CW} obtained from fitting susceptibility data in the temperature range $300 \leq T \leq 390$ K to the Curie-Weiss equation. T_N is taken as the temperature where $\partial\chi/\partial T$ is maximum. Calculated spin-only values of μ_{eff} are also presented.

x	μ_{eff} (μ_B, expt.)	μ_{eff} (μ_B, calc.)	Θ_{CW} (K)	T_N
$MgCr_2O_4$	5.42	5.47	-368	12.5
$x = 0.1$	5.34	5.50	-361	10.5
$x = 0.2$	5.24	5.53	-329	16
$x = 0.43$	5.17	5.59	-314	37, 27
$x = 0.47$	4.94	5.60	-295	38, 29
$x = 0.6$	4.89	5.64	-262	35
$x = 0.8$	4.54	5.69	-202	91
$CuCr_2O_4$	4.48	5.74	-148	128

terferes with *B-B* coupling by adding Cu^{2+}-Cr^{3+} and Cu^{2+}-Cu^{2+} interactions. Additionally, crystal distortions arise in CrO_6 due to the Jahn-Teller effect of Cu^{2+} depending on proximity to CuO_4 tetrahedra. Differences in Cr-Cr distances and Cr-O-Cr angles due to structural distortions break the degeneracy of exchange coupling routes ultimately easing frustration.

Values obtained from fitting high temperature susceptibility data to the CW

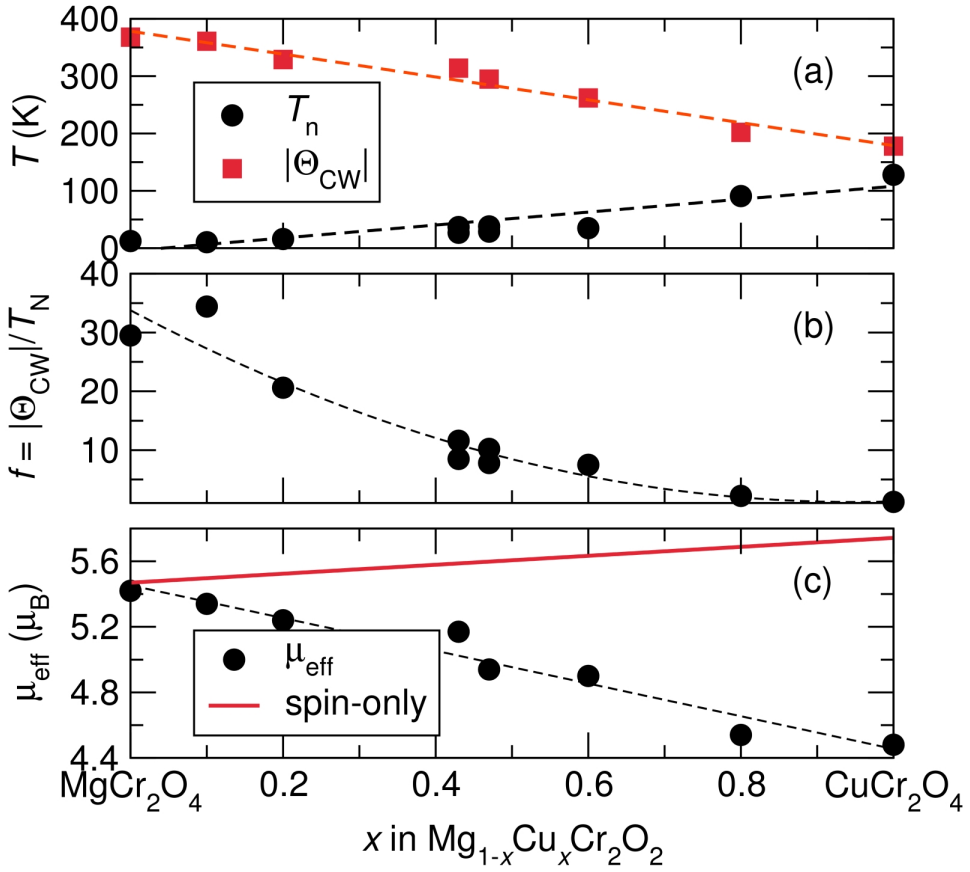

Figure 7.5: Trends in magnetic properties of $Mg_{1-x}Cu_xCr_2O_4$. (a) T_N increases while Θ_{CW} decreases with x. (b)The frustration index $f = |\Theta_{CW}|/T_N$ decreases with x approaching $f = 1$ as $x = 1$. (c) Experimental μ_{eff} decreases with x although the expected spin-only μ_{eff} is predicted to increase. Reproduced with permission from reference [36] © 2012 IOP Publishing Ltd.

equation are presented in Table 7.1 and plotted in Figure 7.5. An expected spin-only effective moment for series compositions is calculated using the expression $\mu_{eff} = \sqrt{x\mu_{Cu}^2 + 2\mu_{Cr}^2}$. The moment of each magnetic cation(c) is calculated using the equation $\mu_c = g\sqrt{S(S+1)}\mu_B$, in which g is the Landé g-factor and has the approximate value 2, S = 1/2 and 3/2 when c is Cu^{2+} and Cr^{3+} respectively. The effective moment is expected to increase with Cu^{2+} concentration. Surprisingly, a decrease in μ_{eff} occurs with Cu^{2+} doping. We speculate that short range interactions develop in the paramagnetic regime in Cu^{2+} rich samples leading to the underestimation of the spin-only effective moment. Curie-Weiss fitting at temperature $\geq$ 390 K may yield μ_{eff} values that are closer to what is expected. The underestimation of μ_{eff} with increased substitution of magnetic ions on the A site of a frustrated magnetic system has been reported in the system $Zn_{1-x}Cu_xCr_2O_4$.[98] The orbital contribution to the effective magnetic moment in octahedral Cr^{3+} and Jahn-Teller active Cu^{2+} is expected to be heavily quenched, hence, the orbital moment is not considered.

A negative theoretical ordering temperature (Θ_{CW}) is determined for all samples, confirming that spin coupling results in antiferromagnetic or ferrimagnetic order. The magnitude of Θ_{CW} decreases with Cu^{2+} content. A similar trend in Curie-Weiss temperature has been reported in the systems $Zn_{1-x}Cu_xCr_2O_4$[98] and $Cd_{1-x}Cu_xCr_2O_4$.[137] These earlier works postulate

that the decrease is due to interactions from the Cu^{2+} sublattice. Strong $B-B$ interactions in $MgCr_2O_4$ yield the largest $|\Theta_{CW}|$ value measured. Possibly, the addition of magnetic Cu^{2+} on the diamagnetic A site of $MgCr_2O_4$ disrupts the $B-B$ interaction contributing to weaker interactions in Cu^{2+} doped samples. The increase in T_N with Cu^{2+} concentration coupled with the decrease in the theoretical ordering temperature (Θ_{CW}) results in a dramatic decrease of the frustration parameter with Cu^{2+} content. In agreement with previous similar studies[37, 98, 137], we find that frustration is strongly quenched with the addition of spins in the *A* sublattice. These results show that lattice geometry does not prevent spin order in Cu^{2+} doped samples. The sample $x = 0.1$ exhibits a curious trend. In this compound, the frustration index increases despite Cu^{2+} doping. This was also observed in the study of magnetism of the series $Zn_{1-x}Co_xCr_2O_4$.[37]

Entropy changes are well described by specific heat measurements. A sharp peak in the specific heat of $MgCr_2O_4$ indicates changes in entropy at $T \approx 12.5$ K [Figure 7.6(a)]. The transition temperature recorded in heat capacity coincides with the magnetic ordering temperature signalling the onset of long range AF order. A broad shallow peak at $T \approx 11$ K appears at the magnetic ordering temperature of the sample $x = 0.1$ suggesting that there is a remanent magnetic entropy below the ordering temperature [Figure 7.6(b)]. In the sample

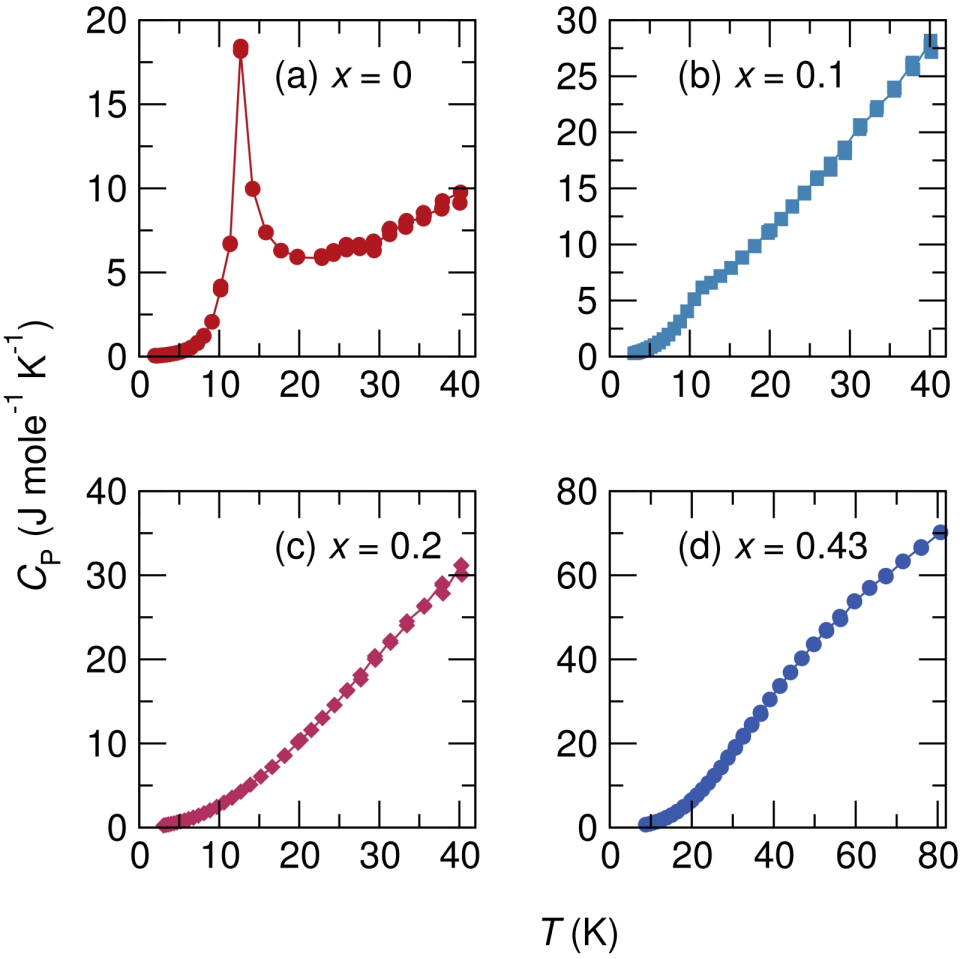

Figure 7.6: Temperature dependent heat capacity of compounds with $x = 0$, 0.1, 0.2, and 0.43 in $Mg_{1-x}Cu_xCr_2O_4$ under zero field. (a) Heat capacity of the sample $x = 0$ showing a sharp peak at 12.5 K; (b) A broader peak occurs at 11.5 K in the sample $x = 0.1$; (c) In the samples with $x = 0.2$, a smooth decrease in heat capacity with temperature is observed (d) The sample with $x = 0.43$ displays a broad bulge in the heat capacity at $\approx$ 50 K. Reproduced with permission from reference [36] © 2012 IOP Publishing Ltd.

$Mg_{0.8}Cu_{0.2}Cr_2O_4$, there is no anomaly in the specific heat at the magnetic ordering temperature while for the sample $Mg_{0.57}Cu_{0.43}Cr_2O_4$, a broad hump develops at 30 K $\leq T \leq$ 70 K [Figure 7.6(d)]. The absence of any entropy changes after the onset of magnetic order suggests the presence of glassy spin states, however, we find no evidence of this is the ac susceptibility measurements [Figure 7.3]. It is likely that non-collinear magnetic ordered states with finite entropy appear in Cu doped samples explaining the absence of any anomalies in the specific heat for these compositions.

A progressive transition from antiferromagnetic to ferrimagnetic order is observed in isothermal field dependent magnetization measurements (Figure 7.7). In $MgCr_2O_4$, a linear dependence of the magnetization on field that is characteristic of antiferromagnetic order is observed. Slight nonlinearity in the field dependent magnetization develops at $\pm$1.5 T in $MgCr_2O_4$ [Figure 7.7(a)]. This nonlinearity originates from a field-driven change in local magnetic structure as postulated by Suzuki *et al.*[135] Antiferromagnetism persists in samples x = 0.1 and 0.2 [Figure 7.7(b,c)], however, coercivity develops as the loops are open upon close examination. Coercivity is highest in samples x = 0.43 and 0.47 [Figure 7.7(d,e)]. Additionally, earlier studies on exchange bias effects in these compounds revealed an increase in the exchange bias field (H_e) with Cu^{2+} in samples x = 0.1, 0.2 and 0.43.[93] Antiferromagnetic-ferrimagnetic interfaces

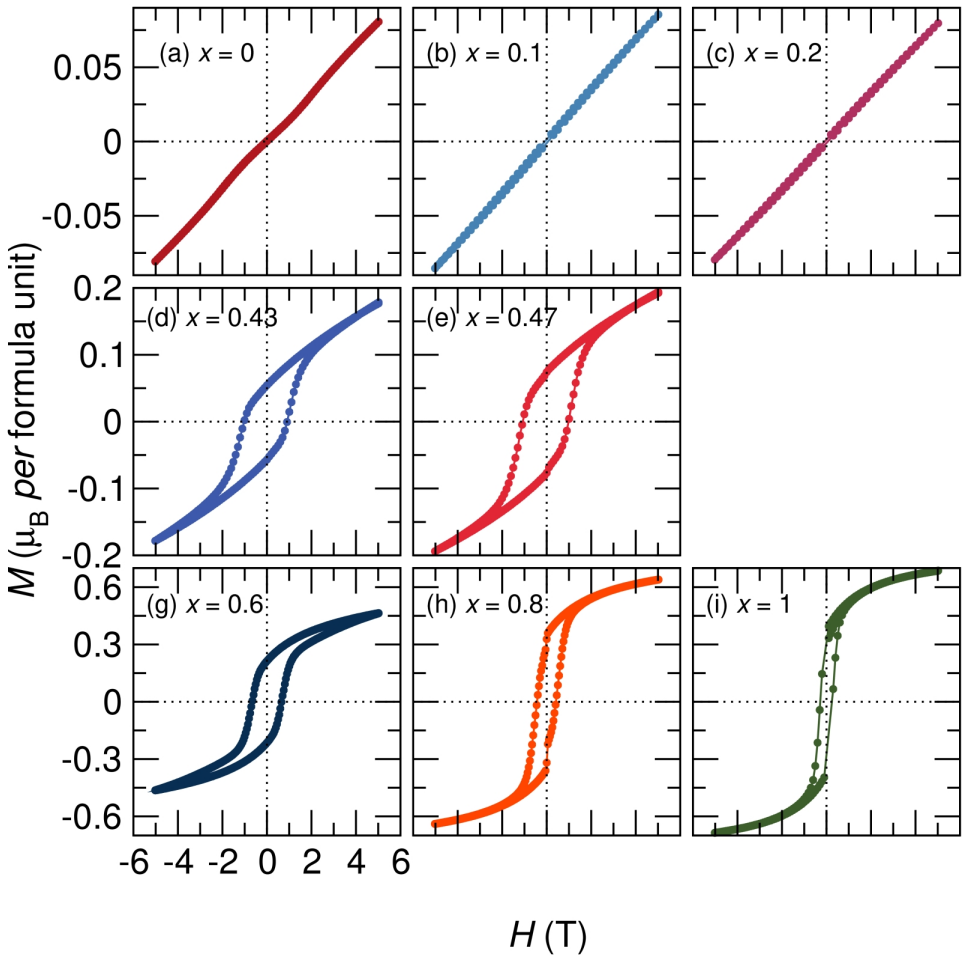

Figure 7.7: Isothermal magnetization traces of the different $Mg_{1-x}Cu_xCr_2O_4$ compounds, measured at 2 K except for the samples with $x = 0.6$ and 0.8 which were measured at 5 K. The compound (a) $x = 0$ shows a linear variation of magnetization with field. Magnetic anisotropy induces slight nonlinearity at $\pm$ 1.5 T as reported by Suzuki *et al.*[135] In (b) $x = 0.1$ and (c) $x = 0.2$ linear dependence of the magnetization on field is again observed. In (d), the $x = 0.43$ sample and in (e) the $x = 0.47$ sample display a larger increase in magnetization as compared to samples with $x =$ 0, 0.1, and 0.2. A large coercive field develops as observed from the wide hysteresis loops. At high fields the magnetization does not saturate. The samples with (f) x = 0.6 and (g) 0.8 are ferrimagnetic with open hysteresis loops and almost saturating magnetization. (h) Field dependence of the magnetization of $CuCr_2O_4$ at 2 K showing well behaved hysteresis and an almost saturated magnetization of 0.7 μ_B per formula unit with small coercive field. Reproduced with permission from reference [36]

are a common cause of enhanced coercivity and shifted hysteresis.[138, 139] Given that the samples $x = 0.43$ and $x = 0.47$ bridge the AF and Fi regions, we propose that pinning of spins at the Fi-AF cluster interfaces contributes to the enhanced coercivity.

Coupled with the increased coercivity in compounds $x = 0.43$ and $x = 0.47$ is the change from AF to Fi behavior that is evident in field- and temperature-dependent behavior. In samples with $x = 0.6$, $x = 0.8$, and $x = 1$, the coercivity decreases and the field dependent magnetization becomes ferrimagnetic. $CuCr_2O_4$ has a coercive field(H_e) of about 0.25 T and a saturation moment of 0.68 μ_B per formula unit. The Néel model of antiferromagnetism predicts a saturation moment of 5 μ_B per formula unit in $CuCr_2O_4$. Since the predicted moment far exceeds the measured value, neutron diffraction measurements in the ordered state were used to resolve this discrepancy.[61] According to the magnetic structure proposed by Prince, triangular arrangement of spins explains the low moment. Cr^{3+} on the 001 planes are aligned parallel and opposite to Cr^{3+} in adjacent planes yielding a net moment from the Cr^{3+} sublattices. The Cu^{2+} sublattice couples antiferromagnetically to the net moment of the Cr^{3+} sublattices creating a triangular configuration of spins. A composition dependent saturation magnetization is observed in samples $x = 0.43$, 0.47, 0.6, 0.8, and 1. The saturation moment increases with Cu^{2+}.

We can assemble the (Mg,Cu)Cr_2O_4 magnetic phase diagram in Figure 7.8 by combining magnetic ordering transitions and heat capacity measurements for the various compositions in this study. Transition temperatures specified by anomalies in susceptibility and heat capacity measurements are used to demarcate phase boundaries. $MgCr_2O_4$ enters a long range AF state at $T = 12.5\,\mathrm{K}$ marked by sharp anomalies in both susceptibility and heat capacity. The sharp cusp in the susceptibility of $MgCr_2O_4$ is replaced with a rounded peak in compositions $x = 0.1$ and 0.2. The linear dependence of the magnetization on field as well as the temperature dependent magnetization of samples $x = 0.1$ and 0.2 show that they are antiferromagnetic. In the range $0.2 \leq x \leq 0.6$, coexisting ferrimagnetic and antiferromagnetic states exist as shown by large coercive fields and the absence of any glassy magnetism in select compositions in this range studied using ac susceptibility. $Mg_{0.57}Cu_{0.43}Cr_2O_4$ and $Mg_{0.53}Cu_{0.47}Cr_2O_4$ show two transition temperatures clearly indicated the phase diagram. In the sample $x = 0.6$, ferrimagnetism develops indicated by the similarities in field and temperature dependent magnetization between the compound and the end-member $CuCr_2O_4$. All compositions are paramagnetic above the magnetic transition temperatures.

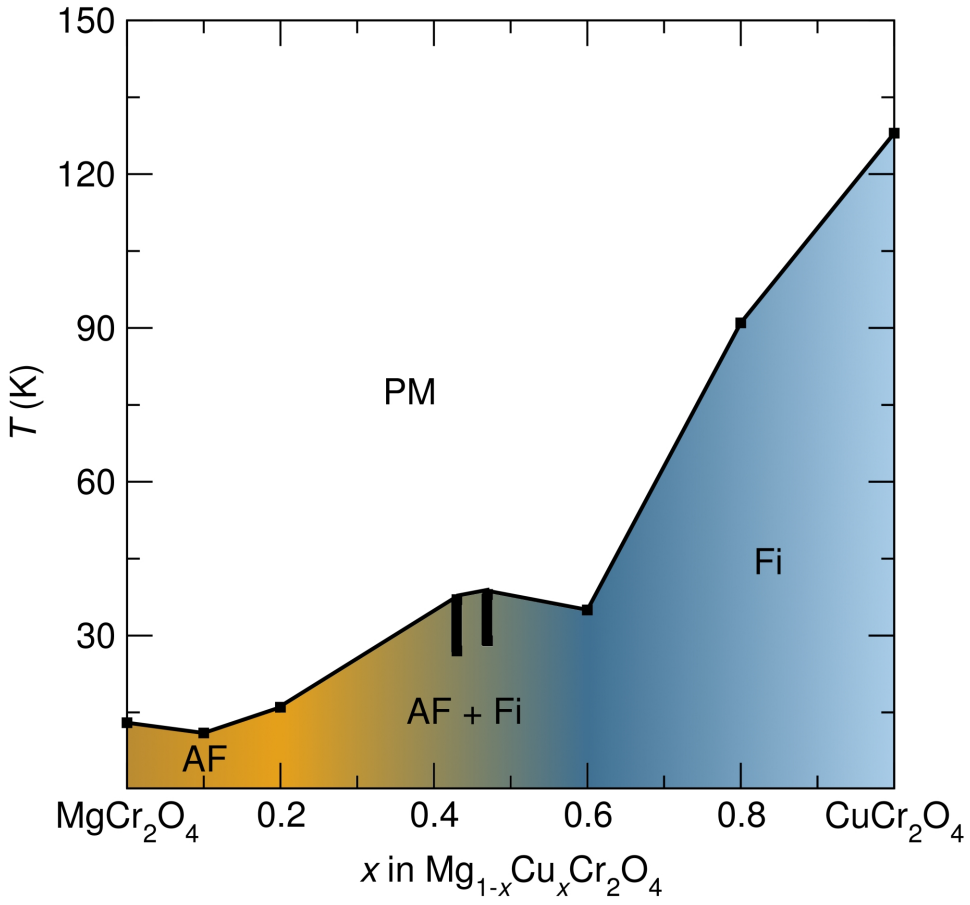

Figure 7.8: Suggested magnetic phase diagram for the solid solution $Mg_{1-x}Cu_xCr_2O_4$ based on susceptibility, heat capacity and magnetization measurements. In compounds with $x \leq 0.2$, the magnetic ordering is antiferromagnetic (AF) below T_N. For compositions with $0.2 \leq x \leq 0.6$, magnetism evolves from antiferromagnetic to ferrimagnetic and for x larger than 0.6, the ordering is largely ferrimagnetic (Fi), albeit not Néel-like. Two magnetic transitions in samples $Mg_{0.57}Cu_{0.43}Cr_2O_4$ and $Mg_{0.53}Cu_{0.47}Cr_2O_4$ are clearly indicated in the phase diagram. Reproduced with permission from reference [36] © 2012 IOP Publishing Ltd.

7.4 Conclusions

Recent years have seen renewed focus on frustrated magnetic systems as a consequence of the recognition that they can give rise to exotic magnetic ground states.[25, 140, 141] The introduction of spins in the *A* site of geometrically frustrated spinels has been suggested as a means of relieving frustration.[37, 98, 137]. We find in agreement with this proposition, that Cu^{2+} alleviates frustration in all $Mg_{1-x}Cu_xCr_2O_4$ compositions studied with the exception of $x = 0.1$. Temperature- and field-dependent magnetization indicate a largely antiferromagnetic ground state in the compositions $x < 0.2$, Coexisting ferrimagnetic and antiferromagnetic states with open hysteresis loops in the range $0.2 \leq x \leq 0.6$, and largely ferrimagnetic ground states for $x > 0.6$, albeit with significantly smaller saturation magnetization than would be found for Néel -ordered states. Specific heat measurements support these conclusions for samples with small x. Emergent behavior at the AF/Fi phase boundary, indicated by large coercive fields and multiple magnetic transition temperatures, suggests microscopic interactions between AF and Fi clusters.

Chapter 8

Summary and Future Directions

We have presented an extensive study of magnetostructural coupling effects in magnetic spinel oxides. We began by showing that although the Jahn-Teller active spinels $NiCr_2O_4$ and $CuCr_2O_4$ are tetragonal at room temperature, they undergo further spin-driven lattice distortions at their respective Néel temperatures. The low temperature nuclear structures of $NiCr_2O_4$ and $CuCr_2O_4$ are described by the orthorhombic space group $Fddd$. The structural distortions of $NiCr_2O_4$ involve an elongation of the NiO_4 tetrahedra while a compression of the CuO_4 tetrahedra is observed in orthorhombic $CuCr_2O_4$. Magnetostructural coupling in $NiCr_2O_4$ and $CuCr_2O_4$ is attributed to exchange striction, a change in bond lengths in order to strengthen exchange coupling interactions.

Non-collinear spin ordering and magnetostructural coupling in $NiCr_2O_4$ and $CuCr_2O_4$ motivated a study of the magnetodielectric properties of these spinels. A change in the dielectric constant of $NiCr_2O_4$ was observed at its Néel temperature. In addition, we observed an unknown dielectric transition at 20 K in $NiCr_2O_4$, which is accompanied by subtle structural and magnetic changes. This result indicated the sensitivity of dielectric measurements to subtle magnetostructural changes in spinels. Magnetodielectric hysteresis is observed below 30 K in $NiCr_2O_4$. Comparisons of the field-dependent dielectric constant of $NiCr_2O_4$ to the squared magnetization shows that magnetodielectric coupling in $NiCr_2O_4$ is described by Ginzburg-Landau theory.

Next, we studied the structural ground states of the frustrated spinels $MgCr_2O_4$ and $ZnCr_2O_4$ finding that tetragonal $I4_1/amd$ and orthorhombic $Fddd$ phases coexist in the antiferromagnetic states of these materials. We present the first complete crystallographic description of these systems. Lattice distortions in these spinels partially lifts spin frustration by distorting the Cr_4 pyrochlore network in the low temperature phases of $MgCr_2O_4$ and $ZnCr_2O_4$. We propose that in addition to frustration, exchange striction could play a role in the magnetostructural distortion of these spinels.

Frustrated systems are characterized by highly degenerate ground states which are susceptible to weak perturbations. We have investigated the ef-

fect of dilute spins on the A sites of $MgCr_2O_4$ and $ZnCr_2O_4$. Specifically, we probe the role of dilute A site spins on the spin-Jahn-Teller transitions of $MgCr_2O_4$ and $ZnCr_2O_4$. We observe that few Co^{2+} cations completely suppress the spin-Jahn-Teller distortion of $Zn_{1-x}Co_xCr_2O_4$ for $x \leq 0.2$. On the other hand, substitutions of Jahn-Teller active Cu^{2+} on the A sites of $MgCr_2O_4$ and $ZnCr_2O_4$ induce Jahn-Teller ordering above the Néel temperatures of these spinels. Despite undergoing a lattice distortion, the spinels $Mg_{1-x}Cu_xCr_2O_4$ and $Zn_{1-x}Cu_xCr_2O_4$ for $x \leq 0.2$, remain paramagnetic down to 20 K. We present temperature-composition phase diagrams that summarize the magnetic and structural properties of these spinel solid solutions.

We then examined magnetostructural coupling in the magnetodielectric spinel Mn_3O_4. We find that it undergoes a partial phase transition at the onset of ferrimagnetic order from tetragonal $I4_1/amd$ symmetry to a phase coexistence regime consisting of tetragonal $I4_1/amd$ and orthorhombic $Fddd$ structures. This partial phase transitions is mediated by large strains at the nucleation of the orthorhombic phase. The orthorhombic a and b lattice constants differ appreciably from the tetragonal a lattice constant. A complete structural description of Mn_3O_4 in the ferrimagnetic state is presented and polyhedral distortions in the ferrimagnetic phase are described. We propose that strain can be used to tune the structure of Mn_3O_4.

Finally, we also present our studies of the evolution of magnetism in the solid solution (Mg,Cu)Cr_2O_4. Frustrated antiferromagnetism in $MgCr_2O_4$ evolves to ferrimagnetism with substitution of Cu^{2+} cations for diamagnetic Mg^{2+}. A temperature-composition phase diagram summarizes the magnetic properties of this solid solution.

Our investigations of spin-lattice coupling in magnetic spinels raise a number of interesting questions. Structural phase coexistence is observed in the spinels $MgCr_2O_4$, $ZnCr_2O_4$, and Mn_3O_4. Transmission electron microscopy in the magnetically ordered phases of these materials is of interest to observe how these different phases coexist and to help develop an understanding of the mechanisms that give rise to such phase coexistence. Further, a quantitatively examination of the chemical composition of the coexisting phases, will determine if compositional variation plays any role in stabilizing a biphasic ground state in these materials.

The magnetic structures of these spinels have been resolved ignoring the observed lattice distortions. A reexamination of the magnetic configurations of these materials considering their true structural ground states is required. Further, it is interesting to understand the consequences of structural phase coexistence on the magnetic structures of these materials. For example, do the various coexisting structural phases show different magnetic conformations? De-

tailed investigations of the magnetostructural phase transition is also important to examine the presence of any hysteretic effects at the magnetostructural phase transition. In addition, systematic investigations of the effects of magnetic fields, strain, and sample heating rates on the low temperature biphasic ground states of these spinels is important. Such a study would highlight changes in the phase fractions of the coexisting phases and the effect of this structural variation on material properties.

We have demonstrated that variable-temperature high-resolution synchrotron x-ray scattering plays an important role in understanding the structure of materials.

Bibliography

[1] M. C. Kemei, P. T. Barton, S. L. Moffitt, M. W. Gaultois, J. A. Kurzman, R. Seshadri, M. R. Suchomel, and Y. Kim. Crystal structures of spin-Jahn-Teller-ordered $MgCr_2O_4$ and $ZnCr_2O_4$. *J. Phys.: Condens. Matter*, 25(32):326001, 2013.

[2] A. P. Ramirez, R. J. Cava, and J. Krajewski. Collossal magnetoresistance in Cr-based chalcogenide spinels. *Nature*, 386:156, 1997.

[3] Y. Yafet and C. Kittel. Antiferromagnetic arrangements in ferrites. *Phys. Rev.*, 87(2):290, 1952.

[4] G. Lawes, B. C. Melot, K. Page, C. Ederer, M. A. Hayward, T. Proffen, and R. Seshadri. Dielectric anomalies and spiral magnetic ordering in $CoCr_2O_4$. *Phys. Rev. B*, 74(2):024413, 2006.

[5] R. Moessner and A. P. Ramirez. Geometrical frustration. *Phys. Today*, 59:24, 2006.

[6] B. G. Levi. New candidate emerges for a quantum spin liquid. *Phys. Today*, 60:16, 2007.

[7] S-H. Lee, H. Takagi, D. Louca, M. Matsuda, S. Ji, H. Ueda, Y. Ueda, T. Katsufuji, J-H. Chung, S. Park, S-W. Cheong, and C. Broholm. Frustrated magnetism and cooperative phase transitions in spinels. *J. Phys. Soc. Jpn*, 79:011004, 2010.

[8] S.-H Lee, C. Broholm, W. Ratcliff, G. Gasparovic, Q. Huang, T. H Kim, and S.-W Cheong. Emergent excitations in a geometrically frustrated magnet. *Nature*, 418(6900):856–858, 2002.

[9] M. Izumi, T. F. Koetzle, G. Shirane, S. C. Hikazumi, M. Matsui, and S. Todo. Structure of magnetite (Fe_3O_4) below the verwey transition temperature. *Acta Cryst.*, B38:2121, 1982.

[10] D. S. McClure. The distribution of transition metal cations in spinels. *J. Phys. Chem. Solids*, 3:311, 1957.

[11] E. J. W. Verwey and E. L. Heilmann. Physical properties and cation arrangement of oxides with spinel structures. *J. Chem. Phys.*, 15(4):174, 1947.

[12] H. S. Oneill and W. A. Dollase. Crystal structures and cation distributions in simple spinels from powder XRD structural refinements - $MgCr_2O_4$, $ZnCr_2O_4$, Fe_3O_4, and the temperature dependence of the cation distribution in $ZnAl_2O_4$. *Phys. Chem. Miner.*, 20:541, 1994.

[13] L. Cervinka, S. Krupicka, and V. Synecek. To the existence of tetragonally distorted MnO_6 octahedra in cubic $MnFe_2o_4$. *J. Phys. Chem. Solids*, 20:167, 1960.

[14] M. R. Suchomel, D. P. Shoemaker, L. Ribaud, M. C. Kemei, and R. Seshadri. Spin-induced symmetry breaking in orbitally ordered $NiCr_2O_4$ and $CuCr_2O_4$. *Phys. Rev. B*, 86(5):054406, 2012.

[15] H. A. Jahn and E. Teller. Stability of polyatomic molecules in degenerate electronic states. I. orbital degeneracy. *Proc. Roy. Soc.*, A161:220, 1937.

[16] H. J. van Hook and M. L. Keith. The system $Fe_3O_4 - Mn_3O_4$. *Am. Mineral*, 43:69, 1958.

[17] A. M. Balagurov, I. A. Bobrikov, M. S. Maschenko, D. Sangaa, and V. G. Simkin. Structural phase transition in $CuFe_2O_4$ spinel. *Crystallogr. Rep.*, 58:710, 2013.

[18] Z.-G. Ye, O. Crottaz, F. Vaudano, F. Kubel, P. Tissot, and H. Schmid. Single crystal growth, structure refinement, ferroelastic domains and phase transition of the hausmannite $CuCr_2O_4$. *Ferroelectr. Lett.*, 162(2):103–118, 1994.

[19] C. G. Shull and J. S. Smart. Detection of antiferromagnetism by neutron diffraction. *Phys. Rev.*, 76:1256, 1949.

[20] R. Moessner and A. P. Ramirez. Geometric frustration. *Phys. Today*, 59:24, 2006.

[21] A. P. Ramirez, A. Hayashi, R. J. Cava, R. Siddharthan, and B. S. Shastry. Zero−point entropy in 'spin ice'. *Nature*, 399:333, 1999.

[22] L. Pauling. The nature of the chemical bond. *(Cornell Univ. Press, Ithaca, New York, 1945)*, page 301, 1945.

[23] C. Nisoli, R. Moessner, and P. Schiffer. Colloquium: Artificial spin ice: Designing and imaging magnetic frustration. *Rev. Mod. Phys.*, 85:1473, 2013.

[24] S.−H. Lee, C. Broholm, T. H. Kim, W. Ratcliff, and S−W. Cheong. Local spin resonance and Spin Peierls like phase transition in a geometrically frustrated antiferromagnet. *Phys. Rev. Lett.*, 84(16):3718–3721, 2000.

[25] A. P. Ramirez. Strongly geometrically frustrated magnets. *Annu. Rev. Mater. Sci*, 24:453, 1994.

[26] R. Moessner and J. T Chalker. Properties of a classical spin liquid: The heisenberg pyrochlore antiferromagnet. *Phys. Rev. Lett.*, 80(13):2929, 1998.

[27] M. T. Rovers, P. P. Kyriakou, H. A. Dabkowska, G. M. Luke, M. I. Luke, M. I. Larkin, and A. T. Savici. Muon−spin−relaxation investigation of the spin dynamics of geometrically frustrated chromium spinels. *Phys. Rev. B*, 66(17):174434, 2002.

[28] L.O−S. Martin, A. J. Williams, C. D. Gordon, S. Klemme, and J. P. Attfield. Low temperature neutron diffraction study of $MgCr_2O_4$ spinel. *J. Phys.: Condens. Matter*, 20(10):104238, 2008.

[29] S. E. Dutton, Q. Huang, O. Tchernyshyov, C. L. Broholm, and R. J. Cava. Sensitivity of the magnetic properties of the $ZnCr_2O_4$ and $MgCr_2O_4$ spinels to non−stoichiometry. *Phys. Rev. B*, 83:064407, 2011.

[30] H. Martinho, N. O. Moreno, J. A. Sanjurjo, C. Rettori, A. J. Garcia−Adeva, D. L. Huber, S. B. Oseroff, W. Ratcliff, S.-W. Cheong, P. G. Pagliuso, J. L. Sarrao, and G. B. Martins. Magnetic properties of the frustrated antiferromagnetic spinel $ZnCr_2O_4$ and the spin-glass $Zn_{1-x}Cd_xCr_2O_4$ (x=0.05,0.10). *Phys. Rev. B*, 64:024408, 2001.

[31] S-H. Lee, G. Gasparovic, C. Broholm, M. Matsuda, J-H. Chung, Y. J. Kim, H. Ueda, G. Xu, P. Zschack, K. Kakurai, H. Takagi, W. Ratcliff, T. H. Kim, and S-W. Cheong. Crystal distortions in geometrically frustrated ACr_2O_4(A = Zn,Cd). *J. Phys.: Condens. Matter*, 19:145259, 2007.

[32] H. Ueda, H. A. Katori, H. Mitamura, T. Goto, and H. Takagi. Magnetic field induced transition to the 1/2 magnetization plateau state in the geometrically frustrated magnet $CdCr_2O_4$. *Phys. Rev. Lett.*, 94:047202, 2005.

[33] J.−H. Chung, M. Matsuda, S.−H. Lee, K. Kakurai, H. Ueda, T. J. Sato, H. Takagi, K. −P. Hong, and S. Park. Statics and dynamics of incommensurate spin order in a geometrically frustrated antiferromagnet $CdCr_2O_4$. *Phys. Rev. Lett.*, 95(24):247204, 2005.

[34] H. Ueda, H. Mitamura, T. Goto, and Y. Ueda. Successive field−induced transitions in a frustrated antiferromagnet $HgCr_2O_4$. *Phys. Rev. B*, 73:094415, 2006.

[35] M. Matsuda, H. Ueda, A. Kikkawa, Y. Tanaka, K. Katsumata, Y. Narumi, Y. Ueda, and S. −H. Lee. Spin−lattice instability to a fractional magnetization state in the spinel $HgCr_2O_2$. *Nature Phys.*, 3:397, 2007.

[36] M. C. Kemei, S. L. Moffitt, D. P. Shoemaker, and R. Seshadri. Evolution of magnetic properties in the normal spinel solid solution $Mg_{1-x}Cu_xCr_2O_4$. *J. Phys.: Condens. Matter*, 24:046003, 2012.

[37] B. C. Melot, J. E. Drewes, R. Seshadri, E. M. Stoudenmire, and A. P. Ramirez. Magnetic phase evolution in the spinel compounds $Zn_{1-x}Co_xCr_2O_4$. *J. Phys. Condens. Matter*, 21:216007(1–7), 2009.

[38] H. M. Rietveld. A profile refinement method for nuclear and magnetic structures. *J. Appl. Cryst.*, 2:65, 1969.

[39] J. D. Dunitz and L. E. Orgel. Electronic properties of transition metal oxides-I:Distortions from cubic symmetry. *J. Phys. Chem. Solids*, 3(1):20–29, 1957.

[40] G. Beni and P. Pincus. Instability of the uniform antiferromagnetic chain. I. XY model in the adiabatic approximation. *J. Chem. Phys.*, 57(1):3531, 1972.

[41] X. Fabreges, S. Petit, I. Mirebeau, S. Pailhes, L. Pinsard, A. Forget, M. T. Fernandez-Diaz, and F. Porcher. Spin-lattice coupling, frustration and magnetic order in multiferroic $RMnO_3$. *Phys. Rev. Lett.*, 103:067204, 2009.

[42] S. Lee, A. Pirogov, M. Kang, K-H. Jang, M. Yonemura, T. Kamiyama, S-W. Cheong, F. Gozzo, N. Shin, H. Kimura, Y. Noda, and J-G. Park. Giant magneto-elastic coupling in multiferroic hexagonal manganites. *Nature*, 451:805–809, 2007.

[43] T. Lottermoser, T. Lonkai, U. Amann, D. Hohlwein, J. Ihringer, and M. Fiebig. Magnetic phase control of an electric field. *Nature*, 430:541–544, 2004.

[44] V. N. Glazkov, A. M. Farutin, V. Tsurkan, H. A. K. von Nidda, and A. Loidl. Spin dynamics of the ordered phase of the frustrated antiferromagnet $ZnCr_2O_4$: A magnetic resonance study. *J. Phys. Conf. Ser.*, 145:012030, 2009.

[45] O. Tchernyshyov. Structural, orbital, and magnetic order in vanadium spinels. *Phys. Rev. Lett*, 93(15):157206, 2004.

[46] T. Rudolf, Ch. Kant, F. Mayr, J. Hemberger, V. Tsurkan, and A. Loidl. Spin-phonon coupling in antiferromagnetic chromium spinels. *New J. Phys.*, 9(76):1, 2007.

[47] Ch. Kant, J. Deisenhofer, V. Tsurkan, and A. Loidl. Magnetic susceptibility of the frustrated spinels $ZnCr_2O_4$, $MgCr_2O_4$, and $CdCr_2O_4$. *J. Phys.: Conf. Ser.*, 200:032032, 2010.

[48] H. Ishibashi and T. Yasumi. Structural transition of spinel compound $NiCr_2O_4$ at ferrimagnetic transition temeperature. *J. Magn. Magn. Mater.*, 310(2):e610, 2007.

[49] S. Klemme and J. C. van Miltenburg. Thermodynamic properties of nickel chromite ($NiCr_2O_4$) based on adiabatic calorimetry at low temperatures. *Phys. Chem. Miner.*, 29:663–667, 2002.

[50] S. Bordacs, D. Varjas, I. Kezsmarki, G. Mihaly, L. Baldassarre, A. Abouelsayed, C. A. Kuntscher, K. Ohgushi, and Y. Tokura. Magnetic-order-induced crystal symmetry lowering in ACr_2O_4 ferrimagnetic spinels. *Phys. Rev. Lett.*, 103(7):077205, 2009.

[51] S. Greenwald. Changes in lattice constants of Cr_2O_3 near the curie temperature. *Nature*, 168(4270):379, 1951.

[52] J. S. Smart and S. Greenwald. Deformations in the crystal structures of antiferromagnetic compounds. *Nature*, 166(4221):523, 1950.

[53] W. L. Roth. Magnetic structures of MnO, FeO, CoO, and NiO. *Phys. Rev.*, 110(6):1333, 1958.

[54] Y.Y. Li. Magnetic moment arrangements and magnetocrystalline deformations in antiferromagnetic compounds. *Phys. Rev.*, 100(2):672, 1955.

[55] O. Crottaz, F. Kubel, and H. Schmid. Jumping crystals of the spinels $NiCr_2O_4$ and $CuCr_2O_4$. *J. Mater. Chem.*, 7(1):143–146, 1997.

[56] K. Ohgushi, Y. Okimoto, T. Ogasawara, S. Miyasaka, and Y. Tokura. Magnetic, optical, and magnetooptical properties of spinel-type ACr_2X_4 (A = Mn, Fe, Co, Cu, Zn, Cd; X = O, S, Se). *J. Phys. Soc. Jpn.*, 77(3):034713, 2008.

[57] Y. G. Chukalkin, V. V. Petrov, V. R. Shtirts, and B. N. Goshchitskii. Effects of radiation disorder in chromium spinels. *Phys. Status Solidi A*, 92(2):347–354, 1985.

[58] J. Kanamori. Crystal distortions in magnetic compounds. *J. Appl. Phys.*, 31(5):S14–S23, 1960.

[59] M. Gerloch. Jahn−Teller distortion in $CuCr_2O_4$. *Inorg. Chem.*, 20(2):638–640, 1981.

[60] M. Tovar, R. Tobari, C. Welker, and F. Fleischer. Structural and magnetic properties of Cu-Ni-Cr spinel oxides. *Physica B (Amsterdam, Neth.)*, 385(1):196–198, 2006.

[61] E. Prince. Crystal and magnetic structure of copper chromite. *Acta Crystallogr., Sect. C: Cryst. Struct. Commun.*, 10(19):554–556, 1957.

[62] W. A. Dollase and H. St. C. O'Neill. The spinels $CuCr_2O_4$ and $CuRh_2O_4$. *Acta Crystallogr., Sect. C: Cryst. Struct. Commun.*, C53:657–659, 1997.

[63] G. Ueno, S. Sato, and Y. Kino. The low−temperature tetragonal phase of $NiCr_2O_4$. *Acta Crystallogr., Sect. C: Cryst. Struct. Commun.*, C55:1963–1966, 1999.

[64] K. Tomiyasu and I. Kagomiya. Magnetic structure of $NiCr_2O_4$ studied by neutron scattering and magnetization measurements. *J. Phys. Soc. Jpn.*, 73(9):2539–2542, 2004.

[65] J. Wang, Brian H. Toby, Peter L. Lee, Lynn Ribaud, Sytle M. Antao, Charles Kurtz, Mohan Ramanathan, Robert B. Von Dreele, and Mark A. Beno. A dedicated powder diffraction beamline at the Advanced Photon Source: Commissioning and early operational results. *Rev. Sci. Instrum.*, 79(8):085105, 2008.

[66] B. H. Toby. EXPGUI. a graphical user interphase for GSAS. *J. Appl. Crystallogr.*, 34:210–213, 2001.

[67] A. C. Larson and R. B. Von Dreele. General structure analysis system (GSAS). *Los Alamos National Laboratory Report*, pages 86–748, 2000 (unpublished).

[68] K. Momma and F. Izumi. VESTA: a three-dimensional visualization system for electronic and structural analysis. *J. Appl. Crystallogr.*, 41:653, 2008.

[69] M. E. Fisher. Relation between the specific heat and susceptibility of an antiferromagnet. *Philos. Mag.*, 7(82):1731–1743, 1962.

[70] T. D. Sparks, M. C. Kemei, P. T. Barton, R. Seshadri, E-D. Mun, and V. S. Zapf. Magnetocapacitance as a sensitive probe of magnetostructural changes in $NiCr_2O_4$. *Phys. Rev. B*, 89:024405, 2014.

[71] T. Kimura. Magneotoelectric hexaferrites. *Annu. Rev. Condens. Matter Phys.*, 3:93, 2012.

[72] T. Kimura, S. Kawamoto, I. Yamada, M. Azuma, M. Takano, and Y. Tokura. Magnetocapacitance effects in multiferroic $BiMnO_3$. *Phys. Rev. B*, 67(18):180401(R), 2003.

[73] Y. Kitagawa, T. Honda Y. Hiraoka, T. Ishikura, H. Nakamura, and T. Kimura. Low-field magnetoelectric effect at room temperature. *Nat. Mater.*, 9:797, 2010.

[74] S. W. Chun, Y. S. Chai, B-G Jeon, H. J. Kim, Y. S. Oh, I. Kim, H. Kim, B. J. Jeon, S. Y. Haam, J-Y. Park, S. H. Lee, J-H Chung, J-H Park, and K. H. Kim. Electric field control of nonvolatile four-state magnetization at room temperature. *Phys. Rev. Lett.*, 108:177201, 2012.

[75] N. Mufti, A. A. Nugroho, G. R. Blake, and T. T. M. Palstra. Magnetodielectric coupling in frustrated spin systems: the spinels MCr_2O_4 (M = Mn, Co, and Ni). *J. Phys.: Condens. Matter*, 22(7):075902, 2010.

[76] V. Kocsis, S. Bordacs, D. Varjas, K. Penc, A. Abouelsayed, C. A. Kuntscher, K. Ohgushi, Y. Tokura, and I. Kezsmarki. Magnetoelasticity in ACr_2O_4 spinels. *Phys. Rev. B*, 87(6):064416, 2013.

[77] A. Maignan, C. Martin, K. Singh, Ch. Simon, O. I. Lebedev, and S. Turner. From spin induced ferroelecricity to dipolar glasses: Spinel chromites and mixed delafossites. *J. Solid State Chem.*, 195:41, 2012.

[78] K. Singh, A. Maignan, C. Simon, and C. Martin. $FeCr_2O_4$ and $CoCr_2O_4$ spinels: Multiferroicity in the collinear magnetic state? *Appl. Phys. Lett.*, 99:172903, 2011.

[79] J. A. Detwiler, G. M. Schmiedeshoff, N Harrison, A. H. Lacerda, J. C. Cooley, and J. L. Smith. Magnetization of UBe_{13} to 60 T. *Phys. Rev. B: Condens. Matter*, 61(1):402, 2000.

[80] G. Catalan. Magnetocapacitance without magnetodielectric coupling. *Appl. Phys. Lett.*, 88(10):102902, 2006.

[81] R. Tackett, G. Lawes, B. C. Melot, M. Grossman, E. S. Toberer, and R. Seshadri. Magnetodielectric coupling in Mn_3O_4. *Phys. Rev. B: Condens. Matter*, 76(2):024409, 2007.

[82] G. Lawes, A. P. Ramirez, C. M. Varma, and M. A. Subramanian. Magnetodielectric effects from spin fluctuations in isostructural ferromagnetic and antiferromagnetic systems. *Phys. Rev. Lett.*, 91(25):257208, 2003.

[83] O. Tchernyshyov, R. Moessner, and S. L. Sondhi. Order by distortion and string modes in pyrochlore antiferromagnets. *Phys. Rev. Lett.*, 88(6):067203, 2002.

[84] I. Kagomiya, H. Sawa, K. Siratori, K. Kohn, M. Toki, Y. Hata, and E. Kita. Structural phase transition and dielectric properties of $ZnCr_2O_4$. *Ferroelectrics*, 268:327–332, 2002.

[85] R. V. Aguilar, A. B. Sushkov, Y. J. Choi, S. −W. Cheong, and H. D. Drew. Spin−phonon coupling in frustrated magnet $CdCr_2O_4$. *Phys. Rev. B*, 77(9):092412, 2008.

[86] H. Ehrenberg, M. Knapp, C. Baehtz, and S. Klemme. Tetragonal low−temperature phase of $MgCr_2O_4$. *Powder Diffr.*, 17(3):230, 2002.

[87] V. N. Glazkov, A. M. Farutin, V. Tsurkan, H.-A. Krug von Nidda, and A. Loidl. Evidence for orthorhombic distortion in the ordered state of $ZnCr_2O_4$: A magnetic resonance study. *Phys. Rev. B: Condens. Matter Mater. Phys.*, 79:024431, 2009.

[88] B. J. Campbell, H. T. Stokes, D. E. Tanner, and D. M. Hatch. ISODISPLACE: a web−based tool for exploring structural distortions. *J. Appl. Crystallogr.*, 39:607, 2006.

[89] S. Klemme, H. S. C. O'Neill, W. Schnelle, and E. Gmelin. The heat capacity of $MgCr_2O_4$,$FeCr_2O_4$, and Cr_2O_3 at low temperatures and derived thermodynamic properties. *Am. Mineral.*, 85(11):1686, 2000.

[90] S. Klemme and J. C. Van Miltenburg. The entropy of zinc chromite ($ZnCr_2O_4$). *Mineral. Mag.*, 68(3):515, 2004.

[91] W. H. Baur. The geometry of polyhedral distortions. Predictive relationships for the phosphate group. *Acta Crystallogr., Sect. B: Struct. Sci*, B30:1195, 1974.

[92] K. Robinson, G. V. Gibbs, and P. H. Ribbe. Quadratic elongation $-$ quantitative measure of distortion in coordination polyhedra. *Science*, 172:567, 1971.

[93] D. P. Shoemaker and R. Seshadri. Total scattering descriptions of local and cooperative distortions in the oxide spinel $Mg_{1-x}Cu_xCr_2O_4$ with dilute Jahn$-$Teller ions. *Phys. Rev. B*, 82(21):214107, 2010.

[94] P. M. Woodward, D. E. Cox, T. Vogt, C. N. R. Rao, and A. K. Cheetam. Effect of compositional fluctuations on the phase transitions in $Nd_{0.5}Sr_{0.5}MnO_3$. *Chem. Mater.*, 11:3528, 1999.

[95] B. Noheda, D. E. Cox, G. Shirane, J. Gao, and Z.$-$G. Ye. Phase diagram of the ferroelectric relaxor $(1-x)PbMg_{1/3}Nb_{2/3}O_3$ $-xPbTiO_3$. *Phys. Rev. B*, 66:054104, 2002.

[96] M. C. Kemei, S. L. Moffitt, L. E. Darago, R. Seshadri, M. R. Suchomel, D. P. Shoemaker, K. Page, and J. Siewenie. Structural ground states of (A, A')Cr_2O_4(A = Mg, Zn; A' = Co, Cu) spinel solid solutions: Spin$-$Jahn$-$Teller and Jahn$-$Teller effects. *Phys. Rev. B*, 89:174410, 2014.

[97] G. L. Pascut, R. Coldea, P. G. Radaelli, A. Bombardi, G. Beutier, I. I Mazin, M. D. Johannes, and M. Jansen. Direct observation of charge order in triangullar metallic $AgNiO_2$ by single crystal resonant x-ray scattering. *Phys. Rev. Lett*, 106(15):157206, 2011.

[98] L. Yan, F. Macia, Z. Jiang, J. Shen, L. He, and F. Wang. Glassy magnetic behavior induced by Cu^{2+} substitution in the frustrated antiferromagnet $ZnCr_2O_4$. *J. Phys.: Condens. Matter*, 20(25):255203, 2008.

[99] A. D. LaForge, S. H. Pulido, R. J. Cava, B. C. Chan, and A. P. Ramirez. Quasispin glass in a geometrically frustrated magnet. *Phys. Rev. Lett.*, 110:017203, 2013.

[100] R. D. Shannon. Revised effective ionic radii and systematic studies of interatomic distances in halides and chalcogenides. *Acta Crystallogr., Sect. A: Found. Crystallogr.*, 32:751, 1976.

[101] P. T. Barton, R. Seshadri, A. Llobet, and M. R. Suchomel. Magnetostructural transition, metamagnetism, and magnetic phase coexistence in $Co_{10}Ge_3O_{16}$. *Phys. Rev. B*, 88:024403, 2013.

[102] P. F. Peterson, M. Gutmann, T. Proffen, and S. J. L. Billinge. PDFgetN: a user friendly program to extract the total scattering structure factor and the pair distribution function from neutron powder diffraction data. *J. Appl. Crystallogr.*, 33:1192, 2000.

[103] C. L. Farrow, P. Juhas, J. W. Liu, D. Bryndin, E. S. Bozin, J. Bloch, T. Proffen, and S. J. L. Billinge. PDFfit2 and PDFgui: computer programs for studying nanostructure in crystals. *J. Phys.: Condens. Matter*, 19:335219, 2007.

[104] N. Menyuk, K. Dwight, and A. Wold. Ferrimagnetic spiral configuration in cobalt chromite. *J. Phys.—Paris*, 25(5):528, 1964.

[105] L. J. Chang, D. J. Huang, W.—H. Li, S.—W. Cheong, W. Ratcliff, and J. W. Lynn. Crossover from incommensurate to commensurate magnetic orderings in $CoCr_2O_4$. *J. Phys.: Condens. Matter*, 21(45):456008, 2009.

[106] V. Tsurkan, S. Zherlitsyn, S. Yasin, V. Felea, Y. Skourski, J. Deisenhofer, H—A. Krug von Nidda, J. Wosnitza, and A. Loidl. Unconventional magnetostructural transition in $CoCr_2O_4$ at high magnetic fields. *Phys. Rev. Lett.*, 110(11):115502, 2013.

[107] J. Rodriguez-Carvajal, G. Rousse, C. Masquelier, and M. Hervieu. Electronic crystallization in a lithium battery material: Columnar ordering of electrons and holes in the spinel $LiMn_2O_4$. *Phys. Rev. Lett*, 81:4660, 1998.

[108] B. C. Melot, K. Page, R. Seshadri, E. M. Stoudenmire, L. Balents, D. L. Bergman, and T. Proffen. Magnetic frustration on the diamond lattice of the A site magnetic spinel $CoAl_{1-x}Ga_xO_4$: The role of lattice expansion and site disorder. *Phys. Rev. B*, 80:104420, 2009.

[109] S. Jin, T. H. Tiefel, M. McCormack, R. A. Fastnacht, R. Ramesh, and L. H. Chen. Thousandfold change in resistivity in magnetoresistive La−Ca−Mn−O films. *Science*, 264(5157):413, 1994.

[110] M. Fath, S. Freisem, A. A. Menovsky, Y. Tomioka, J. Aarts, and J. A. Mydosh. Spatially inhomogeneous metal−insulator transition in doped manganites. *Science*, 285(5433):1540, 1999.

[111] M. Uehara, S. Mori, C. H. Chen, and S.-W. Cheong. Percolative phase separation underlies colossal magnetoresistance in mixed-valent manganites. *Nature*, 399:560, 1999.

[112] K. H. Ahn, T. Lookman, and A. R. Bishop. Strain−induced metal−insulator phase coexistence in perovskite manganites. *Nature*, 428:401, 2004.

[113] A. Llobet, C. Frontera, J. L. Garcia-Munoz, C. Ritter, and M. A. G. Aranda. Chemical heterogeneity in a single phase: $Bi_{0.15}Ca_{0.85}MnO_3$, a case example of macroscopic phase segregation. *Chem. Mater.*, 12:3648, 2000.

[114] H. Y. Hwang, S-W. Cheong, P. G. Radaelli, M. Marezio, and B. Batlogg. Lattice effects on the magnetoresistance in doped $LaMnO_3$. *Phys. Rev. Lett.*, 75:914, 1995.

[115] J. B. Goodenough and A. L. Loeb. Theory of ionic ordering, crystal distortion, and magnetic exchange due to covalent forces in spinels. *Phys. Rev.*, 98(2):391, 1955.

[116] G. B. Jensen and O. V. Nielsen. The magnetic structure of Mn_3O_4 hausmannite between 4.7 K and neel point, 41 K. *J. Phys. C: Solid State Phys.*, 7:409, 1975.

[117] T. Suzuki and T.Katsufuji. Magnetodielectric properties of spin−orbital coupled system Mn_3O_4. *Phys. Rev. B*, 77:220402(R), 2008.

[118] M. Kim, X. M. Chen, Y. I. Joe, E. Fradkin, P. Abbamonte, and S. L. Cooper. Mapping the magnetostructural quantum phases of Mn_3O_4. *Phys. Rev. Lett.*, 104:136402, 2010.

[119] M. Kim, X. M. Chen, X. Wang, C. S. Nelson, R. Budakian, P. Abbamonte, and S. L. Cooper. Pressure and field tuning the magnetostructural phases of Mn_3O_4: Raman scattering and x-ray diffraction studies. *Phys. Rev. B*, 84:174424, 2011.

[120] J-H. Chung, K. H. Lee, Y-S. Song, T. Suzuki, and T. Katsufuji. Low temperature structural instability of tetragonal spinel Mn_3O_4. *J. Phys. Soc. Jpn.*, 82:034707, 2013.

[121] D. P. Shoemaker, E. E. Rodriguez, R. Seshadri, I. S. Abumohor, and T. Proffen. Intrinsic exchange bias in $Zn_xMn_{3-x}O_4 (x \leq 1)$ solid solutions. *Phys. Rev. B*, 80:144422, 2009.

[122] B. Chardon and F. Vigneron. Mn_3O_4 commensurate and incommensurate magnetic structures. *J. Magn. Magn. Mater.*, 58:128, 1986.

[123] B. Boucher, R. Buhl, and M. Perrin. Magnetic structure of Mn_3O_4 by neutron diffraction. *J. Appl. Phys.*, 42:1615, 1971.

[124] K. Dwight and N. Menyuk. Magnetic properties of Mn_3O_4 and the canted spin problem. *Phys. Rev.*, 119:1470, 1960.

[125] V. Podzorov, B. G. Kim, V. Kiryukhin, M. E. Gershenson, and S-W. Cheong. Martensitic accommodation strain and the metal−insulator transition in manganites. *Phys. Rev. B*, 64:140406(R), 2001.

[126] M. M. Thackeray, L. A. de Picciotto, A. de Kock, P. J. Johnson, V. A. Nicholas, and K. T. Adendorff. Spinel electrodes for lithium batteries − a review. *J. Power Sources*, 21(1):1, 1986.

[127] Y. Yamasaki, S. Miyasaka, Y. Kaneko, J.−P. He, T. Arima, and Y. Tokura. Magnetic reversal of the ferroelectric polarization in a multiferroic spinel oxide. *Phys. Rev. Lett*, 96:207204, 2006.

[128] J. K. Zhu and Q. M. Gao. Mesoporous MCo_2O_4 (M = Cu, Mn and Ni) spinels: Structural replication, characterization and catalytic application in CO oxidation. *Micropor. and Mesopor. Mat.*, 124:144, 2009.

[129] A. N. Yaresko. Electronic band structure and exchange coupling constants in ACr_2X_4 spinels (A = Zn, Cd, Hg; X = O, S, Se). *Phys. Rev. B*, 77:115106, 2008.

[130] L. Balents. Spin liquids in frustrated magnets. *Nature*, 464:199, 2010.

[131] A. Miller. Distribution of cations in spinels. *J. Appl. Phys.*, 30:24S, 1959.

[132] P. W. Anderson. Ordering and antiferromagnetism in ferrites. *Phys. Rev.*, 102:1008, 1956.

[133] C. Ederer and M. Komelj. Magnetic coupling in $CoCr_2O_4$ and $MnCr_2O_4$: An LSDA+U study. *Phys. Rev. B*, 76:064409, 2007.

[134] G. Shirane and D. E. Cox. Magnetic structures in $FeCr_2S_4$ and $FeCr_2O_4$. *J. Appl. Phys.*, 35:954, 1964.

[135] H. Suzuki and Y. Tsunoda. Spinel type frustrated system $MgCr_2O_4$ studied by neutron scattering and magnetization measurements. *J. Phys. Chem. Solids*, 68:2060, 2007.

[136] K. S. R. C. Murthy, J. Ghose, and E. N. Rao. Reactivity in the spinel formation reaction in CuO/Al_2O_3, Fe_2O_3, Cr_2O_3 systems. *J. Mater. Sci. Lett.*, 2:393, 1983.

[137] L. Q. Yan, Z. W. Jiang, X. D. Peng, L. H. He, and F. W. Wang. Powder x-ray diffraction and Rietveld analysis of $Cd_{1-x}Cu_xCr_2O_4$(0.1 <= x <= 0.7). *Powder Diffr.*, 22:340, 2007.

[138] C. Leighton, J. Nogues, B. J. Jonsson-Akerman, and I. K. Shuller. Coercivity enhancement in exchange biased systems driven by interfacial magnetic frustration. *Phys. Rev. Lett.*, 84:3466, 2000.

[139] J. Nogues and I. K. Shuller. Exchange bias. *J. Magn. Magn. Mater.*, 192:203, 1999.

[140] B. A. Bernevig and S−C Zhang. Quantum spin Hall effect. *Phys. Rev. Lett.*, 96:106802, 2006.

[141] R. Moessner and J. T. Chalker. Low temperature properties of classical geometrically frustrated antiferromagnets. *Phys. Rev. B*, 58:12049, 1998.